



**Politecnico
di Torino**

ScuDo
Scuola di Dottorato ~ Doctoral School
WHAT YOU ARE, TAKES YOU FAR

Doctoral Dissertation
Doctoral Program in Electrical, Electronics and Communications Engineering
(36th cycle)

Design of Pulse Wave Velocity and Blood Pressure Devices for Cardiovascular Health Evaluation

Andrea Valerio

* * * * *

Supervisors

Prof. Danilo Demarchi, Supervisor
Dr. Brendan O'Flynn, Co-supervisor

Doctoral Examination Committee:

Dr. Matteo Menolotto, Tyndall National Institute, University of Cork
Prof. Guido Pagana, MD, LINKS Foundation
Prof. Marco Vacca, Politecnico di Torino
Dr. Fabrizio Riente, Politecnico di Torino
Dr. Stefano Sapienza, University of Luxemburg

Politecnico di Torino
October, 4th, 2024

This thesis is licensed under a Creative Commons License, Attribution - Noncommercial-NoDerivative Works 4.0 International: see www.creativecommons.org. The text may be reproduced for non-commercial purposes, provided that credit is given to the original author.

I hereby declare that, the contents and organisation of this dissertation constitute my own original work and does not compromise in any way the rights of third parties, including those relating to the security of personal data.

.....

Andrea Valerio
Turin, October, 4th, 2024

Summary

Cardiovascular diseases are the leading cause of death worldwide, making the regular monitoring of critical biomarkers like blood pressure and pulse wave velocity (PWV) essential for prevention. This thesis explores new methodologies and hardware/firmware solutions to enhance the accuracy, convenience, and reliability of non-invasive cardiovascular health monitoring systems. The thesis begins with an overview of the motivation, problem statement, objectives, novelty, and research contributions, emphasizing the critical need for precise and accessible cardiovascular health monitoring. A comprehensive literature review follows, covering the physiological background of the cardiovascular system, including the heart, blood vessels, and blood pressure. It examines biosignals analyzed in this research, such as arterial pulse and photoplethysmogram signals, and provides an overview of both invasive and non-invasive methods for assessing PWV and blood pressure (BP). The review highlights the limitations of existing technologies, establishing the context for the advancements proposed.

This thesis addresses key issues in PWV study from hardware, firmware, and software perspectives. It presents the analysis and application of commercial micro force sensors for PWV assessment, detailing operational principles, calibration processes, and experimental setups. Preliminary results form the foundation for developing the PWV acquisition system. A novel wireless system for real-time PWV assessment is introduced, featuring pen-shaped probes using Bluetooth Low Energy protocol for wireless communication. These custom-designed probes include a printed circuit board, a rechargeable battery, and a piezoresistive load cell, enabling efficient data collection and real-time data transmission to a graphical user interface.

Validation against the gold-standard SphygmoCor device demonstrated a strong linear correlation and reliable PWV estimation. The system, designed for clinical usability, includes user-friendly features and a synchronized acquisition process, reducing complexity for clinical personnel and meeting medical safety standards. The thesis also examines the variability and potential inaccuracies in traditional PWV evaluation methods, specifically fiducial points. A novel region-based cross-correlation (RBCC) method is proposed, using signals with consistent shapes for cross-correlation, ensuring constant portions of the signal for PWV calculation

across different sites. The RBCC method showed high accuracy and robustness to noise compared to the intersecting tangent method, validated with data from 75 healthy participants. Research on cuffless BP monitoring was conducted in collaboration with the Wireless Sensors Network Group at Tyndall National Institute, University College Cork. This included developing a custom device for real-time pulse transit time measurement, focusing on the elbow and thumb. A personalized model for detecting blood pressure variations due to physical or cognitive workload was also developed, using data from the custom device to monitor changes accurately. The study highlights the importance of personalized approaches in improving machine learning model predictions for health monitoring.

Additionally, motion artifacts in PPG data were detected using the *catch22* feature subset and anomaly detection algorithms. Personalized models significantly enhanced motion artifact detection performance compared to generalized models, aligning with broader healthcare trends. Key findings of this thesis include the development of a cost-effective, user-friendly device for PWV measurement, robust algorithms for PWV assessment, advancements in non-invasive BP monitoring, and improved long-term monitoring reliability. These contributions represent significant improvements in non-invasive cardiovascular health monitoring, making it more accessible and practical for widespread clinical use.

Acknowledgements

I would like to express my deepest gratitude to my advisor, Professor Danilo Demarchi, for his unwavering support, invaluable guidance, and insightful feedback throughout my Ph.D. journey. His dedication to his students has been a source of immense inspiration and motivation. Thank you for the opportunity to travel the world and for allowing me to see and be part of realities of excellence that have helped make me a better person and researcher.

I am also grateful to Dr. Brendan O’Flynn for welcoming me into his research group. His encouragement, support, and his insistence on pushing my standards to a higher level have significantly contributed to my growth as a researcher. Thank you for providing an environment that fosters excellence and continuous improvement.

I would also like to extend my heartfelt thanks to Dr. Alessandro Sanginario for his invaluable assistance throughout this journey. His valuable feedback has been essential in shaping my research, and his reassuring reminders to not be overly worried have provided much-needed perspective, often revealing that things are better than they initially appear.

My appreciation also goes to Dr. Salvatore Tedesco for his constant dedication to research excellence. His patience and commitment have been inspiring, and his unfiltered teachings have enriched my understanding and skills throughout the duration of the project.

None of this would have been possible without the unconditional love, support, and encouragement of my parents, Giuseppe and Monica, during these years. Thank you for making me the person that I am today.

To my brother Domenico, thank you for being an endless source of inspiration. Your understanding and motivation guided me throughout this incredible and challenging journey.

To my girlfriend, Agustina, for your unwavering sustain, belief in my potential, and cheering me on through the ups and downs over the years. Your strength and perseverance have been vital in helping me overcome challenges and reach my goals. This thesis stands as a testament to your dedication and the countless ways you have contributed to my success. I am deeply grateful for everything you have done for me.

To Mattia, Marco, Gabriele, Bosche, Fabi, Nico, Sara, Andrea, and Umberto. Thank you for your time, suggestions, and each moment of discussion. Most importantly, thank you for creating such a fantastic environment over the past year. Your support has enabled me to tackle each challenge and achieve the results presented in this thesis.

To Alida, Andrea, Luca, Matteo, Marco, Liudmila, Caroline and all the wonderful friends I made in and out the Tyndall National Institute. Thank you for your support, fellowship, and the occasional commiseration! I appreciated all the beautiful experiences we shared together. You gave me the most beautiful and carefree period of my Ph.D. and made me feel at home even when I was far away from it.

*Nothing in this world that is worth
having comes easy.*

Contents

List of Tables	XIV
List of Figures	XVI
Acronyms	XXIV
1 Introduction	1
1.1 Motivation	1
1.2 Problem Statement	2
1.3 Objectives	3
1.4 Novelty and Contribution	3
1.5 Research Contribution	6
2 Literature Review	7
2.1 Physiological Background	7
2.1.1 The heart	8
2.1.2 Blood Vessels	15
2.1.3 Blood Pressure	18
2.2 Analyzed Biosignals	21
2.2.1 Arterial Pulse	21
2.2.2 Photoplethysmogram Signal	23
2.3 Pulse Wave Velocity	28
2.3.1 Invasive PWV Assessments Methods	29
2.3.2 Non-Invasive PWV Assessments Methods	29
2.3.3 Methodology	31
2.3.4 Pulse Transit Time Assessment Techinques	32
2.3.5 Reference PWV Values	35
2.3.6 Commercial Systems for PWV Assessment	37
2.4 Blood Pressure Assessment	45
2.4.1 Advantages of Cuffless Blood Pressure Measurement	48
2.4.2 Uncalibrated models	49
2.4.3 Calibrated models	49

2.4.4	Machine Learning techniques for non-invasive cuffless measurement of blood pressure	51
2.5	Addressing the Challenges in PWV and BP Monitoring: From Literature to Methodology	57
3	MicroForce Sensors for Pulse Wave Velocity Assessment	59
3.1	MicroForce sensors	59
3.1.1	Sensor Data Readout	61
3.1.2	Definition of the Sampling Frequency	63
3.2	Sensor Characterization	64
3.2.1	Experimental setup	64
3.3	Characterization Results	67
3.3.1	Baseline	67
3.3.2	Constant Weight	68
3.3.3	Load/Unload Cycle	69
4	Wireless Device for Pulse Wave Velocity Assessment	73
4.1	Introduction	73
4.2	Proposed System	75
4.2.1	The Hardware	76
4.2.2	The Firmware	82
4.2.3	Graphic User Interface for PWV assessment	84
4.2.4	Testing Phase	85
4.2.5	Precompliance CE Tests	87
4.3	System Assessment	89
4.3.1	Pre-compliance CE Test	95
4.3.2	Benchmark Comparison	97
4.4	Conclusion	98
5	Algorithms for assessing Pulse Wave Velocity	101
5.1	Introduction	102
5.2	Material and Methods	104
5.2.1	Experimental Data	104
5.2.2	Proposed Algorithm	104
5.2.3	Robustness of the Algorithm	108
5.2.4	Identification of Processing Window	108
5.2.5	Statistical Analysis	110
5.3	Results	113
5.3.1	Processing Window Assessment	113
5.3.2	Pulse Wave Velocity Assessment	114
5.4	Discussion	116
5.4.1	Processing Window Assessment	116

5.4.2	Pulse Wave Velocity Assessment	117
5.5	Conclusions	121
6	Innovations in Personalized Machine Learning for Cuffless Blood Pressure Monitoring and Motion Artifact Detection	123
6.1	Development of a custom PPG acquisition system for real-time estimation of PTT	124
6.1.1	The Hardware	124
6.1.2	Mechanical Design to Control the Contact Pressure	126
6.1.3	The Algorithm	127
6.1.4	System for Validation: Biosignal Flux	130
6.1.5	System Assessment	132
6.2	Development of a personalized model to detect blood pressure variations associated with physical or cognitive workload	134
6.2.1	Cognitive Tests	134
6.2.2	Data Collection Protocol	136
6.2.3	Data Processing	139
6.2.4	Model Training	145
6.2.5	Evaluation Metrics	147
6.2.6	Data Processing Results	148
6.2.7	Model Evaluation Results	149
6.2.8	Discussion	152
6.3	Development of a personalized anomaly detection model to detect motion artifacts over PPG data using <i>catch22</i> features	158
6.3.1	<i>catch22</i> Features Set	159
6.3.2	Methodology	159
6.3.3	Tested Anomaly Detection Models	160
6.3.4	Evaluation Metrics	161
6.3.5	Data Quality Assessment Results	162
6.3.6	Anomaly detection Models Evaluation	162
6.3.7	Discussion	165
7	Discussion, Future Works and Conclusions	169
7.1	Thesis Contributions	169
7.1.1	Cost and Accessibility	169
7.1.2	Variability and Inaccuracies in Traditional Methods	170
7.1.3	Limitations of Traditional Cuff-Based Devices for BP Monitoring	173
7.1.4	Capturing Individual-Specific Variations in BP Monitoring	174
7.1.5	Challenges in Long-Term Monitoring	176
7.2	Future Works	177
7.2.1	Pulse Wave Velocity	177

7.2.2 Cuffless Blood Pressure Assessment	178
7.3 Conclusions	179
A PCB Schematics Wireless System for PWV Assessment	181
B Results of Generalized and Personalized Strategies for Cuffless BP Assessment	187
C Clinical Usability Questionnaire	197
Bibliography	201

List of Tables

2.1	Classification of office Blood Pressure (BP) and definitions of hypertension grade in adults [17].	20
2.2	Fiduciary points of arterial pulse wave used for pulse transit time measurement.	33
2.3	Distribution of pulse wave velocity (m/s) according to the age category in the normal values population (1455 subjects), [79].	36
2.4	Distribution of PWV values(m/s) in the reference value population (11092subjects) according to age and blood pressure categories, [79].	36
2.5	Normal and reference values of PWV parameters for cfPWV and baPWV [80].	37
2.6	PWV values s for men and women, according to age categories, in individuals with and without major CVRF [81]	38
2.7	Overview of the current systems for PWV assessment detailing the recording methodology, acquisition sites, adopted sensing technology, and PTT computation technique.	44
3.1	Diagnostic states in data readout [131].	62
3.2	Tested sampling frequencies, displaying the percentages of stale measurements relative to the total measurements acquired over a 30-second period. The number of incorrect measurements for each frequency is indicated in parentheses.	64
3.3	Mean value and standard deviation of the baseline without weights for the 5N and 15N force range sensors.	67
3.4	Mean value and standard deviation of the baseline for the 5N sensor at each weight in a constant load application.	68
3.5	Mean value and standard deviation of the baseline for the 15N sensor at each weight in a constant load application.	69
4.1	Averaged current absorption in different working modalities.	91
4.2	Results of the validation process	93
4.3	Results from the focus group interview were used to evaluate the clinical usability of the device. Scores for each physician were obtained using a guided response questionnaire. A lower score on the 0 to 4 scale indicates a more favorable opinion of the device.	96

4.4	Reference systems for Non-invasive PWV Assessment.	99
5.1	Indicators employed in the processing window's upper boundary assessment	113
5.2	Clinical characteristics of the study population	114
5.3	Accuracy of cfPWV estimated values compared to those extracted by the reference method (SphygmoCor).	115
6.1	Features of the Biosignal Flux 8-Channels hub [192].	130
6.2	Features of the Biosignal Flux BVP sensor [193].	131
6.3	Features of the Biosignal Flux fNIRS sensor [194].	131
6.4	Overview of the characteristics of the study population	133
6.5	System Assessment's Results	133
6.6	Overview of the characteristics of the study populations.	137
6.7	Criteria for identifying fiducial points on PPG pulse waves.	143
6.8	Definition of the extracted features from PPG pulse wave.	144
6.9	Definition of the extracted features from first and second derivatives of PPG pulse waveform.	145
6.10	Data processing results.	149
6.11	Averaged Reference Blood Pressure Values.	149
6.12	Averaged evaluation metrics per each model.	151
6.13	Computed evaluation metrics per each anomaly detection model.	162
B.1	Test set Results using the person independent model (PIM).	188
B.2	Test set results using person specific model PSM_{SD}	189
B.3	Test set results using person specific model $PSM_{5,30\%}$	190
B.4	Test set results using person-specific model $PSM_{10,30\%}$	191
B.5	Test set results using person-specific model $PSM_{15,30\%}$	192
B.6	Test set results using person specific model $PSM_{5,50\%}$	193
B.7	Test set results using person-specific model $PSM_{10,50\%}$	194
B.8	Test set results using person-specific model $PSM_{15,50\%}$	195

List of Figures

2.1	Section of the heart showing the atria, ventricles, atrioventricular valves, and connections to major blood vessels.	8
2.2	Blood circulation through the cardiovascular system. Pulmonary circulation, systemic circulation, and major blood vessels are reported. Arrows indicate the direction of blood flow.	9
2.3	Propagation of action potentials in the heart. (a) Onset of the action potential in the SA node. (b) Conduction of the action potential up to the atrial muscle. (c) Action potentials propagate through the atria to the AV node. (d) Action potentials travel through the conduction system to the apex of the heart. (e) Action potentials diffuse through the ventricular muscle. (f) Repolarization of the heart muscle until a new action potential is generated.	11
2.4	The cardiac cycle. Diastole corresponds to phases 4 and 1, while systole occupies phases 2 and 3. AV valves close when ventricular pressure exceeds atrial pressure. The aortic valve opens when ventricular pressure exceeds aortic pressure and closes under opposite conditions. The maximum pressure within the aorta is the Systolic Blood Pressure (SBP), the minimum pressure is the Diastolic Blood Pressure (DBP). The mean pressure during the cycle is the Mean arterial Pressure (MAP). The volume of blood pumped from the ventricle with each beat corresponds to the ventricular ejection volume (SV). This corresponds to the difference between the volume reached at the end of diastole, or telediastolic (EDV), and the volume reached at the end of systole, or telesystolic (ESV).	13
2.5	Physiological Electrocardiographic (ECG) waveform showing the P, Q, R, S, T waves, segments and intervals.	15
2.6	Detection of electrical activity of the heart at different locations in the cardiac muscle.	15

2.7	Coloured scanning electron micrograph (SEM) depicting a cross-section of a small human artery, or arteriole. Within the central lumen, red blood cells and some fibrin fibres are visible. The innermost wall, the tunica intima, appears thin and folded, consisting of an endothelial lining and a slender, elastic layer. Encircling this is the thicker tunica media layer, primarily composed of smooth muscle cells, seen here in pink. The outermost tunica adventitia layer blends with the adjacent connective tissue. These structural layers allow the arteriole to contract and expand, thereby regulating arterial BP [14].	16
2.8	Overview of the anatomical differences between different blood vessels.	17
2.9	Atrial, ventricular, and aortic pressure diagram within a single cardiac cycle.	18
2.10	Role of arteries as pressure reservoirs. (a) During systole, the BP in the left ventricle is greater than the aortic pressure. Blood, after entering the aorta, increases its volume, causing its walls to expand. (b) During diastole, the elastic return of the walls pushes the blood forward [11].	19
2.11	Analysis of central pulse pressure waveform [25].	22
2.12	Schematic representation of Lambert-Beer law in a multilayer medium [28].	24
2.13	Transmission versus reflectance PPG modes: the intensity of light received at the photodiode is modulated by the changes in pulsating blood volume occurring in the illuminated tissue.	26
2.14	Principle of Photoplethysmography (PPG) generation and waveform features [36].	27
2.15	PWV acquisition methodologies. (a) The <i>simultaneous acquisition</i> is commonly performed by detecting a characteristic feature on each pulse wave, Then, Pulse Transit Time (PTT) is computed as the delay occurring between pulses. (b) The <i>sequential acquisition</i> employs a single sensor and reference signal ECG. The transit time is evaluated as the difference between the Pulse Arrival Time (PAT) per acquisition site. PAT is defined as the time interval between the R-peak of the ECG and the sequentially detected pulse waveforms on the carotid and femoral artery, respectively. PAT encompasses the duration for the pulse wave to move from the aorta to the measurement location ($t_{R-pulse}$), as well as the pre-ejection period (<i>PEP</i>).	32
2.16	(a) Sphygmocor CvMS device. (b) Sphygmocor XCEL device. [82]	38
2.17	Complior device. [84]	40
2.18	Pulse Pen device. [86]	40
2.19	Arteriograph acquisition system. [87]	41

2.20	Conventional BP measurement methods. Standard or widely used methods include catheterization (a), auscultation (b), and oscillometry (c). Volume clamping (d) and tonometry (e) are less common methods for noninvasive measurement of the BP waveform. All the noninvasive methods require an inflatable cuff, which is not readily available and cumbersome to use. Abbreviations: AD, oscillogram amplitude when cuff pressure is at DBP; AM, maximum oscillogram amplitude; AS, oscillogram amplitude when cuff pressure is at SBP; BP, blood pressure; DBP, diastolic BP; F, force; LED, light-emitting diode; MP, mean BP; PD, photodetector; Pi, internal BP; PPG, photoplethysmography; SBP, systolic BP; t, time; T, arterial wall tension [95].	46
3.1	FMAMSDXX005WCSC3 load cell. (a) Isometric view. (b) Cross-section view highlighting the main components of the sensors. . . .	60
3.2	FMAMSDXX005WCSC3 load cell size comparison.	60
3.3	SPI sensor data readout [130].	61
3.4	Two-Byte force data payload [131].	62
3.5	Optimal range of use of the sensor [132].	63
3.6	Assembly of the support system. (a) Section of assembly of the support system. Circled in red there is the sensor, with below the PCB on which it is soldered in yellow. (b) Isometric view.	66
3.7	Experimental set-up for sensor's characterization.	66
3.8	Constant load application for sensor's characterization.	67
3.9	Voltage output without weights for the 5N (blue) and 15N (red) force range sensors.	68
3.10	Characterization curve of the load cell with constant weights (10g, 20g, 50g, 100g, 200g, 500g) for the 5N (blue) and 15N (red) force range.	69
3.11	Load/Unload cycles with a weight of 20 grams (5 N sensor).	70
3.12	Load/Unload cycles with a weight of 50 grams (5N sensor).	70
4.1	Overview of the first generation the Athos device [139].	74
4.2	Wireless Device for Pulse Wave Velocity Assessment [134].	76
4.3	Acquisition probe overview. (a) Encapsulated load cell used for pulse wave detection. (b) Custom PCB designed to collect and transfer data. (c) Rechargeable polymer Lithium-Ion battery.	77
4.4	Top and bottom views of the PCB layout for the Athos system acquisition probe. (a) Top view. (b) Bottom view.	78

4.5	RF subsystem. (a) Physical layout of the RF section of the PCB, showing the placement of RF components along with the meander antenna. (b) PCB layout highlighting the RF trace and ground vias placements. (c) Schematic diagram of the RF circuitry, including the antenna matching network and low-pass filter, designed to ensure optimal impedance matching and harmonic rejection for the microcontroller unit (MCU)'s RF pin.	79
4.6	Close-up view of the PCB layout detailing the RF trace and component placement. The image highlights critical dimensions such as trace widths, spacing between traces, and via placements to ensure proper impedance matching and minimize parasitic effects.	79
4.7	Recharging station designed for the tested device. (a) Designed PCB connected to USB-Dongle MB1293. (b) PCB top view. (c) PCB bottom view.	81
4.8	Recharging station designed for the tested device. The hardware solution relies on bidirectional sensing between the two MCUs embedded in the acquisition probes, enabling a synchronous initiation of the acquisition process. When one of the components is disconnected from the base, it prompts the initiation of the acquisition process. The USB-Dongle, integrated into the main PCB within the base station, enables BLE communications among all system components.	81
4.9	Schematization of force data management. Bluetooth Low Energy (BLE) payloads sent by the acquisition probes are received and allocated into a circular buffer by the USB-Dongle. The samples are reorganized and sent to GUI via USB connection for real-time processing.	83
4.10	Report generated at the end PWV study.	84
4.11	Current absorption of the acquisition probe during the different function modalities: Advertising, connection, and streaming.	85
4.12	Experienced physician performing PWV assessment using the Athos system.	87
4.13	Anechoic chamber used to assess the electromagnetic compatibility of the system.	88
4.14	Observed delay between carotid (yellow) and femoral (blue) probes at the acquisition start-up using the proposed hardware solution.	89
4.15	Discharge curve of the CELLEVIA BATTERY LP401235 under a pure resistive and constant load.	90
4.16	Events occurring during the <i>streaming</i> mode: BLE connection interval, SPI activity, force data buffer ready to be transferred.	91

4.17	Result of <i>data management</i> routine in the 20-minute acquisition used to validate the data transfer process. No reported cases of lost BLE packets or probe misalignment were observed during this procedure	92
4.18	Scatter plot confronting the averaged PWV values obtained for each recruited subject. A linear regressive model fitted on the available data points shows a strong linear correlation between the two devices.	94
4.19	Bland-Altman plot of the difference between the performances given by the SphygmoCor and the proposed device.	94
4.20	Results of focus group interview to assess the clinical usability of the device. Scores were retrieved for each physician through the guided response questionnaire. A lower score on a scale ranging from 0 to 4 corresponds to a favorable opinion of the device.	95
5.1	Pulse waveforms alignment performed using cross-correlation. Given the carotid pulse (Blue) and the femoral pulse (Green), the cross-correlation function is computed for each value of τ . The timeshift's equivalent which leads to the maximum of the cross-correlation function is taken as pulse transit time, then the alignment is performed.	103
5.2	Illustration of the presented Region-Based Cross-Correlation (RBCC) algorithm divided into its macro stages: <i>pre-processing</i> , <i>processing</i> and <i>evaluation of the outcome</i>	105
5.3	Region Based Cross-Correlation (RBCC) algorithm processing steps. (a) Result of the bandpass filtering procedure: original signal (blue), filtered signal (red). (b) Individuation of the cardiac activity (green points) on the low pass filtered carotid signal (red). (c) Carotid signal (blue) and femoral signal (green) are split into single epochs. (d) Detection of the processed windows on both signals in the current epoch. (e) Processed carotid window. (f) Processed femoral window. (g) Evaluation of the delay through the application of the cross-correlation technique on the mentioned windows. (h) Alignment of the processed signals in the current epoch.	107
5.4	Degradation of the original carotid pulse waveforms (blue window) by introducing noise to achieve SNRs of 10 (red window), 15 (yellow window), 20, and 25 (green window) dB.	109
5.5	Selected points used for the definition of the processing window. End of the diastole (A), the maximum of the first derivative (B1) and the 95% of the systolic peak amplitude (B2). The slope coefficient γ has been computed as the angle between the horizontal line and the tangent line passing through successive samples on the signal. The value assumed by γ in B1 and B2 was defined as γ_{B1} and γ_{B2}	110

5.6	Mean absolute error and related standard deviation associated to carotid-femoral Pulse Wave Velocity (cfPWV) values computed at different Signal to Noise Ratio (SNR)s with respect to those obtained using Intersecting Tangent (IT) and Region Based Cross Correlation (RBCC) on noise-free signals	116
5.7	Percentage coefficient of variation CV computed respectively in B1 and B2, on carotid (blue) and femoral (red) pulses. (a) CV extracted for the slope γ . (b) CV extracted for amplitude values.	117
5.8	(a) Intra-Subject Variability computed for γ respectively in B1 and B2. (b) Inter-Subject Variability computed for γ , respectively in B1 and B2, on carotid (blue) and femoral (red) pulses.	118
5.9	Relationship between cfPWV estimated by the Intersecting Tangent algorithm used by the Athos device and the reference method. (a) Best fitted line (in red) retrieved from the linear regressive model fitted on the experimental data. (b) Bland-Altman plots show the distribution of the averaged measurements differences.	119
5.10	Relationship between cfPWV estimated by the Direct application of Cross-Correlation (DCC) approach and the reference method. (a) Best fitted line (in red) retrieved from the linear regressive model fitted on the experimental data. (b) Bland-Altman plots show the distribution of the averaged measurements differences.	119
5.11	Relationship between cfPWV estimated by the Region Based Cross-Correlation (RBCC) algorithm and the reference method. (a) Best fitted line (in red) retrieved from the linear regressive model fitted on the experimental data. (b) Bland-Altman plots show the distribution of the averaged measurements differences.	120
6.1	System employed to collect PPG raw data from the selected sites, elbow (brachial artery) and thumb (digital artery).	125
6.2	Thumb sensor employed to detect pulse waveform from the digital artery. (a) Sensor's enclosure positioned on the hand of the subject under investigation. (b) Finger clip enclosure for the thumb sensor.	126
6.3	Elbow sensor employed to detect pulse waveform from the brachial artery. (a) Sensor's enclosure positioned on the elbow of the subject under investigation. (b) Elbow sensor enclosure for the thumb sensor. (c) Adjustable screw and rotating head to adjust the sensor's orientation.	126
6.4	Graphic User Interface used by the device in the BP assessment. The upper plots show the thumb signal (red) and elbow signal (blue). Bottom plots depict the intersecting tangent being extracted from gathered signals for PTT estimation.	127
6.5	Flowchart of the algorithm implemented to detect the intersecting tangent point (ITP).	129

6.6	Biosignal Flux Acquisition system. (a) 8-channel Hub. (b) Blood Volume Pressure (BVP) sensor. (c) fNIRS sensor.	130
6.7	Averaged PTT values retrieved for the 5 subjects involved in the trial. Each point represents the mean value of the three acquisitions executed with both systems. The error bars report the standard deviation.	132
6.8	Bland-Altman plot of the differences between the outcomes retrieved by the reference device and the proposed device.	132
6.9	Cognitive test employed to induce a blood pressure variation. (a) Stroop test. (b) N-Back test.	136
6.10	Recommendations for BP measurements [16].	137
6.11	Data collection protocol followed in this study along with the evolution of the averaged pulse waveforms morphology according to each section of the data capture.	138
6.12	Data processing pipeline followed to analyze the collected PPG data.	139
6.13	Data segmentation routine pipeline. (a) The raw PPG signal from the thumb (blue) and its low-pass filtered version (green) over a 3-second time window. (b) The low-pass filtered PPG signal (green) and its first derivative (red dashed) within a specific epoch (i-th epoch). (c) Detailed identification of the diastolic minimum within the region of interest, using the low-pass filtered PPG signal (green) and its first derivative (red dashed). (d) Result of the detection of the diastolic minima employed for the final segmentation.	140
6.14	Extraction of the template from PPG waveforms collected from brachial (left) and digital (right) arteries.	142
6.15	(a) Feature extracted from a PPG waveform (b) Maximum of the first derivative (ms) detected on the velocity plethysmography (VPG) (c) Fiducial points detected on the acceleration plethysmography (APG).	142
6.16	Validation of the positions of fiducial points on high-quality PPG waveforms collected from the elbow (left) and thumb (right) sites. .	143
6.17	Overview of the tested training strategies. (Left) Workflow employed for the generalized approach (PIM). (Center) Tested combinations for Person-Specific Strategies (PSM). (Right) Workflow adopted by every $PSM_{i,j}$	146
6.18	Definition of true positives (TP), false positives (FP), false negatives (FN), and true negatives (TN) instances in a multiclass problem. (a) REST class. (b) Cognitive task (CT) class. (c) After exercise (AE) class.	147
6.19	Values of evaluation metrics (Accuracy, Precision, Recall, and F1-score) according to the training strategy denoted as PSM_{SD}	150

6.20	Averaged values of accuracy score according to different combinations of number of source subjects and diverse fractions of data employed to personalize the RF model.	152
6.21	Comparison of performance metrics (Accuracy, Precision, Recall, and F1-Score) between the Person-Independent Model (PIM) and various Person-Specific Models (PSM). The dashed blue line at 0.95 indicates the threshold employed to discard PSM configurations with unsatisfactory performance.	153
6.22	Evaluation metrics computed per each individual employing a fraction of the target-subject data set equal to 30% and a diverse number of source subjects (N). (a) N=5. (b) N=10. (c) N=15.	155
6.23	Evaluation metrics computed per each individual employing a fraction the target-subject data set equal to 50% and diverse number of source subjects (N). (a) N=5. (b) N=10. (c) N=15.	156
6.24	Motion artifacts distribution across recruited subjects.	161
6.25	F1-score computed for target class across subjects displaying the presence of motion artifacts.	163
6.26	Precision score computed for target class across subjects displaying the presence of motion artifacts.	163
6.27	Recall score computed for target class across subjects displaying the presence of motion artifacts.	164
6.28	Data points distribution between subjects with different quality of pulse waveforms.	164
6.29	Pulse waveforms acquired from subject #17 and subject #8 in blue and green respectively.	165
6.30	Principal component analysis employed to highlight the intrinsic discrepancies between normal data belonging to different subjects. . .	166
6.31	Target class aggregated evaluation metrics computed per each anomaly detection model.	166
A.1	182
A.2	183
A.3	184
A.4	185
A.5	186

Acronyms

AD Anomaly Detection

AE After Exercise phase

ANS Autonomic nervous system

aoPWV aortic Pulse Wave Velocity

BLE Bluetooth Low Energy

BP Blood Pressure

baPWV brachial-ankle Pulse Wave Velocity

CABP central aortic blood pressure

cfPWV carotid-femoral Pulse Wave Velocity

CNN Convolutional Neural Network

CKD Chronic Kidney Diseases

CT Cognitive Testing phase

CVDs Cardiovascular Diseases

CVS Cardiovascular System

DBP Diastolic Blood Pressure

DCC Direct Cross Correlation

DTW Dynamic Time Warping

ECG Electrocardiographic

GUI Graphical User Interface

IF Isolation Forest

ITP Intersecting Tangent Point
HMOD Hypertensive Organ damage
KNN K-Nearest Neighbour
LMICs Low- and Middle-Income Countries
LOF Local Outlier Factor
LSTM Long Short-Term Memory
MAs Motion Artifacts
MAP Mean arterial Pressure
MCU microcontroller unit
ML Machine Learning
OC-SVM One-Class Support Vector Machine
PAT Pulse Arrival Time
PCB Printed Circuit Board
PIM Person Independent Models
PPG Photoplethysmography
PSM Person Specific Models
PTT Pulse Transit Time
PWV Pulse Wave Velocity
PWA Pulse Wave Analysis
RBCC Region-Based-Cross-Correlation
REST REST phase
RNN Recurrent Neural Network
SBP Systolic Blood Pressure
SNR Signal to Noise Ratio
SPI Serial Peripheral Interface
SVM Support Vector Machine

Chapter 1

Introduction

1.1 Motivation

Cardiovascular Diseases (CVDs) are the leading cause of death worldwide, claiming an estimated 17.9 million lives annually [1]. These diseases encompass a range of heart and blood vessel disorders, including coronary heart disease, cerebrovascular disease, and rheumatic heart disease, among others. Over 80% of CVD-related deaths are due to heart attacks and strokes, with one-third of these fatalities occurring prematurely in individuals under 70 years of age.

The World Health Organization (WHO)/Europe report [2] highlights a significant gender disparity in CVD mortality, with men in the region being almost 2.5 times more likely to die from CVDs than women [3]. Geographically, the risk of premature death (ages 30-69) from CVD is nearly five times higher in Eastern Europe and Central Asia compared to Western Europe [4]. Hypertension, or elevated blood pressure (BP), is a medical condition that significantly increases the risks of coronary heart disease such as stroke and heart failure [5]. It is regarded as the primary risk factor for death and disability in the European Region, accounting for almost a quarter of deaths and 13% of disability. Often asymptomatic, uncontrolled high BP can lead to severe outcomes such as heart attacks and strokes [6]. Given the high prevalence of hypertension, implementing effective health system interventions is essential for optimizing healthcare resource utilization. Targeting limited financial and workforce resources toward individuals most vulnerable to heart attacks, strokes, and heart failure is crucial [7]. This approach is vital for resource-constrained settings and Low- and Middle-Income Countries (LMICs) [8]. A total cardiovascular risk approach, which considers a combination of risk factors, can effectively address this need [9].

Therefore, regular monitoring of critical biomarkers, such as BP and Pulse Wave Velocity (PWV), is essential in preventing the insurgence of CVDs. By incorporating these assessments into routine health check-ups, healthcare providers can significantly improve the ability to detect and manage the onset and progression

of CVDs. This proactive approach enhances patient outcomes and reduces overall healthcare costs by preventing severe complications and promoting efficient use of resources [10].

1.2 Problem Statement

This section provides a brief overview of the problem statements relevant to this body of work, setting the context for the upcoming sections. These issues will be elaborated upon in detail in Chapter 2. Specifically, the issues that formed the basis for this research project are reported below:

- **Cost and Accessibility:** The integration of PWV measurements into routine medical practice faces significant hurdles, primarily due to the complexity and time required to perform these measurements. Despite the recognized importance of PWV in assessing arterial stiffness and cardiovascular risk, its adoption in clinical environments is limited. Advanced non-invasive devices, although highly accurate, are often prohibitively expensive and not readily available in all healthcare settings. These cost and accessibility issues hinder the widespread use of PWV measurements.
- **Variability and Inaccuracies in Traditional Methods:** Traditional methods for PWV measurement typically rely on point-to-point feature extraction. This approach can introduce variability and inaccuracies due to the differing morphologies of pulse waveforms at various arterial sites. The estimation of carotid-femoral Pulse Wave Velocity (cfPWV) is particularly susceptible to noise and artifacts, which can significantly compromise the reliability of the measurements. Such inaccuracies limit the effectiveness of PWV as a diagnostic tool in clinical practice.
- **Limitations of Traditional Cuff-Based Devices:** While effective for on-the-spot BP measurements, traditional cuff-based devices are impractical for continuous monitoring. These devices are cumbersome and intrusive, making them unsuitable for long-term use. Continuous monitoring is crucial for managing hypertension and assessing cardiovascular risk, yet the current devices do not provide the necessary comfort and convenience for patients to use them over extended periods.
- **Capturing Individual-Specific Variations in BP Monitoring:** Current BP monitoring methods fall short in capturing individual-specific variations, which are crucial for precise BP management and cardiovascular risk assessment. Personalized approaches are necessary to account for these variations, yet existing methods do not effectively address this need. Improving the accuracy

and reliability of BP monitoring requires models that can accommodate the unique physiological characteristics of each individual.

- **Challenges in Long-Term Monitoring:** A major challenge in long-term monitoring systems, especially in real-world conditions, is the ability to distinguish high-quality signal windows from those affected by motion artifacts. Wearable health monitoring devices, such as those using photoplethysmography PPG sensors, often suffer from signal degradation due to motion artifacts. These artifacts can result from changes in blood flow velocity, relative movement between the sensor and the skin, and low tissue perfusion. Traditional filtering techniques are often inadequate for effectively addressing these issues.

1.3 Objectives

The aim of this thesis is to investigate new methodologies and hardware/firmware solutions aimed at improving the accuracy, convenience, and reliability of non-invasive cardiovascular health monitoring systems.

Specifically, this research project examines two deeply interconnected macro-themes: the estimation of Pulse Wave Velocity and BP monitoring.

The investigation of the first biomarker focuses on the main issues related to the cost, accessibility, and reliability of the reference methodology for PWV assessment. Therefore, the first objective is the development of an affordable and user-friendly device capable of meeting the requirements for reliable estimation. The second objective involves the implementation of an algorithm capable of ensuring accurate PWV evaluation in the presence of noise and motion artifacts.

Concerning BP monitoring, one primary objective is to develop a non-intrusive, long-term BP monitoring system. Traditional cuff-based devices, while effective for single measurements, are cumbersome and intrusive for continuous monitoring, making them unsuitable for long-term use. This research seeks to create a system that allows for comfortable and continuous BP monitoring over extended periods.

Then, a further objective is to enhance the accuracy of BP management by improving current monitoring methods to effectively capture individual-specific variations. Finally, The research aims to develop advanced techniques to reliably identify and separate high-quality signals from noisy data, ensuring accurate and reliable monitoring.

1.4 Novelty and Contribution

The novelty and contribution to the body of knowledge resulting from the present thesis are introduced below in order of appearance:

- Chapter 3 presents the carried-out analysis concerning the application of commercial micro force sensors in assessing PWV. As the first step, this work delves into the operational principles of FMA MicroForce sensors, elaborating on their structure, functionality, and the hardware setup necessary for data acquisition. It discusses the calibration processes and the specific conditions under which these sensors were tested, ensuring the reliability and accuracy of the data collected. The chapter proceeds to describe the experimental setup used for sensor characterization, highlighting the detailed calibration methods involving weights and load/unload cycles. It further explores the preliminary results obtained from these sensor characterizations, providing insights into their performance under various conditions. These results are crucial as they form the foundation for subsequent improvements and the development of the PWV acquisition system, which is elaborated on in the following chapter.
- Chapter 4 introduces a novel wireless system for real-time Pulse Wave Velocity assessment, significantly improving upon existing devices. The system features two pen-shaped probes that use BLE 5.2 for wireless communication, enhancing portability and ease of use. The custom-designed probes include a Printed Circuit Board (PCB), a rechargeable battery, and a piezoresistive load cell, enabling efficient data collection. The wireless setup allows real-time data transmission to a receiving station with a Graphical User Interface (GUI) that provides immediate feedback, facilitating real-time PWV assessment. Validation against the gold-standard SphygmoCor device demonstrated a strong linear correlation and reliable PWV estimation. The system is designed to enhance clinical usability with a user-friendly GUI, real-time feedback, and a synchronized acquisition process. The probes and charging station are engineered for easy handling and efficient operation, reducing the learning curve and operational complexity for clinical personnel. Additionally, the device underwent rigorous electromagnetic compatibility tests and clinical usability evaluations, ensuring compliance with medical device safety standards, making it a significant advancement in non-invasive arterial stiffness assessment for cardiovascular health.
- Chapter 5 introduces a Region-Based-Cross-Correlation (RBCC) approach for assessing cfPWV, which departs from traditional point-to-point feature extraction methods. This new algorithm processes a specific window of the carotid and femoral signals and employs cross-correlation to compute the Pulse Transit Time (PTT). This technique enhances robustness against noise and artifacts, ensuring greater stability and reliability in the measured cfPWV values compared to existing methods. This study emphasizes the use of a standardized and methodical approach to identify the optimal processing window on the pulse waveform, which is less affected by reflected waves and motion artifacts. Finally, the proposed method was validated using a dataset of 75

healthy participants and demonstrated excellent accuracy a mean difference of only 0.16 m/s when compared to the gold-standard SphygmoCor device. The region-based approach showed significantly lower errors in the presence of added noise, highlighting its robustness and suitability for clinical applications. This represents a significant advancement over traditional algorithms that rely on single features of the pulse wave, which can lead to variability and inaccuracies in cfPWV measurements.

- Chapter 6 addresses the challenge of accurately and comfortably monitoring BP over long periods using conventional cuff-based devices. While effective for on-the-spot measurements, these devices are cumbersome and unsuitable for continuous monitoring due to their intrusive nature. To overcome this limitation, a novel hardware and software system utilizing PPG sensors to estimate PTT from brachial and digital arteries is introduced. This system stands as a starting point to provide a more convenient, non-invasive method for real-time BP monitoring, addressing the discomfort and impracticality associated with traditional cuff-based methods. The goodness of data captured through the proposed is validated through a preclinical study, comparing its performance with a reference device.

Then, a personalized multiclass classification model is introduced to detect BP variations associated with physical or cognitive workload. The current methods for BP monitoring face limitations in capturing individual-specific variations, which are crucial for precise BP management and cardiovascular risk assessment. The key innovation lies in using a personalized machine learning approach, employing random forest classifiers calibrated to individual physiological characteristics, which significantly improves classification accuracy. The study explores various pre-training strategies that incorporate data from multiple subjects, enhancing the model's robustness and reducing the data required for effective personalization. The personalized models demonstrated high accuracy and reliability, achieving over 95% accuracy with only a fraction of the data typically needed.

Finally, the problem of Motion Artifacts (MAs) detection over physiological data is examined. This issue is known for significantly impacting the accuracy of wearable health monitoring systems. PPG sensors, commonly used in wearable devices for tracking physiological parameters such as heart rate, oxygen saturation, and BP, often suffer from signal degradation due to motion artifacts. These artifacts arise from changes in blood flow velocity, relative movement between the sensor and skin, and low tissue perfusion, making traditional filtering techniques inadequate. For this purpose, a personalized anomaly detection model using a high-performing subset of time-series features called *catch22* was developed to detect the presence of MAs motion artifacts in PPG data. The study employs three unsupervised algorithms—

One-Class Support Vector Machine (OC-SVM), Isolation Forest (IF), and Local Outlier Factor (LOF) —to identify anomalies. By focusing on these methods, this work aims to improve the reliability of PPG-based health monitoring by effectively distinguishing high-quality signal windows from those affected by motion artifacts. This approach is particularly valuable for long-term health monitoring in real-world conditions, where traditional methods fall short.

1.5 Research Contribution

The resulting research contributions from which this body of work is originated are reported below:

- Live Demonstration: Wireless Device for Clinical Pulse Wave Velocity Evaluations. Valerio, A., Buraioli, I., Sanginario, A., Leone, D., Mingrone, G., Milan, A., Demarchi, D. (2022). 2022 IEEE Biomedical Circuits and Systems Conference (BioCAS), 247–247.
- A New True Wireless System for Real-Time Pulse Wave Velocity Assessment. Valerio, A., Buraioli, I., Sanginario, A., Mingrone, G., Leone, D., Milan, A., Demarchi, D. (2024) in IEEE Sensors Journal, vol. 24, no. 15, pp. 24365–24376, 1 Aug.1, 2024.
- A region-based cross-correlation approach for tonometric carotid–femoral Pulse Wave Velocity Assessment. Valerio, A., Buraioli, I., Sanginario, A., Mingrone, G., Leone, D., Milan, A., Demarchi, D. (2024). Biomedical Signal Processing and Control, 93, 106161.
- Development of a PPG-based hardware and software system deployable on elbow and thumb for real-time estimation of pulse transit time. Valerio, A., Hajzeraj, A., Talebi, O. V., Belcastro, M., Tedesco, S., Demarchi, D., O’Flynn, B. (2023). 2023 45th Annual International Conference of the IEEE Engineering in Medicine and Biology Society (EMBC).
- Development of a Personalized Multiclass Classification Model to Detect Blood Pressure Variations Associated with Physical or Cognitive Workload. Valerio, A., Demarchi, D., O’Flynn, B., Motto Ros, P., Tedesco, S. (2024). Sensors, 24(11), 3697.
- Development of a personalized anomaly detection model to detect motion artifacts over PPG data using catch22 features. Valerio, A., Demarchi, D., O’Flynn, B., Tedesco, S. IEEE Sensors Conference 2024. Accepted in August 2024.

Chapter 2

Literature Review

2.1 Physiological Background

The Cardiovascular System (CVS) is responsible for supplying blood throughout the body. The cardiovascular system comprises the heart, arteries, veins, and capillaries. These components work together to ensure proper circulation across all regions of the body. The regulation of this system is influenced by a wide range of stimuli, including variations in blood volume, hormones, electrolytes, osmolarity, medications, as well as activity from the adrenal glands and kidneys. In addition, the parasympathetic and sympathetic nervous systems play a pivotal role in governing cardiovascular function [11]. The CVS can be subdivided into two main loops: systemic and pulmonary circulation. Pulmonary circulation allows for the oxygenation of the blood, while systemic circulation provides oxygenated blood and nutrients to reach the rest of the body. The cardiovascular system's main functions can be summarized as follows:

- **Transportation of Blood:** blood is pushed throughout the body, ensuring that oxygen, nutrients, and hormones are delivered to cells and tissues, while also transporting carbon dioxide and metabolic waste products for removal.
- **Regulation of body temperature:** Body temperature is kept under control through the regulation of blood flow to the skin and internal organs.
- **Immune Response:** White blood cells, antibodies, and other immune components are transported to sites of infection or injury.
- **Maintenance of Blood Pressure:** Coordinated actions of the heart, arteries, veins, and capillaries help regulate blood pressure (BP) and ensure stable blood flow.
- **Homeostasis:** The cardiovascular system contributes to the balance of fluids, electrolytes, and pH within the body, supporting overall homeostasis.

This section provides an overview of the anatomical structure of the organs comprising the cardiovascular system, along with the key regulatory principles governing its function.

2.1.1 The heart

Anatomy

The heart is the muscle that generates the force necessary to push blood into the blood vessels to flow to the organs and peripheral regions. It is located within the chest cavity, offset from the sternum, and positioned above the diaphragm. As depicted in Figure 2.1, the heart consists of four chambers. The two upper chambers, the atria, receive blood from systemic and pulmonary circulations, while the lower chambers, the ventricles, receive blood from the atria and generate the pressure needed to propel the blood into the major arteries [12]. Functionally, the heart can be divided into a left and right half: the left atrium and ventricle form the left heart; the right atrium and ventricle constitute the right heart.

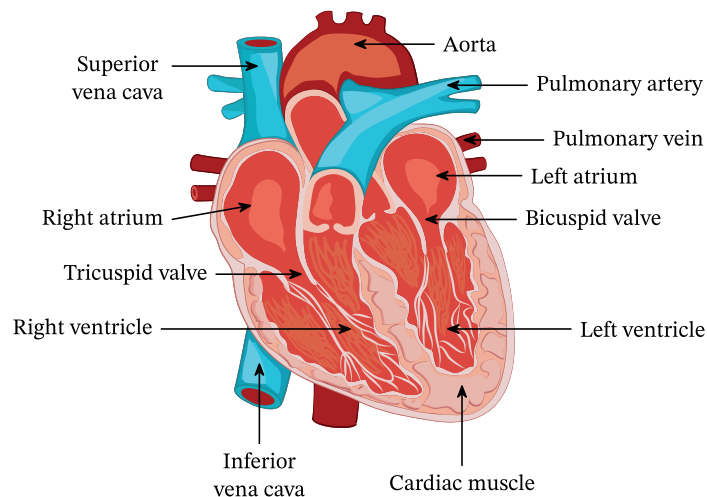


Figure 2.1: Section of the heart showing the atria, ventricles, atrioventricular valves, and connections to major blood vessels.

The atria and ventricles of the two halves are separated by a wall called *septum*, which prevents the blood in the left and right heart from mixing. The portion of the septum that separates the right atrium from the left atrium is known as the interatrial septum; the portion that separates the two ventricles is called the interventricular septum.

Atrioventricular valves separate the atria and ventricles on each side. These valves ensure the unidirectional blood flow from the atria to the ventricles, preventing backflow. The opening and closing of these valves occur in response to the

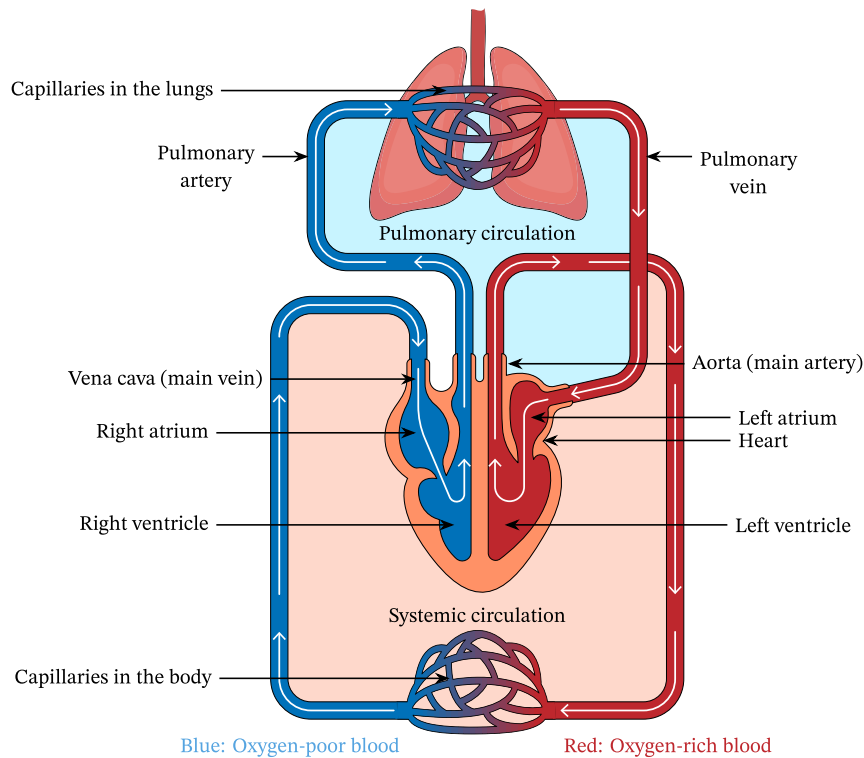


Figure 2.2: Blood circulation through the cardiovascular system. Pulmonary circulation, systemic circulation, and major blood vessels are reported. Arrows indicate the direction of blood flow.

cyclic pressure changes occurring within each heartbeat. The left atrioventricular valve consists of two flaps of connective tissue. It is called the *bicuspid (or mitral)* valve, while its counterpart on the right side is known as the *tricuspid* valve. Similarly to the atrioventricular valves between the atria and ventricles, the semilunar valves are positioned between the ventricles and the arteries. The aortic valve is located between the left ventricle and the aorta, while the pulmonary valve is situated between the right ventricle and the pulmonary trunk.

As blood flows through the cardiovascular system, it alternates between the pulmonary and systemic circuits, returning to the heart at the end of each cycle, Figure 2.2.

1. The left ventricle pumps oxygenated blood into the aorta, whose branches transport blood to the capillary beds of all organs and tissues supplied by systemic circulation.
2. The blood is deoxygenated in the peripheral tissues and then returns to the heart through the venae cavae. The superior vena cava collects blood from tissues above the diaphragm, while the inferior vena cava carries blood from

regions below the diaphragm.

3. From the right atrium, blood passes through the tricuspid valve into the right ventricle.
4. The right ventricle pumps the blood into the pulmonary trunk and pulmonary arteries.
5. The blood is oxygenated in the lungs and sent to the left atrium via the pulmonary veins.
6. From the left atrium, the blood passes through the bicuspid valve and enters the left ventricle.

Electrical Activity

Heart contractions are coordinated by an elaborate conduction system that dictates the sequence of excitation in cardiac muscle cells. The heart's ability to generate signals that periodically trigger contractions, establishing its own rhythm, is known as *autorhythmicity*. This autorhythmicity is attributed to a small percentage of muscle cells called *autorhythmic cells*. These cells, which do not generate contractile force, make up the heart's conduction system and are responsible for coordinating the heartbeat [13]. There are two types of autorhythmic cells: (1) *pacemaker cells*, which initiate action potentials and set the heart's rhythm, and (2) *conduction fibers*, which are responsible for transmitting action potentials through the cardiac tissue. Pacemaker cells are concentrated in two specific regions of the myocardium: the sinoatrial node (SA node), located at the top of the right atrium, and the atrioventricular node (AV node), situated near the tricuspid valve in the interatrial septum. The sequence of electrical events that, under normal conditions, are responsible for the heartbeat is shown in Figure 2.3.

The cardiac cycle

The cardiac cycle encompasses all events related to blood flow through the heart during a single heartbeat [11]. In this subsection, the following aspects of the cardiac cycle are analyzed: (1) the various phases of the heart's pumping action; (2) the opening and closing stages of the heart's valves; (3) changes in atrial, ventricular, and aortic pressures that reflect the contraction and relaxation of cardiac muscle; (4) changes in ventricular volume, which indicate the amount of blood entering and exiting the ventricles with each heartbeat. The relationships among the various aspects of the cardiac cycle are illustrated in Figure 2.4. Since the cardiac cycle includes the events of one heartbeat, a complete cycle encompasses both ventricular contraction and relaxation. As a result, the cycle can be divided into

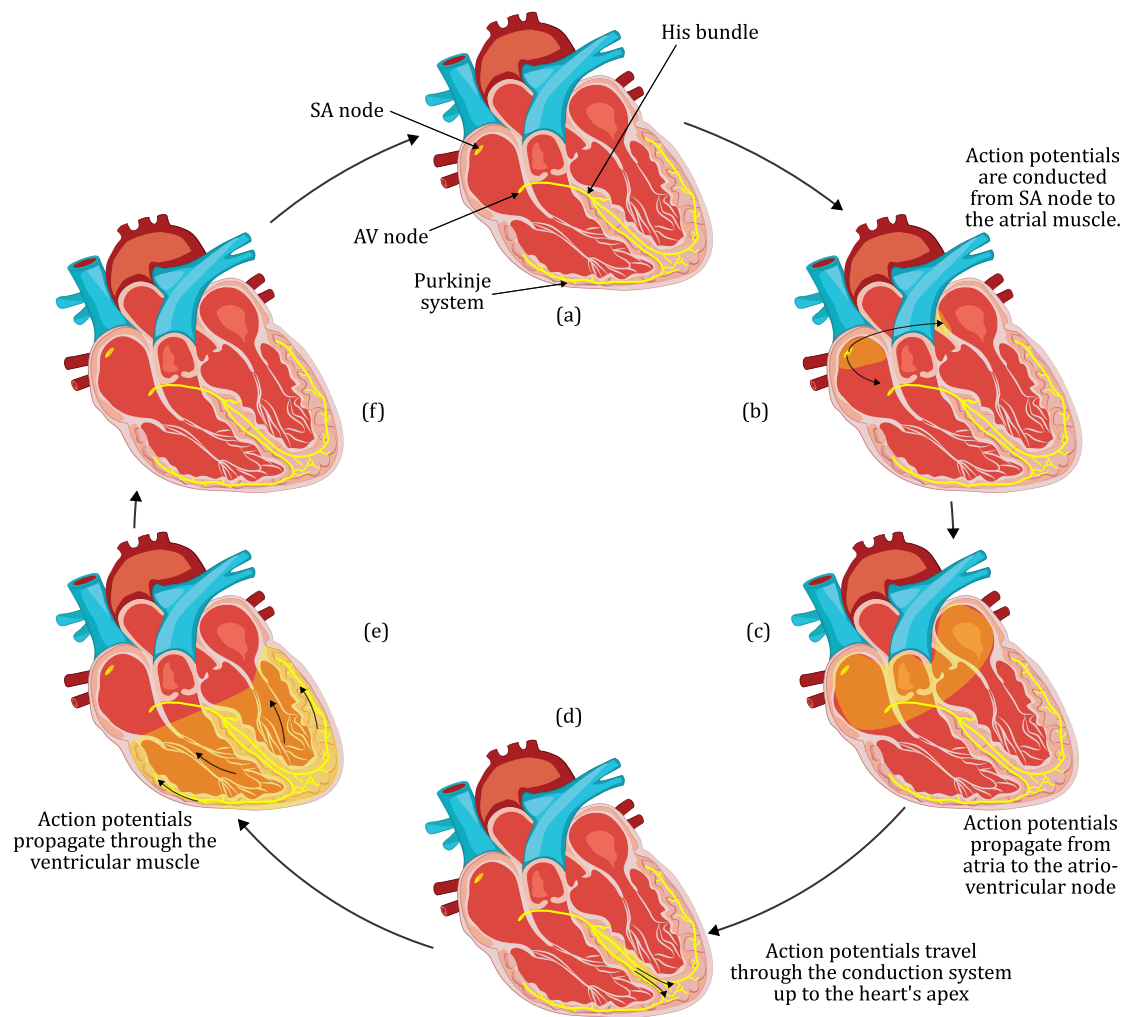


Figure 2.3: Propagation of action potentials in the heart. (a) Onset of the action potential in the SA node. (b) Conduction of the action potential up to the atrial muscle. (c) Action potentials propagate through the atria to the AV node. (d) Action potentials travel through the conduction system to the apex of the heart. (e) Action potentials diffuse through the ventricular muscle. (f) Repolarization of the heart muscle until a new action potential is generated.

two main phases: *systole*, representing ventricular contraction, and *diastole*, representing ventricular relaxation. (Although the atria also have periods of contraction and relaxation—known as atrial systole and atrial diastole here, the terms systole and diastole refer to the ventricular contraction and relaxation events.) The cardiac cycle shown in Figure 2.4 starts in the middle of diastole when both the atria and ventricles are fully relaxed. AV valves close when ventricular pressure exceeds

atrial pressure. The aortic valve opens when ventricular pressure surpasses aortic pressure and closes when the opposite occurs. The maximum pressure within the aorta is known as the SBP, while the minimum pressure is the DBP. The MAP) is the average pressure during the cardiac cycle. The volume of blood pumped from the ventricle with each beat is the ventricular ejection volume (SV), which is the difference between the end-diastolic volume (EDV) and the end-systolic volume (ESV).

1. **Ventricular Filling Phase:** During the second half of diastole (Phase 1 in Figure 2.4), blood returns to the heart through the systemic and pulmonary veins, enters the relaxed atria, passes through the atrioventricular (AV) valves, and fills the ventricles. The venous pressure is high enough to drive blood into the heart (venous return). The pulmonary and aortic (semilunar) valves are closed during this phase because ventricular pressure is lower than the pressures in the aorta and pulmonary arteries. At the end of diastole (the end of Phase 1), the atria contract, pushing more blood into the ventricles. Soon after, the atria relax, and systole begins. This entire phase, where the ventricles fill with blood, is known as ventricular filling.
2. **Isovolumetric Contraction Phase:** At the beginning of systole (Phase 2), the ventricles start contracting, increasing the pressure within them. When ventricular pressure surpasses atrial pressure, the AV valves close; however, the semilunar valves remain closed because ventricular pressure isn't yet high enough to open them. At this point, blood cannot flow into or out of the ventricles because all valves are closed. Thus, even though the ventricles are contracting, the blood volume remains constant, giving this phase its name—Isovolumetric Contraction. Phase 2 ends when ventricular pressure rises enough to force the semilunar valves open, allowing blood to exit the ventricles.
3. **Ventricular Ejection Phase:** During the remainder of systole (Phase 3), blood is pumped into the aorta and pulmonary arteries through the open semilunar valves, reducing the ventricular volume. As blood exits the ventricles, known as ventricular ejection, ventricular pressure reaches its peak and then starts to decrease. When ventricular pressure falls below aortic pressure, the semilunar valves close, ending systole and starting diastole.
4. **Isovolumetric Relaxation Phase:** At the beginning of the subsequent diastole (Phase 4), the ventricular myocardium relaxes. Some blood remains in the ventricles and is still under pressure, as it takes time for the tension in the ventricular muscle to dissipate. The ventricular pressure is too low to keep the semilunar valves open but too high to allow the AV valves to open. Since all valves are closed, and the ventricular blood volume stays constant, this

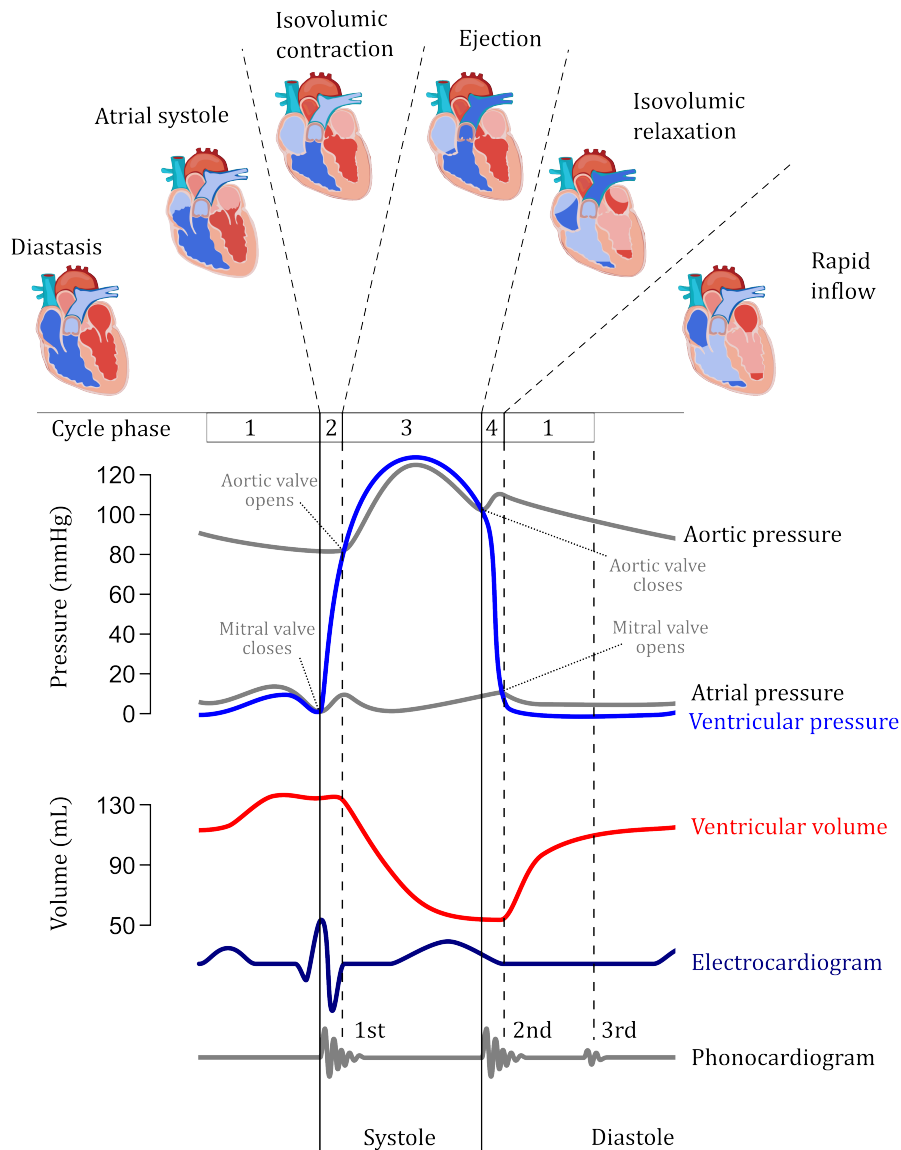


Figure 2.4: The cardiac cycle. Diastole corresponds to phases 4 and 1, while systole occupies phases 2 and 3. AV valves close when ventricular pressure exceeds atrial pressure. The aortic valve opens when ventricular pressure exceeds aortic pressure and closes under opposite conditions. The maximum pressure within the aorta is the SBP, the minimum pressure is the DBP. The mean pressure during the cycle is the MAP. The volume of blood pumped from the ventricle with each beat corresponds to the ventricular ejection volume (SV). This corresponds to the difference between the volume reached at the end of diastole, or telediastolic (EDV), and the volume reached at the end of systole, or telesystolic (ESV).

phase is called Isovolumetric Relaxation. Once ventricular pressure drops low enough to permit the AV valves to reopen, blood flows from the atria into the ventricles. This marks the start of Phase 1, signaling the resumption of the pumping cycle. The duration of systole and diastole is not the same. For a heart with a normal resting heart rate of 72 beats per minute (one beat every 0.8 seconds), most of the cardiac cycle (about 65% or 0.5 seconds) is spent in diastole; systole lasts only about 0.3 seconds. This longer diastolic period allows the heart time to fill with blood, which is crucial for efficient pumping, and also provides the cardiac muscle with more time to relax, helping prevent fatigue.

The electrocardiogram signal

The ECG signal is a recording of the electrical current flow through the heart during a cardiac cycle. The standard ECG recording procedure involves placing electrodes on the skin in an imaginary equilateral triangle formation around the heart. The triangle expands until its corners fall on the right arm, left arm, and left leg, a pattern known as Einthoven's triangle. The electrodes, positioned on the skin at the triangle's corners, are connected in pairs, which are referred to as *leads*. Each specific lead measures the surface electrical potential difference between the positive and negative electrodes. *Lead I* measures the potential difference between the left arm and right arm; *Lead II* measures the potential difference between the left leg and right arm; *Lead III* measures the potential difference between the left leg and left arm.

The ECG typically shows three characteristic types of waves, Figure 2.5:

- The P wave, an upward deflection due to atrial depolarization;
- The QRS complex, a series of upward and downward deflections;
- the T wave, an upward deflection due to ventricular repolarization. Atrial repolarization is usually not detected in the ECG tracing, as it occurs simultaneously with the QRS complex. In normal tracing, between waves, there is a horizontal line indicating no changes in electrical activity, meaning there is no potential difference (isoelectric line).

In addition to waves, some intervals and segments can provide important information about heart function. The P-Q or P-R interval corresponds to the time between the beginning of the P wave and the beginning of the QRS complex and is an estimate of the conduction time through the AV node. The Q-T interval corresponds to the time between the beginning of the QRS complex and the end of the T wave and is an estimate of ventricular contraction time, called ventricular systole. The T-Q segment corresponds to the time from the end of the T wave to the beginning of the QRS complex and is an estimate of ventricular relaxation

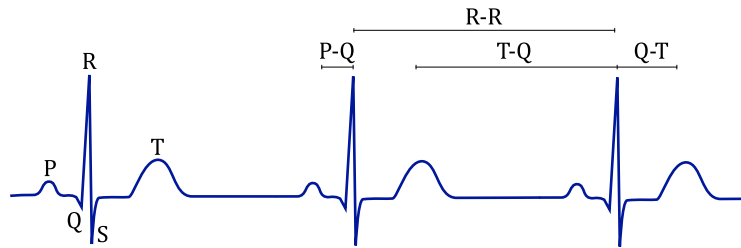


Figure 2.5: Physiological ECG waveform showing the P, Q, R, S, T waves, segments and intervals.

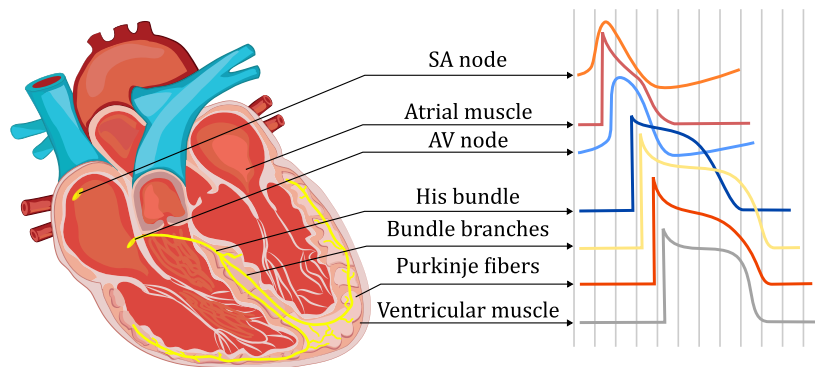


Figure 2.6: Detection of electrical activity of the heart at different locations in the cardiac muscle.

time, called ventricular diastole. The R-R interval corresponds to the time between the peaks of two successive QRS complexes and represents the time between one heartbeat and the next.

In clinical electrocardiography, electrodes are placed on both the chest and limbs to obtain 12 different leads. Each lead provides a different recording of the heart's electrical activity, Figure 2.6. In each lead, the same waves (P, QRS, and T) are always present; however, their shape differs from lead to lead. The waveforms recorded in a standard lead, such as lead II of the ECG, and the action potential of a ventricular contractile cell are shown in Figure 2.5. It's important to note that while the phases of the ECG are due to action potentials propagating through the cardiac muscle, the ECG is not simply a recording of an action potential. During the heartbeat, the discharge of action potentials from cells occurs at different times, and the ECG reflects how action potentials are generated in the entire cellular population that makes up the cardiac muscle.

2.1.2 Blood Vessels

Blood is transported from the heart to various organs, then back to the heart through a closed system of vessels (blood circulation). This system of blood vessels

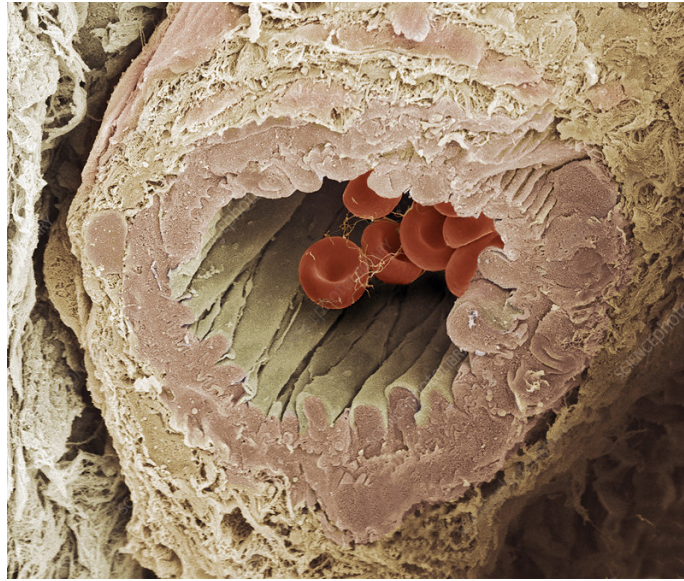


Figure 2.7: Coloured scanning electron micrograph (SEM) depicting a cross-section of a small human artery, or arteriole. Within the central lumen, red blood cells and some fibrin fibres are visible. The innermost wall, the tunica intima, appears thin and folded, consisting of an endothelial lining and a slender, elastic layer. Encircling this is the thicker tunica media layer, primarily composed of smooth muscle cells, seen here in pink. The outermost tunica adventitia layer blends with the adjacent connective tissue. These structural layers allow the arteriole to contract and expand, thereby regulating arterial BP [14].

is generally known as the vascular system [15].

Blood vessels are classified based on their diameter and whether they carry blood from the heart to the tissues or vice versa. Arteries and arterioles carry oxygenated blood from the heart to the capillaries. Here, the deoxygenated blood is collected by venules and subsequently by veins, which return it to the heart. The collection of arterioles, venules, and capillaries is referred to as the microcirculation, where nutrient and gas exchanges (oxygen and carbon dioxide) occur.

Structurally, all blood vessels have a central cavity called the *lumen*, through which blood flows. The lumen is lined with a layer of epithelium known as *endothelium*. In Figure 2.7, a cross-section through an arteriole shows all the different tissues and elements contributing to the circulation of oxygenated blood.

The blood vessels' structural differences are displayed in Figure 2.8, and their main properties are summarized below.

- Arteries: Arteries carry blood away from the heart and distribute it to the tissues; they have relatively large diameters and thick walls. The largest artery, the aorta, has a diameter of 12.5 mm and a wall thickness of 2 mm.

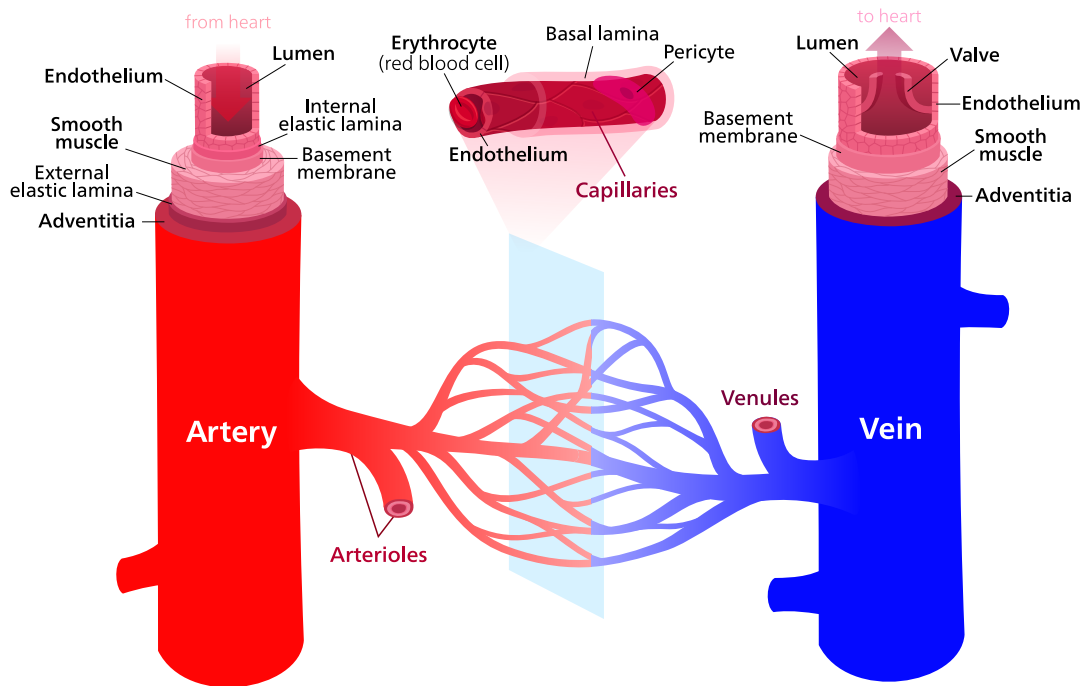


Figure 2.8: Overview of the anatomical differences between different blood vessels.

Smaller arteries branching from the aorta have diameters between 2 and 6 mm and wall thicknesses of 1 mm. Larger arteries offer little resistance to blood flow and primarily serve to conduct blood. Their walls contain large amounts of fibrous and elastic tissue, allowing these vessels to withstand much higher BP than other vessels. As arteries divide into smaller vessels, the amount of elastic tissue in their walls decreases while the amount of smooth muscle increases.

- *Arterioles*: Arteries branch into progressively smaller arterioles, which can lead to a capillary bed. Their walls contain a relatively high proportion of smooth muscle, enabling them to contract and dilate to regulate flow through the capillary beds. Arterioles play a significant role in controlling mean arterial pressure and distributing cardiac output to different tissues. Flow distribution to various organs is regulated by intrinsic control of vascular resistance in each organ, determined by local metabolic activity and blood flow requirements. As a result, the extrinsic control of arteriolar diameter (and thus total peripheral resistance) is crucial in regulating mean arterial pressure. Extrinsic factors involved in this control include the Autonomic nervous system (ANS) and hormones associated with vasoconstriction and vasodilation.
- *Capillaries*: Capillaries have the thinnest walls and are highly permeable to water and small solutes; their primary function is facilitating the exchange of

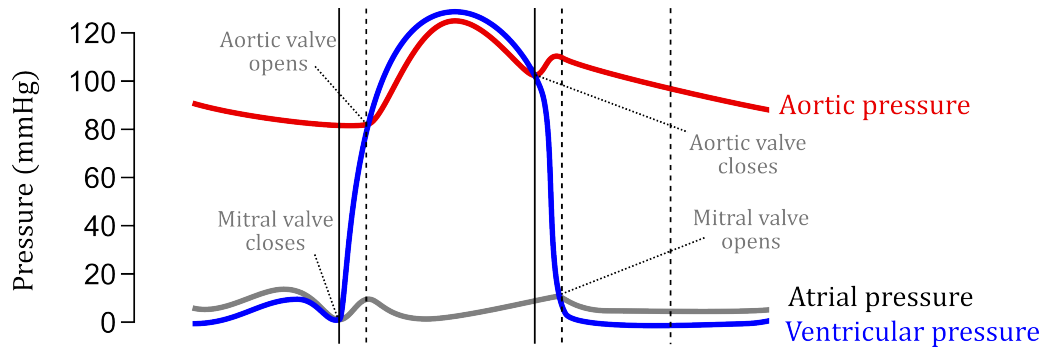


Figure 2.9: Atrial, ventricular, and aortic pressure diagram within a single cardiac cycle.

materials between blood and tissues. Fluid movement through capillary walls depends on the net filtration pressure resulting from Starling's forces. Most of the fluid filtered at the arteriole end of the capillary is reabsorbed at the venule end to return to the vascular system. At the same time, excess fluid removed by the lymphatic system also re-enters the vascular system. Venules, which also have thin walls, participate in the exchange of substances between blood and interstitial fluid.

- *Veins*: Veins are relatively large vessels with thin walls. Most veins contain valves that allow blood to flow toward the heart but prevent it from flowing back toward the periphery. Veins have high compliance and act as volume reservoirs. The pressure in the large thoracic veins is known as central venous pressure, which influences arterial pressure by affecting end-diastolic volume, stroke volume, and cardiac output. When central venous pressure increases or decreases, mean arterial pressure tends to increase or decrease, respectively. Central venous pressure is influenced by the respiratory pump, blood volume, and venomotor tone (regulated by sympathetic nerve fibers that innervate the veins).

2.1.3 Blood Pressure

When blood is pumped from the ventricle into the aorta during systole, aortic pressure reaches the same level as ventricular pressure [16]. However, aortic pressure doesn't remain high because it drops to a minimum during diastole, just before the next systole. Aortic pressure is referred to as arterial pressure.

Figure 2.9 reports that ventricular pressure falls to 0 mmHg at the end of systole, while arterial pressure stays high. Arterial pressure during diastole is due to the elastic recoil of the artery walls. The thickness of the arterial wall, along with its abundant elastic tissue, gives arteries a certain rigidity and the capacity

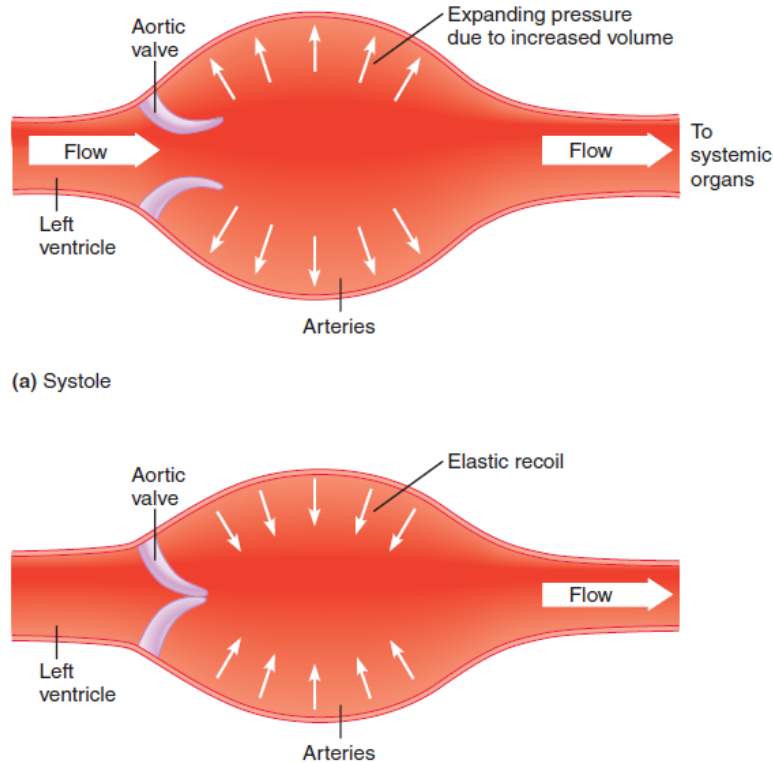


Figure 2.10: Role of arteries as pressure reservoirs. (a) During systole, the BP in the left ventricle is greater than the aortic pressure. Blood, after entering the aorta, increases its volume, causing its walls to expand. (b) During diastole, the elastic return of the walls pushes the blood forward [11].

to expand and contract as BP changes with each ventricular contraction. This combination of rigidity and elasticity allows arteries to act as pressure reservoirs, ensuring a continuous flow of blood through the vessels even when the heart is not contracting (during diastole). When the artery walls expand during systole as blood is pumped through, elastin fibers act like stretched springs. This stored elastic energy is released during diastole when the artery walls retract passively, pushing blood forward. Thus, blood flow continues, first from the push of systole and then from the arterial recoil during diastole. The entire process can be visualized in Figure 2.10. Since arterial pressure varies during the cardiac cycle, the maximum pressure reached during systole is called systolic SBP, while the minimum pressure during diastole is called diastolic pressure DBP. The average pressure throughout the cardiac cycle is the MAP. Two major factors influence blood flow to an organ: MAP and the resistance of the organ. Since MAP affects blood flow to all organs supplied by the systemic circulation, adapting flow to the organ's needs requires maintaining an adequate MAP.

Table 2.1: Classification of office BP and definitions of hypertension grade in adults [17].

Category	Systolic (mmHg)		Diastolic (mmHg)
Optimal	<120	and	<80
Normal	120-129	and/or	80-84
High Normal	130-139	and/or	85-89
Grade 1 hypertension	140-159	and/or	90-99
Grade 2 hypertension	160-179	and/or	100-109
Grade 3 hypertension	>180	and/or	>110
Isolated systolic hypertension	>140	and	<90
Isolated diastolic hypertension	<140	and	>90

Hypertension

Hypertension is the most prevalent cardiovascular disorder globally, affecting 1.28 billion adults aged 30-79 years [18], according to the WHO. In 2019, the global age-standardized prevalence of hypertension among adults in this age group was 34% for men and 32% for women [2, 19]. Hypertension significantly impacts cardiovascular health by inducing hemodynamic changes and organ damage, primarily driven by increased arterial stiffness and altered hemodynamics [20].

The development and progression of hypertension involve multiple mechanisms and systems, including genetic predisposition, environmental influences, and alterations in cardiovascular regulatory systems. Hypertension induces various hemodynamic changes that affect multiple organs, leading to Hypertensive Organ damage (HMOD). These changes are primarily driven by increased arterial stiffness and altered hemodynamics, significantly contributing to cardiovascular risk [21]. As per the 2018 European guidelines [17], hypertension is defined based on repeated office measurements showing SBP values of 140 mmHg or higher and/or DBP values of 90 mmHg or higher. However, there is a continuous relationship between BP and cardiovascular or renal morbidity and mortality, beginning from an office SBP above 115 mmHg and a DBP above 75 mmHg. This definition aims to simplify the diagnosis and management of hypertension. The threshold BP values indicate the point at which the benefits of intervention, whether through lifestyle changes or drug treatment, outweigh the benefits of inaction.

In addition to grades of hypertension, which are based on BP values, 2023 ESH Guidelines [16] classify this pathology and also distinguish stages of hypertension as follows:

- Stage 1: Uncomplicated hypertension (i.e. without HMOD or established CVDs, but including Chronic Kidney Diseases (CKD) stages 1 and 2)
- Stage 2: Presence of HMOD or CKD stage 3 or diabetes.

- Stage 3: Established CVDs or CKD stages 4 or 5.

Arterial stiffness is a critical factor in the pathophysiology of hypertension, referring to the diminished capacity of the arteries to expand or contract in response to pressure changes. This loss of elasticity is often a consequence of aging and chronic hypertension. As arteries stiffen, SBP rises because the heart must exert more force to pump blood through less compliant vessels. Moreover, stiff arteries cause early wave reflection, which can augment central aortic pressure, further increasing cardiac workload. As a result, the heart encounters increased resistance during systole, leading to augmented afterload and placing significant strain on the left ventricle. This phenomenon leads to left ventricular hypertrophy (LVH), elevates the risk of coronary artery disease (CAD), and may ultimately result in heart failure.

End-organ damage due to hypertension is not confined to the heart; it affects multiple organs throughout the body. Hypertension promotes the development of atherosclerosis, characterized by the formation of plaques in the arterial walls. This can lead to narrowed or blocked arteries, increasing the risk of peripheral artery disease (PAD), aortic aneurysms, and other vascular complications. Additionally, hypertension is a leading cause of cerebrovascular disease [22].

Chronic high BP can damage small arteries in the brain, leading to microvascular disease, which heightens the risk of stroke and cognitive impairment. Large artery atherosclerosis also contributes to an increased risk of ischemic stroke [23]. In the kidneys, hypertension promotes the progression of CKD and can ultimately lead to end-stage organ failure. The cumulative effect of hypertension-induced damage across these vital organs underscores the importance of adequate BP management to prevent severe and potentially life-threatening complications [24].

2.2 Analyzed Biosignals

2.2.1 Arterial Pulse

A pulse wave originates from the contraction of the left ventricle, making the arterial pulse an essential physiological indicator of the heart's contraction rate. Arteries, owing to their elasticity, expand during ventricular contraction and then recoil, pushing blood towards the capillaries and veins. This rhythmic expansion and contraction, termed the pulse, can be detected manually or recorded electronically, offering crucial insights into a patient's health.

The arterial pulse is measured in beats per minute (bpm). Clinically, both the strength and rate of the pulse are significant indicators. Factors such as physical exertion or acute events can temporarily increase the pulse rate, but sustained variations can signal underlying cardiac issues. The intensity of the pulse reflects the force of the heart's contraction and cardiac output. A high pulse rate typically

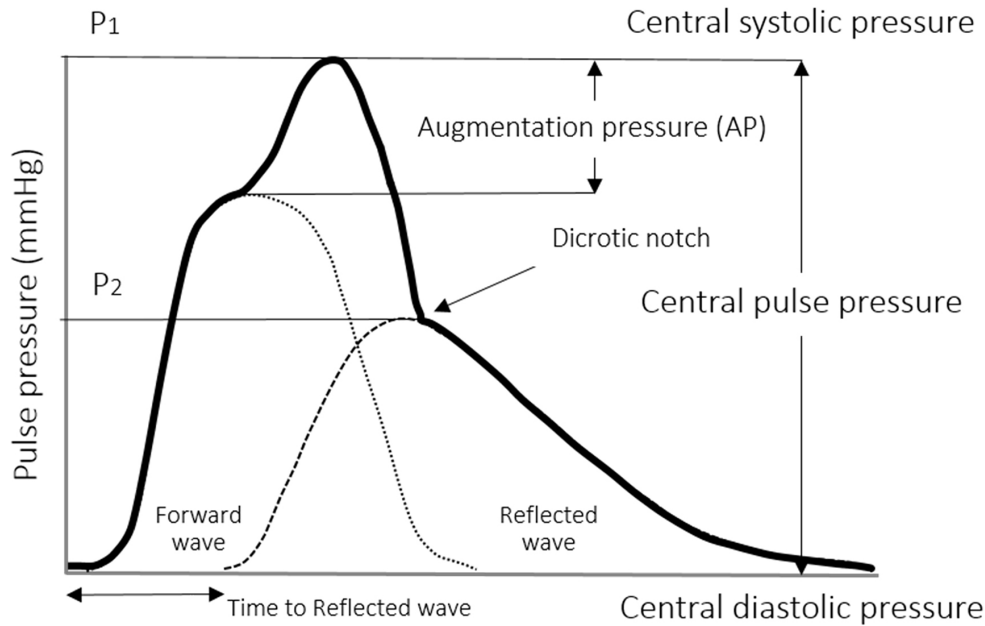


Figure 2.11: Analysis of central pulse pressure waveform [25].

indicates high systolic pressure, while a weak pulse may suggest decreased systolic pressure, potentially necessitating medical intervention.

The central pulse pressure waveform is a critical indicator of cardiovascular health and is characterized by distinct features arising from the dynamic interplay between forward and reflected pressure waves. The waveform is composed of a systolic and a diastolic component. The systolic portion primarily results from the forward pressure wave generated by the contraction of the left ventricle, while the diastolic portion is influenced by reflected pressure waves originating from various peripheral sites within the arterial system. The summation of these forward and reflected waves shapes the central pulse pressure waveform. Pulse morphology refers to the structure of the pressure signal throughout a single cardiac cycle and can be divided into the following components:

- **Systolic Upstroke:** This segment represents the rising edge of the waveform produced by ventricular ejection, characterized by a peak in aortic blood flow when the aortic valve opens. A more gradual slope of this rising edge may suggest aortic stenosis. The systolic component corresponds with the R wave of the ECG, though with a minor delay.
- **Systolic Peak Pressure:** This represents the maximum pressure during ventricular systole. The peak pressure increases with the distance from the heart due to increased pressure and decreased vessel resistance. The shape of the peak is influenced by reflected waves in the vascular system, which can sometimes create an "anacrotic notch" on the systolic upstroke, more pronounced

in the carotid artery than in peripheral arteries.

- **Systolic Decline:** This point signifies the end of systole, indicated by a swift decline in pressure.
- **Dicrotic Notch:** This event is triggered by the closure of the aortic valve, marking the onset of diastole and causing a sharp rise in pressure during the falling edge of the waveform.
- **Diastolic Runoff:** After the aortic valve closes, the pressure within the aorta gradually decreases in an exponential manner as the ventricle stops pumping blood into it.

These waveform components provide detailed insights into cardiovascular function and health, enhancing clinical assessments beyond traditional BP measurements.

2.2.2 Photoplethysmogram Signal

Photoplethysmography (PPG) is a non-invasive optical method used to monitor blood volume changes in the skin's microvascular bed by utilizing the optical characteristics such as absorption, scattering, and transmission of tissues when exposed to specific light wavelengths [26].

The PPG signal arises from three main sources:

- the alignment and deformation of red blood cells (RBCs)
- the distribution of absorbers and blood volume changes (BVs)
- the mechanical actions of capillaries.

The alignment of RBCs changes with the cardiac cycle and significantly influences the PPG waveform. In diastole, with lower blood flow, RBCs are randomly oriented due to decreased shear stress. As blood flow increases, RBCs begin to align with the flow direction, becoming parallel during systole. This alignment affects light attenuation in the tissue, generating the PPG signal. Furthermore, light transmission and reflection from blood vessels vary with blood volume changes and the RBCs' orientation and flexibility. This phenomenon supports the understanding that arterial pulsations are the primary source of the PPG signal [27].

In PPG, a targeted wavelength of light is directed through a perfused tissue region during each heartbeat cycle. The fluctuations in the volume of the pulsatile tissue components from systole to diastole alter the light absorption in the tissue over time, thereby generating a continuous PPG signal. [28].

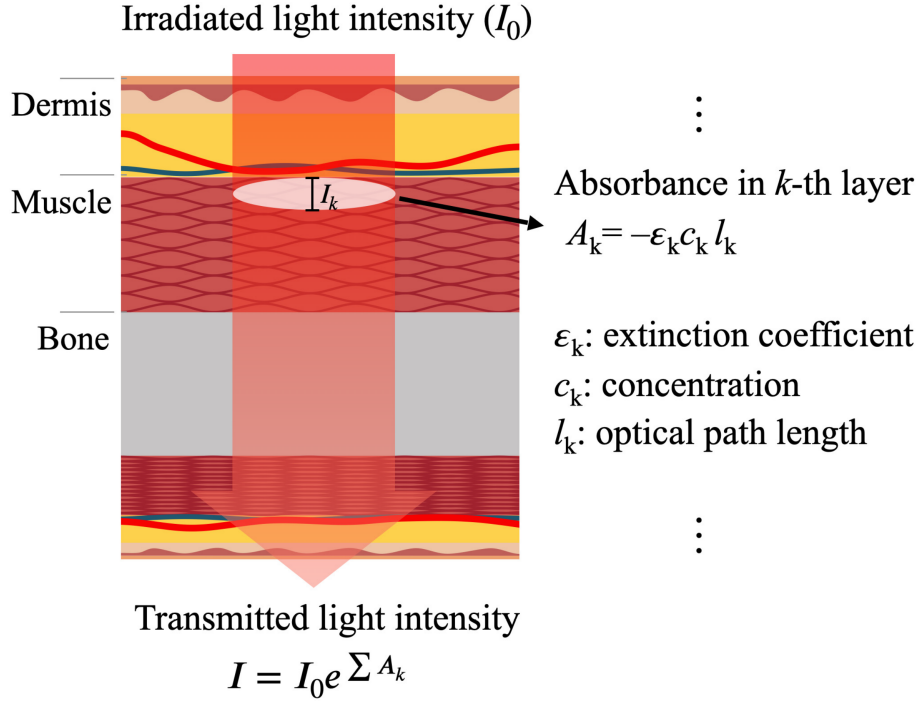


Figure 2.12: Schematic representation of Lambert-Beer law in a multilayer medium [28].

The amount of light transmitted or reflected is influenced by changes in the concentration of substances in the blood and the optical path length due to pulsation [29]. The Lambert-Beer law, as in Eq. 2.1, defines that the transmitted light intensity (I) through a medium will decrease exponentially in irradiated light intensity (I_0) in relation to the absorption coefficient (ϵ), optical path length (d), and concentration of the medium (C).

$$I = I_0 e^{-\epsilon d C} \quad (2.1)$$

Where the exponential term, defined as in Eq. 2.1, identifies the "absorbance" A for light traveling through a homogeneous medium. Figure 2.12 shows the interaction of the irradiated light within the skin structure in a PPG measurement. Light irradiated into the skin interacts with different tissues, veins, and arteries; then, finally, it is detected by a photodetector. Since biological tissues are intricate, heterogeneous environments comprising multiple absorbers (e.g., blood, water, melanin) and scatterers (e.g., collagen, keratin), the Lambert-Beer law has been modified to incorporate scattering effects [30].

The amount of light absorbed or scattered during this process may vary depending on the composition of the skin structure.

The total absorbance throughout skin layers is equal to the total sum of the absorbances of the k layers is defined as in Eq. 2.2:

$$A_{Tot,\lambda} = \sum_{k=1}^N \epsilon_{\lambda,k} \cdot d \cdot DPF_{\lambda} \cdot C_k + G_{\lambda} \quad (2.2)$$

where $\epsilon_{\lambda,k}$ and C_k represent the extinction coefficient and concentration of the k absorber. In a medium where both scattering and absorption occur, such as tissue, the optical path length differs from the actual material thickness. This discrepancy is accounted for by a multiplicative factor known as the "differential pathlength factor" (DPF). The DPF varies with the optical wavelength and the anatomical structure of the tissue [31]. Consequently, the $d \cdot DPF_{\lambda}$ is the total optical path length through the medium. G is a scattering-dependent parameter. Finally, the Eq. 2.1 can be adjusted as reported in Eq. 2.3:

$$I = I_0 e^{-A_{Tot,\lambda}} \quad (2.3)$$

In most PPG applications, the sensor or probe is placed on the skin's surface, illuminating a volume of underlying tissue [32]. The optical characteristics of different tissue layers and sublayers, which vary with wavelength, influence the light as it traverses this tissue volume. Consequently, light-tissue interactions in PPG are governed by two primary factors:

- The anatomical and physiological properties of the tissue region being examined (ROI)
- The configuration of the sensor, encompassing the optical source-detector separation in reflectance mode, the shape and dimensions of the sensor, and the operating optical wavelength.

The geometrical arrangement of the optical source and detector allows the PPG signal to be captured in two distinct modes: transmittance and reflectance [33]. Figure 2.13 provides a diagrammatic representation of these two modalities. A conventional PPG sensor consists of a light emitter, typically light-emitting diodes (LEDs), and a highly sensitive photodetector. Generally, as the wavelength of light increases, the depth of penetration also increases. For example, wavelengths of 470 nm, 570 nm, and 660 nm can penetrate the epidermis with capillaries, the dermis with arterioles, and the subcutaneous tissue with arteries, respectively [34]. Major blood vessels and arteries with strong pulsation are primarily located in the skin dermis or subcutaneous tissue. Consequently, light with red wavelengths of 640-660 nm and infrared wavelengths of 880-940 nm is primarily used for PPG measurements. The photodetector, often a silicon photodiode, can also be a photocell or phototransistor. The configuration of the LED and photodiode within the sensor determines the probe's structure and its suitable measurement site. For transmission probes, the LED and photodiode are placed on opposite sides of a clip, with the

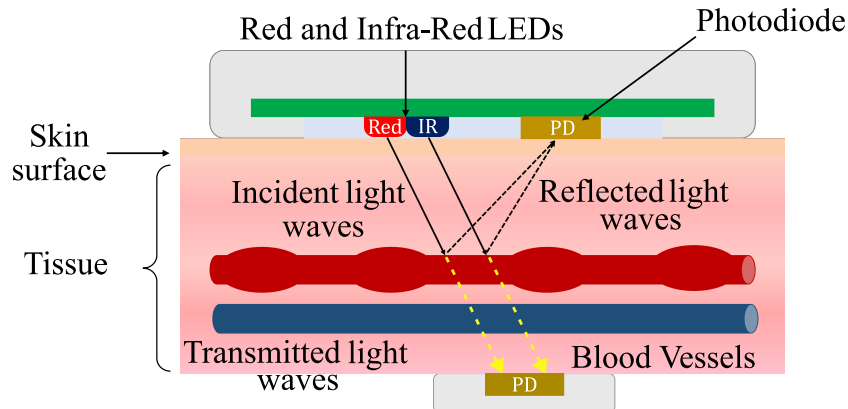


Figure 2.13: Transmission versus reflectance PPG modes: the intensity of light received at the photodiode is modulated by the changes in pulsating blood volume occurring in the illuminated tissue.

LED shining light through the tissue to the photodiode. In contrast, reflectance probes position the LED and photodiode side-by-side, usually a few millimeters apart, allowing the LED to illuminate the tissue while the photodiode detects the reflected light [35]. The choice of measurement mode depends on the application site. PPG signals are generally collected from peripheral tissue sites where pulses are readily detectable. The transmittance mode configuration is ideal for small extremities like the toe, finger, or earlobe. On the other hand, the reflectance mode can be utilized on almost any vascular region of the body.

The PPG waveform is produced by the unabsorbed light detected by an optical sensor, such as a photodiode. As illustrated in Figure 2.14 and mentioned earlier in this subsection, the recorded PPG intensity (I) diminishes exponentially with light absorbance (A) within the tissue volume under examination.

The PPG intensity can be separated into two components based on light absorbance in the pulsatile and non-pulsatile tissue compartments:

- The nonpulsatile, relatively stable direct current (DC) component results from light absorption in nonpulsating tissue regions (e.g., bloodless tissue, muscle, bone). The slow changes in the DC component are also influenced by respiration, the sympathetic nervous system, BP regulation, and thermoregulation.
- The pulsatile alternating current (AC) component arises from light absorption in pulsating arterial blood, fluctuating in accordance with the heartbeat. The AC PPG signal consists of two phases: the anacrotic phase, corresponding to the pulse's rising edge and related to systole, and the catacrotic phase, representing the pulse's falling edge and associated with diastole. The shape of the PPG pulse wave is influenced by multiple factors, including cardiac characteristics (e.g., heart rate, rhythm, and stroke volume), circulatory properties

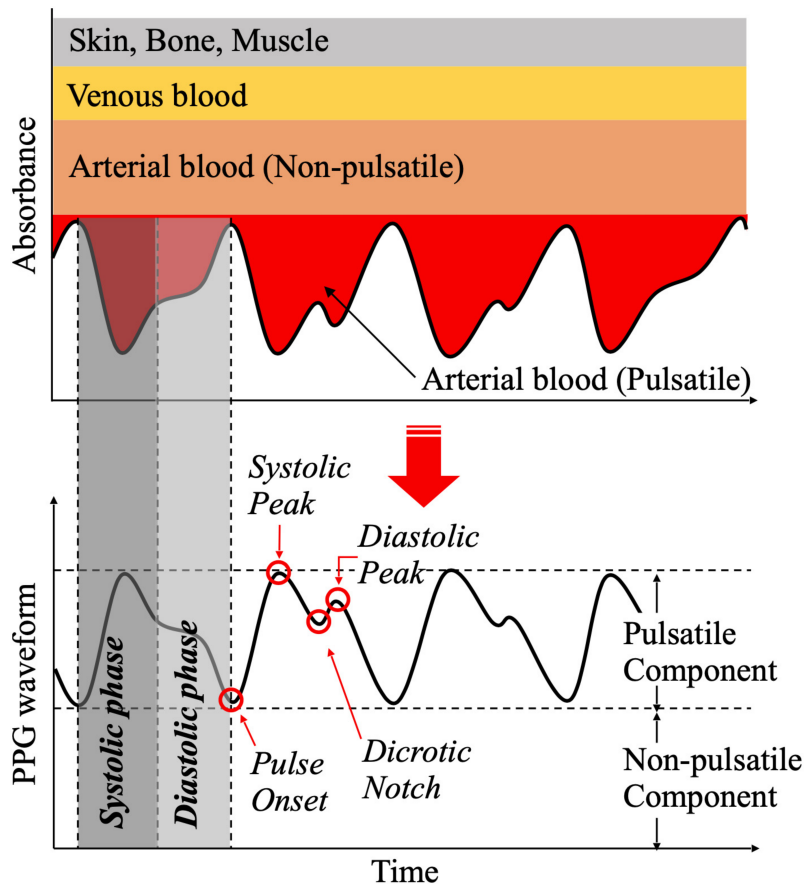


Figure 2.14: Principle of PPG generation and waveform features [36].

(e.g., arterial stiffness and BP), physiological processes (e.g., respiration and the autonomic nervous system), and the presence of disease. The dicrotic notch, shown in Figure 2.14, is a typical feature of the aortic pressure waveform, indicating the transition from systole to diastole.

The simultaneous acquisition of multiple PPG signals from different body sites enables the measurement of PTT, which is the duration taken for the pulse wave to travel along an arterial pathway. As will be discussed in the following chapters, PTT will be extensively examined in the context of assessing biomarkers that are clinically used to evaluate cardiovascular risk. Given this introduction concerning the physiological background and the ensemble of biological signals analyzed in this work, this thesis will now focus on the two target biomarkers that were the object of this research investigation: pulse wave velocity and cuffless BP monitoring.

2.3 Pulse Wave Velocity

CVDs are globally considered the leading cause of death [37, 38, 39]. Arterial stiffness is a multifaceted phenomenon that results from alterations in both the structure and function of the blood vessel wall [40, 41]. A reduction of the elasticity of vessels leads to elevated SBP and reduced DBP. This condition causes a significant workload on the left ventricle, alters coronary perfusion, and promotes chronic arterial inflammation [42]. Arterial stiffness can be clinically assessed by evaluating PWV [43, 44]. Particularly, arterial stiffness is associated with the elastic characteristics of the arteries and PWV by the Moens-Korteweg equation, Eq. 2.4, as follows:

$$PWV = \sqrt{\frac{hE}{2r\rho}} \quad (2.4)$$

Where h represents the thickness of the vessel, r the radius of the vessel and ρ is the density of the blood. Pulse wave velocity measures the speed at which the pressure wave travels through the cardiovascular system due to the ejection of blood at the end of the systolic phase within the cardiac cycle. It depends on the vascular biomechanics and hemodynamics of the circulatory system [45, 46]. It provides information about compliance [47], mean arterial pressure [48], vasomotor tone [47] and therapeutic efficacy in vascular and hypertensive heart diseases [49, 50, 51, 52]. As cited by the European hypertension guidelines [53], PWV keeps its predictive and prognostic value even where others prove unreliable and, therefore, is considered the gold standard among stiffness indices and a significant predictor of cardiovascular risk [54, 55]. Typical locations for evaluating pulse waves include the femoral, tibial, radial, and carotid arteries, where arterial pulsations are easily detectable [56, 57]. In healthy conditions, the pulse wave propagates into the aorta at a speed of about 5 m/s and increases progressively in small arteries up to 10-15 m/s. In 2023, the European Society of Hypertension guidelines [16] recommended brachial-ankle Pulse Wave Velocity (baPWV) [58, 59, 60] as a screening tool for hypertension-mediated organ damage [61]. However, cfPWV is still considered the gold-standard reference in the arterial stiffness assessment [62, 63, 64]. The PWV can be assessed by measuring the pressure wave at two different locations along the arterial system: a proximal site (such as the carotid or brachial arteries) and a distal or peripheral site (such as the femoral or ankle arteries). The time delay between the pressure wave's arrival at the proximal site compared to the distal site can either be measured directly on the patient or calculated using other variables. Consequently, PWV is assessed using the following formula:

$$PWV = \frac{d}{\Delta t} \quad (2.5)$$

Where d represents the distance between two sites and Δt is the time required

by the blood pulse to circulate from one site to the other.

2.3.1 Invasive PWV Assessments Methods

Invasive pulse wave velocity assessment methods are renowned for their accuracy in measuring arterial stiffness, directly evaluating the propagation of pressure waves through the arterial system. These methods utilize intravascular devices to acquire precise hemodynamic data.

High-fidelity pressure sensors, such as micromanometers or fluid-filled catheters, are commonly employed as invasive sensing elements. Micromanometers are favored for their high accuracy and frequency response, while fluid-filled catheters, though more common, require meticulous calibration. These pressure sensors are mounted on catheters that are inserted into the arterial system, typically through the femoral artery, and advanced to specific measurement sites.

The transit time is calculated as the time difference between the *foot* of the pressure wave at the proximal and distal sites. This is typically identified using the intersecting tangent method [65], which will be better explained in Section 2.3.4 and detailed in reported in Table 2.2. The distance between the measurement sites is determined using imaging techniques like angiography or by direct measurement along the catheter path. Pulse wave velocity is then calculated using the distance over time relationship.

The invasive nature of this method poses significant limitations. Invasive PWV measurement is typically used in extreme cases where other evaluation methods are either impractical or insufficient. It carries risks such as bleeding, infection, and arterial damage, and requires specialized equipment and expertise, typically available only in catheterization laboratories. It is also opportunistically performed during cardiac catheterization and other cardiovascular procedures, as these inherently require access to the vascular system. Additionally, the invasive procedure can cause patient discomfort and is associated with procedural risks, limiting its use to cases where detailed assessment is critically necessary. The cost and resources required for invasive PWV assessment are considerable, including specialized catheters, high-fidelity pressure transducers, and imaging equipment, making it an expensive alternative compared to noninvasive methods.

2.3.2 Non-Invasive PWV Assessments Methods

The clinical significance of noninvasive PWV assessment lies in its ability to predict cardiovascular events and monitor the progression of arterial stiffness over time. Elevated PWV is associated with an increased risk of cardiovascular diseases, including hypertension, atherosclerosis, and heart failure. By providing a noninvasive means to assess arterial health, these methods play a crucial role in preventive

cardiology and the management of patients with cardiovascular risk factors. Noninvasive PWV assessment methods are essential tools for evaluating arterial stiffness without the need for invasive procedures. These methods are widely used in clinical and research settings due to their safety, ease of use, and ability to provide valuable hemodynamic information.

Noninvasive PWV measurements typically involve the use of different devices and techniques to capture the pressure or flow waveforms at different arterial sites. One common method is the cfPWV measurement, which is considered the gold standard for assessing aortic stiffness. In cfPWV, sensors are placed on the skin overlying the carotid and femoral arteries to record the pulse waves. The time delay between the waveforms at these two sites is measured, and the distance between the sites is estimated using external measurements. PWV is then calculated by dividing the distance by the time delay, providing an indication of arterial stiffness.

Another widely used noninvasive method is baPWV. This technique measures the pulse wave velocity between the brachial artery in the arm and the ankle. Cuffs similar to those used for BP measurement are placed on these sites, and the transit time of the pulse wave is recorded. baPWV assesses both central and peripheral arterial stiffness, offering a broader view of arterial health compared to cfPWV.

Ultrasound-based methods also play a significant role in noninvasive PWV assessment. High-resolution ultrasound can be used to visualize and measure the pulse wave as it travels along specific arterial segments, such as the carotid or femoral arteries. By capturing the pulse waveforms at different points along the artery, the transit time and distance can be accurately determined, allowing for the calculation of PWV.

Magnetic resonance imaging (MRI) provides another noninvasive approach to PWV measurement. MRI techniques can capture detailed images of the arterial system and measure the velocity of the pulse wave as it travels through the aorta and other large arteries. This method is particularly useful for assessing aortic stiffness and provides high precision and detailed anatomical information without the need for radiation exposure. Each of these noninvasive methods has its own advantages and limitations. cfPWV is highly regarded for its accuracy in assessing aortic stiffness and its strong correlation with cardiovascular risk. However, it requires precise placement of sensors and accurate distance measurements, which can introduce variability. baPWV, on the other hand, is easier to perform and provides information on both central and peripheral arteries, but it may be influenced by factors such as limb length and arterial branching. Ultrasound-based methods offer high spatial resolution and can directly visualize the arteries, making them useful for site-specific PWV measurements. However, they require skilled operators and may be limited by the acoustic window and patient anatomy. MRI-based techniques provide comprehensive and detailed assessments of arterial stiffness, but they are expensive and less accessible compared to other noninvasive methods.

2.3.3 Methodology

As previously mentioned in this section, PWV can be assessed by detecting the passage of the pressure wave in different sites. In clinical practice, the most common regional PWV measurement is carried out where the pulsation can be easily felt: on the right common carotid artery (proximal point) and on the right femoral artery (distal or peripheral point). Due to the proximity of the two acquisition sites to the central aorta, cfPWV is recognized as the most widely measured surrogate of the aortic Pulse Wave Velocity (aoPWV) [66, 67, 68]. Fig. 2.15 summarizes the two alternative methods used to measure the cfPWV throughout the arterial tree. In this manuscript, we will refer to them as the indirect method and the direct method. Both approaches need the carotid and femoral locations to acquire the blood pulse wave. The main difference between the two methods is represented by how the Δt is calculated. The measurement techniques include either sequentially acquiring separate recordings synchronized to a specific point in the cardiac cycle, Fig. 2.15 (right), or simultaneously recording two pulse waveforms using identical sensor probes, Fig. 2.15 (left). The R-peak of the ECG is commonly used as the reference point for synchronizing sequentially measured pulse waveforms from various arterial sites [69]. The sequential method involves using a single blood pulse sensor along with an ECG to measure real-time data from surface arteries. This technique calculates PWV by dividing the PAT, the delay between the ECG’s R-wave and the initial rise of the blood pulse, by the arterial distance from the heart to the measurement site [67, 70]. It is crucial to highlight that this method only offers an indirect estimation of PWV and comes with inherent physiological constraints. The PAT is comprised of:

1. the transit period of the pulse wave from the aorta to the measurement site
2. the ventricular electromechanical delay
3. the isovolumic contraction period

The combined duration of stages (2) and (3) is termed the ‘pre-ejection period (PEP),’ a substantial portion of PAT that does not depend on pulse wave propagation [71, 72]. Thus, the velocity estimate derived from PAT deviates from the actual cfPWV. In the sequential method illustrated in Fig. 2.15 (left), the time interval Δt is assessed as the difference between the distal pulse arrival time (PAT_{fem}) and the proximal pulse arrival time (PAT_{car}) recorded respectively on the femoral and carotid site. In the direct method shown in Fig. 2.15 (right), the PTT is directly evaluated using the recorded waveforms in the two sites without any other references.

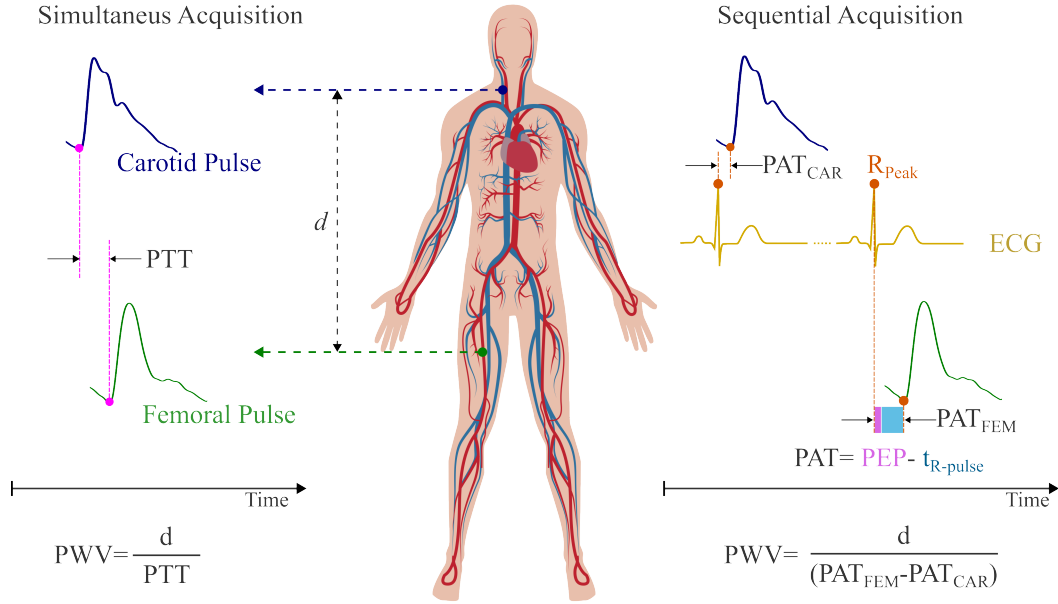


Figure 2.15: PWV acquisition methodologies. (a) The *simultaneous acquisition* is commonly performed by detecting a characteristic feature on each pulse wave, Then, PTT is computed as the delay occurring between pulses. (b) The *sequential acquisition* employs a single sensor and reference signal ECG. The transit time is evaluated as the difference between the PAT per acquisition site. PAT is defined as the time interval between the R-peak of the ECG and the sequentially detected pulse waveforms on the carotid and femoral artery, respectively. PAT encompasses the duration for the pulse wave to move from the aorta to the measurement location ($t_{R-pulse}$), as well as the pre-ejection period (PEP).

2.3.4 Pulse Transit Time Assessment Techniques

Fiducial Points based approaches

The transit time-based approach is the simplest and most straightforward method for PWV measurement. It utilizes the fundamental distance-time relationship, henceforth referred to as the pulse transit time-based approach. With the introduction of PWV as a standard biomarker of arterial stiffness, several methodologies and algorithms have been developed to provide increasingly accurate estimates of PTT. As a result of the analysis of the characteristic morphology of the pulse wave [73], numerous studies over the years have proposed the identification of a specific point or window on the signal that would allow reliable PWV estimation [68]. Different algorithms relying on the extraction of a single feature located on the signal were used for PTT assessment. The fiducial time points are chosen based on the physiological and morphological features of the acquired blood pulse waves. The most frequently utilized method involves using the *foot* of the blood

Table 2.2: Fiducial points of arterial pulse wave used for pulse transit time measurement.

Fiducial Point	Label	Description	Illustration
Waveform foot	A	Minimum amplitude of a pulse cycle between the start of the systole and the end-diastole of the previous cycle.	<p>The illustration shows three vertically stacked waveforms: the top one is the 'Pulse Wave', the middle one is the '1st Derivative', and the bottom one is the '2nd Derivative'. A legend on the right lists points A through H with corresponding colored dots. Point A is a purple dot at the minimum of the pulse wave. Point B is a cyan dot at the intersection of a horizontal line from A and the pulse wave's tangent. Point C is a green dot on the pulse wave at 25% of its peak height. Point D is a grey dot at the peak of the 1st derivative. Point E is a cyan dot on the pulse wave at the peak of its slope. Point F is a green dot at the minimum of the 2nd derivative. Point G is a red dot at the maximum of the pulse wave. Point H is a red dot at the minimum of the pulse wave. A dashed box highlights the region around points A, B, C, and D, with a vertical arrow indicating the 25% height from point A to point C.</p>
Intersecting tangent point	B	The onset of the upstroke of the pulse during the systole	
25% pulse height	C	A point in the systolic upstroke of the pulse cycle positioned at a fixed percentage of the maximum pulse height.	
Second derivative maximum	D	Point corresponding to the onset of the systolic phase.	
First derivative maximum	E	Point on the original pulse at which the slope reaches its maximum.	
Second derivative minimum	F	Proximal point to the systolic peak.	
Pulse peak	G	Maximum amplitude of the pulse corresponding to the systolic peak.	
Dicrotic notch	H	The point corresponding to the aortic valve's closure and preceding the diastole's beginning.	

pulse upstroke as a reference point in the waveform [74]. Table 2.2 outlines numerous techniques that have been suggested to establish different fiducial time points within a pressure pulse cycle.

- A: Represents the minimum amplitude of a pulse cycle between the onset of systole and the end-diastole of the previous cycle. The pulse wave *foot* is characterized by a typically prolonged and flat region with minimal variation between adjacent values. However, multiple wave reflections during the end-diastolic phase and noise in the recorded pulse wave often distort this region, making it difficult to identify accurately.
- B: The start of the pulse upstroke during systole is detected as the intersection of the horizontal line passing through point A and the tangent to the pulse upslope. The Intersecting Tangent Point (ITP) lies within the region of rapid pressure level acceleration and is favored for its accuracy and reliability. The beginning of the upstroke region, where this point is located, is considered unaffected by multiple wave reflections, making it a preferred fiducial point for both invasive and non-invasive methods.
- C: The point on the systolic upstroke of the pulse cycle located at a fixed percentage of the maximum pulse height.

- D: This point marks the onset of the systolic phase and corresponds to the second derivative maxima on the upstroke of pressure pulse waves. It also lies within the region of rapid pressure level acceleration. Like Point B, it is widely accepted for its accuracy and is extensively used in both invasive and non-invasive PWV measurement techniques.
- E: The point on the original pulse where the slope reaches its maximum, occurring approximately halfway up the systolic upstroke of pulse waves. This characteristic point is considered relatively unaffected by arterial wave reflections. Local PWV determined by the first derivative maxima is typically higher than that obtained from the second derivative maxima point.
- F: The point proximal to the systolic peak. PWV values measured from this vicinity tend to be higher than those measured from the first derivative maxima point, reflecting a physiological phenomenon of variation in local PWV within a cardiac cycle.
- G: The maximum amplitude of the pulse corresponding to the systolic peak. This point is significantly influenced by the propagation of reflected arterial pressure waves and is generally not considered a reliable fiducial point due to this influence.
- H: Located in the diastolic phase of the pulse cycle, the dicrotic notch is believed to result from the combined effects of the aortic valve closure and a transient increase in arterial pressure caused by reflection waves. Despite being a distinct feature, it is not sufficiently precise in the context of coronary arteries but is recommended when multiple wave reflections contaminate the *foot* of blood pulse waves.

Statistical based approaches

Nowadays, many clinical indicators, including heart rate and BP, may now be monitored by wearable devices with findings that meet the standards for use in a clinical setting. Many studies have been conducted to assess PWV using standalone wearable devices, following this trend. The extraction of pulse waves from acquisition locations that deviate from clinically defined places may alter the shape of the signals, hence diminishing the estimated precision of the techniques described above. A novel set of algorithms has been developed to address the limitations of relying on a single localized feature for PWV evaluation. These algorithms analyze specific sections of pulse waveforms, avoiding the PWV evaluation based on a single feature extracted from the signal. Although additional validation studies must be undertaken, region-based approaches such as ‘diastole patching’ [74] and ‘region-matching’ [68],[75] provided excellent accuracy in the PWV assessment according to the accuracy criteria reported in 2010 ARTERY Society guidelines [53].

- **Statistical Phase Offset:** This technique compares a range of points from the proximal and distal waveforms over equal time shifts, generating a difference function and calculating the standard deviation for each shift. The time shift that minimizes the standard deviation represents the transit time.
- **Diastole Patching:** In this method, a small region of interest encompassing the *foot* of the proximal pulse wave is extracted using a defined window and is matched to an equitized region in the *foot* of the distal waveform. The window is set at an initial position on the distal waveform and moved across consecutively overlapping regions. The time point from the initial window position where a similarity comparison metric yields a minimum value is attributed as the pulse transit time.
- **Region Matching:** This technique determines the pulse transit time between proximal and distal arterial pulse waveforms by comparing small regions of interest (ROIs) around the *foot* of the pulse waves. It involves sliding a defined window across the distal waveform and using a similarity metric, such as the sum of squared differences, to find the best match with the proximal ROI. The time shift that minimizes this metric represents the pulse transit time.

2.3.5 Reference PWV Values

Arterial stiffness, measured by PWV, is a well-established biomarker for cardiovascular risk and target-organ damage. cfPWV is considered the gold standard for assessing aortic stiffness. While the relationship between aortic stiffness and cardiovascular events is continuous, the 2007 ESH/ESC Guidelines proposed a threshold of 12 m/s as a conservative marker for significant aortic dysfunction, particularly in middle-aged hypertensive patients [76]. A more recent expert consensus [77] revised this threshold to 10 m/s, based on the direct carotid-to-femoral distance, which accounts for the fact that the pressure wave travels over a 20% shorter anatomical distance (i.e., $0.8 \times 12 \text{ m/s} = 10 \text{ m/s}$) [78].

In [79], the authors aimed to establish normal and reference values for PWV in a large European cohort, categories and age groups. Table 2.3 presents typical PWV values for a healthy population based on age. The study found that PWV increases progressively with age and that this increase is more pronounced in individuals with elevated BP. Normal PWV values were derived from a subset of the population with optimal BP (below 120/80 mmHg) and no additional cardiovascular risk factors (CVRFs). In this group, PWV values were relatively low but increased gradually with age.

In the broader reference population, which included individuals with varying BP levels and some cardiovascular risk factors, there was a strong correlation between PWV, age, and BP. The increase in PWV was particularly significant in hypertensive individuals. Specifically, participants aged 60–69 with grade I hypertension

Table 2.3: Distribution of pulse wave velocity (m/s) according to the age category in the normal values population (1455 subjects), [79].

Age Categories	Normotonic group (n=1455)	
	$\mu (\pm 2\sigma)$	Median (10-90 percentile)
<30	6.2 (4.7–7.6)	6.1(5.3-7.1)
30–39	6.5 (3.8–9.2)	6.4 (5.2-8.0)
40–49	7.2 (4.6–9.8)	6.9 (5.9-8.6)
50–59	8.3 (4.5–12.1)	8.1 (6.3-10.0)
60–69	10.3 (5.5–15.0)	9.7 (7.9-13.1)
70+	10.9 (5.5–16.3)	10.6 (8.0-14.6)

Abbreviations: μ : mean value; σ : standard deviation.

(140–160/90–100 mmHg) had a PWV of 11.1 m/s, compared to 9.1 m/s in those with optimal BP in the same age group, Table 2.4. This highlights that elevated BP accelerates arterial stiffening, as reflected by higher PWV values.

Table 2.4: Distribution of PWV values(m/s) in the reference value population (11092subjects) according to age and blood pressure categories, [79].

Age Categories	Blood pressure category (n=11092)				
	Optimal	Normal	High Normal	Grade I Hypertension	Grade II/III Hypertension
	$\mu (\pm 2\sigma)$	$\mu (\pm 2\sigma)$	$\mu (\pm 2\sigma)$	$\mu (\pm 2\sigma)$	$\mu (\pm 2\sigma)$
<30	6.1 (4.6–7.5)	6.6 (4.9–8.2)	6.8 (5.1–8.5)	7.4 (4.6–10.1)	7.7(4.4–11.0)
30–39	6.6 (4.4–8.9)	6.8 (4.2–9.4)	7.1 (4.5–9.7)	7.3 (4.0–10.7)	8.2 (3.3–13.0)
40–49	7.0 (4.5–9.6)	7.5 (5.1–10.0)	7.9 (5.2–10.7)	8.6 (5.1–12.0)	9.8 (3.8–15.7)
50–59	7.6 (4.8–10.5)	8.4 (5.1–11.7)	8.8 (4.8–12.8)	9.6 (4.9–14.3)	10.5 (4.1–16.8)
60–69	9.1 (5.2–12.9)	9.7 (5.7–13.6)	10.3 (5.5–15.1)	11.1 (6.1–16.2)	12.2 (5.7–18.6)
70+	10.4 (5.2–15.6)	11.7 (6.0–17.5)	11.8 (5.7–17.9)	12.9 (6.9–18.9)	14.0 (7.4–20.6)

Abbreviations: μ : mean value; σ : standard deviation.

The study outlined in [80] establishes age-dependent reference values for PWV across two different parameters: carotid-femoral PWV, and brachial-ankle PWV in a large European cohort. Sampling 8,509 individuals aged 19–80, the study established that age and blood pressure are the primary determinants of PWV, significantly affecting its variability. Additionally, sex was found to influence baPWV and cfPWV, while other cardiovascular risk factors, such as cholesterol levels and smoking, showed weaker correlations with PWV values. As reported in Table 2.5, for healthy individuals, cfPWV, often regarded as the gold standard, ranged from approximately 7.2 m/s in individuals aged 18–29 years to 10.5 m/s in those over 70 years. Similarly, baPWV values showed an increase from around 9.2 m/s in the youngest group to 13 m/s in individuals over 70 years.

Table 2.5: Normal and reference values of PWV parameters for cfPWV and baPWV [80].

Age Categories	Normotonic (n=3092)	Reference Group (n=8460)	Normotonic (n=3099)	Reference Group (n=8483)
	$\mu (\pm 2\sigma)$	$\mu (\pm 2\sigma)$	$\mu (\pm 2\sigma)$	$\mu (\pm 2\sigma)$
<30	7.2 (4.2–12.4)	7.3 (4.3–12.5)	9.2 (7.9–10.8)	9.3 (7.9–11.0)
30–39	7.8 (5.0–12.2)	7.9 (5.0–12.4)	9.9 (8.2–11.8)	10.0 (8.2–12.2)
40–49	8.9 (5.4–14.5)	9.1 (5.6–14.8)	10.3 (8.5–12.5)	10.7 (8.5–13.4)
50–59	9.4 (5.9–15.1)	9.9 (6.0–16.4)	11.1 (8.8–13.8)	11.8 (8.9–15.5)
60–69	10.1 (6.1–16.7)	10.7 (6.5–17.6)	12.1 (9.4–15.5)	12.9 (9.8–16.9)
70+	10.5 (6.3–17.7)	11.4 (6.8–19.3)	13.0 (10.1–16.9)	13.9 (10.6–18.4)
PWV-Site:	cfPWV		baPWV	

Abbreviations: μ : mean value; σ : standard deviation.

In [81], reference values for PWV were also established using the Mobil-O-Graph PWA monitor, which measured central blood pressure, augmentation index (AIx), and PWV in a cohort of 6,499 individuals. Participants were divided into two groups: those without cardiovascular risk factors (CVRF-No) and those with at least one major risk factor (CVRF-Yes).

As reported in Table 2.6, in individuals without CVRFs, PWV ranged from 4.9 m/s in women under 30 to 11.3 m/s in women over 70, and from 5.2 m/s to 11 m/s m/s in men across the same age groups. In contrast, individuals with CVRFs exhibited higher PWV values, ranging from 5.3 m/s to 11.8 m/s in women and from 5.5 m/s to 11.2 m/s in men. This underscores the impact of cardiovascular risk factors on arterial stiffness, with higher PWV values observed in individuals with established risk factors.

2.3.6 Commercial Systems for PWV Assessment

Sphygmocor

The SphygmoCor CvMS (Cardiovascular Management System) (AtCor Medical, Sydney, Australia) uses applanation tonometry to record high-fidelity arterial pulse waveforms at the carotid and femoral sites. This method involves flattening the artery against an underlying bone to obtain accurate pressure readings. The CvMS records pulse waveforms sequentially from different arterial sites, such as the carotid and femoral arteries, with the R-waves of a simultaneously recorded ECG used to synchronize the signals. The device calculates PWV by determining the transit time between the *foot* of the waveforms recorded at the carotid and femoral

Table 2.6: PWV values for men and women, according to age categories, in individuals with and without major CVRF [81]

Age Categories	CVRF-NO		CVRF-YES	
	Women (n=531)	Men (n=336)	Women (n=3169)	Men (n=2463)
<30	4.9 (4.4, 5.3)	5.2 (4.9, 5.7)	5.3 (4.7, 6.0)	5.5 (5.0, 6.3)
30–39	5.4 (5.0, 6.1)	5.7 (5.3, 6.1)	5.8 (5.3, 6.7)	6.1 (5.5, 6.7)
40–49	6.4 (5.7, 6.9)	6.5 (5.9, 7.0)	6.8 (6.0, 7.7)	6.8 (6.2, 7.5)
50–59	7.5 (6.7, 8.2)	7.4 (6.9, 8.0)	7.9 (7.1, 8.8)	7.9 (7.1, 8.7)
60–69	8.9 (8.1, 9.4)	8.9 (8.2, 9.6)	9.3 (8.4, 10.4)	9.2 (8.4, 10.2)
70+	11.3 (10.2, 13.2)	11.0 (10.1, 12.3)	11.8 (10.2, 14.0)	11.2 (9.9, 13.2)

Notes: Results are expressed as as 50th (10th and 90th) percentiles.



Figure 2.16: (a) Sphygmocor CvMS device. (b) Sphygmocor XCEL device. [82]

sites, employing the *foot-to-foot* method and intersecting tangent algorithms. Additionally, it provides central BP measurements, offering a comprehensive assessment of cardiovascular health.

However, the SphygmoCor CvMS has several drawbacks. The accuracy of PWV measurements can be affected by heart rate variability, as the sequential nature of the recordings introduces potential timing discrepancies. Sequential pulse acquisition can be time-consuming, requiring careful synchronization and quality controls to ensure accurate measurements. The device may struggle to produce high-quality recordings in patients with lower BP, peripheral arterial disease, or obesity, as peripheral pulses can be more difficult to capture. Moreover, the system requires a high degree of operator expertise for peripheral signal acquisition, impacting the consistency and reliability of the measurements.

The SphygmoCor XCEL (AtCor Medical, Sydney, Australia) is an advanced version of the CvMS, designed to improve user-friendliness and reduce measurement

time while maintaining accuracy. It incorporates a cuff-based acquisition protocol in addition to applanation tonometry. The XCEL uses a brachial cuff to acquire simultaneous pressure waveforms, simplifying the measurement process and reducing operator dependence. By using the cuff-based system, the device allows for simultaneous recording of arterial waveforms, reducing the time required for measurements by more than 50% compared to sequential methods. Like the CvMS, the XCEL calculates PWV using the *foot-to-foot* method and intersecting tangent algorithms, and it also offers central BP measurements. The XCEL is designed to be more user-friendly, with automated features that guide the operator through the measurement process, making it accessible to a broader range of users. Despite its improvements, the SphygmoCor XCEL has certain limitations. The cuff-based acquisition can inherently damp higher-frequency information due to volumetric displacement, potentially affecting the accuracy of the waveform analysis. While the device is more user-friendly, it still faces challenges in producing high-quality recordings in patients with certain conditions, such as peripheral arterial disease or obesity. Additionally, the advanced features and capabilities of the XCEL may come at a higher cost, potentially limiting its accessibility in some clinical settings.

Complior

The Complior device (Alam Medical, Saint Quentin Fallavier, France), is considered one of the most reliable and accurate systems for noninvasive PWV assessment. It simultaneously records arterial wave pulses using up to four piezoelectric transducers applied directly to the skin at sites such as the carotid, femoral, radial, and distal arteries. The transit time between each simultaneously recorded wave is estimated using the second derivative algorithm at the wave *foot*. The distance traveled by the pulse wave is measured between the two recording sites (e.g., carotid-femoral, carotid-brachial, or femoral-dorsalis pedis) by the direct method.

The Complior device is highly regarded for its accuracy, which is mainly due to the precise measurement of the pulse transition time, which is comparable to the accuracy provided by catheter methods. Studies have shown that the mean difference in PWV estimation between Complior and reference invasive methods is relatively small, -0.2 m/s, with a standard deviation of ± 0.45 m/s and a correlation coefficient (r) of 0.99 [83].

However, the Complior system has several limitations. The accuracy of the measurements is highly dependent on the operator's skill in positioning the sensors correctly. The difference between the actual path length of the pulse wave and the distance measured between the transducers can also introduce errors. Additionally, the piezoelectric sensors are highly sensitive to motion and positioning disturbances, which can affect the reliability of the measurements. Some patients find the neck clip used for the carotid sensor to be uncomfortable, which can further impact the ease of use and patient compliance.



Figure 2.17: Complior device. [84]

Pulse Pen

The PulsePen (DiaTecne, Milano, Italy), consists of two small portable tonometers and a small ECG unit, which can be used to detect pressure waveforms at the carotid and femoral arteries either simultaneously or sequentially. The device calculates PWV by determining the transit time between the *foot* of the waveforms at these sites using the intersecting tangent method and measures the travel distance manually with a tape measure.

The PulsePen is highly portable and user-friendly, making it suitable for both clinical and ambulatory settings. It is lightweight and can be operated by a single user, providing high-precision measurements. Studies have shown a mean difference and standard deviation of 0.20 ± 2.54 m/s compared to invasive methods, indicating its reliability and accuracy [85, 86]. However, the device requires skilled operators for accurate sensor placement and measurement, and its accuracy can be affected by the choice between single-probe and dual-probe methods.



Figure 2.18: Pulse Pen device. [86]

Arteriograph

The Arteriograph (TensioMed, Budapest, Hungary) is a widely used noninvasive device for measuring PWV and other cardiovascular parameters. This device

employs an oscillometric brachial cuff to record the supra-systolic waveform at the brachial artery, making it simpler and more user-friendly compared to other PWV measurement devices that require multiple sensor placements. The Arteriograph estimates PWV by measuring the time interval between the first wave peak, which corresponds to left ventricular ejection, and the second wave peak, which is assumed to result from the reflected pressure wave from the aorto-iliac bifurcation. The cuff pressure is set to at least 35 mmHg above the actual SBP to occlude the brachial artery, ensuring that the waveforms recorded are pure pressure waves with minimal motion artifact, as the brachial artery wall is almost still under the cuff.

Differently from the mentioned devices employed for PWV assessment, the distance used in the calculation of PWV is measured from the upper edge of the pubic bone (symphysis) to the sternal notch (jugulum).



Figure 2.19: Arteriograph acquisition system. [87]

Mobil-O-Graph

The Mobil-O-Graph (IEM Healthcare, Aachen, Germany) is a noninvasive device that measures PWV and assesses arterial stiffness using an oscillometric brachial cuff with a high-fidelity pressure sensor. It reconstructs the aortic pulse waveform (AOW) from the brachial pulse waveform (BPW) by applying a generalized transfer function. This process separates the incident and reflected pulse waves to estimate PWV based on the time difference between these waves. The main advantage of the Mobil-O-Graph is its ability to provide a comprehensive assessment of arterial stiffness through a simple brachial cuff measurement, making it accessible for routine clinical use. Studies have shown that it produces reliable measurements, with a mean difference of -1.01 ± 2.54 m/s compared to invasive methods [85]. However, the device's accuracy can be affected by the assumptions made during the waveform reconstruction process and improper cuff placement or patient movement. While it shows a weaker agreement with invasive methods compared to some other noninvasive devices, the Mobil-O-Graph remains a valuable tool for providing comprehensive cardiovascular health assessments in clinical practice.

CAVI-VaSera

The CAVI-VaSera device (Fukuda Denshi, Tokyo, Japan) measures the cardio-ankle vascular index (CAVI) to assess arterial stiffness. It operates by simultaneously recording BP, ECG, and phonocardiogram (PCG) signals to calculate PWV from the heart to the ankle. This measurement provides a stable index of arterial stiffness, less influenced by current BP, making it valuable for tracking changes over time and evaluating therapeutic interventions. The device is user-friendly and suitable for routine clinical use, though accuracy can be affected by sensor placement and patient conditions.

Ultrasound

Ultrasound devices are crucial for non-invasive measurement of PWV and assessment of arterial stiffness. They use high-frequency sound waves to create detailed images and data of the arteries. Two primary techniques are employed: Doppler ultrasound, which measures blood flow speed and calculates PWV based on time delays between arterial sites, and B-mode/M-mode ultrasound, which provides anatomical imaging and measures arterial wall motion and elasticity [88]. These methods offer direct visualization, real-time imaging, and high precision, especially with advanced echotracking systems. However, limitations include frame rate constraints, potential manual measurement variability, and the need for skilled operators. Despite these challenges, ultrasound remains an effective and widely used tool for evaluating cardiovascular health.

Magnetic resonance Imaging

MRI (Magnetic Resonance Imaging) is a powerful non-invasive technique used to assess PWV and evaluate arterial stiffness. Due to its detailed anatomical imaging capabilities, it offers high accuracy in measuring the travel distance of pulse waves within the arteries, particularly in the aorta [89]. In MRI-based PWV assessment, phase-contrast MRI (PC-MRI) is commonly employed. This technique captures blood flow velocities across different anatomical planes, providing a comprehensive view of the pulse wave as it moves through the arterial system. The PWV is calculated by determining the time it takes for the pulse wave to travel between two points along the aorta. This is achieved by measuring the arrival time of the pulse wave at various segments of the artery, typically identified by the intersection between the baseline of the waveform and the upstroke tangent. One of the primary advantages of using MRI for PWV assessment is its ability to accurately measure the distance between arterial segments without relying on geometric assumptions. This is particularly important in cases where the vessel path is tortuous, as MRI can account for these curves and provide precise distance measurements. Despite its accuracy and detailed imaging capabilities, MRI has several limitations. It is an

expensive and non-portable technique, making it less accessible for routine clinical use. The procedure can also be uncomfortable for some patients, especially those who suffer from claustrophobia, due to the enclosed nature of the MRI scanner. Moreover, MRI typically has poorer time resolution compared to other techniques, which can affect the precision of the PWV measurement. One significant challenge associated with assessing PWV is the elevated cost of the equipment. Devices used for accurate PWV measurements, such as applanation tonometers and specialized oscillometric, and/or ultrasound devices, often come with a high price tag due to their advanced sensing technologies, calibration requirements, and complex algorithms. These elevated costs can limit widespread clinical adoption, particularly in resource-constrained settings, and may restrict the use of PWV as a routine cardiovascular assessment tool. Furthermore, the need for ongoing maintenance and potential software updates adds to the long-term financial burden, making it less accessible for smaller healthcare providers or research institutions. Table 2.7 provides a summary of the comprehensive information regarding non-invasive systems used for PWV assessment, including an overview of the current market prices.

Table 2.7: Overview of the current systems for PWV assessment detailing the recording methodology, acquisition sites, adopted sensing technology, and PTT computation technique.

Device	Manufacturer	Market Price (USD)	Recording Methodology	PWV Sites	Sensing Technology	PTT Evaluation Method
Sphygmocor CVS	AtCor Medical Australia	[20K-30K]	Sequential	Carotid-to-femoral	Applanation tonometry and ECG	Intersecting tangent
Sphygmocor XCEL	AtCor Medical Australia	[25K-30K]	Simultaneous	Carotid-to-femoral Carotid-to-brachial	Applanation tonometry and bladder cuff	Intersecting tangent
Complior	Alam Medical, France	[10K-15K]	Simultaneous	Carotid-to-femoral Carotid-to-brachial Carotid-to-radial Carotid-to-tibial	Piezoelectric mechanotransducers	Peak of second derivative
PulsePen	Dia Tecne, Italy	[8K-12K]	Sequential or Simultaneous	carotid-to-femoral	Applanation Tonometry	Intersecting tangent
Arteriograph	TensioMed, Hungary	[12K-15K]	One-site	aortic PWV	Bladder pressure cuff	Peak-to-peak
Mobil-O-Graph	IEM Healthcare, Germany	N/A	One-site	aortic PWV	Bladder pressure cuff	4th derivative
CAVI-VaSera	Fukuda Denshi, Japan	[15K-20K]	Simultaneous	Brachial-to-ankle	ECG and pressure cuffs	wave foot
Artlab System	Esaoite, Italy	[20K-30K]	Simultaneous	Carotid-to-femoral	Ultrasound medical imaging and ECG	-
MRI	-	[1M-1.5M]	Simultaneous	aortic PWV	Phase-contrast	Intersecting tangent

2.4 Blood Pressure Assessment

The increasing interest in cuffless BP measurement is driven by its potential to transform hypertension management, a leading cause of morbidity and mortality worldwide [2]. Advances in technology have paved the way for the development of cuffless BP measuring devices, which promise accuracy, ease of use, comfort, and continuous monitoring. Traditional BP measurement methods, such as tonometry or volume clamp/plethysmography, rely on pulse wave transit time/velocity. In contrast, cuffless BP devices use optical sensors, akin to those found in fitness trackers, to measure beat-to-beat variability and calculate systolic and diastolic readings through mathematical modeling [90, 91, 92].

These optical sensors, typically worn on the wrist or finger, offer the advantage of continuous BP monitoring without the discomfort and sleep disruption caused by traditional cuff inflations. This feature is particularly beneficial for elderly individuals or those with limited mobility. Despite their potential, the accuracy of cuffless BP devices remains a concern. Even after validation, discrepancies of up to 20 mmHg have been observed when compared to standard brachial cuff measurements, especially in individuals with elevated BP. A significant challenge for these technologies is the calibration of local pressure measurement sites [93].

Current pulse-based systems can accurately predict BP trends rather than exact values. Significant fluctuations in these trends can serve as warning signals for users to monitor their BP more closely. Continuous monitoring of BP variations can be instrumental in the clinical management of certain conditions. As technology advances, the development of cuffless BP monitoring devices will likely continue, providing continuous BP data and comprehensive hemodynamic information. This progression could enhance our ability to correlate BP trends with clinical outcomes and improve cardiovascular and renal disease risk prediction. The exploration of this innovative approach is highly valuable and warrants further investigation [69].

BP measurement is crucial for monitoring cardiovascular health. Both hypertension and hypotension represent significant health issues that frequently necessitate medical intervention. Traditional methods for measuring BP include:

- *Arterial Catheterization*: Considered the invasive gold standard, arterial catheterization involves inserting a manometer directly into an artery to measure BP waveforms [94]. This method, often used in critically ill patients requiring continuous BP monitoring, utilizes intra-arterial catheters (also known as "arterial lines"). The technique uses a pressure transducer linked with an invasive catheter that contacts a pulsating artery (such as the radial artery) through fluid, allowing for continuous, direct BP measurement. While arterial catheters offer high accuracy and continuous monitoring, they are invasive, necessitate expert placement and monitoring, and require the patient to remain relatively stationary. Therefore, although it provides true arterial BP values, its invasive nature limits its widespread clinical use.

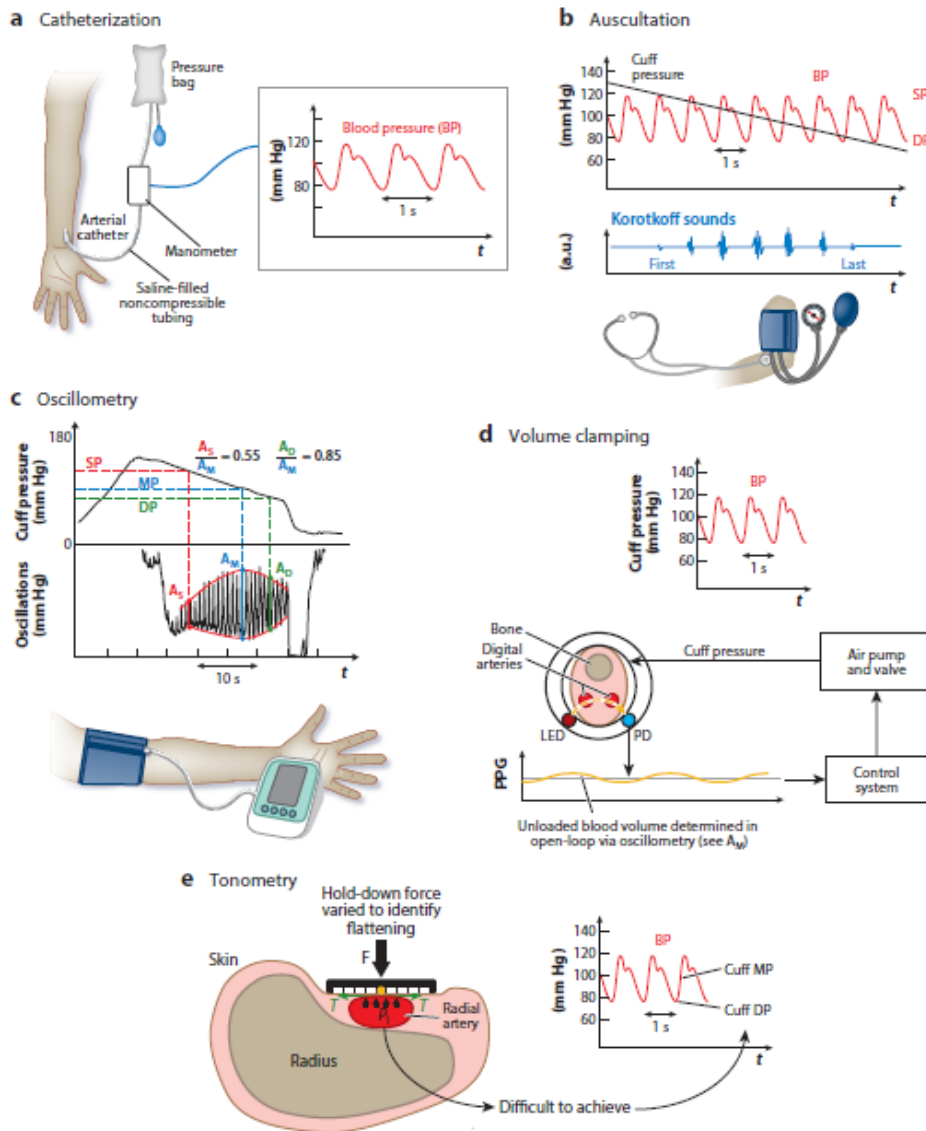


Figure 2.20: Conventional BP measurement methods. Standard or widely used methods include catheterization (a), auscultation (b), and oscillometry (c). Volume clamping (d) and tonometry (e) are less common methods for noninvasive measurement of the BP waveform. All the noninvasive methods require an inflatable cuff, which is not readily available and cumbersome to use. Abbreviations: AD, oscillogram amplitude when cuff pressure is at DBP; AM, maximum oscillogram amplitude; AS, oscillogram amplitude when cuff pressure is at SBP; BP, blood pressure; DBP, diastolic BP; F, force; LED, light-emitting diode; MP, mean BP; PD, photodetector; Pi, internal BP; PPG, photoplethysmography; SBP, systolic BP; t, time; T, arterial wall tension [95].

- *Manual Auscultation*: The standard noninvasive method of manual auscultation employs a stethoscope and an upper arm cuff to detect Korotkoff sounds, which indicate systolic and diastolic BP [95]. Traditionally, mercury or mercury-free sphygmomanometers have been the gold standard for validating the accuracy of new BP measurement technologies. However, due to mercury’s environmental toxicity, these devices have been banned from clinical use. Alternatives include hybrid manual auscultatory devices with LED or LCD displays and high-quality aneroid devices, although these are prone to observer-related errors such as terminal digit preference, observer prejudice, and bias.
- *Oscillometry*: Oscillometry is the predominant automatic, noninvasive method for measuring BP [96]. This technique uses an inflatable cuff to determine BP by analyzing oscillation amplitudes within the cuff pressure. The procedure involves placing the cuff around the upper arm, wrist, or ankle and slowly deflating (or inflating) it between pressures above systolic and below diastolic while monitoring the cuff pressure. Unlike auscultation, the manometer is built into the monitor, reducing the importance of precise sensor positioning. The cuff pressure represents the applied pressure and includes small oscillations that reflect the pulsatile arterial blood volume. The amplitude of these oscillations changes with the applied pressure, adhering to the nonlinear relationship between arterial blood volume and transmural pressure. BP is derived from the oscillogram using algorithms specific to each brand, based on population averages.
- *Volume Clamping*: This noninvasive method uses a finger cuff with a PPG sensor to monitor blood volume oscillations. The PPG sensor detects variations in blood volume within the digital arteries, while a manometer records the cuff pressure [21]. Initially, the cuff pressure is incrementally increased to identify the blood volume at zero transmural pressure, indicating when the artery is unloaded. Then, the cuff pressure is continuously adjusted to keep the PPG-detected blood volume at this unloaded level throughout the cardiac cycle, using a rapid servocontrol system. This technique allows the cuff pressure to approximate the finger BP waveform. Continuous monitoring necessitates regular updates of the unloaded blood volume to accommodate changes in vasomotor tone.
- *Tonometry*: Tonometry is a noninvasive technique that measures BP waveforms from large, superficial arteries using a force sensor applied to the skin over the artery [97]. The goal of applanation tonometry is to record intra-arterial pressure waveforms accurately. This method typically involves a pen-like tonometer probe with a piezoelectric pressure sensor at the tip, although servo-controlled devices with piezoelectric arrays can also be used to minimize

movement artifacts. The sensor is lightly applied perpendicular to the artery, partially flattening the arterial wall (applanation), which eliminates tangential forces and exposes the sensor to the arterial pressure. This setup enables high-quality recordings of the arterial pulse, closely resembling intra-arterial measurements.

2.4.1 Advantages of Cuffless Blood Pressure Measurement

Cuffless BP measurement offers solutions to several limitations associated with traditional methods, enhancing accessibility, convenience, and continuous monitoring capabilities.

Indeed, traditional cuff devices are not always available, particularly in low-resource settings, which limits regular BP monitoring opportunities [95]. In many low-resource areas, individuals lack access to these devices or must go to considerable lengths to use cumbersome equipment. Consequently, many people do not monitor their BP regularly, making it difficult to manage hypertension effectively or stay motivated to adhere to BP-lowering medications. Currently, only about three in seven people with hypertension worldwide are aware of their condition, and just one of these seven has their BP under control. This lack of awareness and management makes hypertension the leading cause of disability-adjusted life years lost globally.

In addition, the repeated inflations and deflations required by traditional cuffs can be disruptive, reducing the effectiveness of ambulatory BP monitoring and hypotension surveillance. The inconvenience and discomfort of using cuffs contribute significantly to the underutilization of ambulatory BP monitoring and can diminish the clinical value of nighttime BP readings. Additionally, the infrequency of BP measurements in postsurgical patients who are at high risk for hypotension—a condition associated with increased mortality—underscores the need for a more convenient solution.

Furthermore, traditional oscillometric devices do not provide continuous BP readings, which are crucial for the immediate detection of hypotension and real-time therapy adjustments during perioperative and critical care. Continuous monitoring is essential to understand the dynamic BP responses to daily physical and mental activities, which are often unknown with intermittent measurements.

Removing the cuff from noninvasive BP measurement addresses several critical issues:

1. Increasing Hypertension Awareness: Encourages regular BP monitoring in daily life, enhancing hypertension awareness among the general population.
2. Improving Long-Term Hypertension Control: Facilitates continuous monitoring, which can reveal high BP readings to patients and motivate better management of their condition.

3. **Enhancing Hypertension Evaluation and Diagnosis:** Allows for unobtrusive BP monitoring throughout the day and night, improving the accuracy of hypertension assessments.
4. **Advancing Hypotension Surveillance and Therapy:** Provides seamless, continuous BP monitoring, which is crucial for detecting and managing hypotension.

By offering comprehensive BP data across various daily circumstances, rather than just periodic snapshots, the cuffless paradigm has the potential to revolutionize hypertension evaluation and management, significantly improving BP assessment.

Cuffless BP measurement techniques can be divided into calibrated and uncalibrated methods. Calibrated methods involve obtaining one or more variables that correlate with BP and then mapping or calibrating these variables to mmHg units using periodic cuff BP measurements or demographic inputs [98]. In contrast, uncalibrated methods do not require such calibration, either from cuff measurements or demographic data, but tend to be less convenient once the initial cuff BP measurement for calibration has been acquired.

2.4.2 Uncalibrated models

Uncalibrated methods for cuffless BP measurement aim to simplify BP monitoring by eliminating the need for periodic calibration. Here are the three main uncalibrated methods: cuffless oscillometry, ultrasound, and volume control.

1. **Cuffless Oscillometry:** Adjusts the transmural pressure of an artery without an inflatable cuff, using force and PPG sensors to measure pressure variations and compute BP from the oscillogram [99].
2. **Ultrasound:** Employs M-mode and Doppler principles to measure blood volume and velocity waveforms in an artery [100].
3. **Volume Control:** Uses a servo-control system to maintain blood volume at its unloaded level throughout the cardiac cycle, enabling continuous BP monitoring.

2.4.3 Calibrated models

1. **Pulse Transit Time:** Measures the time delay for a pressure wave to travel between two arterial sites, typically a proximal and a distal one [101]. PTT is inversely related to arterial stiffness and BP [102]. The calibration process for cuffless BP measurement is essential for establishing a direct mapping relationship between actual BP readings and PTT measurements. This process involves several aspects: the method of calibration, the frequency of calibration, and whether calibration can be generalized for a population or needs

to be individualized. The goal is to create a calibration curve that maps PTT measurements to absolute BP values. The steps involved in calibration include defining a mathematical model to relate PTT to BP, either using physical models or empirical regression models. Physical models typically rely on the Moens–Korteweg and Bramwell–Hill equations with an assumed function to relate the elastic modulus or compliance to BP. Next, multiple pairs of PTT and BP values are measured from a subject during interventions that cause significant BP changes. Common interventions include exercise (e.g., climbing stairs, cycling on an ergometer), postural changes (i.e., seated, supine, standing), sustained handgrip, and the Valsalva maneuver. More substantial BP changes can be induced using anesthesia induction, surgery, and ICU therapies, though these are limited to hospitalized patients and are not suitable for managing chronic hypertension. The parameters of the model are then estimated by fitting it to the multiple PTT-BP measurements. The accuracy of parameter estimation improves with the ratio of the number of data pairs to the number of parameters, with least squares regression commonly used for this purpose. Calibration can be performed once at the beginning or periodically over time [103]. For studies requiring periodic calibration, the interval between calibrations is often within two hours to account for physiological changes such as vascular tone and smooth muscle contraction. Shorter PTT is directly linked to increased arterial stiffness, driven by higher sympathetic nerve activity or elevated BP, necessitating recalibration when such changes occur. Besides individualized calibration, a generalized approach can also be used. This involves using a population average value for one model parameter while estimating the other parameter from cuff BP measurements. This method avoids BP perturbation but may result in less accurate BP values. The process involves collecting training data comprising pairs of PTT estimates and BP values during a set of BP-varying interventions from a diverse group of subjects, estimating the parameters of a calibration model for each subject, and regressing these parameters on simple subject information. Collecting the necessary training data is a significant undertaking but may be the best way to popularize the PTT-based BP monitoring approach. Independent determination of systolic and diastolic BP can be challenging, especially if these values do not vary in the same direction (e.g., isolated systolic hypertension). This issue can be addressed by including additional covariates, such as heart rate, in the calibration model or by estimating multiple PTT values per beat through arterial modeling. PTT estimates should correlate better with BP values than these covariates to offer real value. This chapter provides a general overview of key elements in PWV or PTT-related cuffless continuous BP monitoring. For more detailed information on mathematical models, calibration, and practical approaches, interested readers should refer to relevant literature in this field.

2. Pulse Wave Analysis (PWA): Pulse wave analysis consists of the morphological analysis of the pressure pulse waveform. With the purpose of deducing indicators of cardiovascular health, the technique can provide an indirect means of assessing BP [104].

PWA has emerged as an essential method for non-invasive cardiovascular health monitoring, particularly for cuffless BP measurement. The technique involves examining the pulse waveform, which provides significant insights into various cardiovascular parameters. The integration of Machine Learning (ML) into PWA has considerably enhanced its accuracy and utility, enabling continuous and precise BP monitoring. Pulse wave analysis revolves around measuring and interpreting the pulse wave generated by the heart as it pumps blood through the arteries. Key parameters derived from PWA include PWV, PTT, augmentation index (AIx), and central aortic blood pressure (CABP). As mentioned in the previous sections, PWV measures the speed at which BP waves move through the arteries, directly indicating arterial stiffness. PTT is the time it takes for the pulse wave to travel between two arterial sites and is inversely related to BP. Additionally, AIx reflects the extent of wave reflection, providing information on arterial stiffness and CABP. CABP estimates the pressure in the aorta, offering a more accurate representation of the load on the heart compared to peripheral measurements. Photoplethysmography is a cornerstone technology in PWA. It uses optical sensors to detect blood volume changes in the microvascular bed of tissue, making it non-invasive and suitable for continuous monitoring. ECG and seismocardiography (SCG) are also integral to PWA, with ECG measuring the electrical activity of the heart and SCG capturing mechanical vibrations. Combining PPG with ECG improves PTT measurements and enhances the accuracy of cardiovascular assessments.

By extracting features from an arterial waveform (i.e., PPG or tonometry), and mapping them to BP units through a calibration model, PWA can be performed on PPG waveforms and can enhance PTT accuracy. Moreover, the inclusion of ML into PWA has greatly improved its accuracy and applicability, allowing for more precise and personalized BP monitoring.

2.4.4 Machine Learning techniques for non-invasive cuffless measurement of blood pressure

ML has revolutionized PWA by enabling the extraction of meaningful cardiovascular parameters from complex pulse waveforms. Traditional PWA methods often face challenges due to the intricate and non-linear nature of pulse waveforms, as well as the influence of various physiological and environmental factors. ML approaches address these challenges by learning from large datasets, identifying patterns, and making accurate predictions based on the input data.

Convolutional Neural Network (CNN) are widely used in PWA for their ability to automatically extract features from raw waveform data. In [105] the PPG2BP-Net model employs a comparative paired one-dimensional CNN structure to estimate highly variable intrasubject BP. By comparing PPG signals from dual sensors, the CNN derives the relationship between the waveform features and BP values, providing continuous BP estimates without the need for periodic calibration. Recurrent Neural Network (RNN) [106] and Long Short-Term Memory (LSTM) [107] networks are particularly effective in handling time-series data, such as pulse waveforms. These networks capture temporal dependencies and patterns in the data, enabling more accurate BP predictions. By processing sequences of PPG signals, RNNs and LSTMs can account for the dynamic nature of cardiovascular parameters, improving the robustness of BP estimation.

Support Vector Machine (SVM) are employed for classification tasks in PWA, such as distinguishing between different physiological states based on pulse wave characteristics [108, 109]. In combination with feature extraction techniques like wavelet transforms, SVMs can classify pulse waveforms into categories that correspond to specific BP ranges or health conditions, facilitating targeted interventions. Dynamic Time Warping (DTW) and K-Nearest Neighbour (KNN) are used to align pulse waveforms by minimizing the differences in their shapes, making them suitable for recognizing similar patterns in PWA. When combined with KNN, DTW enhances the accuracy of cardiovascular parameter extraction by matching target waveforms with reference waveforms in a pattern library. This approach is effective in handling variations in heart rate and pulse pressure, providing reliable BP estimates [110].

Ensemble learning techniques, such as random forests and gradient boosting machines, aggregate predictions from multiple models to improve overall accuracy [111]. These methods are used in PWA to integrate information from various sensors and features, resulting in more robust BP predictions. By leveraging the strengths of different models, ensemble methods can mitigate the impact of outliers and noise in the data.

Despite the progress, several challenges remain in PWA-based BP estimation. Motion artifacts, signal noise, and individual variability in vascular characteristics can affect the accuracy of PPG-based BP measurements. Ensuring diverse and high-quality datasets is crucial for robust BP estimation. Incorporating adaptive learning techniques and personalized calibration methods can enhance the long-term accuracy of cuffless BP monitoring. For widespread adoption, ML-based PWA systems must be seamlessly integrated into clinical workflows. Ensuring compatibility with existing medical devices, electronic health records, and regulatory standards is essential for clinical implementation.

Motion Artifacts Recognition in PPG Data

PPG signals are highly susceptible to motion artifacts, which can significantly distort the signal and affect the accuracy of the derived physiological measurements. Motion artifacts in PPG data can arise from various sources, including voluntary and involuntary movements, sensor displacement, and environmental interferences. Recognizing and mitigating these artifacts is crucial to ensure the reliability of PPG-based measurements [112].

Several methods have been developed to recognize and mitigate motion artifacts in PPG signals, ranging from traditional signal processing techniques to advanced machine learning algorithms. Time-domain analysis methods involve directly examining the amplitude and time characteristics of the signal. In [113] the Pan and Tompkins algorithm, initially developed for ECG signals and later adapted for PPG signals. This algorithm involves several preprocessing steps, including filtering, differentiation, squaring, and integration, which enhance the PPG signal and help in detecting peaks corresponding to heartbeats.

Frequency-domain analysis methods employ spectral analysis to identify characteristic frequencies of motion artifacts. Techniques like Continuous Wavelet Transform (CWT) decompose the PPG signal into various frequency components [114]. This decomposition helps distinguish between physiological signals and artifacts by analyzing the frequency content of the PPG signals.

Machine learning approaches have shown significant promise in recognizing and mitigating motion artifacts in PPG signals. These methods involve training models on labeled datasets to learn patterns associated with artifacts and physiological signals. Random Forest classifiers, for example, construct multiple decision trees during training, with each tree voting on the classification outcome. The majority vote determines the final classification. RF classifiers have been effective in distinguishing between acceptable and anomalous PPG segments by training on features such as Kaiser-Teager energy, spectral entropy, and signal skewness. Studies have demonstrated high accuracy in detecting artifacts using RF classifiers [114].

Support Vector Machines (SVMs) are another type of supervised learning model used for classification and regression analysis. SVMs classify data points by finding the optimal hyperplane that separates different classes in the feature space. This method has been applied to PPG data to effectively identify segments affected by motion artifacts by training on extracted features [115].

In general, the procedure that discerns instances deviating from the recurrent patterns or trends within the data is known as anomaly detection [116]. Depending on the field of application, several anomaly detection algorithms have been implemented to detect outliers within an ensemble of data [114, 117, 118]. The design of these techniques is generally tailored to the nature of the data, the characteristics of anomalies, and the availability of labels. Supervised anomaly detection techniques create a predictive hypothesis function to discern abnormal behavior, relying on

annotated instances to establish expected patterns and outlier classes. However, these methods depend on labeling, which poses a challenge for many applications, especially in long-term health monitoring, where expert data labeling is expensive and time-consuming [119]. On the contrary, unsupervised anomaly detection techniques address the detection of outliers in unlabeled data. These methods operate based on the assumption that regular instances are more prevalent than outliers, and normal instances tend to form dense clusters, while outliers are sparser. This approach proves advantageous when acquiring labeled data poses challenges or is impractical, offering a more adaptable and cost-effective solution [119, 120].

The Isolation Forest (IF) algorithm isolates observations by randomly selecting features and splitting values to create a forest of random trees. Anomalies are identified as points with shorter average path lengths. This method is efficient for high-dimensional data and has been successfully applied in healthcare to detect PPG signal anomalies. The Local Outlier Factor (LOF) algorithm measures the local density deviation of a data point with respect to its neighbors. Points with significantly lower density than their neighbors are considered outliers. LOF is effective in identifying local anomalies, making it suitable for detecting motion artifacts in PPG data where density variations are common. The Elliptic Envelope algorithm assumes that data follows a Gaussian distribution and fits an ellipse to the central data points. Points outside the ellipse are identified as outliers. This method is useful for data that approximately follows a Gaussian distribution but may be less effective for complex or non-Gaussian data distributions.

Combining multiple algorithms can enhance the robustness of anomaly detection. By integrating Isolation Forest with LOF can leverage the strengths of both methods, providing a more comprehensive detection mechanism.

Therefore, recognizing and mitigating motion artifacts in PPG signals is essential for obtaining accurate physiological measurements. A variety of methods, from traditional signal processing techniques to advanced machine learning algorithms, are employed to address this challenge.

Personalized Machine Learning Approaches for Cuffless Blood Pressure Assessment

The combination of PWA and ML offers a promising avenue for developing accurate, non-invasive, and continuous BP monitoring systems. The ongoing advancements in ML algorithms and wearable sensor technology are expected to further refine these models, making cuffless BP monitoring a viable option for widespread clinical and personal health applications. A promising solution in the field of cardiovascular health monitoring could be represented by personalized healthcare. An innovative approach involves the successful integration of advanced, unobtrusive hardware solutions with subject-specific BP models. As described in the following section, this combination holds significant potential for improving patient outcomes

by providing more accurate, continuous, and personalized monitoring. By tailoring BP management to the unique physiological characteristics of each individual, this approach offers a transformative leap forward in the prevention and management of cardiovascular diseases.

Although DL and ML have found extensive application in BP assessment, the considerable inter-subject variability has posed challenges in formulating a sufficiently generalized model whose performance could also be maintained outside of the initial dataset. Therefore, drawing inspiration from established practices in the field of human activity recognition [121, 122], numerous studies have suggested the formulation of person-specific models for the examination of this clinical parameter [118, 123, 124, 125]. This task can be approached using Person Specific Models (PSM) or Person Independent Models (PIM). The distinction between these models lies in their training data: PSMs are trained on data from individual users, while PIMs are trained on data from multiple users.

Person-specific models leverage the unique characteristics of an individual’s movements, leading to higher accuracy for known users. These models adapt to the nuances of a user’s gestures, providing a tailored recognition system. However, the primary limitation of PSMs is their reduced generalizability; a model trained on one user’s data may not perform well on data from another user.

On the other hand, person-independent models aim to generalize across different users by incorporating diverse training data. This approach ensures that the model can handle variations in gestures from different individuals. However, PIMs may not achieve the same level of accuracy for individual users as PSMs because they might miss specific user patterns.

An ensemble approach, combining PSMs and PIMs, can create a robust system that benefits from the generalizability of PIMs and the accuracy of PSMs. This ensemble approach can dynamically select or weight models based on the user’s identity or context, enhancing overall performance. The implementation of personalized ML models in this domain holds promise for enhancing the accuracy and reliability of cuffless BP monitoring.

A notable approach involves using a hybrid neural network architecture that combines convolutional, recurrent, and fully connected layers to operate directly on raw PPG time series data, estimating BP every five seconds. This method leverages a transfer learning technique to address the issue of limited personal PPG and BP data. By personalizing specific layers of a network pre-trained with extensive data from other patients, the model achieves high accuracy with minimal personal data—requiring as few as 50 samples per person [126].

Within the context of data-driven approaches, Gaussian Mixture Models (GMM) and an Online Recurrent Extreme Learning Machine (OR-ELM) have been used for continuous learning and prediction [127]. This method adapts to individual physiological characteristics over time, enhancing personalization. A practical application of this approach involved developing a mobile application to provide real-time BP

predictions, demonstrating the practicality and effectiveness of this personalized method.

Research has also evaluated cuffless BP monitoring in specific populations, such as individuals with Parkinson's Disease [128]. One study used a wearable device that utilized ECG and PPG signals to estimate BP, achieving mean absolute errors (MAE) of 7.84 ± 8.12 mmHg for systolic and 7.51 ± 6.16 mmHg for diastolic measurements. This application highlights the importance of real-time, non-invasive monitoring in managing non-motor symptoms of Parkinson's Disease.

Findings in the literature show that, as for human gesture recognition, also cuffless BP monitoring could benefit significantly from personalized machine-learning approaches. In both fields, personalization has proven to be a highly effective method for enhancing the model's accuracy. In gesture recognition, models must adapt to individual users' unique movement patterns, while in BP monitoring, they must adjust for individual physiological characteristics.

Successful personalization in both domains relies on diverse training data. For gesture recognition, models trained on data from various users can generalize better. Similarly, BP monitoring models trained on data from diverse populations can handle a wide range of physiological variations. Combining person-specific and person-independent models in an ensemble approach is effective in both fields, enhancing the model's ability to generalize while maintaining high accuracy for individual users.

Moreover, continuous learning and real-time adaptation could help BP monitoring systems update their predictions based on ongoing physiological data, thus improving the management of chronic conditions such as hypertension, and providing timely health insights. These systems can provide tailored, accurate, and reliable solutions by leveraging data diversity, continuous learning, and ensemble models.

In conclusion, the integration of machine learning approaches in pulse wave analysis for cuffless BP monitoring has significantly advanced the field of cardiovascular health monitoring. By leveraging advanced algorithms and large datasets, ML models can extract meaningful cardiovascular parameters from complex pulse waveforms, offering personalized and non-intrusive health monitoring solutions. As research continues to address existing challenges and refine these technologies, the future of cuffless BP monitoring looks promising, with the potential to revolutionize the way we monitor and manage cardiovascular health.

2.5 Addressing the Challenges in PWV and BP Monitoring: From Literature to Methodology

The analysis of current literature reveals several critical limitations in the existing non-invasive methodologies for assessing PWV and cuffless BP monitoring. While PWV is widely recognized as a valuable biomarker for arterial stiffness and cardiovascular risk assessment, its integration into routine clinical practice remains limited due to the cost, complexity, and operational constraints of available devices. Most of the advanced non-invasive devices that provide accurate PWV measurements are either prohibitively expensive or require specialized training, which reduces their accessibility in general healthcare settings. Additionally, many of these devices involve cumbersome procedures, such as ECG connections, that may limit their usability in continuous monitoring scenarios or in resource-limited settings. Similarly, while cuffless BP monitoring has the potential to transform cardiovascular healthcare by offering continuous and non-invasive measurements, existing technologies still face challenges in terms of accuracy, especially when applied to diverse populations or when used in everyday conditions. Many devices are prone to inaccuracies due to sensor noise, variations in positioning, or inconsistencies in signal acquisition. These challenges pose significant barriers to the widespread adoption of such technologies, particularly for long-term, continuous health monitoring, which is crucial for effective hypertension management and cardiovascular risk reduction.

In response to these identified gaps, this thesis presents a comprehensive exploration of novel methodologies aimed at addressing these challenges and improving the overall reliability, accessibility, and accuracy of cardiovascular health monitoring systems. Chapter 3 introduces a newly designed, low-cost, and user-friendly device for PWV measurement. By focusing on the integration of commercially available micro-force sensors, the device reduces both cost and complexity while maintaining clinical accuracy. A key innovation in this design is the elimination of ECG connections and wired components, enabling real-time data transmission to a graphical user interface that provides immediate feedback to the clinician. This not only improves the usability of the device but also ensures that the clinician can monitor the signal quality and adjust the procedure as needed, enhancing the overall reliability of the measurement.

In Chapter 4, the thesis delves into the technical challenges associated with PWV measurement, specifically addressing the sources of variability and inaccuracy in traditional methods. Traditional PWV measurement techniques often rely on single fiduciary points, such as the foot of the pulse wave, which can introduce errors due to noise, signal artifacts, or inconsistent pulse wave morphology. To overcome these limitations, a new algorithm based on region-based cross-correlation (RBCC)

is proposed. This method improves the accuracy of PWV assessment by analyzing specific regions of the pulse waveform, rather than relying on a single feature. The RBCC algorithm is particularly valuable in mitigating errors caused by sensor positioning, operator expertise, or variations in pulse morphology between subjects. Furthermore, the robustness of the RBCC method under noisy conditions is demonstrated, showing that it outperforms traditional intersecting tangent methods in both high-quality and noisy data environments. This is particularly important for real-world clinical applications, where signal noise is a common challenge.

Chapter 5 shifts the focus to cuffless BP monitoring technologies, which are increasingly important given the limitations of traditional cuff-based methods. The research conducted in this chapter addresses the potential for continuous BP monitoring through the use of PPG sensors and machine learning algorithms. This approach provides a non-invasive and continuous alternative to conventional BP measurements, capturing beat-to-beat variability and BP fluctuations throughout the day. By developing and testing a personalized multiclass classification model, the thesis explores how these technologies can be adapted to account for individual-specific variations in BP, such as those caused by physical or cognitive workload. This personalized approach overcomes the shortcomings of generalized models, which often struggle to account for the high inter-subject variability seen in BP responses. The result is a more robust, accurate, and practical solution for continuous BP monitoring in real-life conditions, offering significant potential for early detection and improved management of hypertension and cardiovascular disease.

Collectively, the methods and innovations presented in the following chapters aim to improve the accuracy, reliability, and accessibility of non-invasive cardiovascular health monitoring systems. By addressing the cost and usability issues associated with PWV measurement, the limitations of cuffless BP monitoring technologies, and the inherent variability in traditional signal processing methods, this thesis contributes to advancing the field of cardiovascular health assessment. These innovations have the potential to not only enhance patient outcomes through more accurate and accessible diagnostic tools but also to reduce healthcare costs by preventing the development of severe cardiovascular complications through early detection and proactive management of risk factors. In this way, the work presented in this thesis represents a significant step forward in addressing the pressing challenges identified in the literature, offering practical solutions that align with the evolving needs of healthcare systems.

Chapter 3

MicroForce Sensors for Pulse Wave Velocity Assessment

This chapter presents an in-depth examination of micro force sensors and their application in the assessment of PWV.

The initial sections provide a detailed discussion on FMA MicroForce sensors, elaborating on their operational principles and the hardware setup required for data acquisition. This is followed by a thorough exploration of the experimental setup used for sensor characterization, with a particular focus on the calibration processes and the specific conditions under which the sensors were tested.

The latter part of the chapter is dedicated to presenting the preliminary results obtained from sensor characterization. These results highlight the performance of the sensors under various testing conditions and provide insights into their reliability and accuracy. The outcomes of these preliminary tests lay the groundwork for subsequent development and refinement of the acquisition system, which will be discussed in Chapter 4.

3.1 MicroForce sensors

The Honeywell FMAMSDXX005WCSC3 microforce sensor is part of the FMA Series, which are piezoresistive-based force sensors designed to provide precise digital outputs for force measurements across specified full-scale force spans and temperature ranges. These sensors are calibrated and temperature compensated for sensor offset, sensitivity, temperature effects, and nonlinearity using an onboard application-specific integrated circuit (ASIC). They provide a stable output directly proportional to the force exerted on the mechanically connected stainless steel sphere. This sphere is mounted directly over a silicone sense die located on top of the sensor, as depicted in Figure 3.1. Optimal performance is achieved when the force is applied along the vertical axis to the top center point of the coupling

sphere. Direct mechanical coupling ensures reproducible performance and a reliable mechanical link to the application, facilitating easy interfacing with the sensor [129].

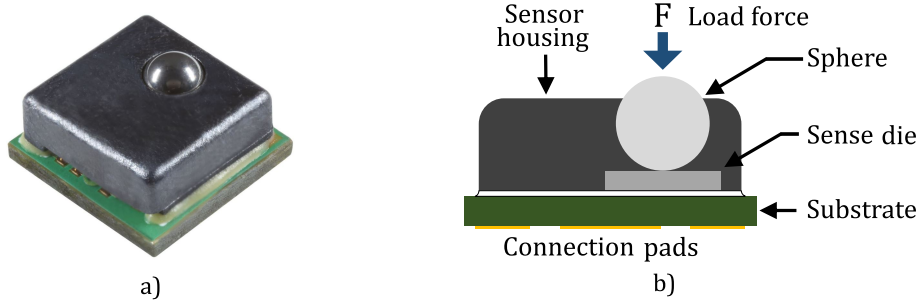


Figure 3.1: FMAMSDXX005WCSC3 load cell. (a) Isometric view. (b) Cross-section view highlighting the main components of the sensors.

The sensor's small form factor, Figure 3.2 (5 mm x 5 mm base, 2.15 mm height), low power consumption (approximately 14 mW), and low cost make it an ideal solution for the objectives of this thesis. The sensing area consists of a sphere with a diameter of 1.6 mm and a height varying between 0.293 mm and 0.483 mm, depending on the sensor's force range.



Figure 3.2: FMAMSDXX005WCSC3 load cell size comparison.

The selected sensor model, FMAMSDXX005WCSC3, is a compensated and amplified sensor featuring mechanical coupling and a sphere as the contact element. It includes a diagnostic function that allows users to verify its operational status. Available in force ranges of 5, 15, and 25 Newtons (N), this sensor enables users to choose the optimal range for their application to maximize sensitivity and resolution. The best results are obtained when measurements are taken as close as possible to the full scale. For the forces involved in this application, sensors with force ranges of 5 N and 15 N have been selected for testing.

3.1.1 Sensor Data Readout

The Honeywell FMAMSDXX005WCSC3 microforce sensor uses the Serial Peripheral Interface (SPI) for digital communication. SPI is a synchronous serial communication protocol that facilitates data exchange between a master device and one or more slave devices. In this protocol, the master initiates communication and provides the clock signal, while the slaves respond with the required data. The FMAMSDXX005WCSC3 operates in half-duplex mode, meaning data is transmitted in only one direction at a time—from the sensor (slave) to the master.

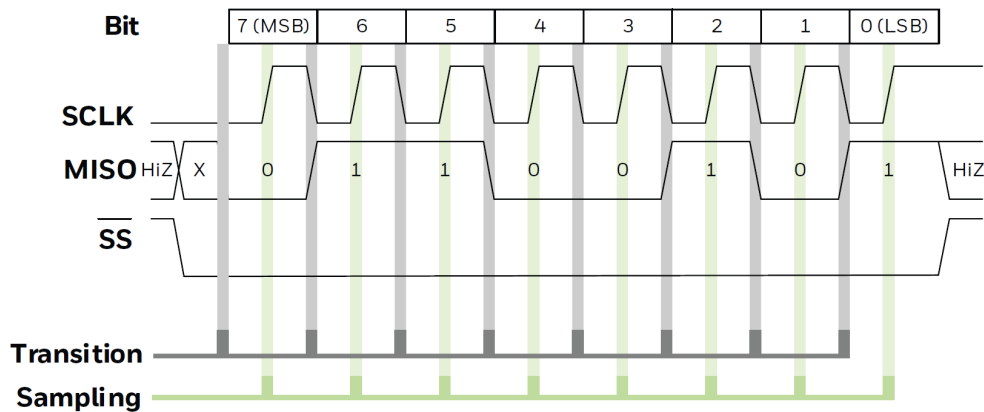


Figure 3.3: SPI sensor data readout [130].

Honeywell digital output force sensors are designed so that data on the MISO bus line changes during the falling edge of clock pulses, requiring the Master device to sample this data on the rising edge of the clock pulse. The sensor provides two options for data readout:

1. Two-Byte Data Readout: This mode retrieves the first two bytes, which include the 14-bit compensated force output and 2 bits of sensor status.
2. Four-Byte Data Readout: This mode includes the compensated force output as well as an additional two bytes for the optional compensated temperature output.

For this application, only the two-byte data readout is used since temperature measurements are not needed for the case study. To read data from the sensor, the Chip Select (CS) pin is brought to a low logic level. During the following 16 clock cycles, the sensor's output register is read, sending 16-bit data through the MISO line into a temporary buffer. Once data acquisition is complete, the CS pin is returned to a high logic level until the next data acquisition cycle.

The timing for toggling the CS level is managed by an internal timer set to the desired sampling frequency, which will be discussed in subsequent sections. When

Table 3.1: Diagnostic states in data readout [131].

S1	S0	Definition
0	0	Normal operation, correct data.
0	1	The device is in command mode, which is used for programming the sensors and is not utilized during regular operation.
1	0	Stale data condition occurs when the sensor is unable to update the output buffer as quickly as the master device polls for data.
1	1	Diagnostic condition refers to a loss of connection to the sense element or a short circuit within the sensing element.

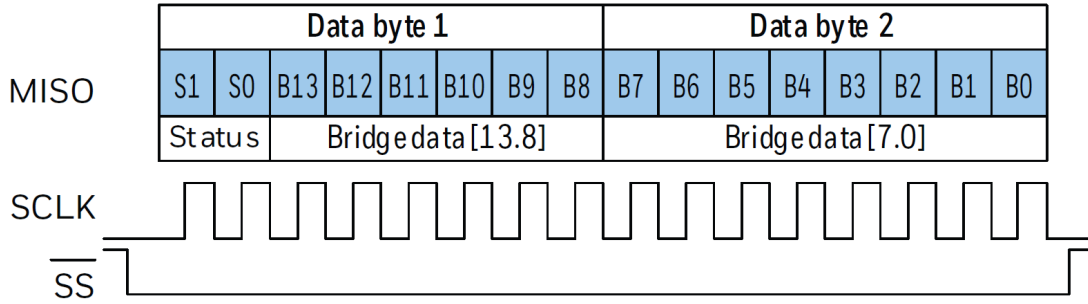


Figure 3.4: Two-Byte force data payload [131].

the set time elapses, the timer generates an interrupt, triggering a callback function that performs the data acquisition. Using interrupt mode for data acquisition ensures that the microcontroller is not blocked during the process, allowing continuous data acquisition without disrupting the microcontroller's normal operations.

The two most significant bits of Data Byte 1 (S1 and S0) indicate the sensor's status. These diagnostic states are crucial for determining whether the system is functioning correctly or if there are issues such as short circuits or stale data. Table 3.1 below shows these status bits' possible combinations and meanings.

A control condition checks these status bits in the firmware immediately after data readout. Only if the status bits are "00" is the data sent to the laptop using the UART protocol for further analysis.

The digital output can be expressed with its transfer function [132], where the digital output is defined as:

$$output = \frac{output_{max} - output_{min}}{Force_{Range}} * Force_{applied} + output_{min} \quad (3.1)$$

where $output_{max}$ and $output_{min}$ are, respectively, the value of the 90% and 10% of the dynamic range. The $Force_{Range}$, expressed in N, is the maximum detectable force by the sensor. In this application, two load cells with different ranges, 5N and

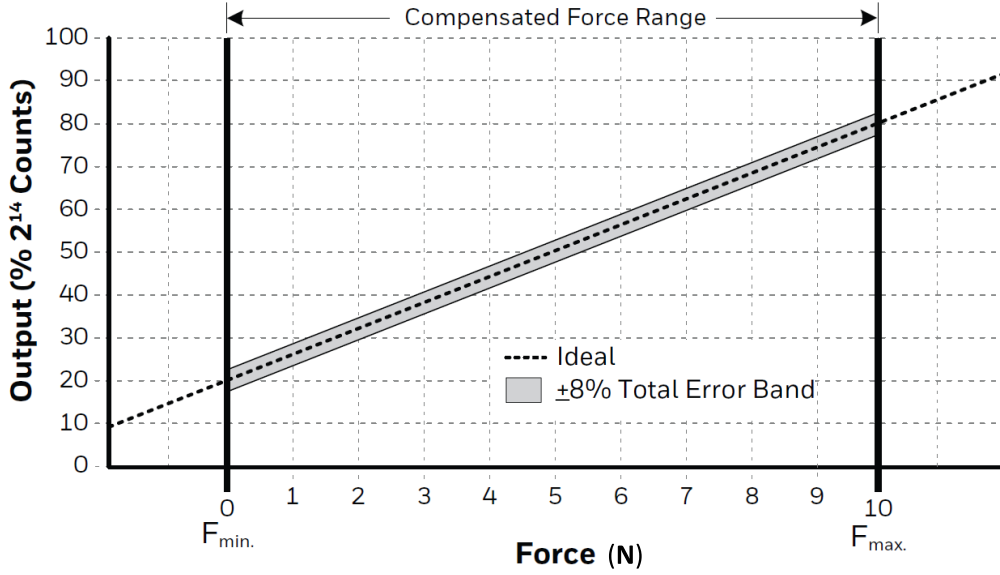


Figure 3.5: Optimal range of use of the sensor [132].

15N, were tested.

Overturning the Eq.3.1, the force applied on the sensing sphere can be calculated as reported in Eq.3.2:

$$Force = \frac{output - output_{min}}{output_{max} - output_{min}} * Force_{range} \quad (3.2)$$

These equations have been implemented in post-processing to retrieve the corresponding voltage value when a defined load is applied on the sensor. The present relationship was ultimately employed to better visualize the behavior of both sensors.

3.1.2 Definition of the Sampling Frequency

The load cell datasheet does not specify the data readout sampling frequency. Therefore, an investigation was conducted to determine an appropriate sampling frequency. A thirty-second period was established for data acquisition from the sensor, during which the status bits of each measurement were checked. If incorrect measurements ("stale data") were detected at the end of this period, it indicated that the sampling rate was too high. Consequently, the sampling rate was incrementally reduced by adjusting the microcontroller's clock frequency and timer settings to optimize the data acquisition timing.

Table 3.2 summarizes the frequency adjustment steps. Starting with a sampling frequency of 2 kHz, the objective was to minimize the number of "stale" measurements relative to the total number of measurements taken during the thirty-second

Table 3.2: Tested sampling frequencies, displaying the percentages of stale measurements relative to the total measurements acquired over a 30-second period. The number of incorrect measurements for each frequency is indicated in parentheses.

System Clock (MHz)	Sampling rate (Hz)	"Stale data" (%)
80	2000	18,05% (10830)
80	1000	5.09% (1527)
80	800	0.7% (181)
60	600	0.2% (37)
60	500	0.16% (25)
45	450	0.1% (12)
44	440	0.04% (5)
80	400	0.04% (0)
80	200	0% (0)

acquisition period. It was observed that decreasing the frequency reduced the number of incorrect readouts, as faster data requests from the microcontroller outpaced the refresh time of the sensor output register.

Following this investigation, a sampling rate of 200 Hz was selected as it was the highest rate at which 100% no loss of data were observed.

3.2 Sensor Characterization

In this section, the characterization of the sensor is discussed. To begin with, the experimental setup employed to ensure a reliable evaluation of each tested sensor is described. Then, the design of the support structure and proceeding through the measurement cycles are presented. Finally, the results of the characterization process are presented and discussed.

The process starts with the design and fabrication of a suitable support for the sensor, ensuring that it is securely mounted and optimally positioned for accurate measurements. The measurement cycles involve systematic testing under various conditions to assess the sensor's performance, accuracy, and reliability.

3.2.1 Experimental setup

For evaluation purposes, two sensors with force ranges of 5 N and 15 N were selected. These are the lowest force ranges available for this sensor type and are well-suited for the thesis application, as the displacement of the carotid or femoral artery generates a force of only a few Newtons.

The sensor was soldered onto a rectangular PCB with headers for each pad,

facilitating testing on a breadboard. This PCB was designed to match the sensor’s layout. This solution was designed in order to connect the assembly to the P-NUCLEO-WB55 Nucleo board (STMicroelectronics, Shanghai, China)[133] employed for data acquisition. A weight kit ranging from 1 to 500 grams was utilized to assess a wide range of sensor output responses, specifically using weights of 10 g, 20 g, 50 g, 100 g, 200 g, and 500 g.

A 3D-printed support structure was designed to ensure precise alignment between the calibration weights and the sensing sphere of the load cell. This configuration enabled consistent measurements under various conditions, facilitating an unbiased comparison between the 5N and 15N load cells. The support system was designed with the following features:

- The top support must direct the weight solely onto the contact sphere, avoiding other points in the system.
- It should include a base that accommodates the PCB while keeping the sensor’s sensing area elevated.
- The top support must attach to the base without transferring weight to it.

The support base was constructed as a cylinder with a diameter of 45 mm and a height of 30 mm. The bottom section includes two L-shaped openings to facilitate the routing of wires from the headers beneath the PCB to the breadboard. The top area includes a rectangular hole (16.25 mm x 9 mm) for placing the PCB, which connects to the L-shaped holes. Additionally, four symmetric round holes (6 mm diameter) were created on the top surface for stability, allowing the top support cylinder to fit securely.

The top support consists of a circular base with a diameter of 45 mm and a thickness of 4 mm. From this base, four symmetric cylinders with a diameter of 5 mm and a height of 10.5 mm were extruded to align with the holes in the base. Their diameter is slightly smaller than the holes to avoid contact with the PCB. To interact with the sensor’s sensing element, a smaller cylinder with a height of 6 mm and a diameter of 2.7 mm was extruded, shifted 0.89 mm from the center to match the sensor’s offset sphere.

The design of these support pieces was created within the SolidWorks environment (Dassault Systèmes SE, Vélizy-Villacoublay France) and 3D printed using a Formlab 3 printer (Formlabs, Somerville, USA).

Several characterization measurement cycles were performed to analyze the sensor’s behavior under different loads. The acquisition time was set to 45 seconds for various types of measurements:

- A cycle without any weights to detect the baseline signal and offset.

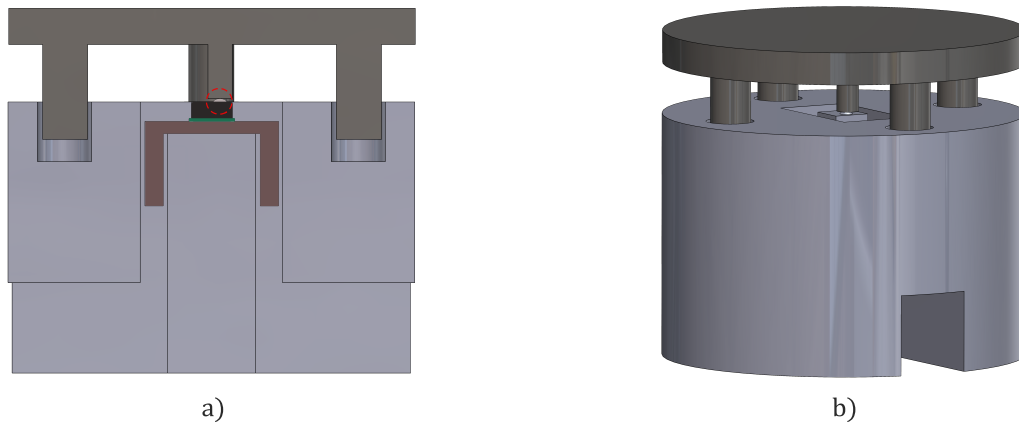


Figure 3.6: Assembly of the support system. (a) Section of assembly of the support system. Circled in red there is the sensor, with below the PCB on which it is soldered in yellow. (b) Isometric view.

- Cycles with constant weights gradually increased from 10 g to 20 g, 50 g, 100 g, 200 g, and 500 g.
- Alternating loading and unloading cycles with different weights to evaluate the sensor's responsiveness to rapid force variations and its ability to quickly restore the baseline.

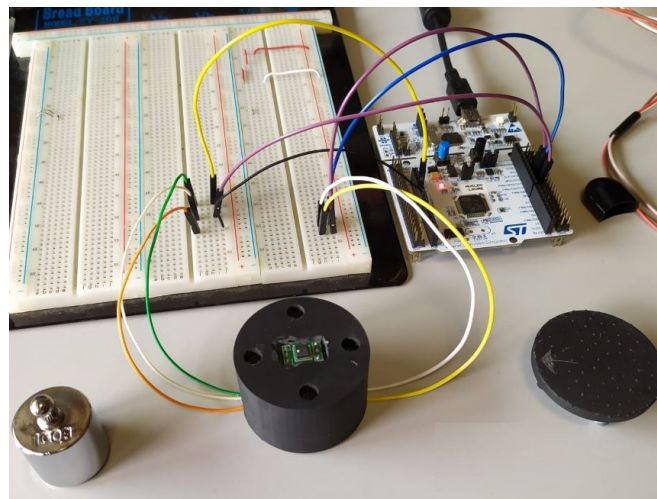


Figure 3.7: Experimental set-up for sensor's characterization.

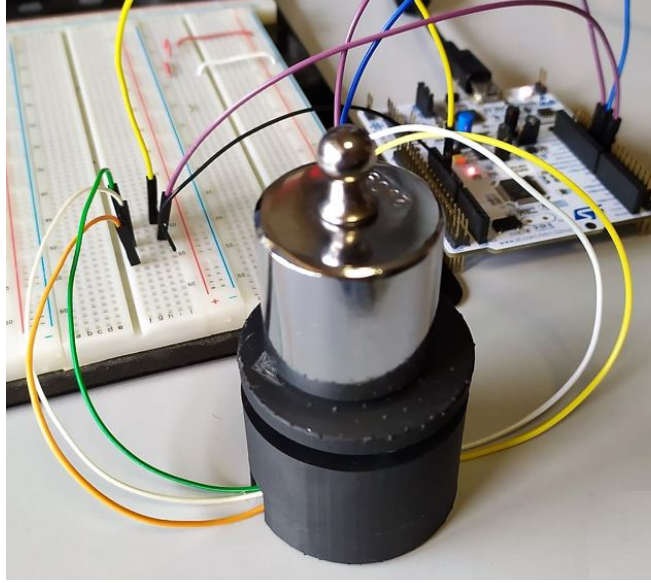


Figure 3.8: Constant load application for sensor’s characterization.

3.3 Characterization Results

3.3.1 Baseline

The initial measurements focused on establishing the baseline. These measurements are crucial to determine the sensor’s stability in idle condition, when no weights were applied. Then, the mean baseline output voltage for both sensors and their standard deviation were computed. As indicated in Table 3.3 and reported in Figure 3.9, both sensors exhibit baseline values of 872 ± 2.510^{-4} mV and 679 ± 4.8610^{-3} mV respectively for 5N and 15N load cell. Furthermore, the minimal standard deviation demonstrates that the sensors consistently maintain their output over time. Significantly, the sensor with a 5N force range shows exceptional stability, with an output variation of less than 0.1% of its mean value.

Table 3.3: Mean value and standard deviation of the baseline without weights for the 5N and 15N force range sensors.

Force Range (N)	Mean Value (V)	Standard Deviation (V)
0-5	0.872	$\pm 2.5E-04$
0-15	0.679	$\pm 4.86E-03$

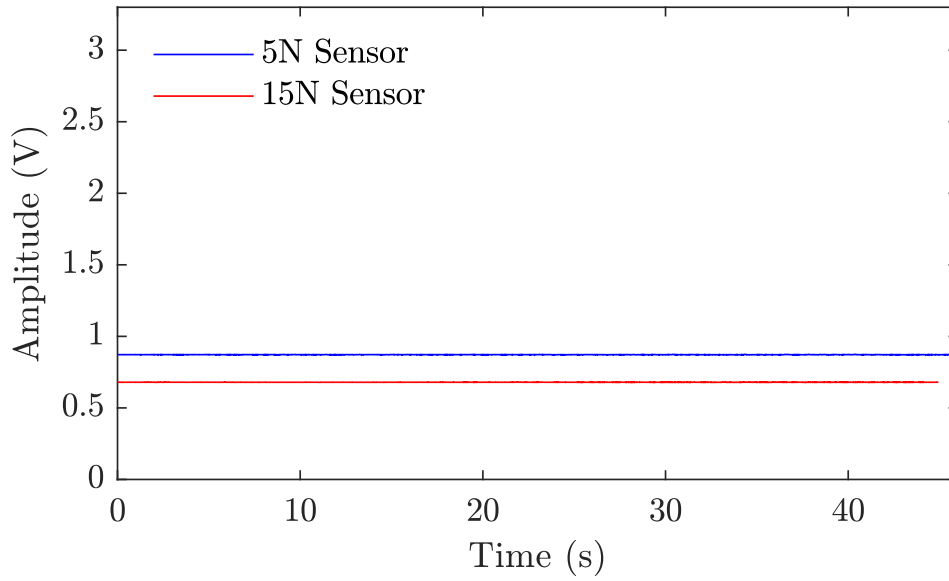


Figure 3.9: Voltage output without weights for the 5N (blue) and 15N (red) force range sensors.

3.3.2 Constant Weight

Once the baseline output value was assessed, the characterization moved forward with different constant weights applied. Specifically, the tests involved applying gradually increasing loads on both load cells to address the sensor’s response in different conditions. The output values, averaged over a 60-second observation window, are listed in Table 3.4 and Table 3.5.

Table 3.4: Mean value and standard deviation of the baseline for the 5N sensor at each weight in a constant load application.

Weight Mass (g)	Mean Value (V)	Standard Deviation (V)
10	0,928	$\pm 4,387E-04$
20	0,968	$\pm 3,886E-04$
50	1,088	$\pm 3,883E-04$
100	1,226	$\pm 1,839E-03$
200	1,573	$\pm 4,836E-03$
500	2,654	$\pm 1,963E-03$

The sensor with a 5N force range shows a larger output dynamic compared to the 15N sensor, although it also has a slightly higher standard deviation, which remains low. Interpolating these data points results in a highly linear curve for both sensors, particularly in the low-weight regions. This linearity is crucial for the

thesis application, as arterial displacement produces forces in the range of 1-2 N.

Table 3.5: Mean value and standard deviation of the baseline for the 15N sensor at each weight in a constant load application.

Weight Mass (g)	Mean Value (V)	Standard Deviation (V)
10	0,698	$\pm 2,47\text{E-}04$
20	0,710	$\pm 1,85\text{E-}04$
50	0,741	$\pm 2,42\text{E-}04$
100	0,799	$\pm 3,43\text{E-}04$
200	0,909	$\pm 5,97\text{E-}04$
500	1,241	$\pm 1,26\text{E-}03$

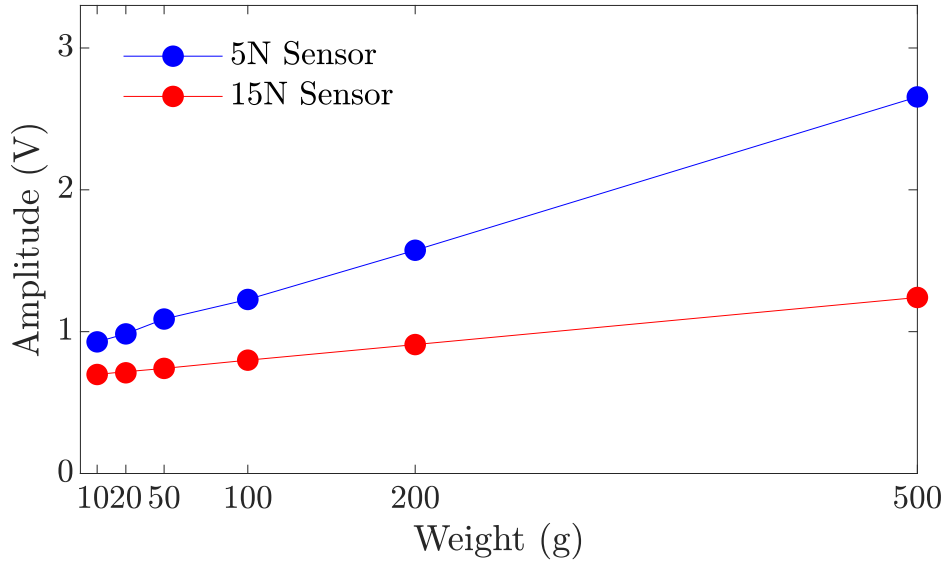


Figure 3.10: Characterization curve of the load cell with constant weights (10g, 20g, 50g, 100g, 200g, 500g) for the 5N (blue) and 15N (red) force range.

3.3.3 Load/Unload Cycle

During load and unload cycles, some instability issues were observed. Increasing the weight on the top support and repeatedly applying and removing it caused system instability. This instability is likely due to the small contact area between the sensor's sensing sphere and the central cylinder of the top support. Additionally, the off-center positioning of the sensing element on the sensor further contributed to the loss of symmetry in the system.

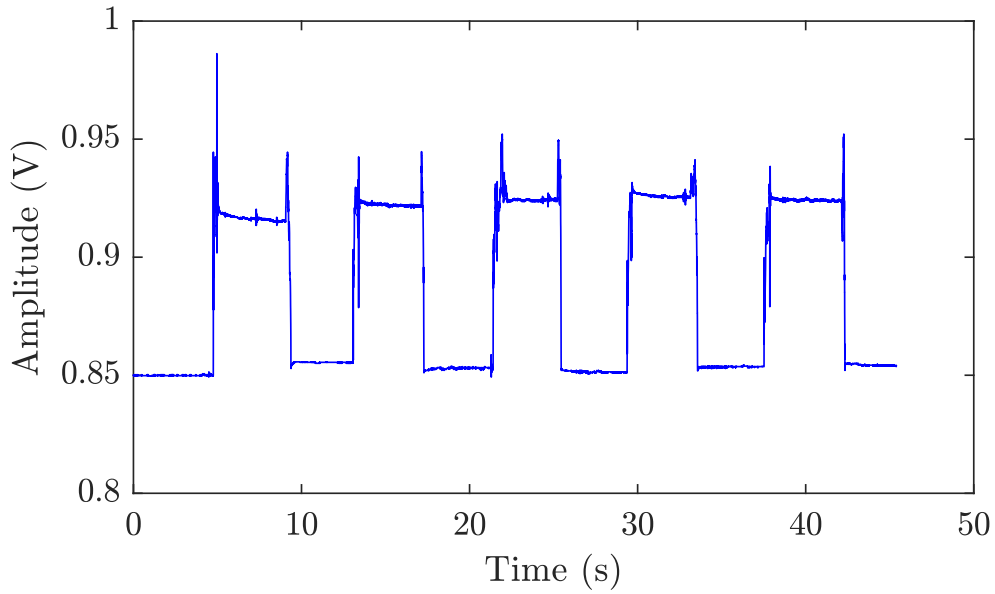


Figure 3.11: Load/Unload cycles with a weight of 20 grams (5 N sensor).

These factors influenced the measurements, particularly with higher weights (100, 200, and 500 grams). As shown in Figure 3.11, positioning the weight on the support caused a drift in the output. For lower weights, the sensor stabilized after about a second and maintained a stable output for the rest of the loading cycle. However, with higher weights, the sensors exhibited sustained drift throughout the loading period, resulting in unstable measurements, as illustrated in Figure 3.12.

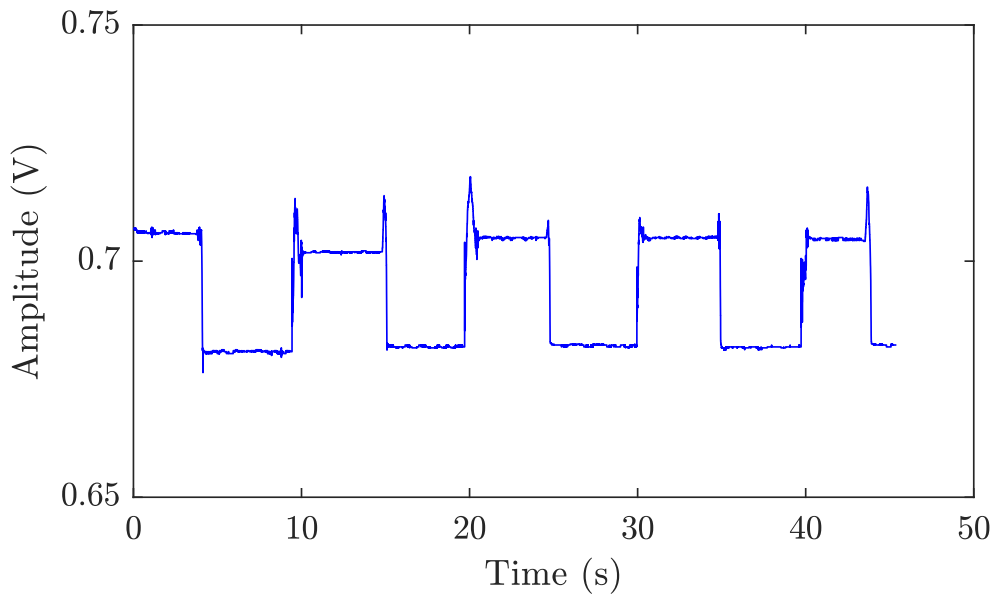


Figure 3.12: Load/Unload cycles with a weight of 50 grams (5N sensor).

The 5N sensor displayed greater output amplitude and load sensitivity during these cycles. Its rising edge under load was sharper compared to the 15N sensor. Overall, the 5N force range sensor provided better resolution and higher sensitivity to small force variations, making it more suitable for detecting pulse waves. Additionally, its stability was slightly higher than that of the 15N sensor in all tested conditions.

$$slope_{0-20} = \frac{0.968 - 0.872}{0.020} = 4.8V/kg \quad (3.3)$$

$$slope_{0-20} = \frac{0.709 - 0.679}{0.020} = 1.5V/kg \quad (3.4)$$

The decision to use the 5N force range sensor was based on its greater slope in the 0 to 20 g range, which corresponds to the force range of interest for this application. This greater slope results in higher sensitivity and amplitude in the output as testified by the computed slope in Eq.3.3 and Eq.3.4. Based on these considerations, the 5N force range sensor was chosen for its superior resolution, higher sensitivity to small force variations, and greater stability, making it more suitable for detecting pulse waves in the desired force range.

Chapter 4

Wireless Device for Pulse Wave Velocity Assessment

This chapter contains parts that have been taken, or partially rephrased, from a previously published work [134].

The following chapter presents a comprehensive approach to improving the measurement of PWV by introducing a true wireless system that is both affordable and reliable. The system's design emphasizes portability, ease of use, and real-time data feedback, which are critical for integrating PWV measurement into routine clinical practice. Validation against the gold-standard device and rigorous testing confirm the system's accuracy and usability, potentially making it a valuable tool in the early detection and management of cardiovascular diseases.

Thanks to the close collaboration with the internal medicine team at the "Città della Salute e della Scienza" hospital in Turin, this instrument was developed to meet the specific demand for a reliable, easy-to-use, and low-cost device. Continuous medical feedback helped address all practical and usability aspects, safety and reliability of the estimation. The adaptation of the graphical interface, presented in subsection 4.2.3, for the real-time estimation of PWV was carried out by one of the co-authors involved in this project.

4.1 Introduction

The propagation of the arterial pulse can be evaluated between any pair of locations within the cardiovascular system. To date, several devices for the assessment of clinical PWV differ in both the procedure and methodology employed [85]. Concerning the latter, the most widely used and reliable approach is applanation

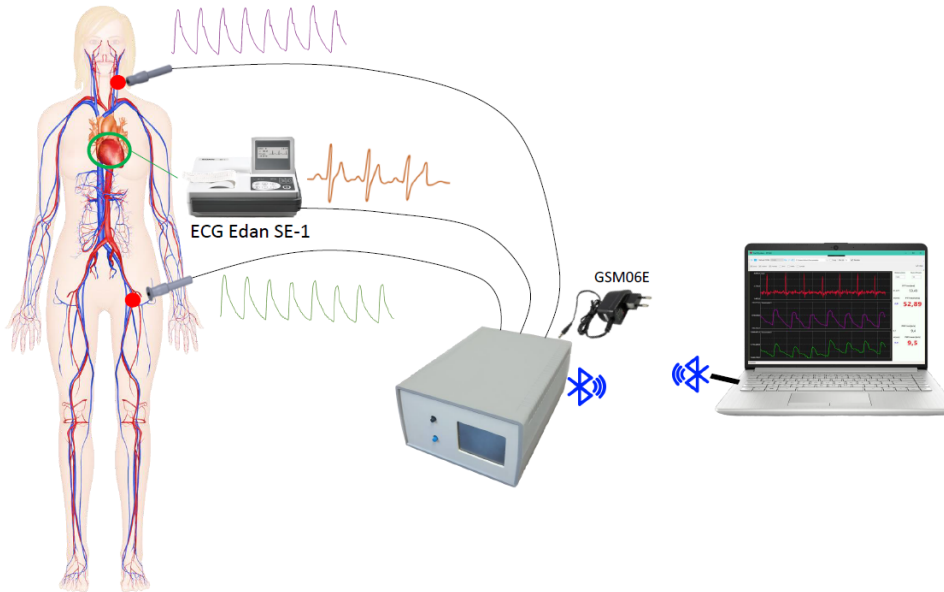


Figure 4.1: Overview of the first generation the Athos device [139].

tonometry [54], followed by oscillometry [135], and optical sensors [136]. Typical locations for evaluating pulse waves include the femoral, tibial, radial, and carotid arteries, where arterial pulsations are easily detectable [56] [57]. In 2023, the European Society of Hypertension guidelines [16] recommended baPWV [58, 59, 60] as a screening tool for hypertension-mediated organ damage [61]. However, cfPWV is still considered the gold-standard reference in the arterial stiffness assessment [62, 63, 64]. Although cfPWV is a robust measure of vascular aging [137] [138], it is not available in many research studies for a variety of reasons, including financial constraints [39] [43], lack of access to the specialized equipment needed to measure it, and the absence of trained personnel. In 2021, the Athos (Arterial stiffness faithful tool assessment) device, Figure 4.1, was created to overcome the barrier of high equipment costs and usability that have restricted the adoption of this technique within clinical settings [72, 139].

Thanks to its two prototypal high-resolution MEMS force sensors and a dedicated graphical user interface (GUI), this system provides real-time feedback to the user and fully reliable offline cfPWV assessment. Following the Artery Society guidelines, a clinical validation study involving ninety healthy volunteer subjects was carried out to assess the accuracy of the device [140] in comparison to the established gold standard device for noninvasive cfPWV assessment, SphygmoCor (AtCorMedical in Sydney, Australia) [141] [142]. The Athos device demonstrated a high degree of concordance with SphygmoCor, even under conditions of elevated PWV values, and exhibited satisfactory reproducibility. However, the restricted

accessibility of the sensor used in creating the first prototype limited its use in clinical practice. To overcome this limitation, the entire system was redesigned using commercial components [143]. That said, the proposed device stands as an entirely novel instrument. Its development results as the culmination of multidisciplinary cooperation with a team of physicians actively engaged in clinical validation. Compared to the first generation, the hardware and software novelties introduced within the proposed device aim to completely transform its portability, streamline usability, and ensure the accuracy of PWV estimation. The primary innovation in terms of hardware is removing the wired connection between the MEMS sensors and the central apparatus that formerly handled data management and transmission to the workstation. Furthermore, to transform the system into an independent device, the ECG connection was also eliminated, significantly enhancing the device’s portability. Therefore, a new custom PCB powered by a small rechargeable battery was designed to collect the force data and wirelessly transfer them to the workstation hosting the GUI responsible for displaying and processing the pulse waveforms. A new piezoresistive load cell has been selected as the sensing element to capture the arterial pulse. The two pen-shaped acquisition enclosures were revised entirely to hold the mentioned components, ensuring clinicians’ easy handling during the PWV assessment. With the decision to incorporate rechargeable batteries into the design, a recharging station was also integrated into the system. The base station, connected to a laptop via USB, acts both as a collector for data streaming and a charging station for the two probes. A USB dongle has been included in the design to handle Bluetooth Low Energy (BLE) communication with the acquisition probes and transmit the gathered data to the workstation. The firmware underwent a comprehensive revision. The Bluetooth stack was updated from 4.2 to 5.2 [144], and different routines to manage the data connection, transfer, and reception were implemented to handle the asynchronous transmission from the two probes to the receiving station. The previously designed GUI has been updated, integrating the real-time data display alongside the PWV assessment. The Matlab algorithm detailed in [139], initially designed for offline extraction of the intersecting tangent points (ITP) on carotid and femoral waves, was modified to operate in the background, delivering real-time feedback to the clinician.

4.2 Proposed System

This section guides the reader to a detailed description of the proposed system’s design, application, and validation phases. The first subsection details the hardware conceptualization and realization of the custom PCB of the two probes and the recharging station constituting the device. Moreover, the description of the 3D-printed enclosures of the probes and recharging station is also provided. Then, subsection 4.2.2 reports the firmware routines implemented for managing the

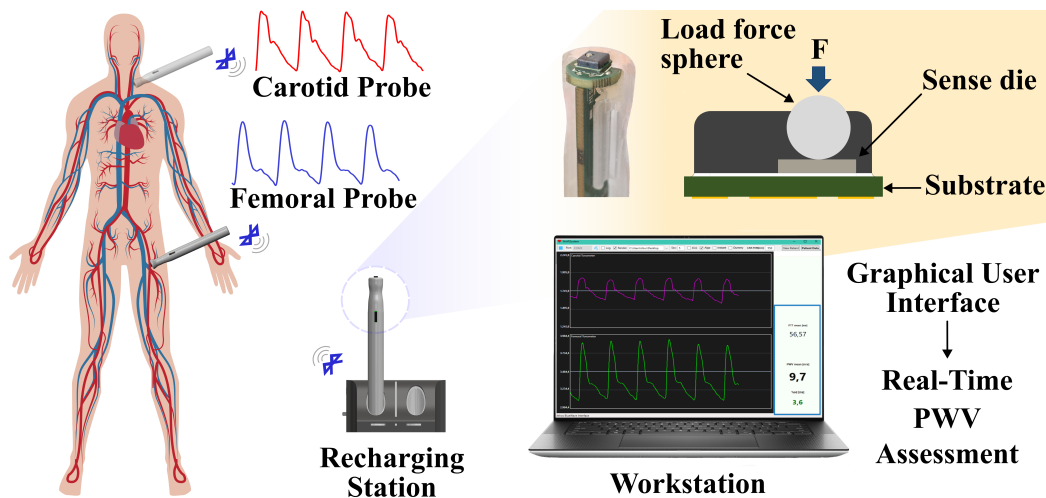


Figure 4.2: Wireless Device for Pulse Wave Velocity Assessment [134].

connection, the data transfer, and the data management between the acquisition probes, the BLE charging station, and the workstation responsible for providing a real-time PWV assessment to the clinical operator.

Subsection 4.2.3 details the GUI and the software algorithm used to manage the commands provided by the user and the real-time estimation of PWV. Subsection 4.2.4 describes the tests performed to assess the power consumption of the probes and the synchronization procedure. Finally, subsections 4.2.4 and 4.2.5 present the procedure used to perform the PWV assessment and the tests conducted to verify the device's compliance according to the clinical safety rules and guidelines described in the IEC-60601 standard for medical devices.

4.2.1 The Hardware

Acquisition Probes

The proposed device consists of three primary units: two probes utilized for data collection and a charging station. The probes, one for the carotid site and one for the femoral site, are intended to be two autonomous devices communicating with the central station through the BLE communication protocol. Since the two probes are identical from a hardware standpoint, the following explanation will pertain to both. As depicted in Figure 4.3, each probe consists of three major components: a pen-shaped enclosure containing the sensor used to capture data Figure 4.3.(a), a custom PCB created for this application Figure 4.3.(b) and the rechargeable battery used to power the board Figure 4.3.(c). The power source used for this device is the LP401235 (Cellevia Batteries), a 3.7V rechargeable polymer Lithium-Ion battery [145]. This model was selected for this application because the

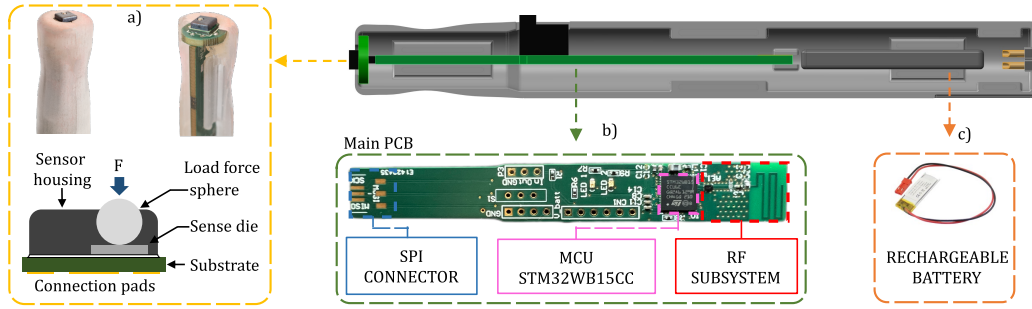


Figure 4.3: Acquisition probe overview. (a) Encapsulated load cell used for pulse wave detection. (b) Custom PCB designed to collect and transfer data. (c) Rechargeable polymer Lithium-Ion battery.

battery’s recharging ability allowed us to minimize its nominal capacity 120 mAh and, as a result, its size and weight, providing the correct voltage to power the board and the sensor

The FMAMSDXX005WCSC3 (Honeywell, United States) load-cell has been selected for pulse wave detection [146]. The small form factor (5 mm x 5 mm for the base, 2.15 mm for the height), low power consumption (about 14 mW), the reduced force range, and low costs made it an ideal solution for this application. As depicted in Figure 4.3.(a), this micro force sensor is actuated by direct mechanical coupling through a stainless steel sphere mounted directly over a silicone sense die. This off-the-shelf, piezoresistive-based force sensor provides a digital output (12-bit data output) for reading force values over the specified full-scale span. A 5 N sensitivity range was chosen from those commercially available to have the sensor dynamics closest to the force values exerted by the arterial pulse passage. Achieving consistent and precise results hinges on the correct sphere alignment and accurate sensor mounting. The sphere transfers the load through a specific point of contact. When this contact point is inconsistent or not perpendicular, it can cause the sphere to exert pressure or friction against the sensor housing, leading to a potential shift in the sensor’s output. For this purpose, the load cell has been soldered onto a 1 cm diameter circular PCB. This setup guarantees the sensing sphere’s proper alignment along the pen-shaped enclosure’s longitudinal axis when the sensor is inserted. Moreover, it serves the dual purpose of powering the sensor and establishing a connection with the main PCB through the SPI communication protocol.

Two LEDs, red and green, respectively, have been included in the board’s design to provide the user with feedback on the proper reading of the sensor and the BLE connection status. A single on/off switch has been placed on the board to power on (or off) the device. The STLQ020 [147] (STMicroelectronics, Shanghai, China) linear voltage regulator has been included to produce 3.3V from the initial 3.7V given by the chosen battery when the board is turned on. The PCB includes the

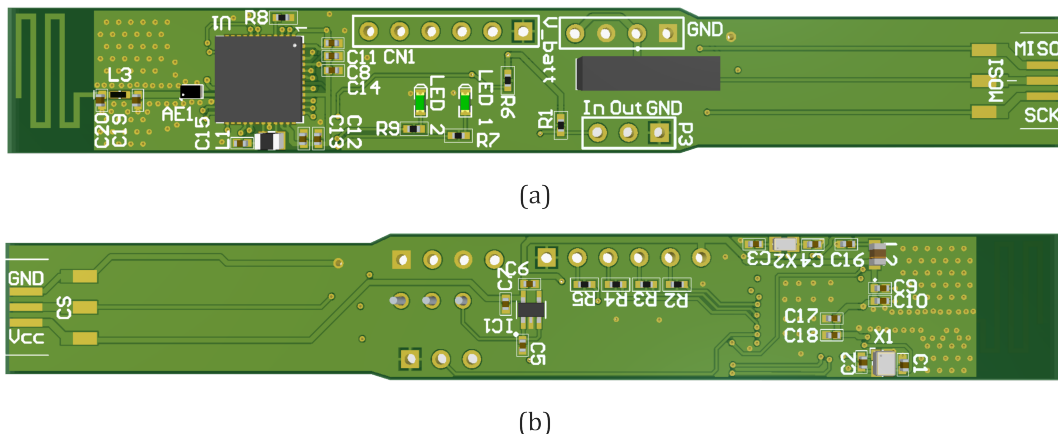


Figure 4.4: Top and bottom views of the PCB layout for the Athos system acquisition probe. (a) Top view. (b) Bottom view.

STM32WB15CC (STMicroelectronics, Shanghai, China), a 32-bit multiprotocol wireless and ultra-low-power device that embeds an RF subsystem that communicates with a MCU including an Arm® Cortex®-M4 CPU (CPU1) where the host application runs [148].

Two external oscillators, Figure 4.5, were employed according to the specifications reported in [148, 149] concerning hardware development for RF applications. The NX2012SA low-speed external (LSE) oscillator [150], with 32.768 kHz frequency, was used for the RTC subsystem. The 32MHz crystal oscillator NX2016SA-32M-EXS00A-CS06465 was chosen as the high-speed external (HSE) clock source [151]. This latter is required by the MCU to trim the RF subsystem responsible for managing BLE activities. The mentioned crystal was selected based on the criteria outlined in the microcontroller datasheet [148]. Moreover, it is characterized by a frequency tolerance of 10 ppm (at 25°), which ensures a low drift during data acquisition sessions.

The RF subsystem, Figure 4.5.(a), comprises an RF analog front end and a specialized Arm® Cortex®-M0+ microcontroller (CPU2) compliant with the Bluetooth® Low Energy SIG specification 5.2. CPU2 implements the entire BLE stack, restricting the CPU1’s interface to high-level exchanges. To enhance the RF performance, careful attention was given to the impedance matching between the antenna and the chip’s input, as well as between the chip’s output and the antenna. Maximum power transfer is achieved when the source’s internal resistance matches the load resistance. A matching network and RF low-pass filter were employed for optimal RF performance—specifically maximum transmission power, optimum reception sensitivity, and sufficient spurious and harmonic rejection, Figure 4.5.(c). Components C20 and L3 were used to match the MCU’s RF pin impedance to 50 Ohm, which is the required impedance for the antenna. Meanwhile, C19 and the integrated low-pass filter AE1 were utilized to reject harmonic frequencies. To

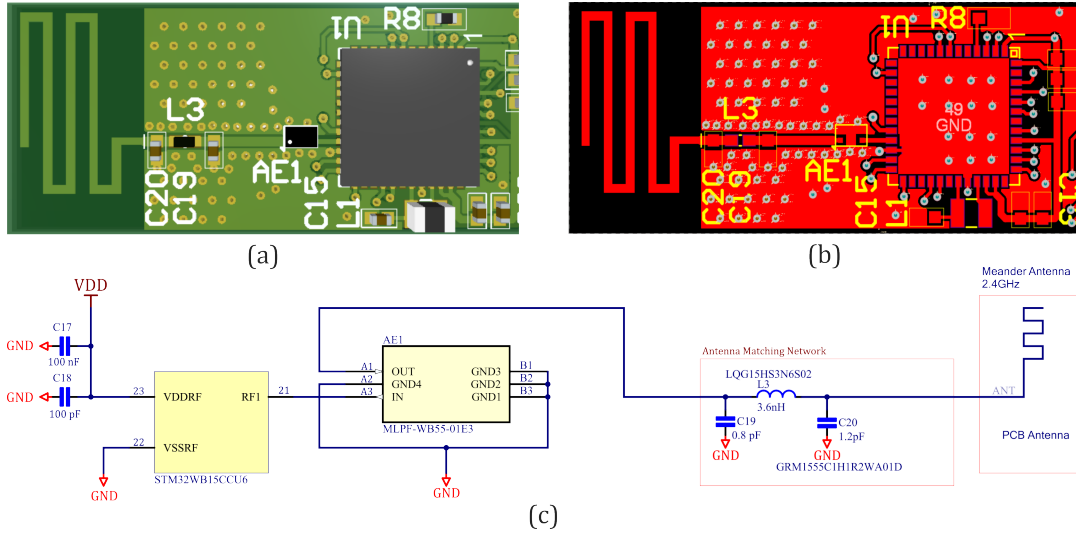


Figure 4.5: RF subsystem. (a) Physical layout of the RF section of the PCB, showing the placement of RF components along with the meander antenna. (b) PCB layout highlighting the RF trace and ground vias placements. (c) Schematic diagram of the RF circuitry, including the antenna matching network and low-pass filter, designed to ensure optimal impedance matching and harmonic rejection for the MCU’s RF pin.

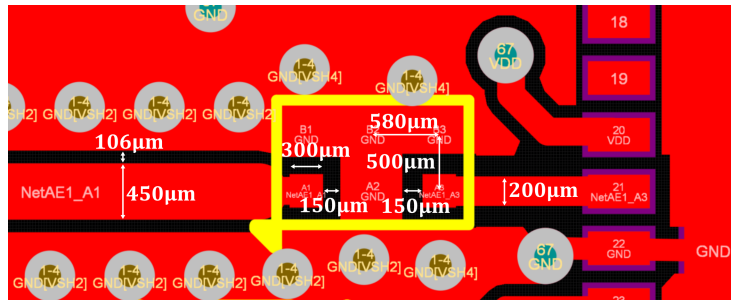


Figure 4.6: Close-up view of the PCB layout detailing the RF trace and component placement. The image highlights critical dimensions such as trace widths, spacing between traces, and via placements to ensure proper impedance matching and minimize parasitic effects.

prevent parasitic ground inductance and cross-coupling from RF and other signal lines, ground vias were placed throughout the PCB’s RF section, Figure 4.5.(b). These vias were spaced approximately 1/10th of the wavelength apart, as recommended in [149]. The layout of the power supply and ground layers was carefully considered to manage the return current for the components, avoiding any signal routing between these layers. Finally, because the impedance of a PCB trace at RF frequencies is influenced by factors such as the trace’s thickness, its height above

the ground plane, and the dielectric properties of the PCB material (including the dielectric constant and loss tangent), the physical characteristics of the RF line were determined according to the guidelines provided in [152] and illustrated in Figure 4.6. The schematics detailing the design of the acquisition probe PCB are reported in Figure A.1, Figure A.2 and Figure A.3 in Appendix A

Multiple factors were taken into account during the design of the probe enclosure. Specifically, its shape and dimensions depended on the size of the battery and the custom PCB. For this reason, the PCB and battery dimensions have been reduced as much as possible. The enclosure section close to the sensor was shaped differently to simplify the operator's handling. In particular, the carotid probe was intended to be handled like a pen, whereas the femoral probe was designed to be held between two fingers. Thus, stable simultaneous deployment of sensors becomes feasible, resulting in enhanced and more steady signal acquisition. A series of indentations on the enclosure's side aids the operator in correctly positioning the unit within the charging base. The interface connections are situated on the lower portion of each probe. Specifically, two of the four available pins connect the probe's battery and the circuit within the charging station. The two remaining pins enable a physical linkage between the two probes as a sensing solution to distinguish if they are connected. This solution will be explained later in the acquisition start-up routine.

Charging Station

The charging base realized for this application represents the central fulcrum of the device. It can be divided into three main sections: the enclosure, the MB1293 USB dongle (STMicroelectronics, Shanghai, China) used to manage the BLE communication and the dedicated PCB built to perform the battery charging inside the probes and the circuit used to perform the acquisition start-up, Figure 4.7. The schematics detailing the design of the acquisition probe PCB are reported in Figure A.4 and Figure A.5 in Appendix A. The structure of the charging base presents two slots, one for each probe, and a set of LEDs that give the user an indication of the battery recharge. The inner surface of the housings has been shaped to complement the geometry created on each probe to ensure their proper position within the charging base. The connection between the PCB and the bottom part of each probe has been realized using a 4-pin spring-loaded header. This solution allowed us to build a more reliable contact with the charging and synchronization circuit.

The charging circuit consists of the MCP73831 integrated circuit (Microchip, Shanghai, China) [153]. Through a specific resistor linked to the mentioned integrated circuit, the charging current has been set according to the datasheet requirements of the connected battery. According to [145], a 68 kOhm resistor has been selected for this purpose, setting a recharge current of 16 mA.

The circuit employed for the synchronous start of acquisition is based on the

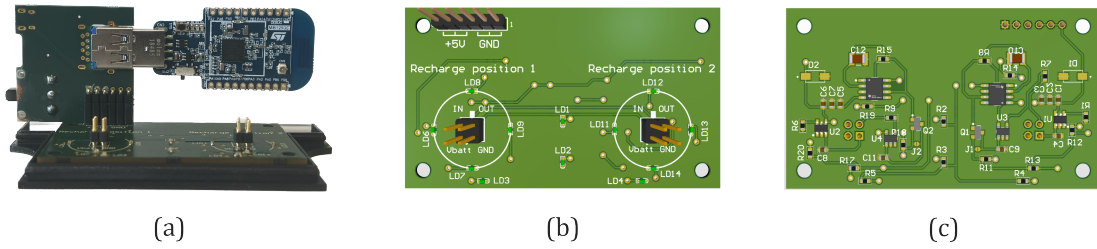


Figure 4.7: Recharging station designed for the tested device. (a) Designed PCB connected to USB-Dongle MB1293. (b) PCB top view. (c) PCB bottom view.

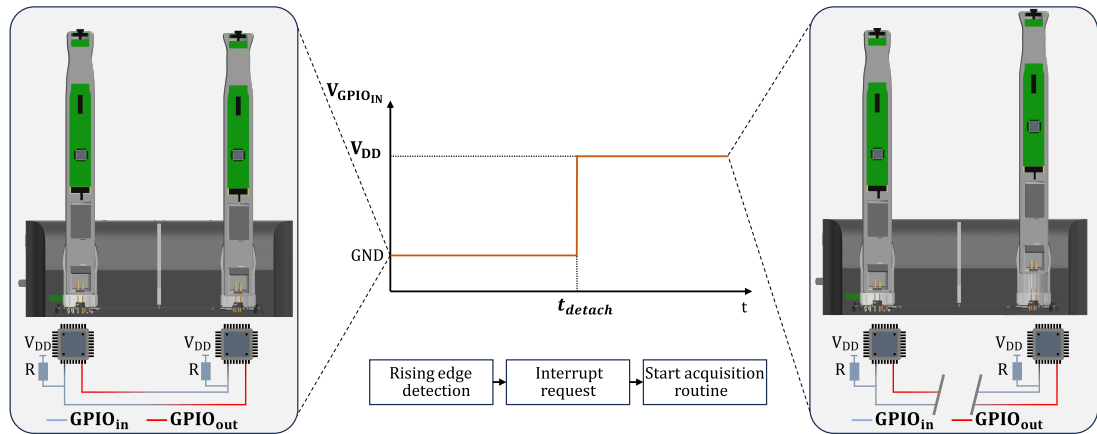


Figure 4.8: Recharging station designed for the tested device. The hardware solution relies on bidirectional sensing between the two MCUs embedded in the acquisition probes, enabling a synchronous initiation of the acquisition process. When one of the components is disconnected from the base, it prompts the initiation of the acquisition process. The USB-Dongle, integrated into the main PCB within the base station, enables BLE communications among all system components.

bidirectional sensing of the two probes. When connected, each probe can detect whether the other gets detached from the base. Connecting two pins between each slot made it possible to couple the microcontroller on each probe with the other. Two GPIOs have been involved in this process: One was configured in input mode and the other in output mode, depicted respectively in blue and red in Figure 4.8. Both GPIOs in output mode have been set to provide a low logical state. The GPIOs set as input have been programmed to trigger an interrupt when the transition from the low to the high logical state occurs (Figure 4.8). The interrupt is enabled when the user presses the play button on the graphical interface. A pull-up resistor, placed on each line connecting the two MCUs, makes the transition from the low to the high logical state possible when one of the two probes gets disconnected from the base. As introduced earlier in this section, the BLE communication

and data transmission are managed by the USB dongle manufactured by STMicroelectronics (Shanghai, China). The dongle hosts an STM32WB55CG MCU [154], a low-power 32-bit device with a dual-core Arm® Cortex®-M4/M0+ architecture with similar characteristics to those previously described microcontroller used for the probes. The dongle has been coupled to the PCB via a USB connector mounted on this latter. The ensemble has been further connected by cable to one of the 5 V-powered USB ports on the workstation running the graphic interface for real-time PWV assessment. The following section will describe the communication protocol used to handle data transmission.

4.2.2 The Firmware

The first step in developing the BLE protocol is the implementation of the routine responsible for connecting all the components constituting the proposed device. The reference roles within the BLE protocol are *central* and *peripheral*. In this project, the dongle is the central device; it acts as the master during the connection process and establishes the physical layer connection. On the other hand, the two probes perform as peripheral units; they serve as slaves during the connection process and are responsible for accepting the physical layer connection.

Connection Routine

Based on the information presented in the preceding section, a connection routine was built to identify and connect the two peripheral units with the core unit. This operation begins with the central unit (dongle) scanning the two peripheral units engaged in the advertising phase and enabling the connection. The scan phase (with a *white-list* to filter undesired devices) continues until the connection units are located. Once discovered, the connection procedure proceeds progressively, firstly establishing contact with the carotid probe and then with the femoral probe. The main criticality identified during the development of this algorithm is the identification of the connection parameters. The selection of the latter, in accordance with the timing constraints provided by STMicroelectronics [155] [156], enabled the establishment of the two connections and ensured the correct transfer of the acquired data in real-time [157] [142].

Data Transfer

The data transfer protocol represents a fundamental part of developing a device for the real-time acquisition system. The user initiates data transfer using commands accessible via the GUI. The command to *start* (or *stop*) data acquisition is forwarded by the central unit (dongle) to the two peripheral units. After receiving the command, each board begins reading the sensor. A four-wire bidirectional SPI communication protocol connects the load cell to the mentioned MCU. The sensor

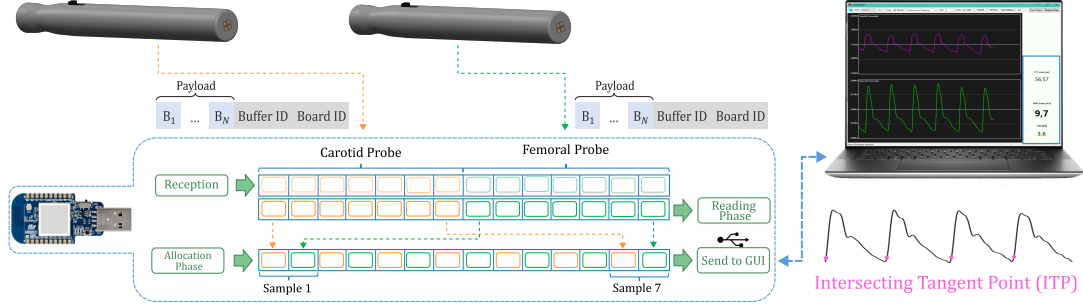


Figure 4.9: Schematization of force data management. BLE payloads sent by the acquisition probes are received and allocated into a circular buffer by the USB-Dongle. The samples are reorganized and sent to GUI via USB connection for real-time processing.

is programmed to work with a sampling frequency of 200 Hz enabling the acquisition of 12-bit force data output each 5 ms. A circular buffer structure was chosen to allocate the data and subsequently send them into a BLE packet structured as follows:

1. Bytes 1-14: contain the samples acquired by the sensor;
2. Byte 15: it is a progressive value representing the current BLE packet filled with force data;
3. Byte 16: it can be either 1 or 2 according to which probe is transmitting the data.

Data Management

The next step in the development process of the device is the implementation, on the central unit, of a procedure for managing and processing received data before its transmission to the laptop. When dealing with the reception problem, it's important to note that, besides the transmission phase of the acquisition's *start* command, there's a misalignment between the central unit and peripheral devices. This misalignment happens because the central unit can't receive data from the peripherals simultaneously. The routine is divided into three major phases:

1. *Read phase*: it involves the reception of the BLE data packets sent by each peripheral. Based on the last two bytes, the packet sequence number is sorted, and data is assigned to the proper sensor (carotid or femoral buffer).
2. *Allocation phase*: involves the copying of data within a circular buffer divided into 28 bytes as follows:

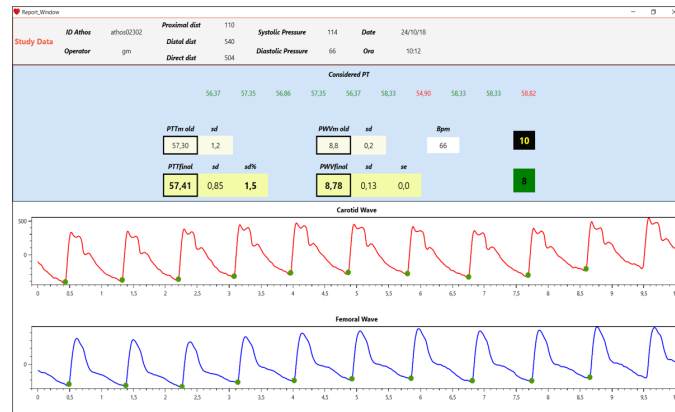


Figure 4.10: Report generated at the end PWV study.

- (a) Bytes 1-14: contain the data from the carotid probe;
- (b) Bytes 15-28: contain data from the femoral probe.

Once the buffer is full, the samples within are alternately reordered according to the diagram in Figure 4.9.

3. *Transmitting phase*: The data set is sent to the workstation for real-time display via a USB connection.

4.2.3 Graphic User Interface for PWV assessment

Once the system’s physical structure and communication protocols were defined, the GUI was implemented for controlling the device from a computer using Visual StudioCode. The software is designed to execute three distinct functions. The first task involves recognizing the USB-Dongle responsible for establishing the connection and managing data communication with the acquisition probes. Secondly, the software interprets and transmits user commands to the peripheral units. Lastly, the BLE packets containing gathered data are reorganized for real-time plotting and are processed for PWV calculation. The patented algorithm [158], originally developed and detailed in [139], has been adjusted to operate in the background, providing updated values of PTT, PWV, and corresponding standard deviation every 1,5 seconds. Figure 4.10 shows the comprehensive report generated when the acquisition is terminated. This report represents a summary of the PWV test just run and considers the last ten seconds of the waves, as foreseen in the standard procedure. The report includes the subject’s personal information, the PTT and PWV values, and, finally, the acquired carotid and femoral pulses with the related ITPs.

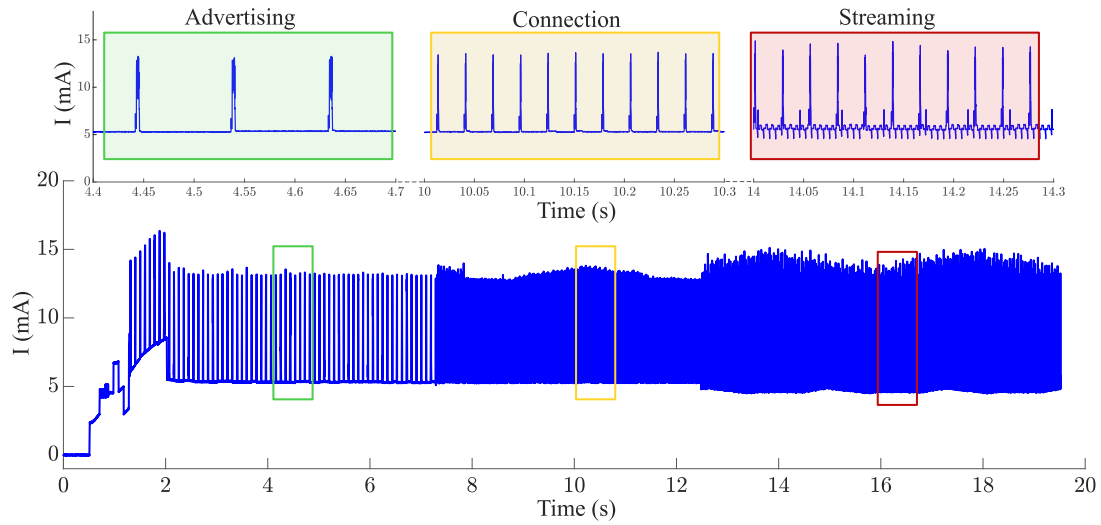


Figure 4.11: Current absorption of the acquisition probe during the different function modalities: Advertising, connection, and streaming.

4.2.4 Testing Phase

The forthcoming section introduces the setup employed to conduct a comprehensive series of tests to evaluate the device’s performance.

Setup for Synchronization Assessment

A crucial aspect for ensuring a trustworthy measurement is the achievement of precise synchronization in the reception of the initial data acquisition *start command* from peripheral units. Even a minor deviation of a few milliseconds could introduce uncertainty and reduce the measurement’s reliability. Synchronization was assessed using an oscilloscope. One accessible General Purpose Input/Output (GPIO) pin was configured to be toggle to a high logical state as soon as the *start command* is received. By establishing a connection between the oscilloscope probes and the specified and the mentioned GPIO, it became feasible to visually see and quantitatively determine the time delay associated with the reception of the start command by the two probes.

Setup for Power Consumption Evaluation

Given the integration of a rechargeable battery within the acquisition probes, the absorbed current during each device’s operation phase was analyzed. For this purpose, the DMM7510 digital graphical multimeter was used. The sampling frequency of 10 kHz was employed to detect the BLE module activity.

To perform the measurement, the multimeter probes were placed on power lines

connecting the battery to the PCB. An ensemble of three acquisitions lasting between 3 and 5 minutes was collected, and data was further analyzed offline using Matlab. The duration of each acquisition was chosen to replicate the average time used to conduct the PWV study in a clinical setting. Figure 4.11 displays a snapshot of the four main working modalities of the probe:

1. Initialization of the probe: when the probe is switched on, the microcontroller is initialized along with the load cell. If this latter is successfully read, the LEDs are switched on and off to give feedback to the user.
2. Advertising: after the initialization, the probe starts the *advertising phase* to inform the charging station about its presence.
3. Connection establishment: once the dongle initializes the BLE link with the two probes, all the units enter into a stable connection status. Both the central and peripheral units regularly assess the status of the other to confirm ongoing activity.
4. Data stream: every 35 ms, a new circular buffer is filled on the probe and sends a notification command to the BLE stack that prompts the transmission of the packet during the subsequent available connection interval.

The averaged absorbed current values were evaluated for the mentioned working conditions. The highest current value was employed to derive the discharge curve and estimate the actual battery life of each probe. Parallely, the minimum voltage so that all components could work properly in the worst-case scenario was assessed. The discharge curve was obtained through an equivalent circuit consisting of the battery, the voltage regulator on the PCB, and a resistor equal to 560 Ohm. The latter was dimensioned to represent the total consumption of the probe in the streaming mode with an absorbed current of 5.9 mA when supplied with a regulated voltage of 3.3 V. This setup was made according to datasheet specifications, under constant load conditions and with a discharge current at most 24 mA. The battery voltage was monitored using the NI USB-6259 board (National Instruments) [159] for the entire experiment. Data was acquired via serial interface using Matlab with a sampling rate of 1 Hz.

Setup for BLE Data Transfer Analysis

This subsection presents the setup used to evaluate the transmission efficiency of BLE packets. Both probes are programmed to transmit a signal with a sawtooth shape to evaluate better the result of the data management protocol developed on the dongle. The data are saved through the previously described dedicated GUI, in *.bin* format, and analyzed offline in the Matlab environment. A single 20-minute acquisition was performed, and then the order of packet arrival, correct reordering of simulated samples, and any packets lost during transmission were evaluated.



Figure 4.12: Experienced physician performing PWV assessment using the Athos system.

PWV Assessment

To assess the efficacy of the presented system, a clinical trial was conducted at the "Città della Salute e della Scienza" Hospital in Turin, Italy. Following the experimental protocol approved by the "University of Turin Bioethical Committee", described by [139], ten healthy volunteers were recruited to compare the results gathered using the proposed device w.r.t those of the SphygmoCor, available in the hospital. Before commencing each data capture session, informed consent was obtained from every participant. Then, two experienced clinical operators conducted the data collection process to ensure the acquisition of high-quality and stable signals, Figure 4.12. Following the standard practice for clinical PWV evaluation detailed in [53], each participant involved in the study underwent three acquisitions using both systems, with the clinical operators alternating the usage of both devices from subject to subject. Finally, a representative PWV value is derived for each individual by calculating the average data acquired from the three acquisitions collected using both systems.

4.2.5 Precompliance CE Tests

Electromagnetic Compatibility

The set of tests was carried out inside an anechoic chamber in the facility equipped for performing immunity tests up to a frequency of 6 GHz. In accordance

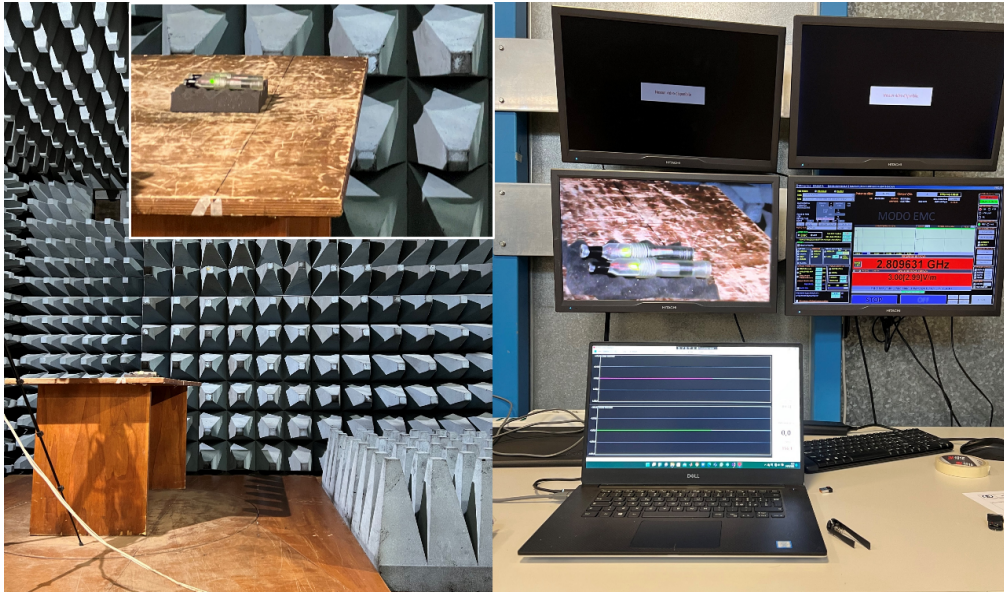


Figure 4.13: Anechoic chamber used to assess the electromagnetic compatibility of the system.

with the requirements of IEC 60601-1-2, the device was placed on a rotating table inside the chamber at a distance of 3 m from the antenna used to generate the electromagnetic field used in the test. Given the electromagnetic field strength of 3 V/m, immunity was evaluated over 3 frequency ranges: 80 MHz-800 MHz, 800 MHz-2.7 GHz, 2.7 GHz-6 GHz. Each range was tested by varying the orientation of the device w.r.t. the antenna on each of the four sides for a total of twelve tests. In each test, observations were made to determine if the application of the disturbing field resulted in any changes in the force values recorded at no-load by the load-cell sensor on the probes. Additionally, any loss of data was monitored during transmission between the two probes and the dongle, which was also placed inside the chamber, as shown in Figure 4.13.

Clinical Usability

The clinical evaluation of the device was carried out at the A.O.U. Città della Salute e della Scienza di Torino to verify the effectiveness, efficiency, and ease of use of the Athos system. This assessment was overseen by an external certified consultant to ensure accuracy and compliance with the guidelines outlined in IEC 62366-1:2015 and IEC TR 62366-2:2016 concerning the application of usability engineering to medical devices. These standards focus on the importance of understanding user needs, translating them into design specifications, and conducting usability testing to ensure that devices are safe, effective, and user-friendly. Moreover, they emphasize the identification, assessment, and mitigation of use-related

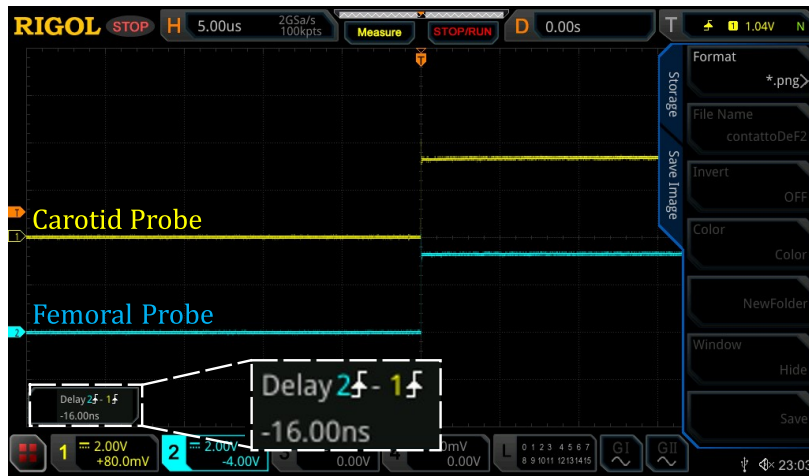


Figure 4.14: Observed delay between carotid (yellow) and femoral (blue) probes at the acquisition start-up using the proposed hardware solution.

hazards to minimize risks to users. In the investigation process, five specialized clinical operators and the project’s technical referees were involved in supervising operations and collecting user feedback on the device.

Each operator, aged between 28 and 47 years with varying degrees of experience in pulse wave velocity measurement, performed an ensemble of three acquisitions with the proposed acquisition system. The physicians who took part in this test filled out an interview report guided by questions posed by the team. To avoid interaction bias, the moderators briefly described the report to the participants, and therefore, it was autonomously compiled using a PC or tablet interface. The users provided feedback on a graded scale ranging from 0 to 4, in which a lower rating corresponds to a favorable opinion of the device.

4.3 System Assessment

In this section, the results of the introduced tests are reported and discussed, starting with the synchronization of the peripheral units, the current absorbed by each probe, the validation of the data exchange routine, and, finally, the results of the pre-compliance tests carried out on the device.

Synchronization

using the setup described in II-D.1, the synchronous start of the acquisition was evaluated. As a first step, an evaluation of the time lag related to the settings of the BLE stack was performed. Given a connection interval ranging between 15 ms to 40 ms, the observed lag was 20.94 ms. This delay can be attributable to the

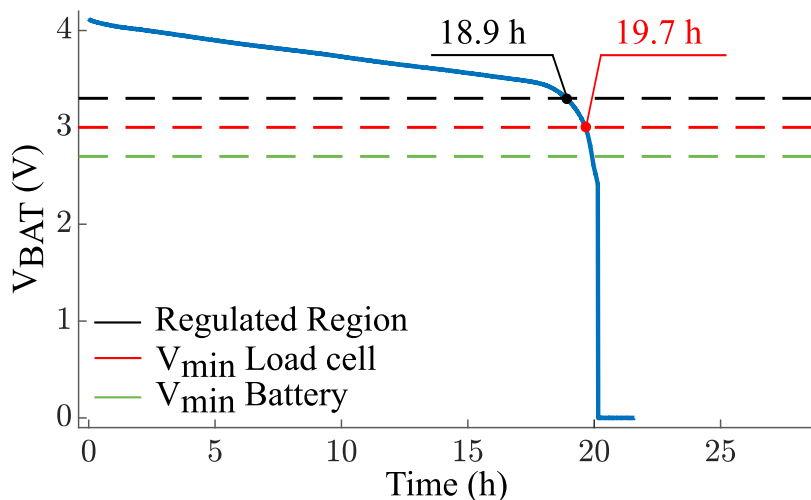


Figure 4.15: Discharge curve of the CELLEVIA BATTERY LP401235 under a pure resistive and constant load.

BLE stack transmitting the *start* command within the same connection interval. Therefore, the initial step taken to solve this issue was to find a compromise between parameters. However, this strategy was ineffective, as the average delay value obtained from 5 tests was 11.56 ms, considered unsatisfactory for this application. Since a software approach did not solve the issue, a hardware solution was chosen. This latter is based on the detachment from the charging station of one of the two peripheral units described in section 4.2.1. The synchronization was again evaluated through the oscilloscope, and the result can be seen in Figure 4.14. The second approach reduced the acquisition start-up delay to a value of 16 ns, considered acceptable for this application. As reported in section 4.2.1, a 32MHz crystal oscillator was selected as a high-speed external clock source to trim both the MCU and the RF subsystem. The 10 ppm frequency tolerance ensures a low drift during data acquisition sessions. It is important to note that the proposed system is not mentioned for long-term monitoring, and the time required for a single acquisition ranges between 5 and 20 minutes. Therefore, the eventual drift was assumed to be negligible in the defined operative window. In addition, before starting each session, both probes must be attached to the base station to ensure a synchronous start-up; consequently, the clock drift is reset when a new acquisition is started.

Power Consumption

The battery's autonomy introduced in Section 4.2.1 was evaluated in the laboratory using the setup detailed in Section 4.2.4. Table 4.1 shows the expected autonomy computed by dividing the nominal capacity by the averaged absorbed current values for the defined working conditions. The minimum value is registered

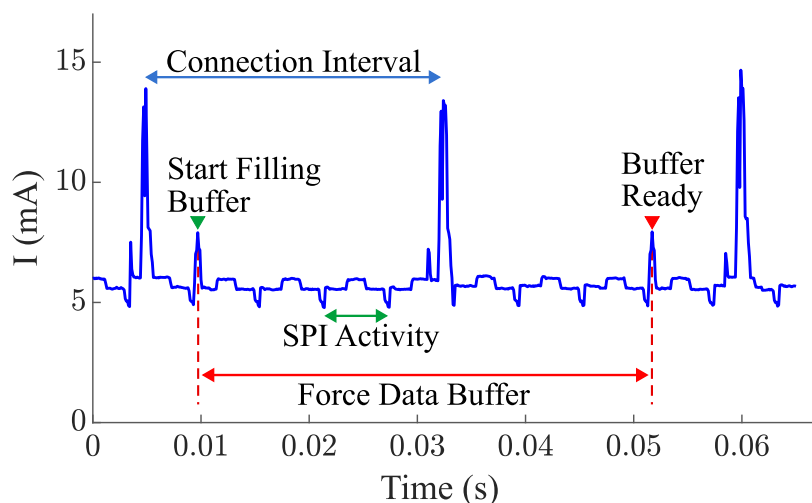


Figure 4.16: Events occurring during the *streaming* mode: BLE connection interval, SPI activity, force data buffer ready to be transferred.

Table 4.1: Averaged current absorption in different working modalities.

	Advertising	Connection	Streaming
Absorbed Current (mA)	5.49	5.48	5.90
Expected Battery Life (h)	21.81	21.79	20.30

during the connection phase (i.e., 5.48 mA), attributed to the activation of the status LED, RF activity, and ultimately the enabling of sensor readout. The highest value occurs during the streaming mode (i.e., 5.9 mA), in which the BLE packets containing the force data are sent. Following the trend of the mean value, the standard deviation computed in each working modality assumes the lowest value in the connection phase and the highest when the streaming occurs. Based on these results, the discharge curve of the battery, Figure 4.15, was derived to estimate the actual battery life of each probe and the minimum voltage so that all components could work properly. In these conditions, designed to mimic the maximum consumption modality, it took 20.2 hours for the battery to get fully discharged, thus matching the expected battery life computed on nominal characteristics (i.e. 20.3 hours). However, when evaluating the minimum voltage value to ensure proper operation of the components, the reference voltage values of the integrated components mounted on each probe were considered: the microcontroller [148], the load cell [146], and the linear voltage regulator [147] (equal to 1.7 V, 3 V, and 2.75 V, respectively). By selecting the reference value of the LDO to establish a supply voltage within the regulated range of 3.3 V, the autonomy decreases to 18.9 hours. However, under these circumstances, each probe has approximately a further hour

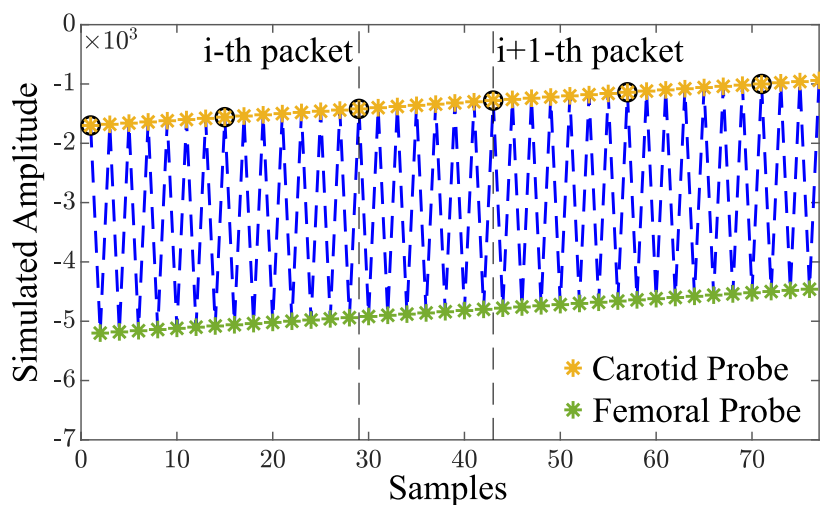


Figure 4.17: Result of *data management* routine in the 20-minute acquisition used to validate the data transfer process. No reported cases of lost BLE packets or probe misalignment were observed during this procedure

before reaching the minimum supply voltage required for the load cell to work reliably. Subsequently, the consistency of the BLE activity w.r.t. the settings chosen for this application was verified.

In Figure 4.16, a representative window of 70 ms, captured during the streaming mode, is reported. As it is possible to observe, the variations of the current absorbed by the probe are coherent with the specifications of the BLE protocol and the firmware implemented to read the load-cell sensor. Few regular events alter the baseline:

1. The highest peaks, reaching up to 15 mA, correspond to the transmission of BLE notifications. This operation necessitates the activation of the RF module, albeit for a very brief period. These peaks consistently occur every 28 ms due to the chosen connection interval.
2. The peaks below 10 mA, highlighted in red, indicate when the circular buffer is filled with force data and ready to be sent in the following connection interval. The load cell is programmed to read a new sample every 5 ms. The periodic trapezoidal pattern represents the SPI activity.

BLE Data Transfer Analysis

the last step in evaluating the proposed system is to validate the implemented routines for data management and transfer. In the power consumption subsection, Figure 4.15 allowed to visualize the consistency of the BLE and SPI activity w.r.t.

Table 4.2: Results of the validation process

Subject	Proposed Device		Sphygmocor	
	PWV (ms^{-1})	$\sigma\%$	PWV (ms^{-1})	$\sigma\%$
1	6.48 ± 0.83	12.81	6.52 ± 0.81	12.46
2	8.02 ± 0.54	6.73	8.80 ± 0.51	5.80
3	6.18 ± 0.22	3.56	6.83 ± 0.19	2.78
4	7.66 ± 0.48	6.27	8.80 ± 0.51	5.80
5	6.10 ± 0.17	2.79	6.77 ± 0.24	3.25
6	5.12 ± 0.03	0.59	5.93 ± 0.09	1.52
7	7.05 ± 0.41	5.82	7.44 ± 0.44	5.91
8	4.12 ± 0.33	8.01	5.33 ± 0.28	5.25
9	5.38 ± 0.76	14.13	5.43 ± 0.26	4.79
10	4.77 ± 0.61	12.79	5.83 ± 0.61	10.46

Notes: PWV, averaged values of the three acquisitions executed during the data collection, $\sigma\%$, percentage of the standard deviation.

the proposed configuration of each acquisition probe. In this section, the emphasis is directed toward the activities of the dongle related to receiving data and its subsequent handling for processing and display in the GUI. To do so, each probe is programmed to transmit a signal with a known growing shape. A representative window showing the results of the data management routine is reported in Figure 4.17. The samples are color-coded according to the probe ID identifying the unit responsible for transmitting the data packet: yellow for the carotid and green for the femoral probe.

A black circle has been added to highlight the beginning of each data buffer sent to the GUI. By utilizing signals with a predetermined periodic pattern, it became feasible to confirm the reordering of samples as detailed in Section 4.2.2 and to detect any potential data loss, which would manifest as anomalies in the plot. The potential risk of data loss was assessed through a 20-minute data acquisition session. During this procedure, the quantity and synchronization of BLE packets between probes have been monitored at consistent 20-minute intervals. No reported cases of lost BLE packets or probe misalignment were observed during this procedure.

PWV Assessment

Table 4.2 reports the averaged PWV values acquired across all examined subjects and the associated standard deviations. The accuracy of the proposed system was assessed by examining the correlation of PWV values between the two instruments and by analyzing the measurement agreement across the study population.

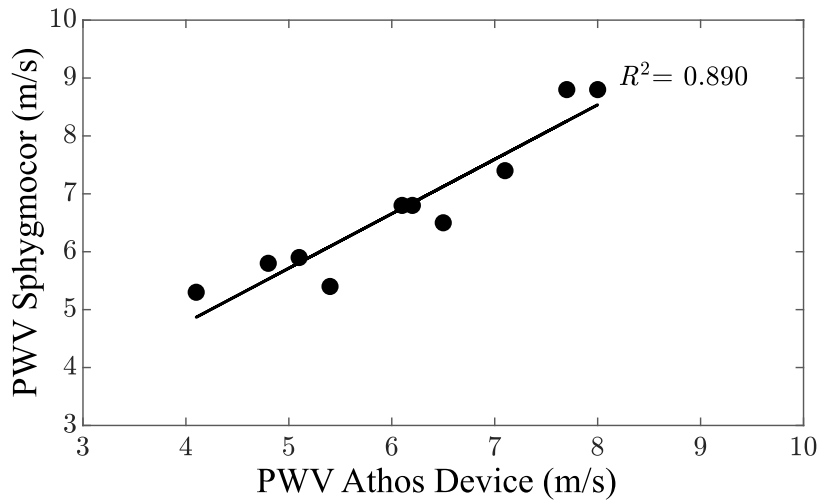


Figure 4.18: Scatter plot confronting the averaged PWV values obtained for each recruited subject. A linear regressive model fitted on the available data points shows a strong linear correlation between the two devices.

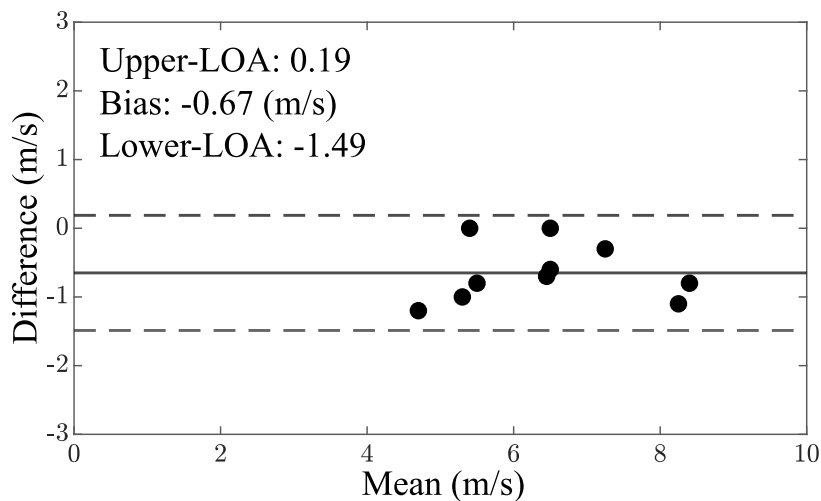


Figure 4.19: Bland-Altman plot of the difference between the performances given by the Sphygmocor and the proposed device.

The scatter plot shown in Figure 4.18 exhibits the mean PWV values for each participant. A linear regression model was employed to quantify the relationship between measurements, and its quality was assessed using the determination coefficient (R^2). The robust linear correlation between the two devices is evident from the dispersion of the actual data points around the model's best-fit line, as indicated by the coefficient R^2 , which yielded a value of 0.89. The Bland-Altman plot reported in Figure 4.19 represents the agreement distribution between the two instruments. As shown, the PWV mean difference is about -0.67 ± 0.67 m/s. The

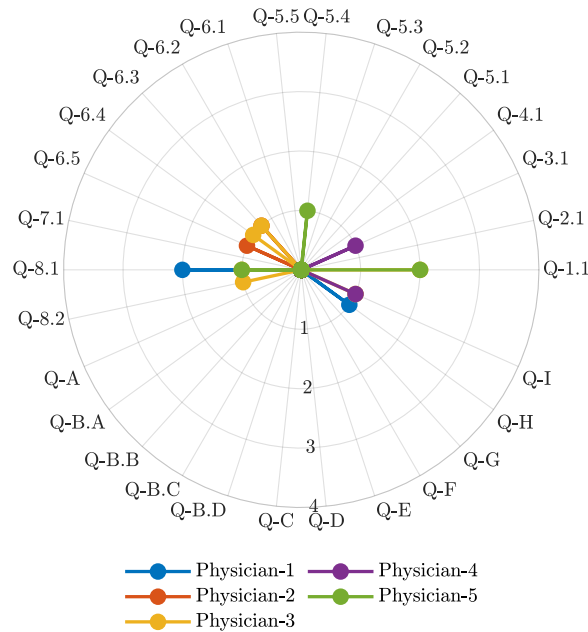


Figure 4.20: Results of focus group interview to assess the clinical usability of the device. Scores were retrieved for each physician through the guided response questionnaire. A lower score on a scale ranging from 0 to 4 corresponds to a favorable opinion of the device.

comparison between the two devices reveals that the proposed system yields PWV values that closely match those of the gold standard. The reliability of the measurements was validated by the regression model, which highlighted their strong linear correlation, and by the Bland-Altman plot, which indicated a bias well below the 1 m/s limit stipulated by the guidelines for an excellent cfPWV estimation [160].

4.3.1 Pre-compliance CE Test

This section outlines the results of the pre-compliance CE test conducted on the Athos system.

Clinical Usability

As stated in section 4.2.5, the clinical usability was assessed according to IEC 62366-1:2015 and IEC TR 62366-2:2016 concerning the application of usability engineering to medical devices. The evaluation considered key aspects such as patient preparation, system setup, and application during PWV assessment. In addition, safety measures, cleaning, and storage procedures were examined to mitigate user-related risks and preserve the device’s integrity.

In general, during the simulated use of the device by participants, no usage or

Table 4.3: Results from the focus group interview were used to evaluate the clinical usability of the device. Scores for each physician were obtained using a guided response questionnaire. A lower score on the 0 to 4 scale indicates a more favorable opinion of the device.

Question	Physician-1	Physician-2	Physician-3	Physician-4	Physician-5
Q-1.1	0	0	2	0	2
Q-2.1	0	0	0	0	0
Q-3.1	0	0	0	1	0
Q-4.1	0	0	0	0	0
Q-5.1	0	0	0	0	0
Q-5.2	0	0	0	0	0
Q-5.3	0	0	0	0	1
Q-5.4	0	0	0	0	0
Q-5.5	0	0	0	0	0
Q-6.1	0	0	0	0	0
Q-6.2	0	1	1	0	0
Q-6.3	0	0	1	0	0
Q-6.4	0	1	0	0	0
Q-6.5	0	0	0	0	0
Q-7.1	0	0	1	0	1
Q-8.1	2	0	1	0	0
Q-8.2	0	0	0	0	0
Q-A	0	0	0	0	0
Q-B.A	0	0	0	0	0
Q-B.B	0	0	0	0	0
Q-B.C	0	0	0	0	0
Q-B.D	0	0	0	0	0
Q-C	0	0	0	0	0
Q-D	0	0	0	0	0
Q-E	0	0	0	0	0
Q-F	0	0	0	0	0
Q-G	0	0	0	0	0
Q-H	1	0	0	0	0
Q-I	0	0	1	1	0

technical errors occurred. All users measured according to the proposed workflow without encountering significant difficulties, even when the operator had no prior experience with the device. The results of their experience were evaluated through a guided response questionnaire (see Appendix C) using a scale from 0 to 4, where a lower score corresponds to a favorable opinion of the device. The overall scores,

depicted in Figure 4.20 and reported in Table 4.3, can be considered very positive, as most of them fall within the non-risk zone (scores equal to or lower than one), indicating a generally favorable opinion of the device.

Electromagnetic Compatibility

The outcome of the tests for RF electromagnetic emission, according to CISPR 11, classifies the Athos acquisition system in Group 1, Class A, defining its RF emissions in a way that does not cause any interference for electronic systems in the vicinity. From an electromagnetic compatibility perspective, the device is deemed suitable for the application of interest.

4.3.2 Benchmark Comparison

After examining the performance of the proposed device in the preceding sections, the retrieved findings were contextualized within the existing literature. Given the extensive field of non-invasive PWV assessment, the clinical devices considered the most pertinent for a comprehensive comparative analysis were selected. Specifically, the Arteriograph, Complior, Sphygmocor, and Pulse Pen, were included as they are clinically graded, commercially available, and utilize diverse sensing mechanisms. Table 4.4 reports the main advantages and disadvantages of the commercially available systems routinely used in the diagnostic clinic environment according to the available literature. Our evaluation encompasses factors such as sensitivity to motion, level of operator independence, portability, preparation time required for patients, and comfort levels. Utilizing a single oscillometric brachial cuff, the Arteriograph (TensioMed, Hungary) stands out for its portability and operator independence, making it versatile for various settings [59, 135]. However, its sensitivity to motion and cuff placement may affect accuracy. [161, 162]. In contrast, the Complior (ALAM Medical, France) system records arterial wave pulses concurrently using up to 4 piezoelectric transducers placed directly on the skin (carotid, femoral, and radial distal arteries) [160]. Despite being acknowledged as a gold-standard device for non-invasive PWV assessment, it is operator-dependent and may lack comfort during use [84, 163]. Similarly to the Complior, the Sphygmocor offers unparalleled accuracy but requires an ECG, is less portable, and has higher costs. Moreover, it requires a high level of operator expertise in peripheral signal acquisition [64, 139, 160]. PulsePen (DiaTecne, Italy) detects pressure waveforms at the carotid and femoral arteries either simultaneously or sequentially using applanation tonometry. It comprises two small portable tonometers and a compact ECG unit [64, 85, 163]. Starting from the device’s main drawbacks reported in the literature, a low-cost, non-invasive, yet reliable system was created. Numerous efforts were made to improve portability and ease of use by removing the acquisition system for ECG and introducing two wireless and lightweight sensing

probes. Nonetheless, it's essential to address the limitations that emerged in this study. First of all, the small sample size is attributed to the restricted number of participants. It is essential to note that the pre-clinical trial enabled the evaluation of the hardware and firmware updates implemented in the device, as well as the feasibility of the new sensor used for PWV assessment. Additionally, the disparity between the sensor dynamics, ranging from 0-5 N, and the forces involved in the arterial pulse passage might reduce sensor resolution. Nevertheless, upon analyzing the accuracy of PWV estimation, the comparison with the gold standard device did not unveil any significant concerns regarding the measurement's reliability while simultaneously achieving all goals regarding portability and enhanced usability. Thus, considering all the aforementioned factors, the proposed system aligns with the current state-of-the-art literature. Moreover, it completely fulfills its intended purpose in non-invasive Pulse Wave Velocity assessment.

4.4 Conclusion

This chapter presents a wireless device to provide a real-time cfPWV assessment. The entire hardware of the device was re-engineered to improve the portability and ease of use w.r.t the former system. The prototypal sensor originally employed in the Athos device [164] was removed in favor of a commercial piezoresistive load cell that proved to be well-suited for detecting arterial pulses. The firmware received an update, and a novel communication protocol was devised to facilitate the interconnection of the units, accompanied by procedures to manage and transfer data. The graphical user interface was improved by integrating real-time PWV assessment. The electromagnetic compatibility test was conducted to verify the system's adherence to medical device design guidelines. Clinical usability was validated by five clinical operators with varying experience in assessing PWV, indicating a generally favorable opinion of the device. The evaluation of PWV estimation accuracy against the gold standard device did not reveal any significant concerns regarding the reliability of the measurement. In conclusion, it was demonstrated that the proposed system effectively enhanced the key aspects that inspired the design of the former device. Improved portability and ease of use were achieved through a redesign of the device on all levels to provide a system capable of broadening the accessibility of this measurement in the clinical environment.

Table 4.4: Reference systems for Non-invasive PWV Assessment.

Device	Disadvantages	Advantages	Execution mode	Sensor	Reference
Arteriograph	High sensitivity to motion Cuff Placement Time-consuming Brachial PWV	Portability Operator independence	One-step	Arm pressure cuff	[161, 162]
Complior	Operator dependent Low comfort High sensitivity to motion	Excellent accuracy	One-step	Piezoelectric mechanotransducers	[84, 163]
Sphygmocor	Operator dependent Need of ECG Reduced portability Time-consuming Elevated costs	Excellent accuracy	Two-step	Applanation tonometry	[64, 139, 140]
Pulse Pen	Operator dependent Need of ECG according to the selected setup	Portability Excellent accuracy	One or two steps	Applanation tonometry	[64, 85, 163]
Athos	Operator dependent	Portability Excellent accuracy Ease of use Real-time feedback	One-step	Piezoresistive load cell	Present work

Chapter 5

Algorithms for assessing Pulse Wave Velocity

This chapter contains parts that have been taken, or partially rephrased, from a previously published work [165].

This chapter introduces a novel region-based algorithm to determine cfPWV, decoupling the assessment of this biomarker from point-to-point feature extraction. A dataset of 75 healthy participants, previously recruited to compare the performances of a new instrument, Athos, with the gold standard for non-invasive PWV (SphygmoCor), was used to set up a new algorithm for determining the clinical cfPWV. The proposed approach locates and processes a specific window on the carotid and femoral signals. Cross-correlation is employed to compute the pulse transit time within the pulses. Finally, the cfPWV is assessed. A set of indicators has been defined to quantify the stability and reliability of the window used by the algorithm. The results obtained through the proposed algorithm, the Intersecting Tangent method, and the direct application of the cross-correlation technique on signal epochs have been systematically compared with outcomes derived from the SphygmoCor device. The proposed algorithm showed a high correlation with the gold-standard SphygmoCor device, thus resulting in excellent accuracy for the evaluation of this clinical biomarker. In addition, it also proved more robust to noise than the Intersecting Tangent Point (ITP) method, making it a reliable alternative for non-invasive cfPWV assessment in clinical settings.

5.1 Introduction

Vascular aging has been demonstrated to be linked with an increment in the chance of developing chronic illnesses such as CVDs, type 2 diabetes and renal disorder [166, 167, 168]. Among the non-invasively possibilities, the PWV measurement is the most reliable.

PWV can be measured between any two sites in the circulatory system. However, the two acquisition points determine whether the parameter obtained is local or global [169]. Due to the proximity of the two acquisition sites to the central aorta, cfPWV is recognized as the most widely measured surrogate of the aoPWV [66, 67, 68].

With the introduction of PWV as a standard biomarker of arterial stiffness, several methodologies and algorithms have been developed to provide increasingly accurate estimates of PTT. As a result of the analysis of the characteristic morphology of the pulse wave [73], numerous studies over the years have proposed the identification of a specific point or window on the signal that would allow reliable PWV estimation [68].

Different algorithms relying on the extraction of a single feature located on the signal were used for PTT assessment. Among these, the most employed technique is the *foot* of the upstroke of the blood pulse as a reference point in the waveform [74]. However, as reported in [170, 171, 172], these approaches, when applied to identical waveforms, might result in differing PWV values.

Nowadays, many clinical indicators, including heart rate and blood pressure, may now be monitored by wearable devices with findings that meet the standards for use in a clinical setting. Many studies have been conducted to assess PWV using standalone wearable devices, following this trend. The extraction of pulse waves from acquisition locations that deviate from clinically defined places may alter the shape of the signals, hence diminishing the estimated precision of the techniques described above.

A novel set of algorithms has been developed to address the limitations of relying on a single localized feature for PWV evaluation. These algorithms analyze specific sections of pulse waveforms, avoiding the PWV evaluation based on a single feature extracted from the signal. Although additional validation studies must be undertaken, region-based approaches such as ‘diastole patching’ [74] and ‘region-matching’ [68],[75] provided excellent accuracy in the PWV assessment according to the accuracy criteria reported in 2010 ARTERY Society guidelines [53].

In this chapter, a novel region-based algorithm for the estimation of cfPWV is presented. Specifically, the proposed method applies several processing steps to the waveform recorded on both sites, then, it uses the cross-correlation technique to assess the PTT.

Given two generic time series $X_c(t)$ and $X_f(t)$, both defined in the time interval T , the cross-correlation is a statistical technique used to quantify their delay along

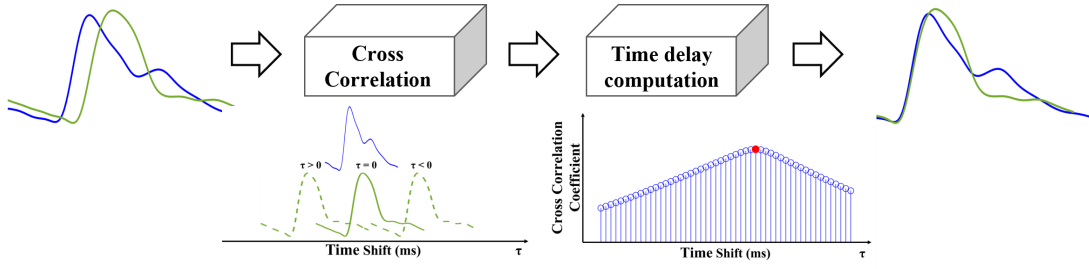


Figure 5.1: Pulse waveforms alignment performed using cross-correlation. Given the carotid pulse (Blue) and the femoral pulse (Green), the cross-correlation function is computed for each value of τ . The timeshift's equivalent which leads to the maximum of the cross-correlation function is taken as pulse transit time, then the alignment is performed.

the abscissa according to the continuous time shift τ . It is defined as expressed in Eq. 5.1.

$$R_{X_c, X_f}(\tau) = \frac{1}{T} \int_{-\frac{T}{2}}^{\frac{T}{2}} X_c(t) X_f(t + \tau) dt \quad (5.1)$$

In this case, the two time series to be compared are the pulse waveforms detected on the carotid and femoral sites, respectively defined as X_c and X_f . T represents a fraction of the full cardiac cycle and τ constitutes the time shift along the abscissa by which the cross-correlation coefficient is computed. The cross-correlation function, $R_{X_c, X_f}(\tau)$, is estimated for each value of τ . When the maximum of $R_{X_c, X_f}(\tau)$ occurs, the best achievable similarity condition is reached and τ is considered as the PTT. Figure 5.1 shows an example of the realignment of two pulse waveforms using cross-correlation. As mentioned in [169, 173, 174], cross-correlation was previously used to calculate the PTT. However, its application was employed only in a local assessment of the PWV. This limitation was mainly due to morphological differences presented by the pulse waves at the two distant acquisition sites. The proposed approach aims to overcome this issue by giving as input for the cross-correlation a set of signals characterized by a known shape in which the portion of signal used for the PTT calculation remains unchanged along the sites. Results equivalent to those obtained from the reference device were achieved, representing a significant improvement over the direct application of cross-correlation to the original signals. This article is structured as follows. Section 5.2 introduces the available data, the proposed algorithm, the methodology employed to identify the processing window and the carried out statistical analysis. Section 5.3 summarizes the results obtained by the Region-Based Cross-Correlation (RBCC) approach compared to the Direct Cross Correlation (DCC) application technique and the output of the two presented devices. The reported results are discussed in section 5.4. Finally, in section 5.5, conclusions are presented.

5.2 Material and Methods

5.2.1 Experimental Data

Two devices for PWV analysis were used to collect the pulse waveforms obtained in this study: the Athos system, whose hardware and firmware conceptualization and development are detailed in [139], and the SphygmoCor. The former was used to retrieve the blood pulse raw data, while the latter was used as the reference method to compare the achieved outcomes. The SphygmoCor is widely regarded as the clinical gold-standard device used for the noninvasive cfPWV assessment [17, 53]. Both devices determine the PWV value by locating the intersecting tangent point (ITP) method recognized as the most reliable among the single-feature algorithms introduced in the previous section. The data used for developing the algorithm were acquired at the "Città Della Salute e Della Scienza" hospital in Turin (Italy) according to the experimental protocol approved by the "University of Turin Bioethical Committee." A cohort of 75 healthy subjects was recruited to validate the precision and accuracy of the Athos device [140]. In this particular context, the device was analyzed from a clinical perspective, emphasizing its application, intra-operator variability, and estimation accuracy. As a result of the mentioned study, the Athos device was employed for three main reasons: an excellent level of agreement with the Sphygmocor, high quality of pulse waveforms, and finally, differently from the reference device, it provides access to the raw data. The pulse waveforms collected in the mentioned study were recorded with a sampling frequency of 680 Hz and subsequently stored for offline processing in the Matlab environment.

5.2.2 Proposed Algorithm

The main steps of the herein-reported RBCC algorithm are summarized in Figure 5.2. In particular, this can be divided into three main phases: *pre-processing*, *processing* and *evaluation of the outcome*. The pre-processing phase is characterized by a series of filter steps used to remove the DC-bias and high-frequency noise and to retrieve the cardiac activity of the subject under investigation. The delay and the phase distortion introduced by the application of each filter were removed by applying this latter forward and backward onto the signal. Figure 5.3 reports the steps used for extrapolating the cfPWV of the acquired signals.

- i) To get a high time resolution for the assessed PTT, the tonometer signal is resampled to 2040 Hz through a cubic spline. As a result of this resampling, the signal temporal resolution is increased to 0.49 ms. Interpolation is accomplished using a third-degree polynomial with forced continuity in the second derivate.

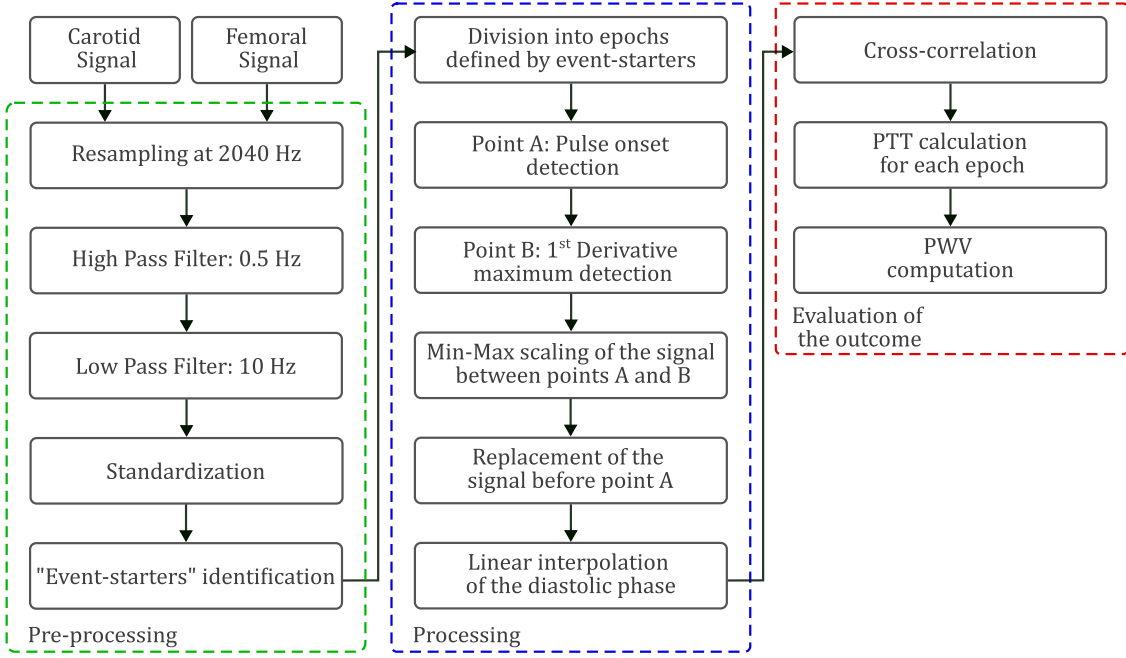


Figure 5.2: Illustration of the presented Region-Based Cross-Correlation (RBCC) algorithm divided into its macro stages: *pre-processing*, *processing* and *evaluation of the outcome*.

- ii*) As reported in [139, 174], high pass filter with a cut-off frequency equal to 0.5 Hz is applied to remove the DC offset.
- iii*) Subsequently, a low pass filter with a cut-off frequency equal to 10 Hz is used to remove the high-frequency noise [174].
- iv*) Once done with the filter steps, pulse waveforms are standardized [174] according to Eq. 5.2:

$$x = \frac{x - \mu_s}{\sigma_s} \quad (5.2)$$

Where μ_s and σ_s are respectively the mean value and the standard deviation of the signal. The result of the filtering steps is shown in Figure 5.3(a).

- v*) This step uses the carotid signal to evaluate the subject cardiac periodicity (T), which in turn is employed to split the signals into single epochs. To do so, a low pass filter with a cut-off frequency of 1.5 Hz is applied. The beginning of each cardiac period is detected as the minimum points of the filtered carotid signal, as represented by green asterisks in Figure 5.3(b).
- vi*) The projection of the points, found in the previous step, on the abscissa, is used as the common reference to divide both carotid and femoral signals,

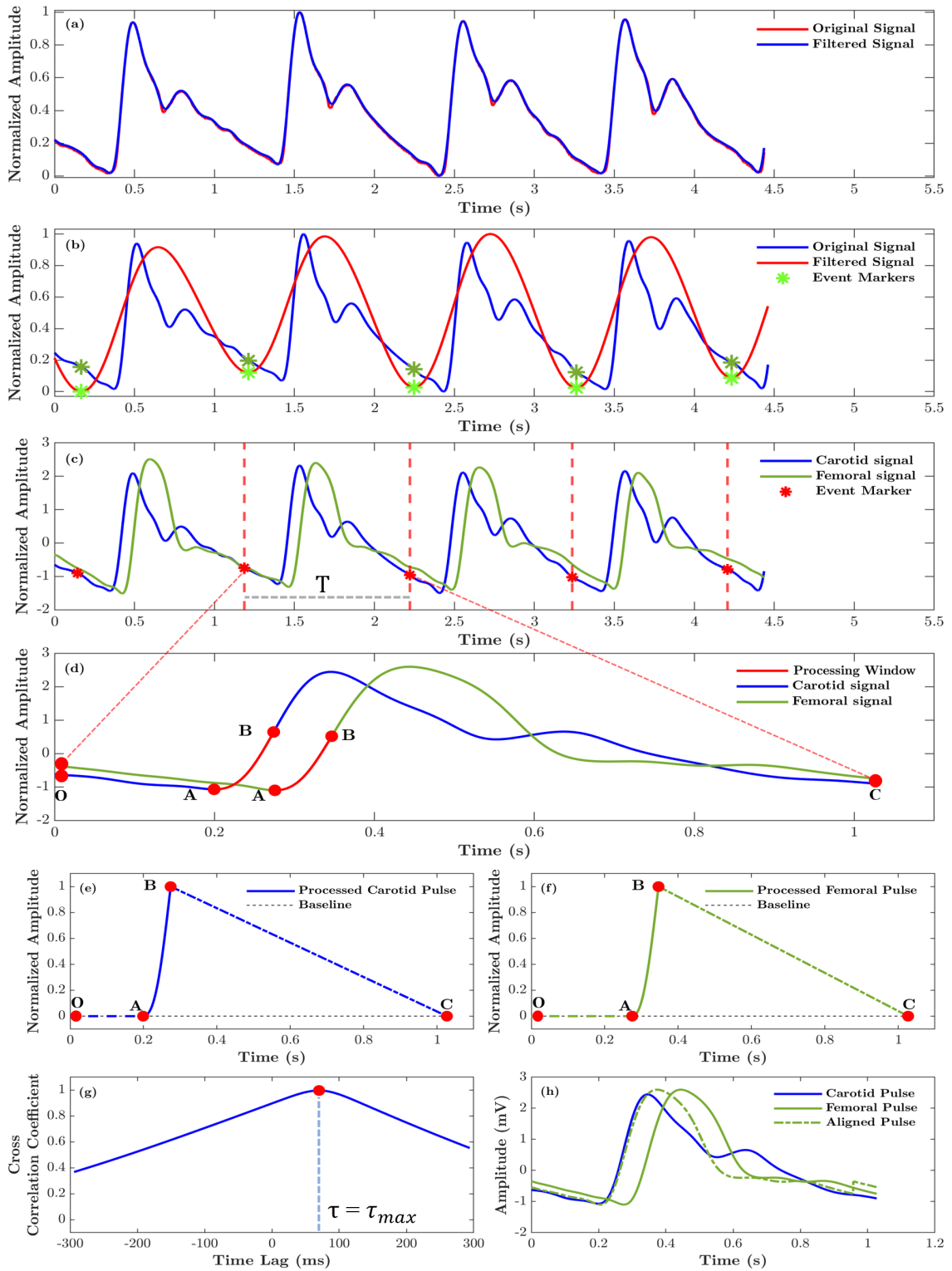


Figure 5.3: Region Based Cross-Correlation (RBCC) algorithm processing steps. (a) Result of the bandpass filtering procedure: original signal (blue), filtered signal (red). (b) Individuation of the cardiac activity (green points) on the low pass filtered carotid signal (red). (c) Carotid signal (blue) and femoral signal (green) are split into single epochs. (d) Detection of the processed windows on both signals in the current epoch. (e) Processed carotid window. (f) Processed femoral window. (g) Evaluation of the delay through the application of the cross-correlation technique on the mentioned windows. (h) Alignment of the processed signals in the current epoch.

Figure 5.3(c). In this way, it is possible to process each couple of blood pulses preserving the information concerning the time delay related to the propagation of the pulse wave between the two sites.

- vii*) The initial step in the processing phase is to find the closest minimum point preceding the upslope of the pulse. This position corresponds to the diastolic minimum, point A in Figure 5.3(d). Point O identifies the beginning of each pulse wave.
- viii*) Point B, depicted in Figure 5.3(d), represents the second point used to define the window on the original signal. This characteristic point is located at the maximum point of the first derivative of the signal. Finally, point C identifies the end of the pulse wave.
- ix*) Once the window is recognized on both pulses, these are normalized [174]. This is to ensure that both waves are on the same baseline and to avoid the different amplitudes of the rising fronts that could affect the cross-correlation result, Figure 5.3(e, f).
- x*) To preserve the time delay between the two waves, the portion of the pulse between points O and A is replaced by a number of samples equal to the number of samples on the original signal. Concerning the portion of the signal between points B and C, this section is linearly interpolated on the same number of samples which separates B and C on the abscissa.
- xi*) The time delay at which the maximum of cross-correlation coefficient occurs indicates the time shift that gives the best alignment, Figure 5.3(g,h).
- xii*) Once the PTT value for the current epoch is found, the process starts again from step *(vii)*. The procedure continues until the PTT values for all N epochs, segmented at *(vii)*, are obtained.

- xiii*) The standard deviation (σ) is calculated for the retrieved data. To enhance comparison with the Sphygmocor device, the same outlier rejection criteria was adopted. Hence, PWV values outside the range of $\pm 0.9\sigma$ are rejected.
- xiv*) Finally, the remaining PWV values, E , are computed and averaged as reported in Eq. 5.3.

$$PWV = \frac{1}{E} \sum_{j=1}^E \frac{d}{PTT_{car-fem}(j)} \quad (5.3)$$

Where d represents the distance measured between the femoral and the carotid acquisition sites multiplied by a correction factor equal to 0.8 [70] [169]. This correction factor accounts for the overestimation of the aortic length calculated on the subject's skin.

5.2.3 Robustness of the Algorithm

The term algorithm robustness refers to the algorithm's capacity to perform the cfPWV assessment despite interference conditions caused by the presence of noise or artifacts superimposed on the signal. Within the context of this application, a white Gaussian noise was introduced onto the pulse wave signals in order to obtain SNR of 10, 15, 20, and 25 (dB) across the bandwidth of the signal (i.e., 0.5-10 Hz) [173]. Each measured pulse wave signal was denoised through the application of filtering stages reported in the processing steps *(ii)* and *(iii)* of the proposed algorithm. Subsequently, the resultant signal served as the starting point for the addition of noise needed to achieve the specified SNRs. Then, both algorithms, RBCC and ITP, were applied to the noisy pulse wave signals. Finally, the resulting differences between noisy-cfPWV values and those derived from the application of each method to noise-free signals were compared.

5.2.4 Identification of Processing Window

Since the proposed algorithm relies on the application of the cross-correlation on a specific portion of the signal, it is necessary to point out how the processing window was defined. As stated in [175], pulse waveforms acquired from different places on the human body have distinct morphologies. Particularly, the shape of blood pulses may be altered by several factors, including the positioning of sensors on the skin, the experience of the operator collecting the data and the subject's anatomy. The decision to define a specific section of the signal derives from the necessity of minimizing the morphological disparities between individual pulse waves while preserving the temporal information. As reported in [74, 176, 177, 178], the early systolic and end-diastolic portions of the blood pulse are identified as the least likely to be impacted by reflected waves and motion artifacts compared to the diastolic component. Therefore, the search for processing window was made

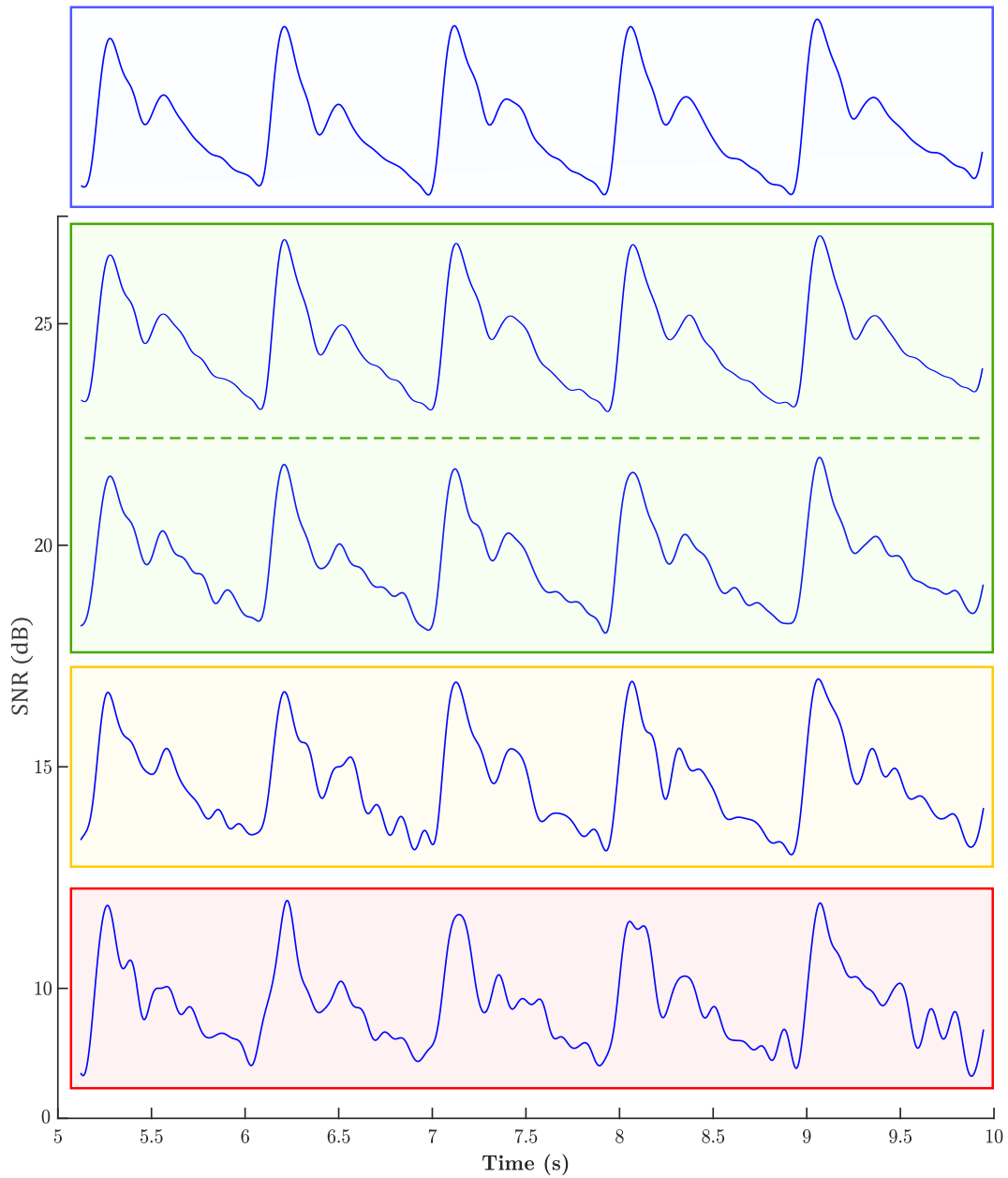


Figure 5.4: Degradation of the original carotid pulse waveforms (blue window) by introducing noise to achieve SNRs of 10 (red window), 15 (yellow window), 20, and 25 (green window) dB.

by analyzing the amplitude and the slope of the rising front of all the waveforms available in the dataset. The inclination of the curve was derived by computing the point-by-point slope γ of the tangent line with respect to the horizontal. The tangent to the curve was determined using the known equation of the line passing

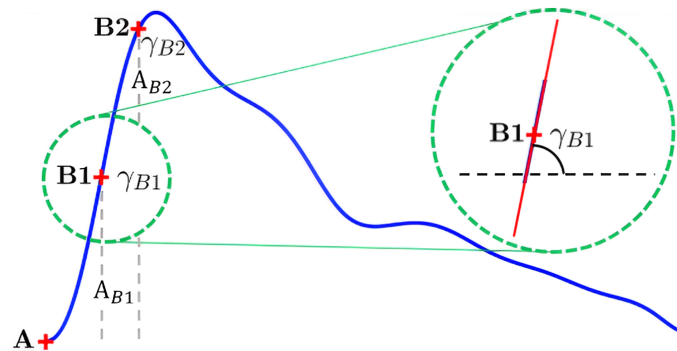


Figure 5.5: Selected points used for the definition of the processing window. End of the diastole (A), the maximum of the first derivative (B1) and the 95% of the systolic peak amplitude (B2). The slope coefficient γ has been computed as the angle between the horizontal line and the tangent line passing through successive samples on the signal. The value assumed by γ in B1 and B2 was defined as γ_{B1} and γ_{B2} .

between two points for each pair of successive samples. The slope γ has been computed according to Eq. 5.4.

$$\gamma = \arctan\left(\frac{df(t)}{dt}\right) \quad (5.4)$$

Where $f(t)$ represents the pulse waveform as a function of time t . Figure 5.5 illustrates the points considered for defining the processing window. The minimum preceding the ascending portion of the systolic phase, indicated as A, represents the window's lower boundary.

Concerning the definition of the upper limit, two specific points have been considered. The first one corresponds with the maximum of $\gamma(t)$, (B1), and the one located at 95% of the systolic peak's amplitude (B2). This latter option was preferred to the systolic peak since the calculated slope at the signal's maximum would always be zero, as the tangent line becomes horizontal whenever a local, or global, minimum, or maxima occurs.

5.2.5 Statistical Analysis

The following subsection describes the statistical analysis used to determine the upper bound of the window as well as the parameters employed to evaluate the algorithm's performance for estimating from the PWV. Three different indicators have been defined to quantify the stability of the mentioned upper boundary across the entire dataset: the intra-subject variability (*intraSV*), the inter-subject variability (*interSV*) and the coefficient of variation (*CV*). The (*intraSV*) evaluates

the overall point-to-point difference of the considered features in B1 and B2 on the carotid and femoral sites. This information enabled us to determine which of the two points leads to the section of the signal presenting the highest similarity, hence improving the algorithm's precision. As reported in Eq. 5.5, the first step in the calculation of this parameter is to determine the absolute difference, D_i , of the considered feature for each couple of carotid and femoral waves.

$$D_i = |feat_{CAR,i} - feat_{FEM,i}| \quad feat = A, \gamma. \quad (5.5)$$

Where A , refers to the amplitude value and γ to the slope coefficient assumed in B1 or B2. Subsequently, the average difference \bar{D}_k was computed for each subject k , Eq. 5.6.

$$\bar{D}_k = \frac{1}{n_k} \sum_{i=1}^{n_k} D_i \quad (5.6)$$

Where n_k is the number of pulses available for the k -th subject. Once obtained a representative value for each subject, they have been further averaged according to Eq. 5.7

$$\bar{\mu}_D = \frac{1}{M} \sum_{i=1}^M \bar{D}_k \quad (5.7)$$

M represents the number of subjects in the dataset.

Then the standard deviation $\bar{\sigma}_D$ has been computed according to Eq. 5.8

$$\bar{\sigma}_D = \sqrt{\frac{1}{M} \sum_{i=1}^M (D_i - \bar{\mu}_D)^2} \quad (5.8)$$

Combining Eq. 5.7 and Eq. 5.8 the intra subject variability (*intraSV*) is finally retrieved, Eq. 5.9

$$intraSV = \bar{\mu}_D \pm \bar{\sigma}_D \quad (5.9)$$

The second parameter defined for this purpose is inter-subject variability (*interSV*). This indicator assesses the variability of the values assumed by the amplitude and the slope in B1 and B2. It provides information on the variation of the features, in the mentioned points, on the carotid and femoral signals. The first executed step in the calculation of this parameter is the mean value \overline{feat}_k defined in Eq. 5.10

$$\overline{feat}_k = \frac{1}{n_k} \sum_{i=1}^{n_k} feat_i \quad feat = A, \gamma. \quad (5.10)$$

Where n_k is the number of pulses available for the k -th subject. The standard deviation σ_k for the k -th subject is computed according to Eq. 5.11

$$\sigma_k = \sqrt{\frac{1}{n_k} \sum_{i=1}^{n_k} (feat_i - \overline{feat_k})^2} \quad (5.11)$$

Similar to what was conducted with *intraSV*, the results obtained for each subject using Eq. 5.10 and Eq. 5.11 were combined to calculate representative values for the entire dataset using Eq. 5.12 and Eq. 5.13.

$$\bar{\mu} = \frac{1}{M} \sum_{i=1}^M \bar{\alpha}_k \quad (5.12)$$

$$\bar{\sigma} = \sqrt{\frac{\sum_{k=1}^M (n_k - 1) \sigma_k^2}{\sum_{k=1}^M (n_k) - M}} \quad (5.13)$$

Where M is the number of participants. Inter-subject variability (*interSV*), defined as Eq. 5.14, is reported below

$$interSV = \bar{\mu} \pm \bar{\sigma} \quad (5.14)$$

The coefficient of variation (*CV*) defined in Eq. (5.15), as the ratio between the average standard deviation $\bar{\sigma}$ and the mean value $\bar{\mu}$, has been used to compare the variability of the measurement respect to its mean value, in the mentioned points, using the extracted angles and the amplitude.

$$CV(\%) = \frac{\bar{\sigma}}{\bar{\mu}} \cdot 100 \quad (5.15)$$

Concerning the PWV estimation, each participant was evaluated through 3 acquisitions using the two available devices. The results obtained have been expressed in terms of mean value and standard deviation. The performance of the proposed algorithm has been evaluated by comparing the average PWV values with those obtained with the Athos system, the SphygmoCor, and the simple cross-correlation technique (i.e. applied without carrying out the steps to select the processing window previously described). The Pearson correlation coefficient and the paired *t*-test analysis have been used to assess the relationship between the available PWV values. Furthermore, a linear regressive model has been used to quantify the concordance of the measurements and its goodness evaluated through the determination coefficient R^2 . Measurement accuracy was assessed by calculating the mean value, standard deviation, and root mean square error (RMSE) of the difference between the reference method and the method to be tested. The concordance of the measurements with the reference device was examined employing the Bland-Altman plot, and the significance of the data was evaluated by setting $P < 0.05$. Regarding the application of the proposed algorithm w.r.t the IT, both approaches were applied to the noisy pulse wave signals; the resulting PWV values were compared to

Table 5.1: Indicators employed in the processing window’s upper boundary assessment

Feature	Indicator	B1		B2	
		CAR	FEM	CAR	FEM
Slope	CV (%)	4.3	5.4	22.9	18.8
	interSV (DEG)	73.10 ± 3.14	71.80 ± 3.88	43.04 ± 9.84	40.21 ± 7.52
	intraSV (DEG)	6.22 ± 3.14		14.87 ± 7.15	
Amplitude	CV (%)	19.9	19.8	20.5	24.8
	interSV (μV)	51.53 ± 10.22	51.81 ± 10.24	110.11 ± 22.51	110.60 ± 27.73
	intraSV (μV)	19.59 ± 12.01		41.89 ± 25.53	

Abbreviations: CV; coefficient of variation, interSV; inter-subject variability, intraSV; intra subject variability.

those obtained with those derived from the application of IT and RBCC on noise-free signals. Specifically, the absolute error for the i -th subject, w.r.t the noise-free cfPWV, was computed as follows:

$$error [i]_{\alpha, \beta} = \left| cfPWV [i]_{\alpha, \beta} - cfPWV [i]_{\alpha, noise\ free} \right| \quad (5.16)$$

Where $cfPWV [i]_{\alpha, \beta}$ refers to the cfPWV value for the i -th subject according to tested method ($\alpha \in \{RBCC, IT\}$) and β to the related SNR value ($\beta \in \{10\text{ dB}, 15\text{ dB}, 20\text{ dB}, 25\text{ dB}\}$). Then, the mean absolute error was computed for each SNR for the two algorithms. The multi-sample non-parametric Friedman test [173, 179] was employed to assess the statistical significance of the observed errors for IT and RBCC, paired according to the tested SNRs (e.g. $error_{IT, 10\text{ dB}}$ with $error_{RBCC, 10\text{ dB}}$ etc.) for a total of four tests (i.e. one for each SNR value). The significance of the identified variations was determined by establishing a threshold at $P < 0.05$.

5.3 Results

5.3.1 Processing Window Assessment

In the prior section, three different indicators have been employed to define the correct feature to identify the best location on signals. The *CV* indicator was used to determine whether to select the slope or the amplitude as the parameter to define the processing window’s upper boundary. The *intraSV* was used to quantify the consistency of the tested points within each subject. Finally, *interSV* was employed to assess the stability of those across the entire dataset. Table 5.1 reports the CV indicator computed in B1 and B2 for each feature on each acquisition site. For

Table 5.2: Clinical characteristics of the study population

Characteristics	$\mu \pm \sigma$	Range
Number of subjects	75	-
Number of acquisitions	3	-
Number of pulses per acquisition	-	5-14
Total number of pulses	2128	-
Male	43 (57.3%)	-
Age (years)	46 ± 17	19-82
Height (cm)	170.5 ± 10.57	153-195
Weight (Kg)	68.84 ± 14.07	45-106
BMI (Kg m ⁻²)	23.56 ± 3.72	17.8-37.11
SBP (mmHg)	117.88 ± 11.53	93-147
DBP (mmHg)	72.89 ± 8	59-94
HR (bpm)	64.44 ± 10.24	41-90

Abbreviations: μ , mean value; σ , standard deviation; BMI, body mass index; SBP, systolic blood pressure; DBP, diastolic blood pressure; HR, heart rate; bpm, beats per minute.

the slope γ , CV is equal to 4.3% and 5.4% in B1 and 22.9% and 18.8% in B2. Concerning the amplitude value, CV results are equivalent to 19.9% and 19.8% in B1 and 20.5% and 24.8% in B2. Table 5.1 also shows the outcomes of the *intraSV* and *intraSV* used to define the extreme point of the window. For the carotid site, *interSV* results to be equal to $73.10 \pm 3.14^\circ$ in the first point and $43.04 \pm 9.84^\circ$ for the second. For the femoral site, however, *interSV* takes a value of $71.80 \pm 3.88^\circ$ in B1 and $40.2 \pm 7.5^\circ$ in B2. The analysis of the *intraSV* reports an average difference value of $6.22 \pm 3.10^\circ$ for the first case and $14.87 \pm 7.15^\circ$ for the second. Both indicators were utilized to evaluate the stability of the tested points. *IntraSV* specifically examined the variability within data from the same subject, while *inerSV* was computed to observe variations across different subjects.

5.3.2 Pulse Wave Velocity Assessment

Table 5.2 displays the clinical features of the participants who were enrolled in the study. Of the 75 healthy subjects recruited, 43 (57.3%) were men. The average age of the population was 46 ± 17 years, distributed heterogeneously between 19 and 82 years old. The comparison results between the IT method used by the Athos device, the proposed algorithm RBCC, and the direct application of the cross-correlation technique to the signal epochs (DCC) are presented in Table 5.3. The comparison is performed in relation to the SphygmoCor device. The results obtained show a high correlation between the PWV values obtained in two out

Table 5.3: Accuracy of cfPWV estimated values compared to those extracted by the reference method (SphygmoCor).

Method	$\mu^* \pm \sigma$ (m s ⁻¹)	RMSE (m s ⁻¹)	r	R^2
Intersecting Tangent	-0.07 ± 0.52	0.52	0.97	0.93
Region Based Cross-Correlation	0.16 ± 0.54	0.57	0.96	0.92
Direct Cross-Correlation	-1.04 ± 2.21	2.44	0.82	0.64

Abbreviations: RMSE; root mean square error, r ; Pearson’s correlation coefficient, R^2 ; determination coefficient

*Difference of cfPWV estimated values compared to those extracted by the reference device, SphygmoCor.

of three cases. The Pearson’s coefficient retrieved in the three cases is equal to 0.97, 0.96 and 0.82, respectively for IT, RBCC and DCC. The determination coefficient R^2 , used to assess how well the regression predictions approximate the real data points, is 0.93, 0.2 and 0.64, revealing the poorer performance of the cross correlation approach when compared to the other methods. The average difference $\pm 2\sigma$ calculated concerning the PWV values estimated by the SphygmoCor and shown in the Bland-Altman plot is -0.07 ± 0.52 m/s for IT, 0.16 ± 0.54 m/s for the RBCC and -1.04 ± 2.21 m/s for the cross-correlation (DCC). The Athos device shows the lowest bias (absolute mean difference) and standard deviation values of the tested methods while the cross-correlation technique represents the worst case for all indicators seen so far. A similar condition occurs for the RMSE it is 0.52 for the first method, 0.57 for the second and 2.44 for the third. Figure 5.6 shows the performance of RBCC and IT algorithms when applied on carotid and femoral pulse waveforms corrupted by different levels of noise. The mean absolute error computed w.r.t the PWV values derived from noise-free signals reveals the poor noise tolerance of the IT method despite the tested SNR. Across all four tested cases, the RBCC algorithm exhibited greater robustness to the introduced noise, demonstrating a lower mean difference along with the associated standard deviation. The statistical analysis, conducted through the Friedman test, consistently yielded $P < 0.05$ in all tested cases when comparing cfPWV absolute differences for each noise level. Three out of four cases (15 dB, 20 dB, and 25 dB) values largely below 0.01. The only exception lies for the test with an SNR of 10 dB, where the resulting P value was still below 0.05. Nevertheless, despite the increased error and associated standard deviation observed in this instance, all these findings testify the existence of significant differences between cfPWV values derived from the application of IT and RBCC across different noise levels.

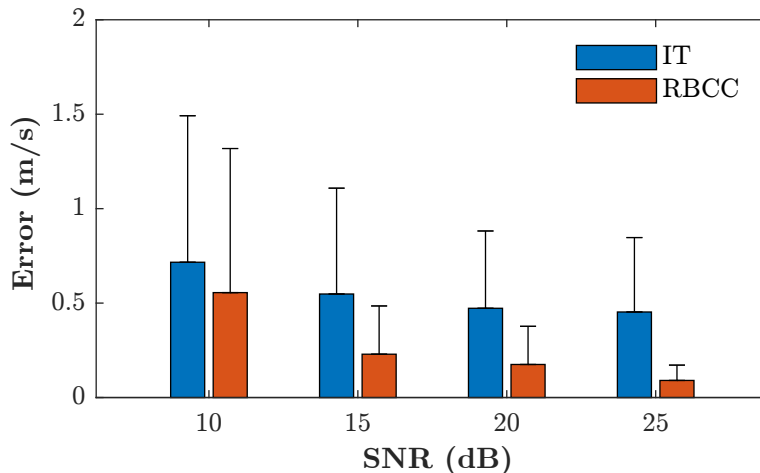


Figure 5.6: Mean absolute error and related standard deviation associated to cfPWV values computed at different SNRs with respect to those obtained using Intersecting Tangent (IT) and Region Based Cross Correlation (RBCC) on noise-free signals

5.4 Discussion

5.4.1 Processing Window Assessment

Within this study, a particular focus is given to the methodology used to identify a signal window that enhances the algorithm's performance. The literature suggests that the ascending part of the systolic peak is least affected by motion artifacts and reflection phenomena near vessel branches [74, 176, 177, 178]. As a result, the minimum point before the systolic peak was chosen as the lower boundary of the processing window. Furthermore, it limited the study of the upper boundary to the aforementioned points B1 and B2. The amplitude and the slope are the features used to characterize points B1 and B2 on every pulse for each of the 75 subjects.

Figure 5.7 shows the CV indicator computed in B1 and B2 for each feature on the carotid site (blue) and femoral site (red). Figure 5.7.(a) shows that the CV takes on values that are equivalent to 4.3% and 5.4% in B1 and 22.9% and 18.8% in B2 when applied to γ . In the second case, Figure 5.7.(b), CV is equal to 19.9% and 19.8% in B1 and 20.5% and 24.8% in B2 for amplitude values. B1 displays lower CV values than B2, indicating it as the location with less variability. A small value of CV is indicative of greater stability of the identified pulse section over the entire dataset. This is important because although there are intra and inter-subject differences, the chosen portion of the signal maximizes the efficiency of the realignment performed through the proposed approach while preserving the information of interest. In addition, the values of point B1 and point B2 differ more in the bar plot, considering the slope with respect to the one considering the

amplitude, where the values are comparable. This mismatch may be due to the pressure produced by the operators during acquisitions, resulting in differing signal amplitude values. Consequently, it can be concluded that γ allows a more precise distinction between B1 and B2 when determining the processing window's upper limit. Figures 5.8.(a) and 5.8.(b) depict the computed *intraSV* and *interSV* for the slope γ . Both indicators confirm B1 as the most stable point. In particular, the *intraSV* shows an average difference between the carotid and femoral angles of $6.22 \pm 3.10^\circ$ in B1 compared with $14.87 \pm 7.15^\circ$ in B2, indicating a smaller difference between the two waves at the two sites in the former case. Respectively for B1 and B2, Figure 5.8.(b) indicates for the carotid site (blue) a *interSV* of $73.10 \pm 3.14^\circ$ and $43.04 \pm 9.84^\circ$. At the femoral site (red), it is equal to $71.80 \pm 3.88^\circ$ in the first point and $40.21 \pm 7.52^\circ$ in the second. The average value is higher in B1 because, by definition, it represents the point of the maximal signal slope. In comparison, the standard deviation for the same location at the carotid and femoral sites is lower, indicating less variability in terms of slope among the 75 patients in the dataset. In view of the carried-out analysis, B1 proved to be the most stable point to be used for the application of the algorithm.

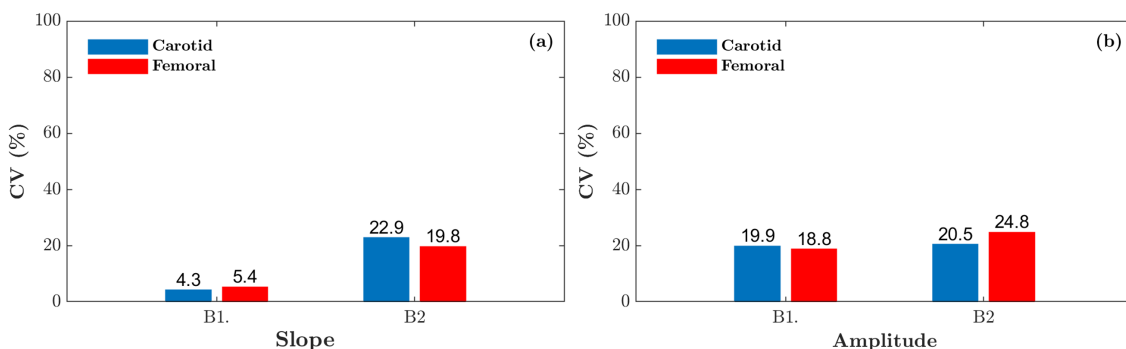


Figure 5.7: Percentage coefficient of variation CV computed respectively in B1 and B2, on carotid (blue) and femoral (red) pulses. (a) CV extracted for the slope γ . (b) CV extracted for amplitude values.

5.4.2 Pulse Wave Velocity Assessment

Given the results reported in Table 5.3, it is possible to assume that the proposed algorithm is a viable option to provide a reliable assessment of cfPWV. The objective of the comparison was to assess the proposed approach in relation to the technique utilized by the clinical gold standard used for non-invasive PWV assessment. The statistic indicators reported in the previous section determine the algorithm adopted by the Athos device (i.e., IT) as the best of the tested approaches. This result is attributable to the method adopted by the two devices. Both Athos and SphygmoCor use the intersecting tangent point as the algorithm

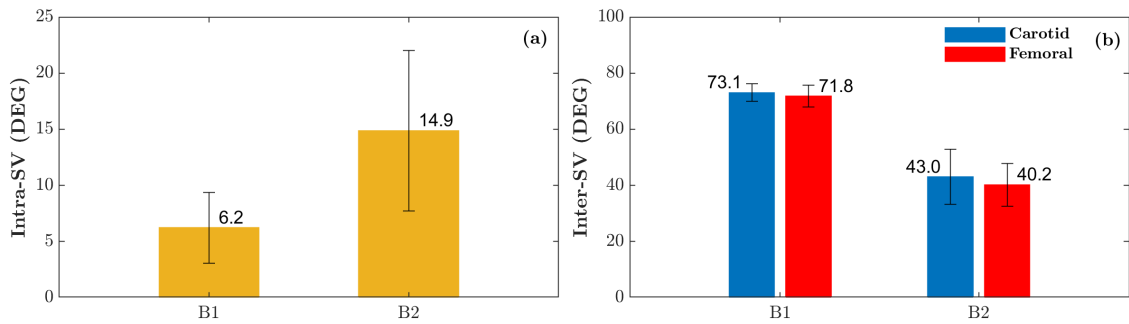


Figure 5.8: (a) Intra-Subject Variability computed for γ respectively in B1 and B2. (b) Inter-Subject Variability computed for γ , respectively in B1 and B2, on carotid (blue) and femoral (red) pulses.

for the estimation of PWV. In particular, Figure 5.9.(a) illustrates the outcomes of the linear regression model applied to the PWV values obtained from the Athos device in comparison to the Sphygmocor, exhibiting an R^2 value of 0.93. On the other hand, Figure 5.9.(b) depicts the concordance between the two methods in terms of mean value and average difference across the measurements. In this case, the Bland-Altman plot demonstrates an average difference, or bias, of -0.07 m/s for cfPWV values, along with narrow limits of agreement (LOA) values of 0.96 and -1.1 . In contrast, the comparison between the DCC technique and SphygmoCor gave the worst results. The application of this approach, without the previously mentioned processing phases, was utilized to establish a starting point for evaluating the performance of the suggested method. In this case, the mean difference, the standard deviation, and the RMSE reached their highest values, -1.04 ± 2.21 m/s and 2.43 m/s respectively, while the Pearson correlation coefficient and the coefficient of determination R^2 were equal to 0.82 and 0.64, Figure 5.10.(a). The reason for these results is the different morphology of the pulse wave when the proximal and distal sites are far apart confirming why this technique was applied just for a local evaluation of PWV. The lack of agreement of these two methods is also reflected in Figure 5.10.(b). Specifically, the systematic bias equal to -1.04 m/s along with a wider distribution of points and limits of agreement values respectively equal to 3.15 and -5.24 due to the presence of outliers in the PWV values. However, part of them was not included in Figure 5.10.(b) to keep the consistent scale on the y-axis along the three cases. The restriction of the comparison section combined with the normalization of the latter has made it possible to obtain a signal with a known shape while keeping the temporal information intact. In line with the previous cases, Figure 5.11 represents the linear regression model and the corresponding (Bland-Altman) plot. In this latter case, there is an improvement in all the presented statistical indicators. In particular, the bias is 0.16 while the R^2 and the r are respectively equal to 0.92 and 0.96. These values demonstrate a strong relationship between the predicted and observed values, indicating an excellent level

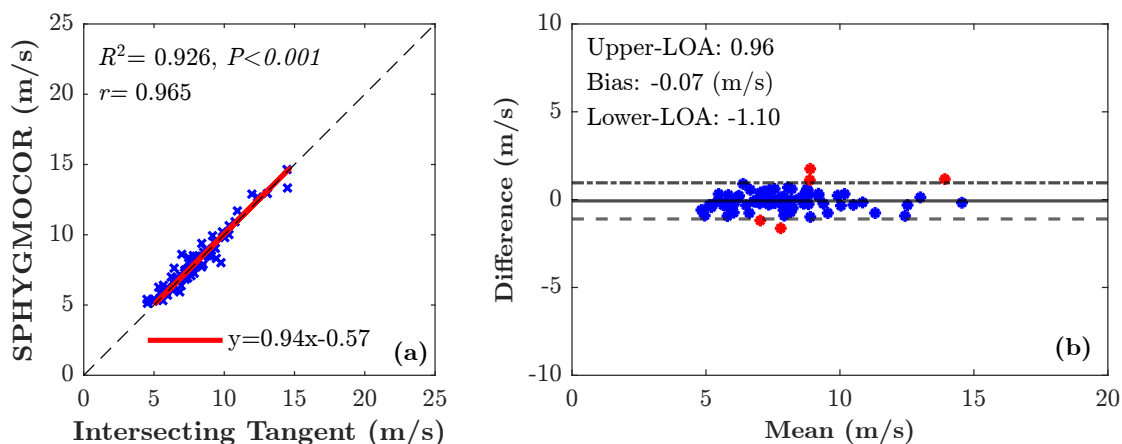


Figure 5.9: Relationship between cfPWV estimated by the Intersecting Tangent algorithm used by the Athos device and the reference method. (a) Best fitted line (in red) retrieved from the linear regressive model fitted on the experimental data. (b) Bland-Altman plots show the distribution of the averaged measurements differences.

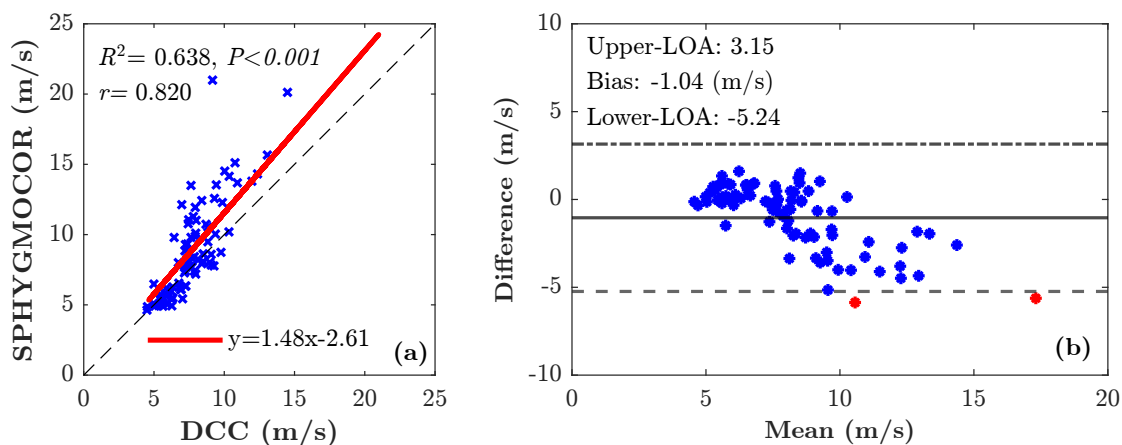


Figure 5.10: Relationship between cfPWV estimated by the Direct application of Cross-Correlation (DCC) approach and the reference method. (a) Best fitted line (in red) retrieved from the linear regressive model fitted on the experimental data. (b) Bland-Altman plots show the distribution of the averaged measurements differences.

of accuracy and agreement in the model's performance according to the performance criteria stated in the 2010 ARTERY Society guidelines [53] (mean difference < 0.5 m/s and SD < 0.8 m/s). From the comparison between the IT method and RBCC, it is possible to notice that the only substantial difference concerning the best case occurs for the average difference of the PWV values equal to -0.07 m/s

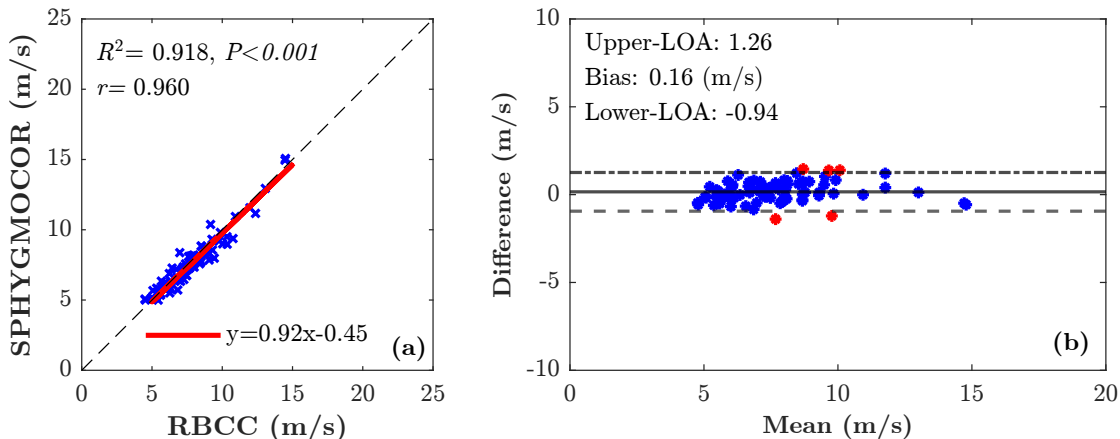


Figure 5.11: Relationship between cfPWV estimated by the Region Based Cross-Correlation (RBCC) algorithm and the reference method. (a) Best fitted line (in red) retrieved from the linear regressive model fitted on the experimental data. (b) Bland-Altman plots show the distribution of the averaged measurements differences.

and 0.16 m/s respectively. The RMSE in the two cases presents a difference of less than 10%, while the standard deviation of the measurements mean difference, the Pearson correlation coefficient and the coefficient of determination R^2 present an average difference of less than 1%. The analysis conducted to determine the algorithm’s robustness in the presence of different noise levels highlighted the greater tolerance of the latter compared to the IT method. Statistical significance was established using the Friedman test, which assessed the differences in cfPWV values between IT and RBCC across the four noise levels. In all tested cases, the P value consistently remained below 0.05, with three values well below 0.001 (10^{-5} , 10^{-8} , and 10^{-8} , respectively, for 15, 20, and 25 dB). The exception occurred with an SNR of 10 dB where P resulted equal to 0.04. This outcome aligns with comparable values of mean absolute error and standard deviation reported in Figure 5.6. In addition, it is necessary to consider that 10 dB represents a limiting case, which might not be suitable for a clinical application. Findings in [180] reveal an inverse relationship between RMSE and SNR at a constant sampling frequency, underscoring the substantial impact of SNR on estimation error. Furthermore, in [181], 15 dB was identified as the SNR value below which all the compared algorithms for peak detection showed a performance decline exceeding 20%. Finally, it is crucial to acknowledge that the acquisition process relies on a skilled operator who would reject a signal displaying distorted morphology. However, in all the remaining comparisons, the proposed method exhibited significantly reduced mean absolute error in the evaluation of the individual’s PWV compared to the reference values derived

from noise-free signals. This result highlights the impact of relying on a single feature in the signal for PTT assessment, indicating that errors in estimating PWV can be significant when detection is potentially affected by the presence of noise or artifacts. Furthermore, the assessment of PTT based on the realignment of pulse's upslope, and therefore for a higher number of data points, allows for mitigating a potential misdetection of points A or B in favor of a more robust and still accurate PWV assessment. Thus, although the RBCC method performs slightly differently from the intersecting tangent method, it turned out to be an excellent and more robust method to be used to estimate PWV. Furthermore, compared to the standard application of the cross-correlation approach, it was proved that through the reported processing steps it is possible to overcome the limitations responsible for the application of this technique to perform a local estimation of PWV. Our proposed approach's primary limitation stems from excluding non-healthy subjects during the validation process. This omission is noteworthy because non-healthy subjects are more likely to exhibit alterations in cfPWV associated with irregular vascular compliance and the potential impact of vasoactive medications. Regrettably, the ethical approval granted for this study imposes restrictions on testing the proposed algorithm exclusively on healthy subjects, as the use of the Athos device is authorized solely within the context of healthy individuals. In future endeavors, the developed device's validation will be extended to include non-healthy subjects to verify the applicability and robustness of RBCC across a broader spectrum of health conditions.

A second limitation of the proposed approach could be represented by the computational cost incurred by the cross-correlation process when comparing two windows on pulse waveforms to estimate cfPWV using a single feature. Nevertheless, it is crucial to note that the primary objective of this study is to explore the feasibility of the proposed algorithm for an offline assessment of cfPWV. The current focus is on the algorithm's performance in a non-real-time setting. Therefore, the optimization of the RBCC method for a real-time application will be further investigated in future works.

5.5 Conclusions

In this chapter, a novel method for calculating cfPWV was presented. The PTT is determined by computing the correlation between a specific portion of the signals, eliminating the requirement to identify characteristic points often utilized for this purpose. Particular attention was paid to finding an indicator that could be used to define the window on the signal. Thanks to the slope analysis, it was possible to locate the target section between the early systolic and end-diastolic portions of the blood pulses. Hence, by reducing the pulse wave section utilized for PWV assessment, we have developed an algorithm that yields results comparable to the

gold standard employed in clinical practice. The proposed approach demonstrated that it is feasible to overcome the inherent limitation of the direct application of cross-correlation, which restricted its use in this sector to a local estimation. Moreover, for various SNRs, the RBCC algorithm was more robust than the IT method when applied to carotid and femoral pulse waveforms. Thus confirming the capability of the proposed approach to provide a non-invasive assessment of cfPWV in different conditions accurately and robustly. In conclusion, it was possible to prove that the RBCC algorithm is a suitable solution for assessing the cfPWV, and it has the potential to be used in clinical practice as an alternative method to *foot-to-foot* algorithms.

Chapter 6

Innovations in Personalized Machine Learning for Cuffless Blood Pressure Monitoring and Motion Artifact Detection

This chapter contains parts that have been taken, or partially rephrased, from a previously published work [65, 71].

The research activities described in this thesis were conducted in collaboration with the Wireless Sensors Network (WSN) Group at the Tyndall National Institute (University College of Cork).

This chapter delves into the intricate process of developing and deploying a custom device designed for real-time pulse transit time measurement, specifically tailored for application on the elbow and thumb. The initial section introduces the design and realization of this innovative device, highlighting its functionality and potential for continuous health monitoring.

Following the device introduction, the chapter progresses to discuss the implementation of a personalized model aimed at detecting BP variations. This model leverages data collected using the custom device to accurately monitor changes associated with physical or cognitive workloads, thereby offering insights into the body's response to various stressors.

Finally, the chapter addresses a personalized approach for detecting motion artifacts (MAs) within PPG time series data. By refining the accuracy of PPG signal analysis, this approach enhances the reliability of health monitoring systems, particularly in dynamic and real-world settings where MAs are prevalent.

6.1 Development of a custom PPG acquisition system for real-time estimation of PTT

The following section provides a comprehensive overview of the proposed system, detailing both its hardware and software components. Initially, a detailed description of the system's architecture is presented, encompassing the sensors, signal processing units, and software algorithms utilized for data analysis. Subsequently, the data capture procedure is explained, highlighting the steps taken to ensure accuracy and reliability. Additionally, the reference device employed to validate the system is outlined, ensuring that the comparative analysis is grounded in established standards. Finally, the results of the system assessment are presented, along with an analysis of the agreement with the reference device. This structured approach aims to offer a clear understanding of the system's performance and its potential applications in the field of continuous, non-invasive pulse transit time assessment finalized to BP monitoring.

6.1.1 The Hardware

In this work, PPG sensors were used to assess variations in blood volume between the brachial artery and the thumb. To retrieve a good quality PPG signal from the brachial artery, brighter LEDs and more sensitive photodiodes have been employed compared to the conventional wrist-based PPG sensors. A PPG sensor includes DAC LED drivers (AFE), ADC Photodiode (PD) signal acquisition, LEDs, Photodiodes (PDs), and an optional ambient light cancellation (ALC). Because of their size, power consumption, and adaptability, integrated PPG sensors are more suited for wearable applications. Among the types of integrated PPG sensors available in the market, an integrated sensor which allows for connection with external LEDs and photodiodes (PDs) has been selected for our purpose. The MAX86141 (Maxim Integrated, San Jose, USA) from Maxim Integrated was chosen as the PPG sensor after analyzing all constraints as size, power consumption, adaptability, and availability.

The MAX86141 is an ultra-low power, fully integrated optical data acquisition system [182]. On the transmitter side, it has three programmable high-current LED drivers, and on the receiver side, it has two optical readout channels that can operate simultaneously. The device includes a low noise signal conditioning analog front-end (AFE) with a 19-bit ADC and an ambient light cancellation (ALC) circuit. The MAX86141 can carry out sampling at frequencies of up to 4096 samples per second. For our application, the sampling rate was set at 500 Hz to allow real-time data processing while ensuring an adequate time resolution (2 ms). Due to the limited number of studies on the penetration of light within the body when used for obtaining PPG from the brachial artery, the initial prototype employs LEDs of varying wavelengths to define the optimum wavelength to be used. The SFH

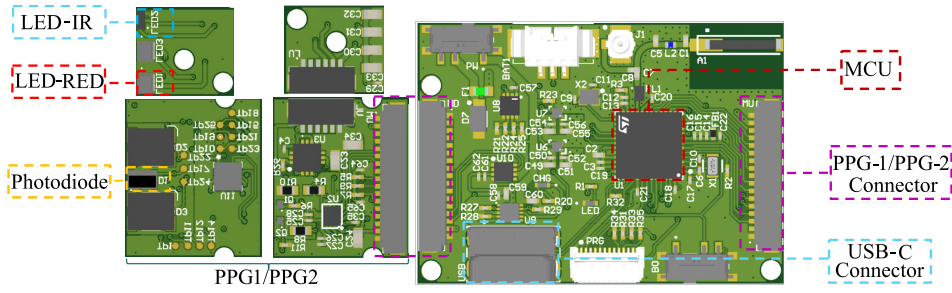


Figure 6.1: System employed to collect PPG raw data from the selected sites, elbow (brachial artery) and thumb (digital artery).

7015 [183] (Osram Licht AG, Munich, Germany) contains a hyper red LED and a 940nm infrared LED along with a Green LED CT DBLP31.12 [184] (Osram Licht AG, Munich, Germany) were also used. Up to two external photodiodes can be connected to MAX86141. According to the selected LEDs, at least one of them should be capable of receiving infrared light under a variety of conditions. In this regard, VEMD5080X01 [185] (Vishay Intertechnology Inc., Malvern, USA) from Vishay has been chosen to receive IR and red light. Vishay’s VEMD5510CF [186] and Osram’s SFH 2713 [187] contain IR cut filters and can pass light up to 670nm, hence they can only be used with green LEDs. The system employs an ultra-low power consumption microcontroller capable of simultaneously handling real-time sensor reading along with data transfer to the dedicated graphical user interface. STM32WB55CGU6 [188] (STMicroelectronics, Geneva, Switzerland) is a dual-core, multi-protocol, and ultra-low-power 2.4 GHz MCU system-on-chip developed by ST Microelectronics. This device is meant to be exceptionally low-power, with a high-performance Arm® Cortex®-M4 32-bit core working at up to 64 MHz. The entire system is powered by one of the available 5V COM-Ports on the laptop that is used to run the software responsible for the PTT assessment. A USB-C cable is used to power and control the device, allowing reliable data transmission. Two LDO regulators from the NCP170 [189] (ON Semiconductor, Phoenix, USA) family of ON Semiconductor have been employed to provide the correct working supply voltage required by all the components belonging to the system. This LDO family drop-out voltage is 170mV, and the quiescent current for the NCP170 series is very low. The reduced dimensions of the selected packaging XDFN4 (1mm x 1mm), make this family ideal for wearable applications. NCP170AMX190TCG generates 1.9V, which keeps enough margin from the maximum and minimum supply voltages of all components. Another regulator is NCP170AMX310TCG, which generates 3.1V, and the main reason for having this is to provide the supply voltage for LEDs and LED drivers of PPG sensors.

6.1.2 Mechanical Design to Control the Contact Pressure

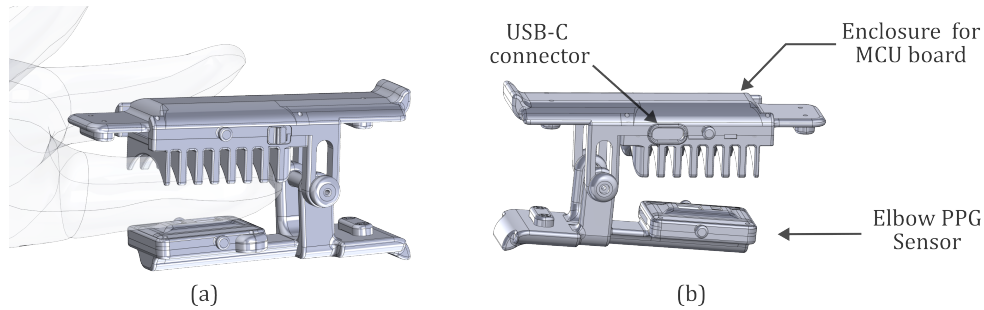


Figure 6.2: Thumb sensor employed to detect pulse waveform from the digital artery. (a) Sensor’s enclosure positioned on the hand of the subject under investigation. (b) Finger clip enclosure for the thumb sensor.

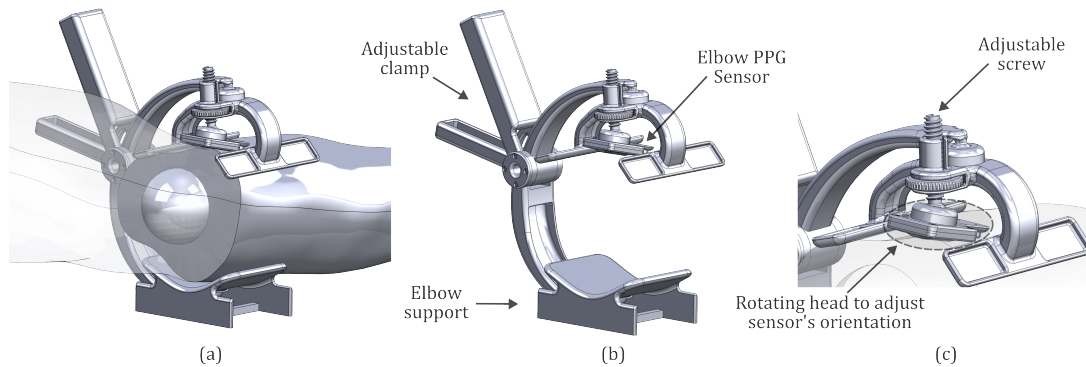


Figure 6.3: Elbow sensor employed to detect pulse waveform from the brachial artery. (a) Sensor’s enclosure positioned on the elbow of the subject under investigation. (b) Elbow sensor enclosure for the thumb sensor. (c) Adjustable screw and rotating head to adjust the sensor’s orientation.

During the creation of the proposed device, Figure 6.2 and Figure 6.3, the design of the enclosures housing the hardware described in the preceding section was given careful consideration. The enclosures were designed to guarantee that the sensor adheres to the sample site, applying steady pressure and avoiding the presence of the operator to keep it in its position. This feature enables the user to reproduce the acquisition setup for a particular subject, hence improving measurement reproducibility. Figure 6.2.(a) and Figure 6.3.(a) depict both the fabricated supports and their placement on the subject’s body during data collection. The thumb-mounted holder, Figure 6.2.(b), resembles the design of a standard pulse oximeter. The presence of an elastic spring allows the sensor to adhere to the finger during its usage. Figure 6.3.(b) shows the sensor holder positioned on the elbow.



Figure 6.4: Graphic User Interface used by the device in the BP assessment. The upper plots show the thumb signal (red) and elbow signal (blue). Bottom plots depict the intersecting tangent being extracted from gathered signals for PTT estimation.

The side structure allows the operator to adjust the pressure exerted on the arm making it steady during the data acquisition process as recommended in [95, 190], Figure 6.3.(c). Through a graduated scale, it is possible to note the opening set for each subject. The sensor has been placed in the upper section of the holder. As shown in Figure 6.3.(c), the location of the latter can be modified vertically using a rotating wheel while the sensor’s orientation relative to the vessel can be adjusted using a spherical head that permits sensor rotation. All the enclosures presented have been designed using the SolidWorks environment (Dassault Systèmes SE, Vélizy-Villacoublay France) and 3D printed using a Formlab 3 printer (Formlabs, Somerville, USA).

6.1.3 The Algorithm

The datasets gathered by the system, stored in synchronized buffers, are sent through a USB cable connection to the laptop running the algorithm used for real-time processing. Using one of the COM ports available on the workstation, the GUI can receive, visualise and manage the data transferred by the device. Real-time acquisition, display of samples and PTT computation are made possible thanks to a multi-thread process involving two buffers, named respectively acquisition buffer and processing buffer.

The GUI is divided into four different plots and a separate box showing the real-time update of the computed features Figure 6.4. The first two plots are used to display the acquired signals, while the last two depict the result of the application of the algorithm used to compute the PTT on each pulse. This feature is later used to compute the systolic blood pressure (SBP), the diastolic blood pressure (DBP), and heart rate (HR) in a 6 seconds window. The user interface allows the user to store the collected raw data and extracted features in a separate file for later study. The aim of the algorithm employed by the developed system is the extraction of a characteristic that detects the passage of the pulse throughout each cardiac cycle. Specifically, among the several foot-to-foot algorithms reported in the literature, the intersecting tangent method has been chosen for our purpose since it has been shown to be the most reliable method for PTT estimation [139]. This technique consists of the detection of the intersection between the horizontal line passing through the minimum that precedes the systolic peak and the tangent line to the ascending part of the signal. The application of several filter steps to remove the DC-bias and the high-frequency noise affecting the signal. To accomplish this, a 4th-order Chebyshev II band-pass filter with cut-off frequencies ranging from 0.5 to 10 Hz was used to process the data. The phase distortion introduced by the usage of the filter was removed by applying the filter twice through forward-backward filtering. The steps constituting the algorithm used to extract the PTT, Figure 6.5, from the collected signals are reported in detail below.

- i)* Firstly, the collected signal is separated into epochs of similar length, with a duration of 6 seconds (e.g., 3000 samples @500Hz). According to the subject's heart rate, a range of 4-10 pulses at a frequency between 40 and 100 bpm is expected.
- ii)* The signal is filtered with a Chebyshev II band-pass filter of the 4th order with cut-off frequencies of 0.3 and 10 Hz to remove DC offset and high-frequency noise from the signal [32].
- iii)* Following the pre-processing steps, the analysis of the current window's pulses begins. Firstly, the first derivative of the signal is calculated and then, using two dynamic thresholds, the peaks associated with each pulse are recognized.
- iv)* The first threshold (*trh-1*) is computed by averaging the positive points within the first derivative of the signal across the entire window.
- v)* Later, the second threshold (*trh-2*) is determined by averaging the points detected above *trh-1* in the preceding stage. A peak is localized inside the window when a minimum number of samples above *thr-2* are observed. The sample with the largest amplitude is chosen as the local maximum of the first derivative for each pulse. It is then employed to construct the tangent line to each pulse used in defining the intersecting tangent point.

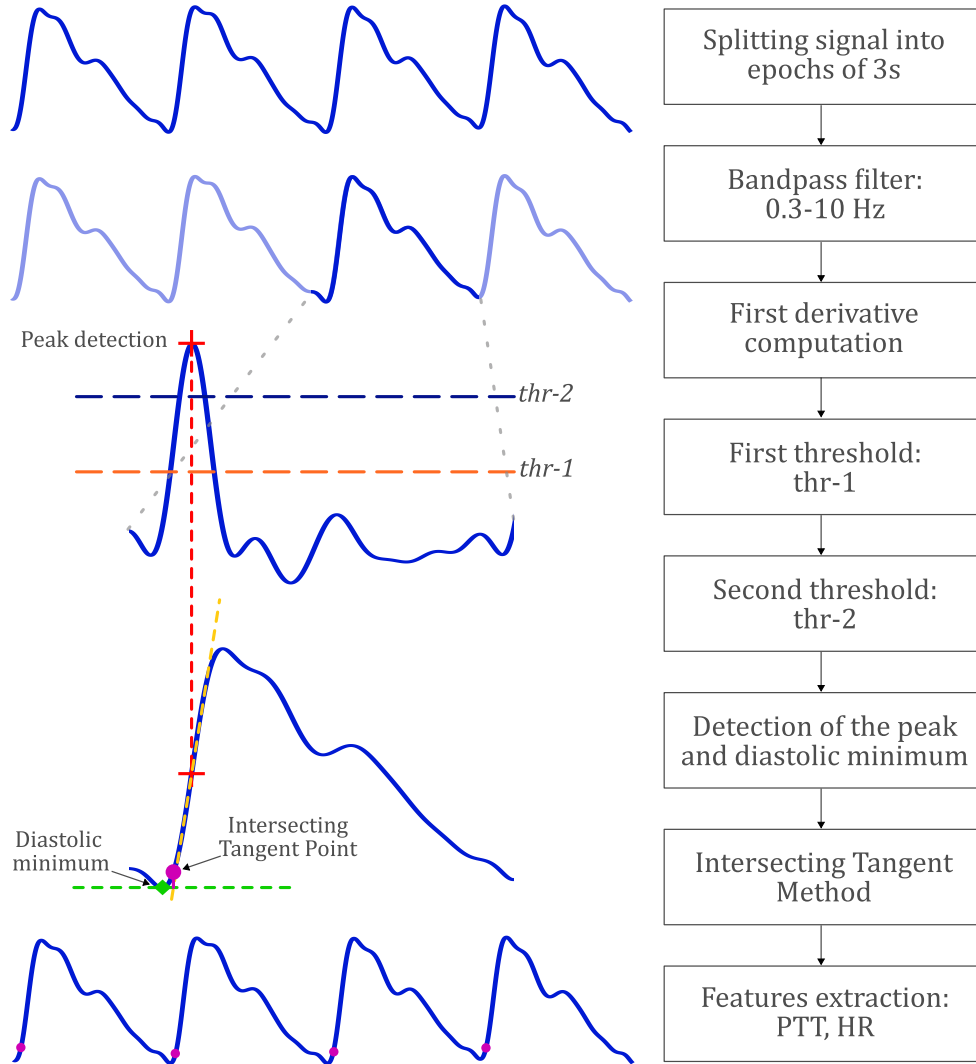


Figure 6.5: Flowchart of the algorithm implemented to detect the intersecting tangent point (ITP).

- vi)* For every pulse, the end of the diastolic phase was determined on the original signal by detecting the zero-derivative point before the maximum on the first derivative. The horizontal line passing through the minimum preceding the ascending part of the systolic phase is used to compute the intersection of the two lines.
- vii)* Finally, the intersection of the two tangents marks the arrival of the pulse.
- viii)* The preceding stages are applied to signals collected from both the elbow and the thumb. Every crossing tangent point calculated is paired with its counterpart in the opposite window, and the PTT is computed as the delay

between these two locations. The average of each window’s retrieved PTT data is then used to calculate the BP readings according to the relationship reported in [191].

6.1.4 System for Validation: Biosignal Plux

The Biosignal Plux acquisition system was employed as the reference device in the validation process of the proposed system.

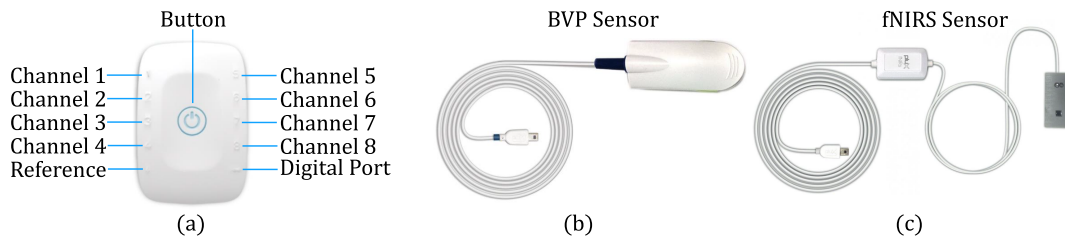


Figure 6.6: Biosignal Plux Acquisition system. (a) 8-channel Hub. (b) Blood Volume Pressure (BVP) sensor. (c) fNIRS sensor.

Table 6.1: Features of the Biosignal Plux 8-Channels hub [192].

Specifications	Description
Analog ports	8
Auxiliary ports	1 common ground; 1 digital I/O for accessories
Sampling rate	up to 3kHz per channel
Sampling resolution	8-bit or 16-bit per channel
Communication	Bluetooth class II (up to 10m in line of sight); USB
Battery	700 mAh 3.7V LiPo rechargeable
Hub size	54x85x10 mm
Weight	45 g

The biosignal Plux acquisition system consists of an 8-channel acquisition hub, a BVP sensor, and an fNIRS sensor, providing a comprehensive solution for simultaneously acquiring and analyzing multiple physiological signals. Here’s an overview of each component:

- **8-Channel Acquisition Hub:** The 8-channel acquisition hub serves as the central data acquisition device in the system [192]. It collects and digitizes all signals from the sensors and accessories and transmits them via Bluetooth to the computer, where they are recorded and visualized in real-time. The channels support up to 16-bit resolution and 3000Hz sampling frequency per channel (i.e. up to 8 channels with 3000 16-bit samples per channel per

Table 6.2: Features of the Biosignal Plux BVP sensor [193].

Specifications	Description
Operating wavelength	670 nm (red band)
Operating principle	Transmittance
Communication	SPI
Consumption	4.8 mA
Bandwidth	0.02-2.1 Hz
Size	10x18x4 mm

Table 6.3: Features of the Biosignal Plux fNIRS sensor [194].

Specifications	Description
Peak emission	IR: 860 nm; RED: 660 nm
Spectral bandwidth	IR: 30 nm; RED: 25 nm
Half intensity beam angle	IR: + 13 deg; RED: +18 deg
Wavelength of max sensitivity*	850 nm
Range of sensitivity*	400-1100 nm
Radiant sensitive area*	7 mm ²
Dimension of radiant sensitive area*	2.65x2.65 mm ²
Resolution	16-bit
Sampling frequency	500 Hz
Communication	SPI

second, or 4000Hz sampling frequency per channel when using only up to 3 channels simultaneously.)

- BVP Sensor: The BVP (Blood Volume Pulse) sensor is designed to measure changes in blood volume in peripheral blood vessels, typically using a transmittance PPG sensor [193]. It detects variations in the amount of light absorbed by blood vessels, providing insights into cardiovascular activity, including heart rate, BP, and vascular reactivity. The BVP sensor is commonly used for monitoring physiological responses to stress, exercise, and emotional arousal. This BVP is an optical, non-invasive sensor that measures cardiovascular dynamics by detecting changes in the arterial translucency. When the heart pumps blood, the arteries become more opaque, allowing less light to pass from the emitter on the sensor to the receiver. The light emitter (red band - 670 nm) and receptor are encapsulated inside a plastic finger clip, designed to improve the signal-to-noise ratio by preventing other light sources from interacting with the photodiode surface.

- fNIRS Sensor: The fNIRS (functional Near-Infrared Spectroscopy) sensor utilizes near-infrared light to measure changes in blood oxygenation levels on the brachial artery [194]. By detecting alterations in hemoglobin concentration, fNIRS sensor allowed the detection of the arterial pulse propagating deeper in tissue.

6.1.5 System Assessment

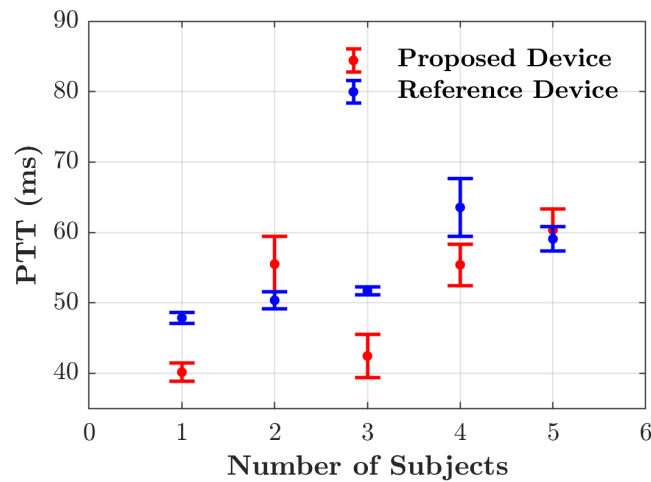


Figure 6.7: Averaged PTT values retrieved for the 5 subjects involved in the trial. Each point represents the mean value of the three acquisitions executed with both systems. The error bars report the standard deviation.

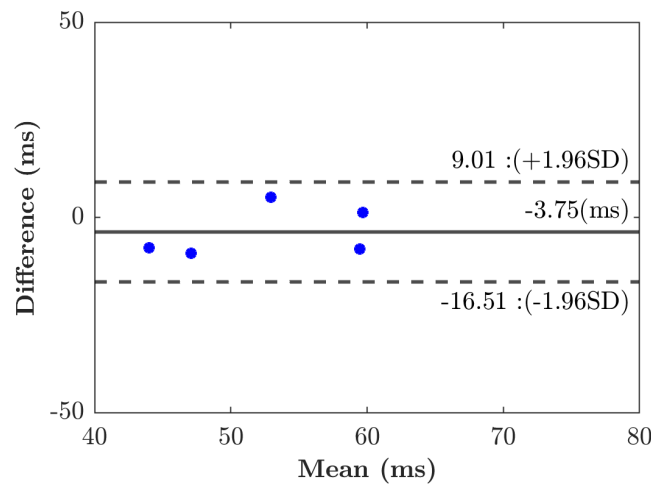


Figure 6.8: Bland-Altman plot of the differences between the outcomes retrieved by the reference device and the proposed device.

Table 6.4: Overview of the characteristics of the study population

Characteristics	$\mu \pm \sigma$.	Range
Number of subjects	5	-
Number of acquisitions	3	-
Male	2 (40%)	-
Age (years)	28 ± 3.27	23-32
Height (cm)	172.22 ± 6.8	164-180
Weight (kg)	66.61 ± 12.32	55-82
BMI (kg m ⁻²)	23.56 ± 3.72	17.81-37.11
SBP (mmHg)	108.71 ± 12.03	92-125
DBP (mmHg)	67.22 ± 8.24	56-84
HR (bpm)	-	52-74

Abbreviations: BMI, body mass index, SBP, systolic blood pressure, DBP, diastolic blood pressure, HR, heart rate, bpm, beats per minute, μ . mean value, σ , standard deviation

Table 6.5: System Assessment's Results

Subjects	Proposed Device	Reference Device
	$\mu \pm \sigma$	$\mu \pm \sigma$
SUB-1	40.15 ± 1.27	47.85 ± 0.79
SUB-2	55.50 ± 3.90	50.36 ± 1.18
SUB-3	42.45 ± 3.09	51.70 ± 0.52
SUB-4	55.40 ± 2.95	63.57 ± 4.13
SUB-5	60.33 ± 3.01	59.08 ± 1.72

Abbreviations: μ , mean value, σ , standard deviation.

A study was undertaken at the Tyndall National Institute in University College Cork (UCC), Ireland, for the evaluation of the developed device. In this experiment, which was approved by the UCC Clinical Research Ethics Committee of the Cork Teaching Hospitals, a comparison between the performance of the developed device with that of the Biosignal Flux acquisition system was carried out. As described, the developed device allows for the extraction of the raw data gathered by two PPG sensors applied on the previously mentioned sites, namely, the thumb and elbow. This trial included five volunteer individuals ranging from 23 to 30 years. Table 6.4 details the physiological parameters of the people involved. Each data collection was performed in a climate-controlled environment with a temperature set to 20°C.

Every individual was asked to refrain from smoking or consuming coffee 30 minutes before the session. After collecting the participant information, the subject

was requested to stay supine for 10 minutes to have hemodynamic conditions and vasomotor tone close to baseline level. The next step in gathering PTT data was to locate the two measurement sites so that they do not vary from the reference system to the proposed device. Finally, PTT measurements for each subject at rest were carried out for three consecutive one-minute data captures. Each acquisition was carried out when the patient was seated, with both feet on the floor and hands on the table at the same level as the heart of the subject. PTT values retrieved from the algorithm's real-time application were used for the system assessment. On the other side, the acquisitions gathered using the reference device were processed offline using the procedure described in the previous section. The final PTT values averaged across the three tests are shown in Figure 6.7 for all the participants; the error bars indicate the measurement dispersion. In Figure 6.8, the Bland-Altman plot is reported. The PTT mean difference is about -3.75 ± 3.64 ms $[-16.51 \ 9.01]$. Table 6.5 provides a summary of the average PTT values acquired by the two devices for each participant, as well as their respective standard deviations (σ). From these results, it is clear that the PTT measurements obtained by the proposed device are significantly equivalent to those obtained by the reference system. Moreover, assessing the standard deviation reveals that both systems involved have comparable repeatability.

6.2 Development of a personalized model to detect blood pressure variations associated with physical or cognitive workload

In this section, the previously introduced custom PPG acquisition system was employed to collect data from 31 healthy volunteer subjects. The aim is to investigate the factors influencing BP regulation under various conditions. The section begins with an overview of the data capture protocol and data processing pipeline, including a detailed description of the training strategies and evaluation metrics used to assess the performance of the machine learning model. Following this, the results from the data processing stage are presented, along with individual results for each subject in the dataset. A comprehensive discussion of the findings, including the limitations of the proposed analysis, is then provided.

6.2.1 Cognitive Tests

As will be discussed later in this section, a specific data collection protocol is implemented to accurately assess BP variations induced by both physical and cognitive tasks. To this end, it is essential to introduce the two cognitive tests selected to progressively stress each participant from a cognitive perspective. The

Stroop test [195] and the N-back [196] test were chosen to challenge the tested subjects using diverse visual and auditory stimuli, thereby inducing variations in blood pressure due to the action of the autonomous nervous system (ANS) [197].

Stroop Test

The Stroop Test is a psychological test used to measure a person's cognitive processing speed, attention, and ability to manage interference from conflicting information. It was named after John Ridley Stroop, who first published the test's findings in 1935. The test is widely used in cognitive psychology and neuroscience research to assess executive functions and selective attention.

In its classic form, the Stroop Test involves a set of color words (like "red," "blue," "green," etc.) displayed in different ink colors. The participant is asked to name the color of the ink rather than read the word itself (e.g., the word "red" might be printed in blue ink, and the task is to say "blue" rather than "red."). This creates a conflict between the word's meaning and the ink's color, requiring the participant to suppress the automatic tendency to read the word and instead focus on the ink's color. As shown in Figure 6.9.(a), the test typically has two main components:

- **Congruent Condition:** The word's color matches the word itself (e.g., "red" written in red ink). This condition provides a baseline for performance since there is no conflict.
- **Incongruent Condition:** The word's color differs from the word itself (e.g., "red" written in blue ink). This condition introduces interference and requires cognitive control to override the automatic reading response. The difference in response time and accuracy between these two conditions is often used as a measure of cognitive flexibility and executive function. The greater the delay or error rate in the incongruent condition, the more difficulty the individual has in managing conflicting information.

The Stroop Test has been used in various research contexts, including studies on attention, cognitive control, brain injuries, and neurological or psychiatric disorders. It is also commonly employed in neuropsychological assessments to evaluate attention-related impairments and executive function deficits.

N-Back Test

The N-Back Test is a cognitive task used to assess working memory, which is the ability to hold and manipulate information in the mind over short periods of time. It's a commonly used test in cognitive psychology and neuroscience to study memory, attention, and executive function. The N-back task involves the serial presentation of a stimulus (e.g., a shape) spaced several seconds apart. The

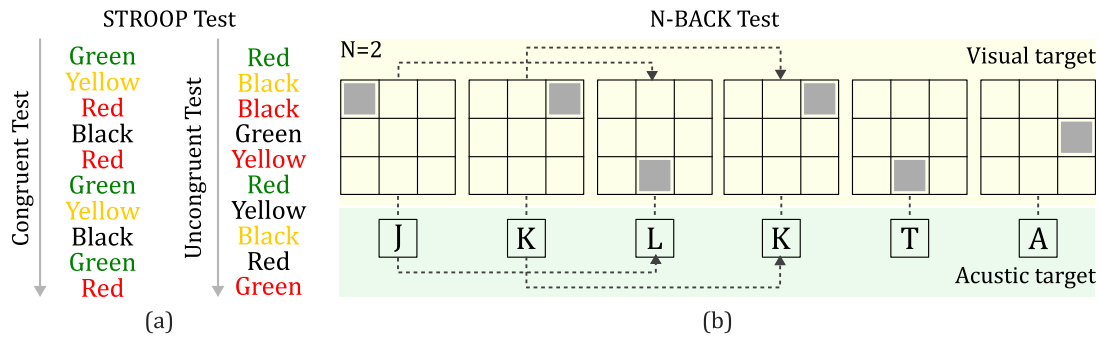


Figure 6.9: Cognitive test employed to induce a blood pressure variation. (a) Stroop test. (b) N-Back test.

participant must decide whether the current stimulus matches the one displayed n trials ago, where N is a variable number that can be adjusted up or down to respectively increase or decrease the cognitive load. In a 1-back test, participants compare the current stimulus to the one immediately preceding it. In a 2-back test, Figure 6.9.(b), they compare the current stimulus to the one that was presented two steps back, and so on. Higher values of "N" increase the cognitive load and complexity of the task. The N-Back Test is widely used to investigate working memory capacity, executive function, and cognitive flexibility. It is often applied in research on aging, cognitive development, neurological disorders, and the impact of various interventions or training programs on working memory. It is also used in neuroimaging studies to examine brain activity patterns related to working memory and cognitive control.

6.2.2 Data Collection Protocol

A second pre-clinical trial has been carried out at the Tyndall National Institute in University College Cork (UCC), Ireland, to study the BP variations related to the execution of cognitive and physical tasks. In this experiment, approved by the UCC Clinical Research Ethics Committee of the Cork Teaching Hospitals (protocol code ECM 4 (ff) 10/11/2020 and ECM 3 (b) 13/12/2022), a cohort of 31 healthy volunteers ranging from 21 to 34 years was recruited. Table 6.6 details the physiological parameters of the people involved. In accordance with the guidelines established for accurate BP measurement [17], every participant included in this study did not have a pre-existing cardiovascular condition and was not undergoing treatment with medications that could influence BP readings. Moreover, every individual was asked to refrain from smoking or consuming coffee in the 60 minutes before the session. The first step in the data capture consisted of the individual reclining in a supine position for 10 minutes to ensure that their hemodynamic

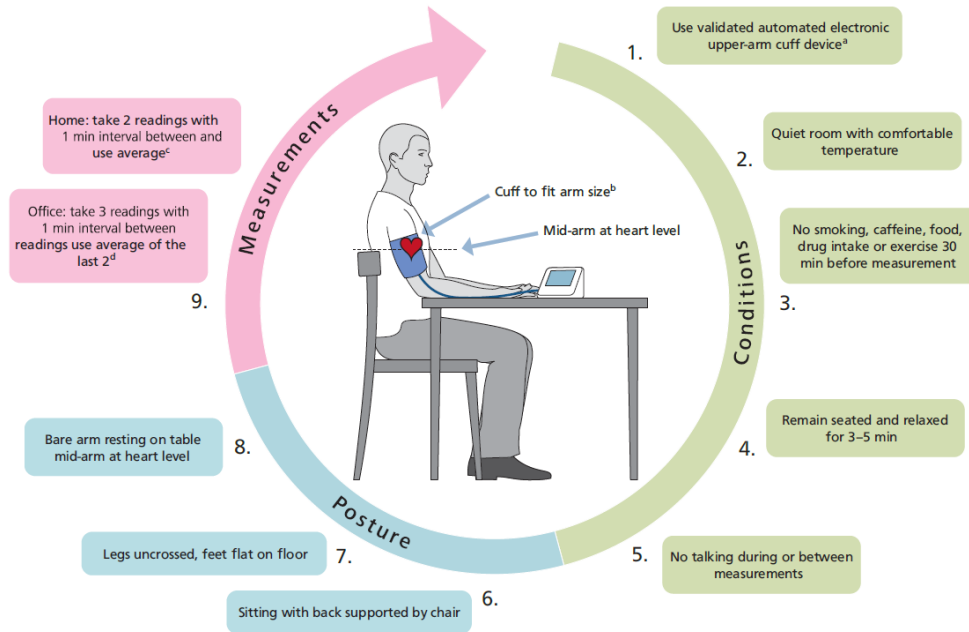


Figure 6.10: Recommendations for BP measurements [16].

conditions and vasomotor tone returned to a baseline level. Subsequently, the subject received instructions regarding the prescribed posture for data capture, which included sitting with back support, both feet flat on the floor, and hands resting on the table at a height equivalent to that of the heart, as shown in Figure 6.10 [16].

Table 6.6: Overview of the characteristics of the study populations.

Characteristics	$\mu \pm \sigma$	Range
Number of Subjects	31	-
Male	20 (64%)	-
Smokers	4 (13%)	-
Age (years)	27.77 ± 3.70	21 - 34
Height (cm)	172.74 ± 9.27	158 - 192
Weight (kg)	69.52 ± 12.72	53 - 99
BMI (kg m^{-2})	23.22 ± 3.30	18.16 - 31.24

Abbreviations: BMI, body mass index, μ , mean value, σ , standard deviation.

In accordance with the study protocol reported in Figure 6.11, after obtaining the anamnesis information, the operator identified the best location for the brachial artery through tactile arterial palpation. Once located, the spot was marked with ink to be sure that the acquisition site did not change over the duration of the data capture. Each data collection session was divided into three principal sections,

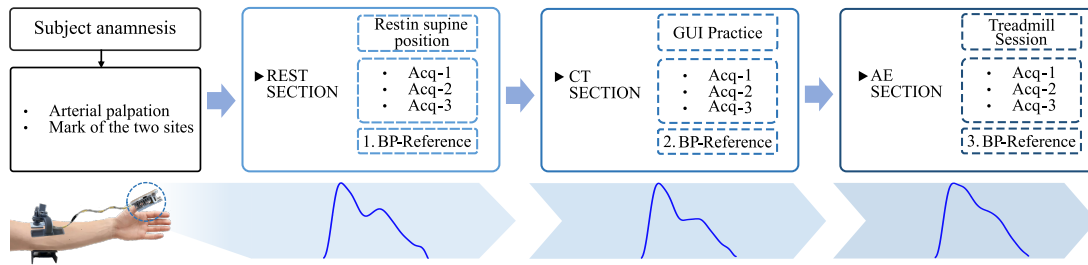


Figure 6.11: Data collection protocol followed in this study along with the evolution of the averaged pulse waveforms morphology according to each section of the data capture.

denoted as follows: the REST phase (REST), the phase dedicated to Cognitive Testing phase (CT), and the After Exercise phase (AE). During each phase, a series of three data acquisitions, each one lasting one minute, was performed using the presented device. Then, the commercial cuff-based device, BPM Connect [198] (Withings, Issy-les-Moulineaux, France), was used as a gold standard to measure the reference BP values for each specific section. In total, a set of three reference measurements was collected throughout the entire data collection. To prevent any potential recovery effects between measurements using both devices, the reference assessment immediately after completing the three acquisitions was conducted. Each phase was designed to induce changes in both BP and PPG data collected from each participant. The resulting alterations in the PPG pulse waveforms are illustrated in the bottom section of Figure 6.11. In the CT section, the subject is cognitively stimulated through two cognitive tests: the Stroop test [199] and the N-Back test [200, 201]. Both tests were executed through a custom-designed graphical user interface (GUI) structured to make a gradual augmentation in the level of complexity. Prior to commencing the actual measurement, the operator provided the participant with detailed instructions regarding the tests to be undertaken. Additionally, the participants had the opportunity to familiarize themselves with the GUI through the execution of a short demonstration. Then, the device was positioned on the subject. The last three minutes of this section were recorded during the execution of the N-Back test and later subdivided into the three acquisitions related to the CT part. Hence, the reference BP measurement was taken again with the Withings device. Finally, the AE section of the data capture was performed. During this stage, each subject was engaged in a 10-minute walking session on a calibrated treadmill. The treadmill's configuration was kept uniform across all data collection sessions. The speed was configured at 8 km/h, and the inclination was adjusted to its maximum level to induce BP variation even in trained subjects. Then, the last three acquisitions with the proposed device were carried out along with the last reference BP measurement.

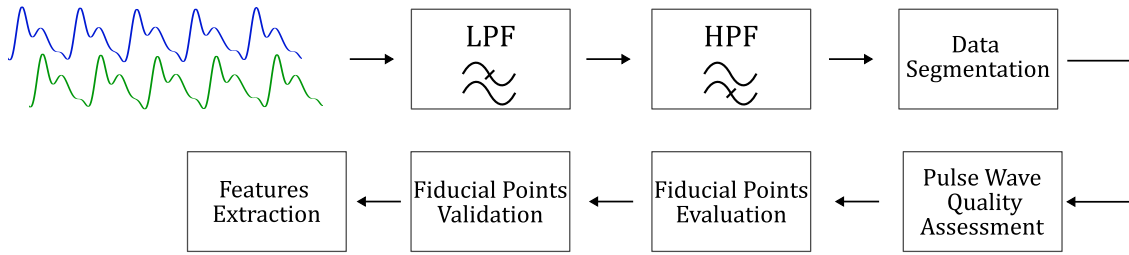


Figure 6.12: Data processing pipeline followed to analyze the collected PPG data.

6.2.3 Data Processing

Since the PPG measurements from both the thumb and elbow were processed using the same procedure, the following explanation applies to both. The data processing pipeline designed for this application can be divided into three major sections, as depicted in Figure 6.12. The pre-processing phase begins with standardizing the length of all 12 acquisitions collected for each subject to ensure consistency. Next, low-pass and high-pass filtering stages are applied to the pulse waveforms to remove the DC offset and the high-frequency noise. The pre-processing phase begins with the standardization of the length of all 12 acquisitions collected for each subject. Low-pass and high-pass filtering stages are then applied to the pulse waveforms to remove noise and retain relevant signal components. Addressing the challenges of time series segmentation and labeling, [202, 203], the study initially segments the collected data into 3-second, consecutive, non-overlapping windows. This initial segmentation helps identify and remove portions of the signal potentially corrupted by MAs [204]. Subsequently, a customized segmentation routine identifies every single pulse wave within the acquisition by localizing the pulse onset, which marks the beginning of the systolic phase within the cardiac cycle. In the quality assessment section, the *template matching* technique is utilized to identify pulses that exhibit abnormal morphology or are corrupted by MAs. This step ensures that only high-quality, reliable data proceeds to the next stage, improving the accuracy of subsequent analyses. Finally, specific points on the PPG waveform and its derivatives, known in the literature as fiducial points, are identified. These fiducial points are crucial for extracting features that will be used in the data analysis section. Following this summary, a more comprehensive description of the processing pipeline is presented.

1. High-Pass Filtering: Initially, a high-pass filter with a cut-off frequency of 0.5 Hz is applied to remove the DC offset from the signal [101].
2. Low-Pass Filtering: Subsequently, a low-pass filter with a cut-off frequency of 15 Hz is employed to eliminate high-frequency noise [101].
3. Standardization of Acquisition Duration: To ensure consistency across diverse

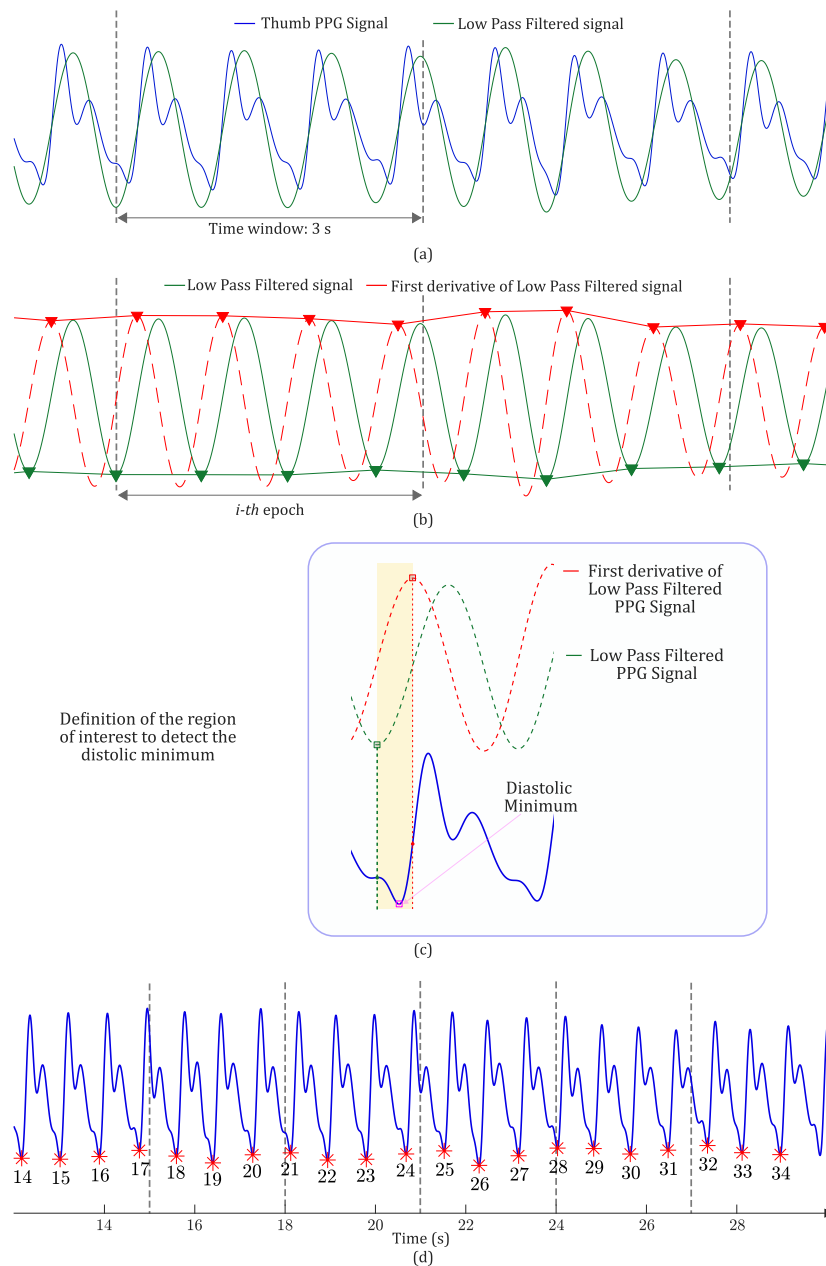


Figure 6.13: Data segmentation routine pipeline. (a) The raw PPG signal from the thumb (blue) and its low-pass filtered version (green) over a 3-second time window. (b) The low-pass filtered PPG signal (green) and its first derivative (red dashed) within a specific epoch (i -th epoch). (c) Detailed identification of the diastolic minimum within the region of interest, using the low-pass filtered PPG signal (green) and its first derivative (red dashed). (d) Result of the detection of the diastolic minima employed for the final segmentation.

subjects, the duration of each acquisition is standardized to 60 seconds.

4. Amplitude Standardization: The amplitude of the acquisition is standardized using the following equation:

$$x = \frac{x - \mu_s}{\sigma_s} \quad (6.1)$$

Where μ_s and σ_s are, respectively, the mean value and the standard deviation of the signal.

5. A custom data segmentation routine is employed to detect the pulse onset and divide the 60-second signal into single pulses. The main steps of the segmentation routine are represented in Figure 6.14 and reported below:
 - (a) Smoothing the Signal: A low-pass filter with a cut-off frequency of 2 Hz is applied to smooth the signal morphology and highlight its periodicity, Figure 6.13.(a).
 - (b) Computing the First Derivative: The first derivative of the low-pass filtered signal is computed, Figure 6.13.(b).
 - (c) Epoch Segmentation: The entire acquisition is segmented into 3-second, non-overlapping windows.
 - (d) Detection of Minima and Maxima: Within each window, minima and maxima are detected on the low-pass filtered signal and its derivative, respectively, as depicted in Figure 6.13.(b).
 - (e) Validation of Minima and Maxima: The relative positions of minima and maxima are checked to ensure that for each minimum, there is exactly one corresponding maximum.
 - (f) Pulse Onset Detection: Finally, each pair of points (minima and maxima) is projected onto the original signal to define the region of interest for detecting the pulse onset, Figure 6.13.(c, d).
6. The template matching approach [205] was chosen to conduct the pulse wave quality assessment (SQA) [205]. Initially, a reference template was generated from all the available epochs. Pearson's correlation coefficient was then employed as the signal quality index (SQI) to compare each individual pulse with the template, Figure 6.14. Pulses with an SQI below the specified acceptance thresholds (0.95 for REST, 0.95 for CT, and 0.9 for AE) were deemed unacceptable and subsequently discarded.
7. These points, usually known as fiducial points, are distinct points that can be identified on either the pulse wave or its derivatives. Figure 6.15 illustrates commonly used fiducial points. The key fiducial points on the original

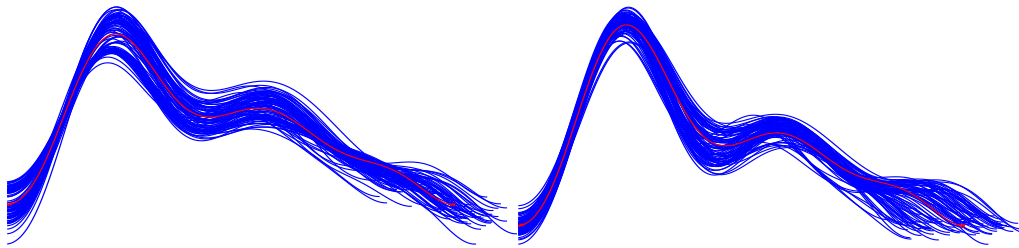


Figure 6.14: Extraction of the template from PPG waveforms collected from brachial (left) and digital (right) arteries.

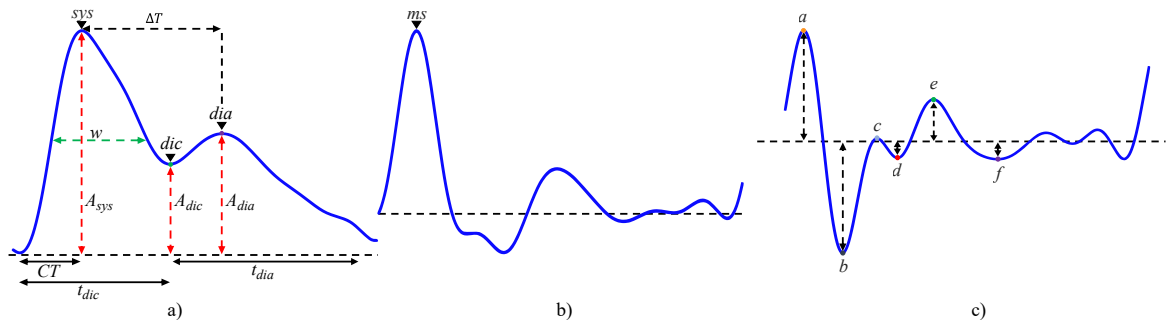


Figure 6.15: (a) Feature extracted from a PPG waveform (b) Maximum of the first derivative (ms) detected on the velocity plethysmography (VPG) (c) Fiducial points detected on the acceleration plethysmography (APG).

PPG pulse wave, referring to Figure 6.15.(a), are the pulse onset, the systolic and diastolic peaks, and the dicotic notch. The maximum point on the first derivative is shown in Figure 6.155 (b), indicating the point of maximum slope in the original signal. On the second derivative, four distinct points occurring in systole can be identified, known as the a-, b-, c-, and d-waves (Figure 6.15.(c)). The e-wave can be used to determine the location of the dicotic notch. The detected fiducial points and the criteria employed to detect them are listed in Table 6.7 [206, 207, 208, 209].

On the original pulse wave, the systolic peak is usually identified as the maximum point, and the pulse onset as the minimum. When the dicotic notch is present, it can be identified from the timing of the e-wave on the second derivative. The diastolic peak can then be determined as the maximum point after the location of the dicotic notch. When the diastolic peak is not present (such as in older subjects), the corresponding location of this point can be estimated as the first local maxima in the second derivative after the e-wave or from the first derivative. On the first derivative (VPG), the point of maximum upslope can be easily obtained as the location of the maximum value of the first derivative. To detect the key fiducial points on the second derivative (APG) several criteria and methods are reported in literature[32].

Table 6.7: Criteria for identifying fiducial points on PPG pulse waves.

Signal	Fiducial Point	Description
PPG, s	Sys	Maximum of the pulse waveform
	Dic	First local minimum after the systolic peak or coincident with e
	Dia	First local maximum after dic and before $0.8T$ (where T is the duration of the cardiac cycle)
VPG, s'	ms	Maximum of the first derivative, s'
APG, s''	a	The maximum of s'' preceding the maximum of the first derivative ms
	b	First local minimum following a
	c	The greatest maximum of s'' between b and e (or if no maxima then the first maximum on x' after e)
	d	The lowest minimum on s'' after c and before e (or if no minima then coincident with c).
	e	The second maximum of s'' after ms and before $0.6 T$ (unless the c wave is an inflection point, in which case take the first maximum).
	f	The first local minimum of s'' after e and before $0.8 T$.

Abbreviations: PPG, photoplethysmogram, VPG velocity plethysmogram, APG, acceleration plethysmogram, s , original pulse, s' , first derivative of the original pulse, s'' , second derivative of the original pulse.

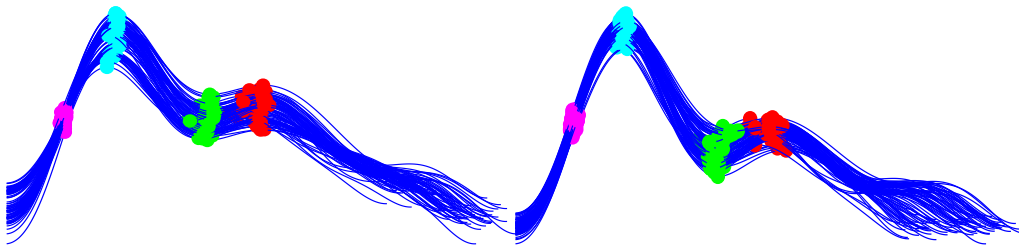


Figure 6.16: Validation of the positions of fiducial points on high-quality PPG waveforms collected from the elbow (left) and thumb (right) sites.

8. Upon detection, the position of each fiducial point is verified on each pulse to ensure accurate feature extraction. Figure 6.16 illustrates the positions of fiducial points on high-quality PPG waveforms collected from the elbow (left) and thumb (right) sites.
9. Finally, features listed in Table 6.8 and Table 6.9 are extracted from each pulse.

Table 6.8: Definition of the extracted features from PPG pulse wave.

Signal	Feature	Definition	Formula
PPG, s	ΔT	Time delay between systolic and diastolic peaks	$t_{dia} - t_{sys}$
	SI	Stiffness Index, h is the subject's height	$\frac{h}{t_{dia} - t_{sys}}$
	CT	Crest Time: time occurring between pulse onset e systolic peak	$t_{sys} - t_0$
	w	Pulse width at 50% of systolic peak amplitude, A_{sys}	-
	IPR	Instantaneous pulse rate	$60/T$
	T	Period of the cardiac cycle	-
	t_{dia}	Duration of the diastole	$T - t_{dic}$
	t_{dic}	Time to dicrotic notch	$t_{dic} - t_0$
	A_0	Amplitude of pulse onset	$s(t_0)$
	A_{sys}	Amplitude of the systolic peak	$s(t_{sys})$
	A_{dic}	Amplitude of the dicrotic notch	$s(t_{dic})$
	A_{dia}	Amplitude of the diastolic peak	$s(t_{dia})$
	RI	Reflection index	$\frac{s(t_{dia}) - s(t_0)}{s(t_{sys}) - s(t_0)}$
	K	Pulse waveform characteristic value	$\frac{s_{\mu} - A_0}{(A_{sys} - A_0)}$
	K_1	Systolic characteristic value	$\frac{s_{\mu, sys} - A_0}{(A_{sys} - A_0)}$
	K_2	Diastolic characteristic value	$\frac{s_{\mu, dia} - A_0}{A_{sys} - A_0}$
	$s_{\mu, sys}$	Mean value of the systolic phase of the pulse waveform	-
	$s_{\mu, dia}$	Mean value of the diastolic phase of the pulse waveform	-
	s_{μ}	Mean value of pulse waveform	-
	s_{σ}	Standard deviation of pulse waveform	-
	$s_{skewness}$	Skewness of pulse waveform	-
	$s_{kurtosis}$	Kurtosis of pulse waveform	-
	A_1	Area under the curve between the pulse onset (t_0) and the dicrotic notch (t_{dia})	-
	A_2	Area under the curve between the dicrotic notch (t_{dia}) and the end of the pulse (t_{end})	-
	IPA	Inflection point area	$\frac{A_2}{A_1}$

Table 6.9: Definition of the extracted features from first and second derivatives of PPG pulse waveform.

Signal	Feature	Definition	Formula
VPG, s'	t_{ms}	Time to the maximum slope computed on the first derivative of the pulse	$t_{ms} - t_0$
	A_{ms}	Amplitude of the maximum slope	$s'(t_{ms})$
	t_{bd}	Time elapsing between b and d	$t_d - t_b$
APG, s''	t_{bc}	Time elapsing between b and c	$t_d - t_c$
	b/a	Amplitude ratio early systolic negative wave over early systolic positive wave	$\frac{s''(t_b)}{s''(t_a)}$
	c/a	Amplitude ratio late systolic re-increasing wave over early systolic positive wave	$\frac{s''(t_c)}{s''(t_a)}$
	d/a	Amplitude ratio late systolic decreasing wave over early systolic positive wave	$\frac{s''(t_d)}{s''(t_a)}$
	e/a	Amplitude ratio early diastolic positive wave over early systolic positive wave	$\frac{s''(t_e)}{s''(t_a)}$
Combined	AGI	Aging index	$\frac{s''(t_b) - s''(t_c) - s''(t_d) - s''(t_e)}{s''(t_a)}$
	$IPAD$	Inflection point area combined with d-peak	$\frac{A_2}{A_1} + \frac{s''(t_d)}{s''(t_a)}$
	k	Elasticity constant	$\frac{s''(t_{sys})(s(t_{sys}) - s(t_0))}{s(t_{sys}) - s(t_{ms})}$

Abbreviations: VPG velocity plethysmography, APG, acceleration plethysmogram, s' , first derivative of the original pulse, s'' , second derivative of the original pulse.

6.2.4 Model Training

This study examines the efficacy of personalized against generalized training strategies to identify significant alterations in blood pressure levels. As delineated in section II-B, the data collection protocol was meticulously structured to induce BP variations through the execution of both physical and cognitive tasks. This setup enabled a thorough investigation of BP fluctuations in individuals subjected to diverse stimuli. In this context, a macroscopic variation of BP is defined as the difference between the reference values measured throughout the data collection procedure, regardless of the magnitude. Consequently, the phases of the data capture process (e.g., REST, CT, AE) were used as target labels for the analysis, as they inherently reflect BP changes.

Our investigation compares the outcomes derived from applying ten different person-specific models (PIM) against those obtained by a person-independent

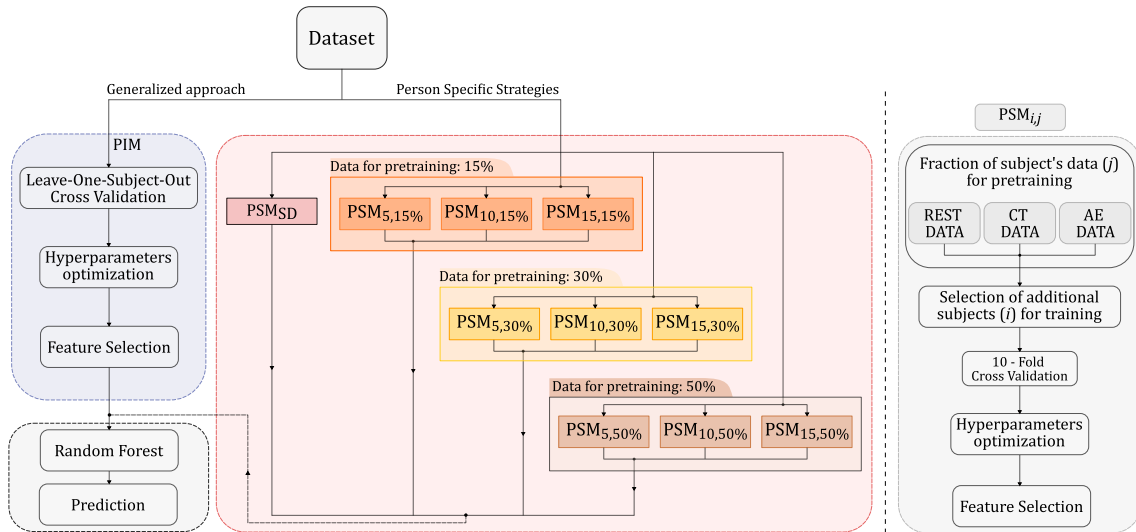


Figure 6.17: Overview of the tested training strategies. (Left) Workflow employed for the generalized approach (PIM). (Center) Tested combinations for Person-Specific Strategies (PSM). (Right) Workflow adopted by every $PSM_{i,j}$.

model (PIM) when applied to the identical dataset, utilizing an RF classifier. Although features were extracted from signals at both sites, only those from the thumb were utilized. Pulse waves collected from the elbow were used to calculate the PTT, which was then used as a feature. Figure 6.17 (left branch) shows the workflow for our generalized approach. A Leave-One-Subject-Out strategy was adopted to optimize the model’s performance across all users in the dataset. The optimization process involved the following parameters: the number of trees in each forest, which ranged from 50 to 100; the maximum depth of each tree in the forest, which ranged from 10 to 50; and the number of features used in the training process, which ranged from 3 to 25. The feature selection process was applied only at the training stages by ranking the first n features according to the mutual information between each feature and the target label. The right branch, highlighted in red, summarizes the ten personalized strategies. The tested PSMs differ in the amount of data used during the training phase and the fraction of the target subject data employed to personalize the model. Starting from PSM_{SD} , in which 50% of data from the k^{th} subject for training was employed, data from randomly selected individuals were gradually added to the training set. Specifically, the number of source subjects varied across 5, 10, and 15 individuals. Different fractions of the target subject data were also tested to customize the model. This feature was progressively expanded, beginning from an initial value of 15%, and subsequently increased to 30% and 50%. Each combination of these parameters, when applied to the RF, was labeled as $PSM_{i,j}$ where i identifies the number of source individuals, $i \in 5, 10, 15$, and j refers to the percentage of data belonging to the k^{th} target subject

		Predicted Label		
		REST	CT	AE
True Label	REST	TP _{REST}	FN _{CT,REST}	FN _{AE,REST}
	CT	FP _{REST,CT}	TN _{REST}	TN _{REST}
	AE	FP _{REST,AE}	TN _{REST}	TN _{REST}

(a)

		Predicted Label		
		REST	CT	AE
True Label	REST	TN _{CT}	FP _{CT,REST}	TN _{CT}
	CT	FN _{REST,CT}	TP _{CT}	FN _{AE,CT}
	AE	TN _{CT}	FP _{CT,AE}	TN _{CT}

(b)

		Predicted Label		
		REST	CT	AE
True Label	REST	TN _{AE}	TN _{AE}	FP _{AE,REST}
	CT	TN _{AE}	TN _{AE}	FP _{AE,CT}
	AE	FN _{REST,AE}	FN _{CT,AE}	TP _{AE}

(c)

Figure 6.18: Definition of true positives (TP), false positives (FP), false negatives (FN), and true negatives (TN) instances in a multiclass problem. (a) REST class. (b) Cognitive task (CT) class. (c) After exercise (AE) class.

$j \in 15\%, 30\%, 50\%$. The right side of Figure 6.17 details the workflow followed by each $PSM_{i,j}$ before applying the RF model. The initial step involves randomly selecting a portion of data samples from each class. To avoid class imbalance, each class was equally represented by selecting 15%, 30%, or 50% of pulse waveforms from each class. Following this, pulse waveforms from different source subjects (5, 10, or 15) were included. Then, unlike the generalized approach, the PIM method incorporates 10-fold cross-validation to fine-tune the model’s hyperparameters and identify the most informative subset of features. Finally, all the mentioned solutions apply the RF model to predict the actual class of the input pulses. The output from each subgroup was merged for visualization purposes, although each PIM was tested individually.

6.2.5 Evaluation Metrics

As described in the previous subsection, the four presented models were trained and tested per each subject in the dataset. Therefore, metrics such as accuracy, precision, recall, and F1-score were computed to evaluate the fluctuations of classification performance from subject to subject. Finally, an average of all indexes was computed along with its standard deviation to summarize the performance of each model. In a multiclass classification problem with three classes (REST, CT, and AE), the definitions are as follows:

- True Positives (TP): Correctly predicted instances of a class.
- False Positives (FP): Instances incorrectly predicted as a certain class.
- False Negatives (FN): Instances of a class that are incorrectly predicted as another class.

- True Negatives (TN): all instances that are correctly not classified as the class under evaluation.

The accuracy score, computed as the ratio of correctly predicted instances over of the total number of instances, was used to quantify the correctness of the predicted labels compared to the actual labels Eq.6.2.

$$\text{Accuracy} = \frac{\sum \text{True Positives for All Classes}}{\text{Total Instances}} \quad (6.2)$$

Given these definitions, the evaluation metrics such as precision, and recall scores are computed, individually, for each of the three classes referring to different sections of the data capture ($\alpha \in \text{REST, CT, AE}$) as specified in Eq.6.3 and Eq.6.4.

$$\text{Precision}_\alpha = \frac{TP_\alpha}{TP_\alpha + FP_\alpha} \quad (6.3)$$

$$\text{Recall}_\alpha = \frac{TP_\alpha}{TP_\alpha + FN_\alpha} \quad (6.4)$$

Where FP_α and FN_α are the overall number of false positives and false negatives referred to the target class $\alpha \in \text{REST, CT, AE}$ under evaluation. Then, for every tested subject sub_i , the macro averaged value of precision and recall, Eq.6.5 and Eq.6.6., was calculated according to the following:

$$\overline{\text{Precision}}_{sub_i} = \frac{1}{N} \sum_{\alpha=1}^N \text{Precision}_\alpha \quad (6.5)$$

$$\overline{\text{Recall}}_{sub_i} = \frac{1}{N} \sum_{\alpha=1}^N \text{Recall}_\alpha \quad (6.6)$$

where N is the number of classes occurring in this study. Finally, the the macro averaged F1-score was computed as reported in Eq.6.7:

$$\overline{F1}_{sub_i} = \frac{1}{N} \sum_{\alpha=1}^N \frac{2 * \text{Precision}_\alpha * \text{Recall}_\alpha}{\text{Precision}_\alpha + \text{Recall}_\alpha} \quad (6.7)$$

6.2.6 Data Processing Results

Table 6.10 shows the results of the three processing stages described divided per section of the data capture (REST, CT, AE), for a single site.

After eliminating epochs corrupted by MAs, the total number of segmented waveforms amounts to 19,274, distributed as follows: 6,348 for the resting phase (REST), 6,213 during cognitive testing CT, and 6,713 after the physical exercise phase (AE). Data collected from subject #26 was discarded due to corruption of the recording on both sites during the CT section. The variance in the number

Table 6.10: Data processing results.

Data Capture	Segmented Pulses	PWQA	Fiducial Points Validation
REST	6348	6074	5935
CT	6213	5849	5630
AE	6713	6620	6321
Total Pulses	19724	18543 (96.8%)	17886 (92.8%)

Abbreviations: REST, measurements at rest; CT, cognitive task section; AE, measurements after physical tasks; PWQA, pulse wave quality assessment

Table 6.11: Averaged Reference Blood Pressure Values.

Data Capture	SBP (mmHg)	DBP (mmHg)	HR (bpm)
REST	109.03 ± 11.61	67.81 ± 6.71	71.69 ± 8.29
CT	114.53 ± 3.03	71.24 ± 8.24	70.04 ± 8.71
AE	115.42 ± 12.24	72.87 ± 7.31	77.31 ± 11.90

REST, measurements at rest, CT, cognitive task section, AE, measurements after physical tasks, SBP, systolic blood pressure, DBP, diastolic blood pressure, HR, heart rate

of detected waves aligns with the execution of the scheduled tasks during the data capture. Specifically, the approximately 400-wave difference between the REST section and the measurement following treadmill walking can be attributed to the observed increases in heart rate (HR) and BP in the measurements conducted with the reference device. Regarding the CT section, although there was an increase in SBP and DBP values (Table 6.11), the heart rate remained essentially constant compared with the resting value. This phenomenon is reflected in the number of waves detected (6,213, CT vs 6,348, REST).

As a result of the Pulse Wave Quality Assessment (PWQA), approximately 3.2% of the total pulses were excluded due to their insufficient similarity to the reference template. Due to the low data quality found in the CT section, data from subjects #17 and #29 were discarded from the dataset used for data analysis. Finally, following the validation of the fiducial points, an additional 4% of data points were discarded for a total of 17,886 pulse waves used in the analysis phase collected from 28 out of 31 subjects.

6.2.7 Model Evaluation Results

Table 6.12 compares the aggregated BP classification performance between ten different PSMs with the results achieved using a generalized approach. The results

were expressed in terms of mean value and related standard deviation using the scoring criteria (accuracy, precision, recall, and F1-score) mentioned in Section 6.2.5. The evaluation metrics computed per each subject according to training strategy are reported in Tables B.1 - B.8 in Appendix B. The person-independent model, denoted as PIM , was trained across the complete dataset employing Leave-One-Subject-Out cross-validation. Subsequently, performance evaluation was conducted by aggregating the outcomes obtained for each individual. No personalization was applied in this case. The low scores retrieved for each metric (0.36, 0.36, 0.31, 0.37) suggest the requirement for personalization to model the PPG-BP relationship effectively. Figure 6.19 displays the results gathered using the RF trained using 50% of the data of the target subject under investigation (PSM_{SD}). In this case, subjects #2, #14, #21, #25, and #28 display a marked decrease in classification performance, showcasing accuracy values of 0.63, 0.67, 0.75, 0.78, and 0.67, alongside precision values of 0.43, 0.5, 0.8, 0.8, and 0.5. Through systematic assessment using the proposed training approaches, the impact of altering the number of subjects and the percentage of data used for model customization on classification performance was examined. The evaluation metrics computed per each personalized model ($PSM_{i,j}$) are reported in Table 6.12, and the average accuracy score is represented in Figure 6.20. In this latter, two discernible trends can be identified. Specifically, the average accuracy is directly correlated with the increase in the percentage of data utilized during the pre-training phase and inversely correlated with an augmentation in the number of subjects.

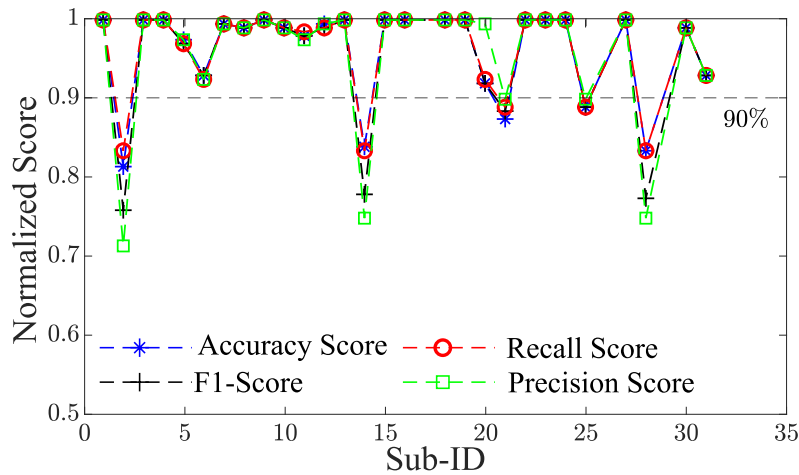


Figure 6.19: Values of evaluation metrics (Accuracy, Precision, Recall, and F1-score) according to the training strategy denoted as PSM_{SD} .

Table 6.12: Averaged evaluation metrics per each model.

MLA	Training Strategy	Training Set				Test Set			
		Accuracy	Precision	Recall	F1-Score	Accuracy	Precision	Recall	F1-Score
RF	PIM	0.99	0.99	0.99	0.99	0.360 ± 0.200	0.360 ± 0.180	0.310 ± 0.180	0.370 ± 0.180
	PSM _{SD}	1	1	1	1	0.925 ± 0.117	0.912 ± 0.165	0.926 ± 0.113	0.912 ± 0.147
	PSM _{5,50%}	1	1	1	1	0.964 ± 0.041	0.964 ± 0.040	0.963 ± 0.038	0.962 ± 0.042
	PSM _{10,50%}	1	1	1	1	0.957 ± 0.030	0.958 ± 0.028	0.955 ± 0.030	0.956 ± 0.028
	PSM _{15,50%}	1	1	1	1	0.945 ± 0.028	0.947 ± 0.028	0.945 ± 0.026	0.944 ± 0.027
	PSM _{5,30%}	1	1	1	1	0.951 ± 0.039	0.952 ± 0.037	0.950 ± 0.038	0.950 ± 0.037
	PSM _{10,30%}	1	1	1	1	0.926 ± 0.051	0.930 ± 0.044	0.922 ± 0.052	0.923 ± 0.051
	PSM _{15,30%}	1	1	1	1	0.916 ± 0.045	0.918 ± 0.043	0.914 ± 0.045	0.914 ± 0.045
	PSM _{5,15%}	1	1	1	1	0.914 ± 0.043	0.916 ± 0.043	0.913 ± 0.042	0.913 ± 0.042
	PSM _{10,15%}	1	1	1	1	0.874 ± 0.069	0.885 ± 0.061	0.872 ± 0.072	0.871 ± 0.072
	PSM _{15,15%}	1	1	1	1	0.860 ± 0.083	0.867 ± 0.083	0.852 ± 0.091	0.853 ± 0.091

Abbreviations: MLA, machine learning algorithm, PIM, person independent model, PSM_{SD}, person-specific model 50% of data from k^{th} subject for the training set, 25% as validation set and 25% as test set, PSM _{i,j} person-specific model where i identifies the number of source individuals, $i \in 5, 10, 15$, and j refers to the percentage of data belonging to the k^{th} target subject $j \in 15\%, 30\%, 50\%$.

Notes: * Macro averaged values computed on the 28 subjects employed for the analysis.

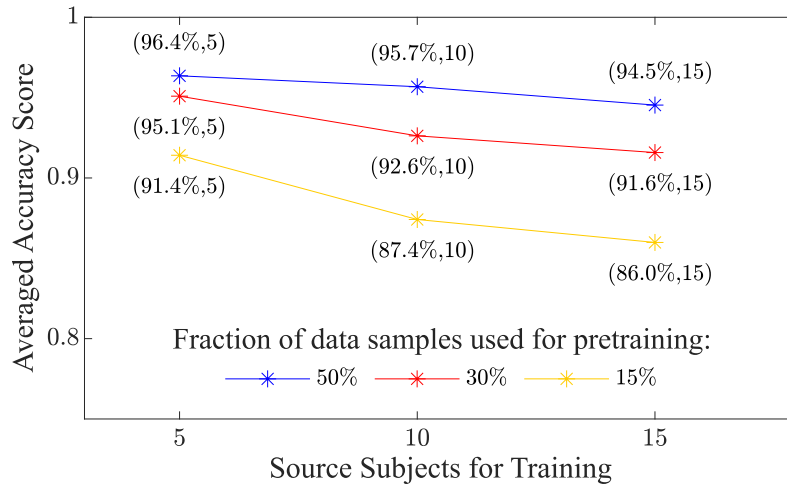


Figure 6.20: Averaged values of accuracy score according to different combinations of number of source subjects and diverse fractions of data employed to personalize the RF model.

The observed accuracy values of 96.4% , 95.7%, and 94.5% in the first set (e.g., $PSM_{5,50\%}$ $PSM_{10,50\%}$ $PSM_{15,50\%}$) decline to 95.1%, 92.6%, and 91.6% in the second set (e.g., $PSM_{5,30\%}$, $PSM_{10,30\%}$, $PSM_{15,30\%}$), and further decrease to 91.4%, 87.4%, and 86% in the third set (e.g., $PSM_{5,15\%}$, $PSM_{10,15\%}$, $PSM_{15,15\%}$). Combinations that demonstrated overfitting across multiple subjects were excluded by discarding those with accuracy and F1 values below 0.95, Figure6.21. Therefore, $PSM_{5,30\%}$ $PSM_{5,50\%}$ $PSM_{10,50\%}$ were selected. Given the comparable overall performances across subjects for these combinations, our choice for the best combination was guided by a balance between performance metrics and the minimized data requirement for model customization. This led us to favor $PSM_{5,30\%}$.

6.2.8 Discussion

This study compares the performances of person-dependent and generalized models adopted to track BP macro-variations associated with physical or cognitive workload using a Random Forest classifier. This model was chosen due to its ability to handle the nonlinear relationships that exist between the extracted features and the variation in BP [207]. In other studies, RF has outperformed other nonlinear models such as SVM, adopting a non-linear kernel, and neural networks [210]. Moreover, RF is less prone to overfitting compared to the other two mentioned MLA [108]. Generalized solutions often struggle with the high inter-subject variability within the dataset, making it challenging to develop a universally applicable model. The choice between personalized and universal models depends on the specific context and objectives of the problem being addressed.

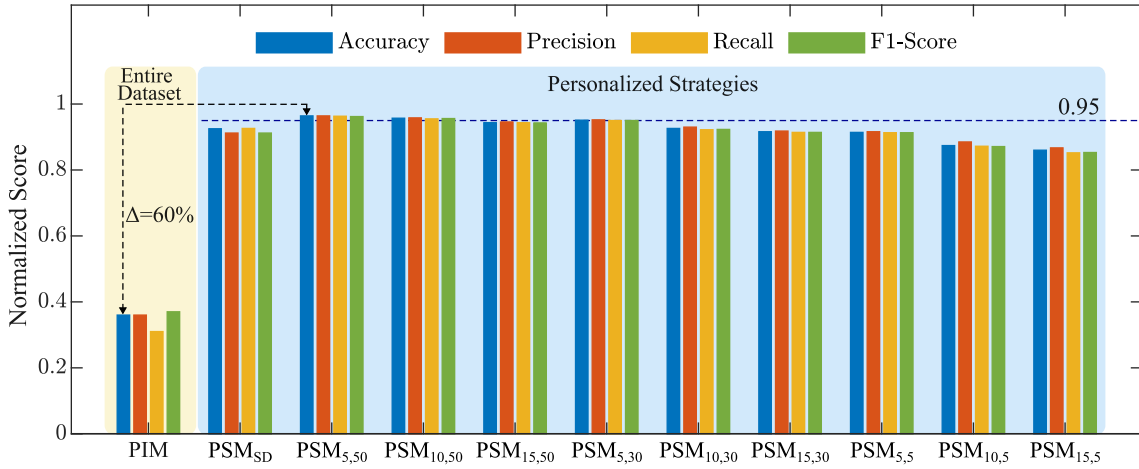


Figure 6.21: Comparison of performance metrics (Accuracy, Precision, Recall, and F1-Score) between the Person-Independent Model (PIM) and various Person-Specific Models (PSM). The dashed blue line at 0.95 indicates the threshold employed to discard PSM configurations with unsatisfactory performance.

Personalized models, finely tuned to individual users' characteristics, take into account factors like age, gender, medical history, and lifestyle to provide more accurate and relevant predictions of BP. This tailored precision proves particularly crucial for individuals affected by complex health conditions or unique risk factors. Despite these advantages, the construction and maintenance of personalized models for each user pose challenges. This process can be resource-intensive, especially in the field of large-scale applications involving a significant number of subjects. Moreover, privacy and data protection concerns come to the forefront, as the development of personalized models often necessitates access to sensitive user data.

Generalized models, in contrast, are crafted to exhibit proficiency across a diverse spectrum of users without the need for individual customization. This inherent versatility makes them more scalable and simpler to implement, eliminating the necessity for tailoring to each user's unique attributes. The cost-effectiveness and ease of maintenance associated with generalized models make them particularly advantageous for applications boasting a large user base. However, this broad approach comes with a trade-off since generalized models may fail to capture the distinctive characteristics and preferences of individual users. Consequently, the predictions generated by these models may result in a lack of accuracy compared to their personalized counterparts.

This phenomenon, highlighted in [211], is also reflected in the presented findings where the averaged metrics of the generalized approach (0.36, 0.36, 0.31, 0.37) underline the difficulties in defining a univocal representative model for subjects with different physiological characteristics. A hybrid approach combining personalized and universal models, as investigated in this study, may be beneficial for blood

pressure monitoring. A universal model could be used as a baseline to provide initial predictions for all users, and personalized models could be applied to increase the model’s performance where personalization is deemed critical, such as users with complex health conditions or unique risk factors accommodating the inherent diversity in BP patterns among different subjects.

In [126], the authors used a transfer learning technique that personalizes specific layers of a pre-trained network to improve the performance of PPG-based BP estimation, highlighting the influence of the number of data samples and source subjects used for training. As illustrated in Figure 6.21, the analysis of the results indicates that all PSMs enhanced the performance of the generalized model, with improvements reaching up to 60% for $PSM_{5,50\%}$. This enhancement occurred regardless of the number of source subjects used for training, compared to a single generalized model trained on the same dataset. Moreover, by observing the metrics displayed in Table 6.12, strategies including data obtained from different individuals demonstrate better performance in comparison to the model constructed exclusively using data from the tested subject (PSM_{SD}) where, as reported in Figure 6.19, the classification performance of eight subjects witnessed a substantial decline. Subject #2 emerged as the most adversely affected, exhibiting a notable drop of all metrics up to 0.63, 0.43, 0.67, and 0.52 for accuracy, precision, recall, and F1-score, respectively. These fluctuations in classification performance are a direct consequence of the phenomenon of overfitting whereby the model cannot correctly predict data that differ from the small training set available. To mitigate this issue, data from 5, 10, or 15 randomly selected subjects from the dataset were included in addition to diverse fractions of the target subject’s data (15%, 30%, 50%). In this way, the behavior of the model was assessed according to different sizes of the training set, degrees of personalization, and combinations of hyperparameters. Table 6.12 reveals a distinct inverse correlation between the classification metrics and the increase of the number of individuals. This diminishing pattern suggests the potential implications linked to higher variability introduced by additional source subjects w.r.t to the initial amount of data used to pre-train the model. Hence, this phenomenon may reduce random forest customization and consecutively lead to poorer classification performance for the target subject under evaluation. In fact, as depicted in Figure 6.20, $PSM_{5,15\%}$, $PSM_{10,15\%}$ and $PSM_{15,15\%}$ show a more pronounced decrease in accuracy value as the number of subjects increases compared to the cases with 30% and 50%.

This phenomenon is further visible in Figure 6.22 and Figure 6.23. Notably, when utilizing only 30% of the data for the pre-training stage, this adverse trend is further accentuated by a more pronounced variability (Figure 6.22b, and 6.22c) compared to the scenario with 50% (Figure 6.23b, and 6.23c), where the standard deviation is progressively reduced. In the definition of the best solution within the context of our application, any tested combinations exhibiting aggregated accuracy and F1 values below 0.95 were discarded. This approach ensured that combinations

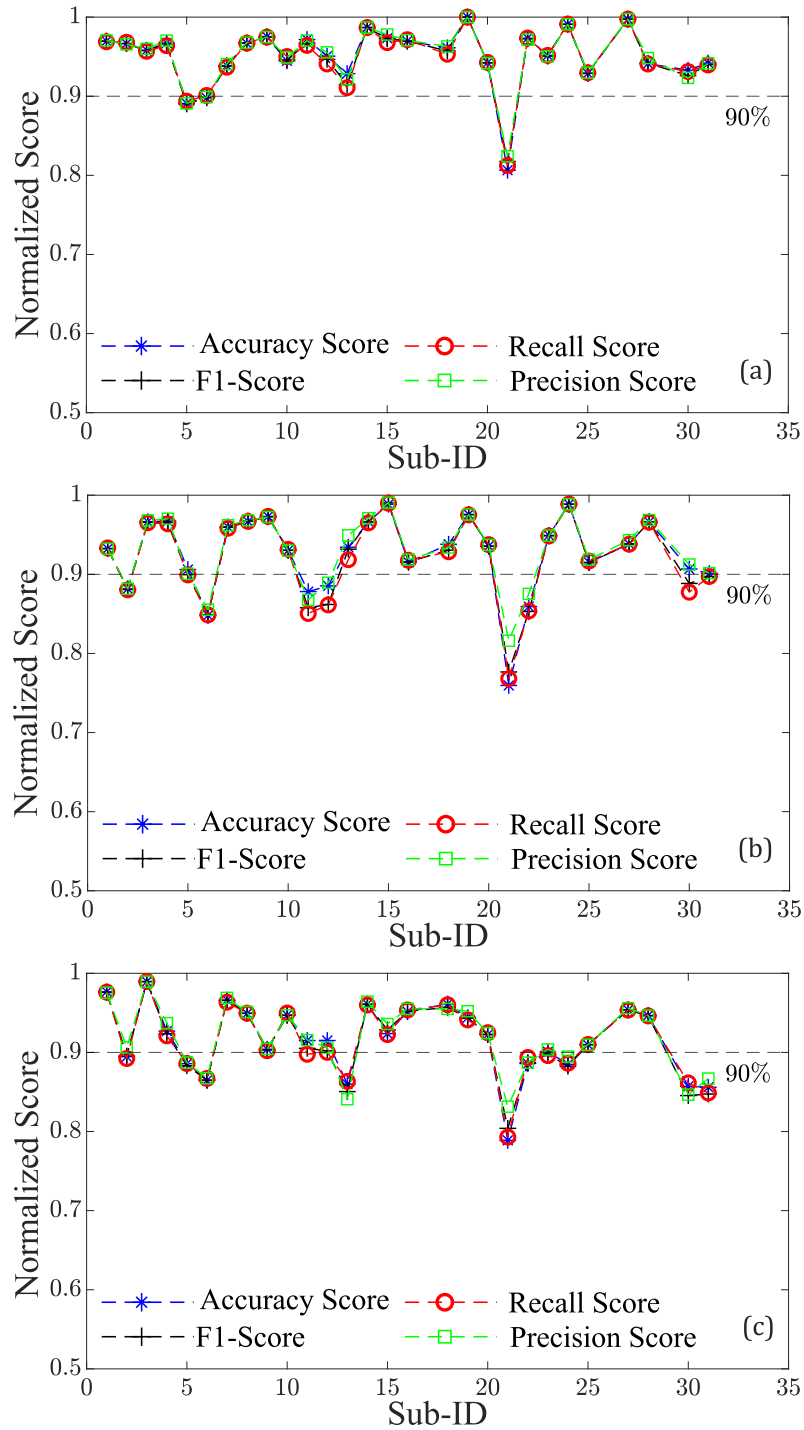


Figure 6.22: Evaluation metrics computed per each individual employing a fraction of the target-subject data set equal to 30% and a diverse number of source subjects (N). (a) N=5. (b) N=10. (c) N=15.

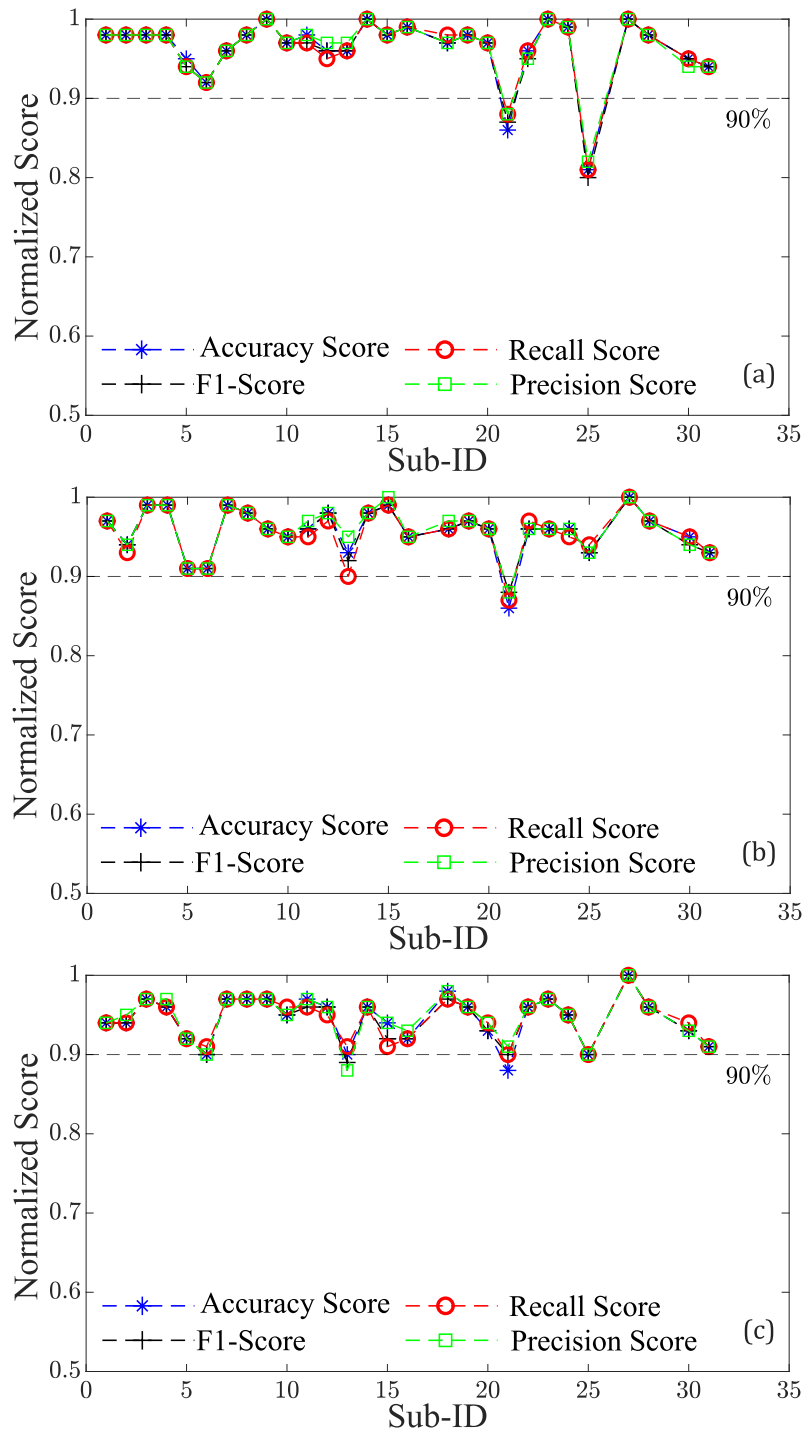


Figure 6.23: Evaluation metrics computed per each individual employing a fraction the target-subject data set equal to 50% and diverse number of source subjects (N). (a) $N=5$. (b) $N=10$. (c) $N=15$.

displaying overfitting across multiple subjects were not considered. As result, our selected PSMs are confined to $PSM_{5,30\%}$, $PSM_{5,50\%}$, $PSM_{10,50\%}$. Upon analyzing the performance of various combinations across subjects within the dataset, it is evident that their overall performances are generally comparable. However, an exception arises with subject #21, Figure 6.22a, Figure 6.23a, and Figure 6.23b, which exhibit a drop in performance exceeding 10% compared to the training phase in all three combinations although slightly less evident in $PSM_{10,50\%}$. This trend is attributed to subject #21 having the lowest number of pulses in the dataset, resulting in a diminished dataset for personalization compared to other subjects. Notably, the combination $PSM_{15,50\%}$ demonstrates a substantial improvement, utilizing more data for personalization along with an increased number of individuals. Hence, due to the similarity observed among the performance metrics, the selection of the best combination was guided by the consideration of the data required for model customization, leading us to favor $PSM_{5,30\%}$. Employing 30% of the total available data, equivalent to approximately 162 sec for the personalization phase, represents a noteworthy outcome as it allowed to keep the evaluation metrics above 95%. This achievement is particularly significant as it reflects a substantial reduction in the time required for this task compared to the approach outlined in [126] where 250 sec of data recording per subject were used for the pre-training stage. Therefore, combining a subset of source subjects, in conjunction with an adequate fraction of data for pre-training, leads to increased robustness and generalizability of personalized models across a broader spectrum of cases in BP assessment when compared to standard generalized models. Despite the mentioned improvements, some limitations of the proposed study need to be discussed. In this study, the performance of the proposed approach was evaluated on a limited sample of 28 subjects, falling short of the 85 subjects required by the AAMI [16, 108]. To enhance model validation and generalization for accurate BP monitoring, it is crucial to include a diverse range of values that truly represent the population, including both males and females across different age ranges. Future endeavors will aim to extend the validation process to encompass a larger and more diverse cohort of individuals, aligning with the standards set by AAMI. Typically, to assess blood pressure variations, multiple sets of data collection over several days are conducted to ensure the algorithm's consistent performance over time for the same individual. However, it is crucial to note that our data collection protocol was designed to induce short-term variations in BP linked to diverse stimuli rather than long-term monitoring. Moreover, increased proficiency in the cognitive tests section would likely result in reduced BP variation due to heightened familiarity with the tasks.

6.3 Development of a personalized anomaly detection model to detect motion artifacts over PPG data using *catch22* features

Wearable health monitoring devices incorporating PPG sensors have demonstrated significant potential in advancing cardiovascular disease monitoring [113]. PPG sensors are widely utilized in wearable healthcare due to their low cost and convenience. In addition, these sensors have proven effective in tracking physiological signals such as heart rate (HR), oxygen saturation (SpO₂), and blood pressure [212, 213]. However, their accuracy is still considered unsatisfactory especially during user motion, primarily due to MAs [214]. Signal quality degradation arises from changes in blood flow velocity induced by motion, relative movement between PPG sensors and human skin, and low tissue perfusion [28]. The wide frequency range and time-varying nature of MAs pose challenges for conventional filtering techniques in their removal [215]. Consequently, various signal quality index (SQI) methods have been implemented to differentiate between high and low quality segments within the measured PPG signals [216].

In artifact detection, many studies traditionally utilize features derived from waveforms, including heart rate, amplitude, waveform morphology, and spectral features. Feature-based techniques for detecting anomalies in PPG data have several limitations. Firstly, the sliding-window approach commonly used in these methods limits the resolution at which artifacts can be detected. This is because each window must be evaluated individually, which can be computationally expensive and often fails to capture the global context of the signal. Additionally, handcrafted features, which are often used in these techniques, rely on predefined criteria that may not be consistent across different subjects or activities. This variability means that features effective for one individual might not work for another, necessitating constant adjustments. Furthermore, these methods frequently depend on accurate peak detection, which is challenging in PPG signals due to their nature, leading to potential inaccuracies in Anomaly Detection (AD) [217]. In this section, the feasibility of detecting low-quality signal sections is explored by employing a feature subset named *catch22* [218]. This subset is used to feed three different AD algorithms, tailored specifically to individual subjects, and compared to the traditional training process conducted over the entire dataset.

The *catch22* feature subset is known for its high performance in capturing a diverse and interpretable time series signature. It incorporates properties such as linear and non-linear autocorrelation, successive differences, value distributions, outliers, and fluctuation scaling properties. These characteristics enhance the classification and clustering performance in time-series analysis. This approach ensures a more robust and generalizable method for detecting low-quality sections in PPG signals. The primary focus of this work is the identification of motion artifacts

within the acquired signals, emphasizing the accurate detection and classification of these disturbances. The goal is to ensure the integrity of the signals used for clinical assessment by identifying segments affected by artifacts, rather than directly correcting or replacing those portions of the signals. However, the correction or replacement of artifact-contaminated signal segments represents a valuable and promising future direction for this research. By addressing these next steps, the overall robustness and accuracy of the signal processing pipeline could be further improved, ultimately enhancing the reliability of the system for clinical and real-world applications. The following section is structured as follows. Firstly, the data processing pipeline and the feature extraction process involving the *catch22* library are presented. Then, the tested AD algorithms are introduced. Subsequently, the gathered results are presented and discussed.

6.3.1 *catch22* Features Set

The *catch22* (CAnonical Time-series CHaracteristics) subset of features is a carefully selected set of 22 time-series features derived from a comprehensive time-series feature library. The selection process aimed to capture the dynamical properties of time series efficiently and interpretably. The *catch22* subset was designed to provide strong classification and clustering performance across diverse time-series datasets while minimizing redundancy among features. These features capture a diverse range of time-series properties, including distribution characteristics, temporal statistics, linear and non-linear autocorrelation, successive differences, and fluctuation analysis. This subset was designed to be computationally efficient and to provide meaningful, interpretable insights into the dynamical behavior of time series across various applications. Additionally, it eliminates the need for user-specific parameter adjustments and avoids dependence on hand-crafted features, such as peak-to-peak amplitude, heart rate, and pulse width that may not universally apply to subjects [206, 217]. In this application, the use of *catch22* features eliminates the need for user-specific parameter adjustments and avoids dependence on hand-crafted features like peak-to-peak amplitude, heart rate, and pulse width, which may not be universally applicable to all subjects.

6.3.2 Methodology

All the collected pulse waveforms underwent processing using the same standardized approach. The data processing pipeline devised for this application comprises three main segments: pre-processing, data segmentation, and labeling. Finally, the feature extraction section was performed using the *catch22* library. As the first step, the duration of all records was standardized to retrieve the same amount of data samples. In particular, the length was set at 60 seconds. Then,

to remove the presence of the DC offset and high-frequency noise, each acquisition underwent band-pass filtering between 0.3 Hz and 15 Hz, implemented with a 4th-order Chebyshev II filter [28]. Subsequently, the signal was divided into non-overlapping 3-second windows for a total of 20 epochs per each record. This segmentation served the purpose of partitioning the signals into segments of equal length. Moreover, it allowed the identification of the pulse waveforms corrupted by the presence of MAs. All detected epochs were annotated and subsequently utilized as labels for assessing the performance of the tested algorithms. Finally, the *catch22* library was used to extract the 22 features from all windows along with mean value, standard deviation, skewness, kurtosis, and the pairwise correlation coefficient between two epochs sharing the same ID and derived from the two mentioned electrode placements.

6.3.3 Tested Anomaly Detection Models

For the purpose of AD, three algorithms representing the current state-of-the-art were selected: One Class-SVM (OC-SVM), Isolation Forest (IF), and Local Outlier Factor (LOF). Each algorithm offers unique methodologies in detecting anomalies within datasets. Specifically, OC-SVM establishes a boundary for standard data points, labeling those outside the boundary as anomalies [219]. Instead, LOF evaluates the local density of data points, flagging outliers based on their isolation within their neighborhood [220]. In contrast, Isolation Forest aggregates predictions from multiple decision trees to assign a final anomaly score to each data point [221]. Unlike the previous AD methods that define "normal" data and classify deviations as anomalies, IF operates independently to isolate outliers, regardless of surrounding data points. This study performs a comparative analysis of AD algorithms, assessing their efficacy when customized for specific subjects w.r.t the conventional training process applied across the entire dataset. The outlier detection performance of the mentioned methods was compared when applied directly to the entire dataset and individually to each subject. In both cases, an offline and automated hyperparameter optimization was conducted for the adopted algorithms. In the first case, optimization was performed on the entire population, while in the second case, tuning was customized for each individual subject. Consequently, models were trained and tested for each subject in the dataset, with the optimization process involving various parameters. Firstly, the number of features used ranged from 1 to 27. Initially, highly mutually correlated features were removed, followed by sequential removal of features until the best subset was identified. Subsequently, the contamination parameter, which defines the proportion of outliers in the dataset, was varied between 0.001 and 0.1. This parameter significantly influences the model's ability to accurately identify anomalies.

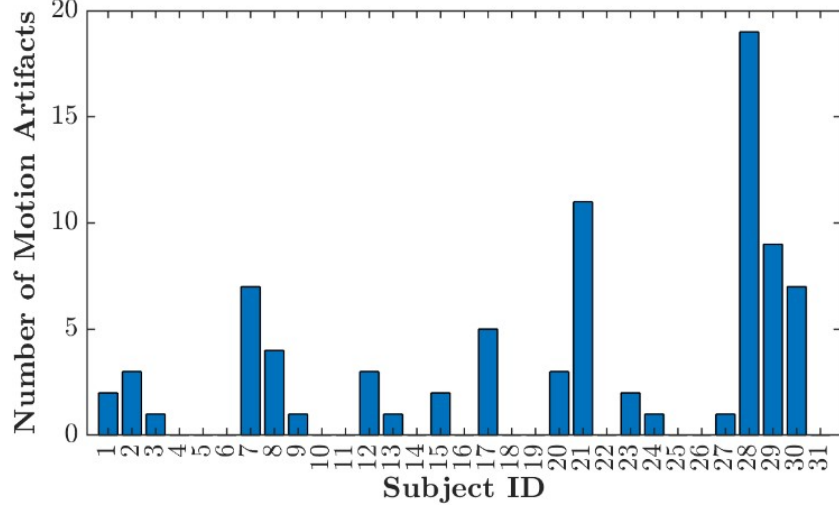


Figure 6.24: Motion artifacts distribution across recruited subjects.

6.3.4 Evaluation Metrics

As stated in the previous subsection, the presented models were trained and tested per each subject in the dataset. Given the significant class imbalance between the two classes, the performances of the OC-SVM, IF, and LOF were quantified through evaluation metrics such as precision, recall, and F1-score. Finally, an average of all metrics was computed along with its standard deviation to summarize the performance of each model. Within this set of indices, the score was computed by considering the combination of true positives (TP), true negatives (TN), false positives (FP), and false negatives (FN). The precision and recall scores computed in Eq.6.8 and Eq.6.9 were computed for each of the two classes referring to the presence of MAs ($\alpha \in \text{Normal, Artifact}$). In the context of this application, the scoring criteria for both classes were presented, with a specific emphasis on the Artifact class. This decision arises from the notable imbalance between the two classes, which, in the context of an overall assessment, could result in a biased evaluation of the scoring criteria.

$$Precision_{\alpha} = \frac{TP_{\alpha}}{TP_{\alpha} + FP_{\alpha}} \quad (6.8)$$

$$Recall_{\alpha} = \frac{TP_{\alpha}}{TP_{\alpha} + FN_{\alpha}} \quad (6.9)$$

Finally, the F1-score was computed as reported in Eq.6.10:

$$F1_{\alpha} = \frac{2 * Precision_{\alpha} * Recall_{\alpha}}{Precision_{\alpha} * Recall_{\alpha}} \quad (6.10)$$

6.3.5 Data Quality Assessment Results

As a result of the detailed processing pipeline, a comprehensive total of 14,880 epochs were systematically segmented, labeled, and subjected to feature extraction. Among the extensive dataset, only 85 epochs (approx. 0.57%) were identified as corrupted by MAs. These instances were distributed across 18 out of the total 31 participants. The MAs distribution across the entire dataset is displayed in Figure 6.24.

6.3.6 Anomaly detection Models Evaluation

Table 6.13: Computed evaluation metrics per each anomaly detection model.

Training Strategy	MLA	Precision _{AD}	Recall _{AD}	F1-Score _{AD}	Precision	Recall	F1-Score
Entire Dataset	OC-SVM	0.39	0.35	0.37	0.69	0.68	0.68
	IF	0.53	0.49	0.51	0.77	0.74	0.75
	LOF	0.43	0.39	0.41	0.71	0.69	0.70
Aggregated*	OC-SVM	0.50±0.17	0.64±0.31	0.55±0.20	0.75±0.09	0.82±0.16	0.77±0.10
	IF	0.91±0.14	0.94±0.11	0.92±0.12	0.95±0.07	0.97±0.05	0.96±0.06
	LOF	0.74±0.17	0.75±0.26	0.74±0.27	0.87±0.14	0.87±0.16	0.87±0.14

Abbreviations: MLA, machine learning algorithm, Precision_{AD}, Recall_{AD} and F1-Score_{AD} refer to the scoring criteria computed for the anomaly class.

* Evaluation metrics computed averaging the results achieved across subjects within dataset.

Table 6.13 compares the performance of three AD models—OC-SVM, IF, and LOF—under two training strategies: using the entire dataset and a personalized approach. Key metrics include Precision_{AD}, Recall_{AD}, and F1-Score_{AD} for detecting anomalies, along with overall Precision, Recall, and F1-Score.

When trained on the entire dataset, OC-SVM shows modest performance, with a Precision_{AD} of 0.39, Recall_{AD} of 0.35, and F1-Score_{AD} of 0.37. Its overall metrics are similarly limited, indicating a weaker balance between precision and recall compared to other models. IF, on the other hand, performs better, achieving a Precision_{AD} of 0.53, Recall_{AD} of 0.49, and F1-Score_{AD} of 0.51, along with stronger overall metrics, making it more reliable for AD. LOF, while better than OC-SVM, still lags behind IF, with a Precision_{AD} of 0.43, Recall_{AD} of 0.39, and F1-Score_{AD} of 0.41, indicating moderate performance.

The personalized training strategy significantly enhances the performance of all models. OC-SVM sees notable improvement, achieving a Precision_{AD} of 0.50 ± 0.17, Recall_{AD} of 0.64 ± 0.31, and F1-Score_{AD} of 0.55 ± 0.20, but it still does not surpass IF or LOF. IF remains the top performer under this strategy, with impressive metrics across the board: a Precision_{AD} of 0.91 ± 0.14, Recall_{AD} of 0.94 ± 0.11, and F1-Score_{AD} of 0.92 ± 0.12. Its overall performance is equally strong, reaffirming its robustness. LOF also improves with aggregation, showing significant

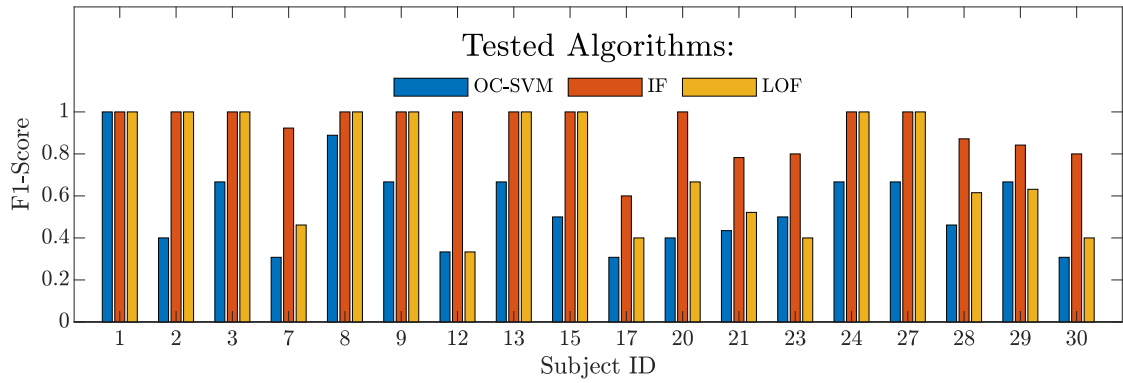


Figure 6.25: F1-score computed for target class across subjects displaying the presence of motion artifacts.

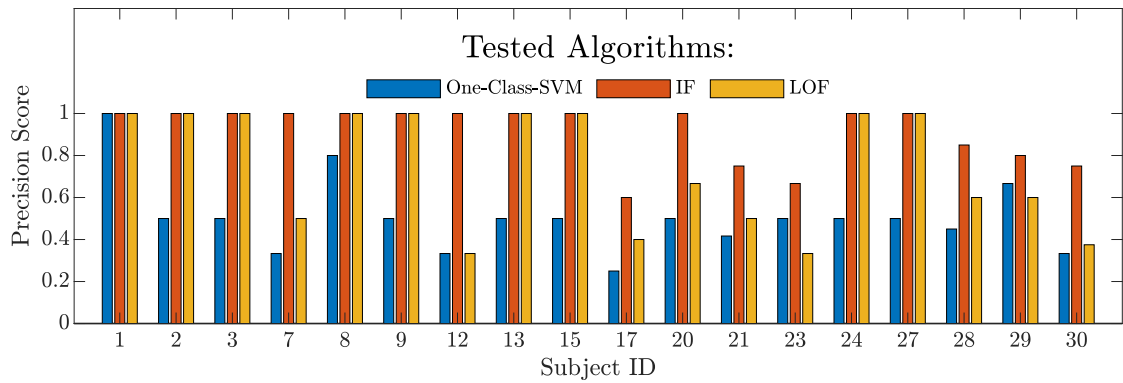


Figure 6.26: Precision score computed for target class across subjects displaying the presence of motion artifacts.

gains with a Precision_{AD} of 0.74 ± 0.28 , Recall_{AD} of 0.75 ± 0.26 , and F1-Score_{AD} of 0.74 ± 0.27 , though it remains slightly behind IF.

Figure 6.25, Figure 6.26, and Figure 6.27 show respectively the F1-score, precision, and recall score performance for each subject according to the three proposed algorithms. In all comparisons conducted, IF emerges as the top-performing AD algorithm, maintaining a score of at least 0.8 for all subjects except subject #17, where performance degradation is observed across all methods. Conversely, OC-SVM consistently ranks as the least effective method, yielding an F1-score of 0.3. Although LOF matches IF's performance in half of the subjects, its effectiveness decreases significantly in the remaining cases. The observed subpar performance in subject #17's results can be attributed to the quality of pulse waveforms. To gain insights into this issue, Principal Components Analysis (PCA) was employed for visualization. In Figure 6.28, the distribution of data points collected from subjects #8 and #17 is illustrated based on the first two principal components (explained variance equal to 98%). Meanwhile, Figure 6.29 showcases a segment

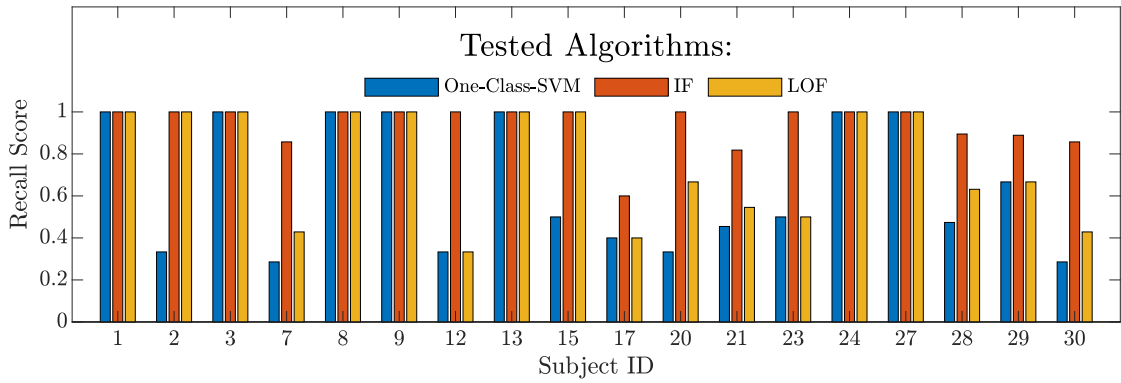


Figure 6.27: Recall score computed for target class across subjects displaying the presence of motion artifacts.

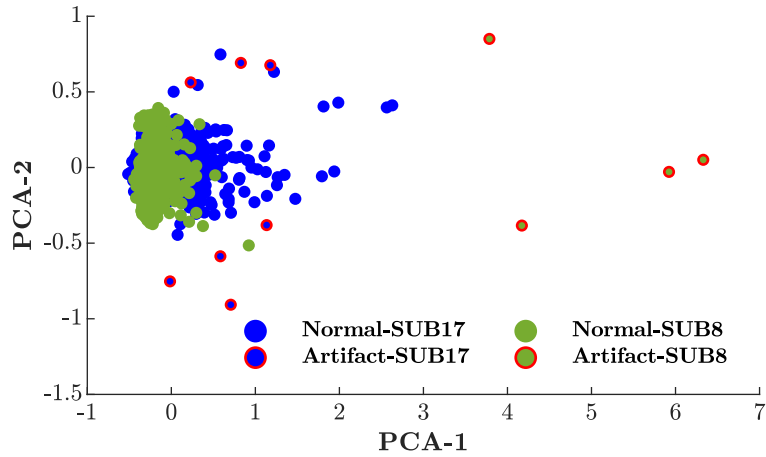


Figure 6.28: Data points distribution between subjects with different quality of pulse waveforms.

of pulse waveforms used for feature extraction. A comparative analysis of the waveform morphology and regularity between subjects #8 and #17 elucidates the sparser distribution observed in the latter. This observation provides clarity on the challenges associated with subject #17’s pulse waveforms, contributing to the suboptimal performance in MAs detection.

These findings underscore the efficacy of IF in AD while highlighting the limitations of OC-SVM. While LOF manages to match IF’s performance in half of the subjects, its effectiveness decreases significantly in the remaining cases. The higher consistency of IF w.r.t LOF is also reflected in the standard deviation computed for all scoring criteria. Indeed, IF achieves half of the standard deviation compared to LOF across all metrics. Notably, for subject #12, LOF exhibits a reduction in performance equal to 65% when compared to IF, highlighting the variability in efficacy across different subjects.

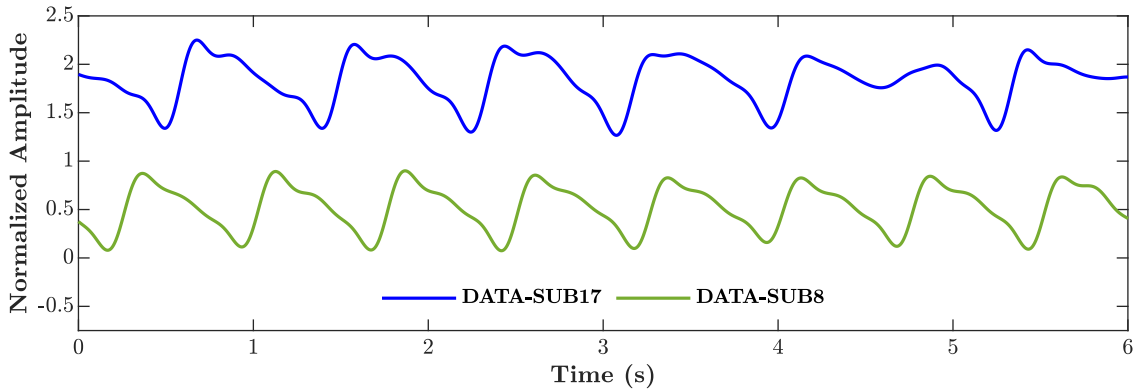


Figure 6.29: Pulse waveforms acquired from subject #17 and subject #8 in blue and green respectively.

6.3.7 Discussion

This work investigated the identification of MAs in PPG signals collected from diverse locations through a high-performing feature subset known as *catch22* along with AD algorithms. In artifact detection, numerous studies have traditionally employed waveform-derived features, such as heart rate, amplitude, waveform morphology, and spectral features [206, 217]. However, a significant limitation arises from the inter-subject variability in participants with diverse pulse waveform morphologies. In addressing this drawback, *catch22* emerges as a promising solution as it prevents the need for user-specific parameter adjustments and avoids reliance on pre-defined features that may not be universally applicable across subjects. Moreover, they captures a diverse and interpretable signature of time series, encompassing properties like linear and non-linear autocorrelation, successive differences, value distributions, and outliers, as well as fluctuation scaling properties making them suitable for this application. In addition, this study scrutinizes the performance differences when customizing the methods for individual subjects versus employing a more generalized approach. In the context of AD, three specific algorithms were thoughtfully chosen: OC-SVM, IF, and LOF [117, 118, 222]. Analyzing the motion artifact recognition algorithms across the entire dataset, as outlined in Table 6.13, unveils a pervasive challenge in achieving consistent and robust performance in the identification of MAs within PPG data. These results can be clarified by examining the underlying mechanisms of the tested AD algorithms. These unsupervised models employ distinct methodologies for identifying anomalies, leading to diverse performances on the same dataset. PCA was employed to visualize the distribution in space available in the dataset. Figure 6.30 provides a representation based on the first two principal components (explained variance equal to 98%), highlighting epochs affected by artifacts in red and normal instances depicted in blue.

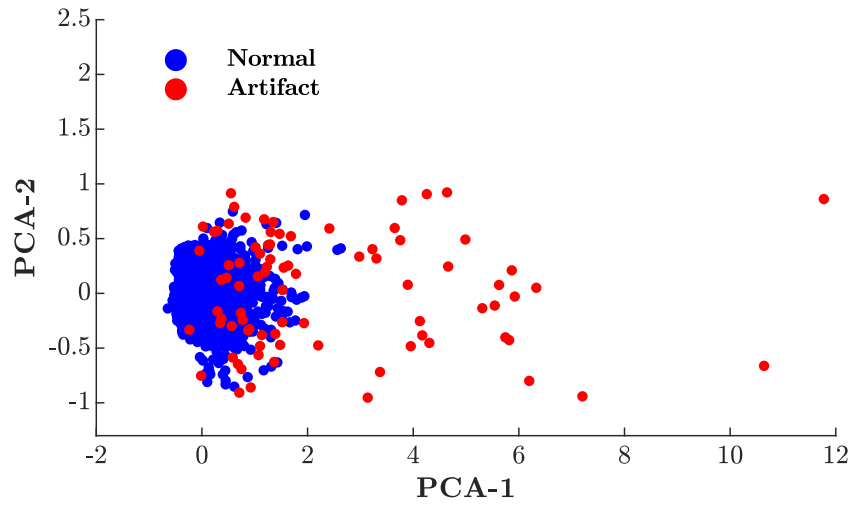


Figure 6.30: Principal component analysis employed to highlight the intrinsic discrepancies between normal data belonging to different subjects.

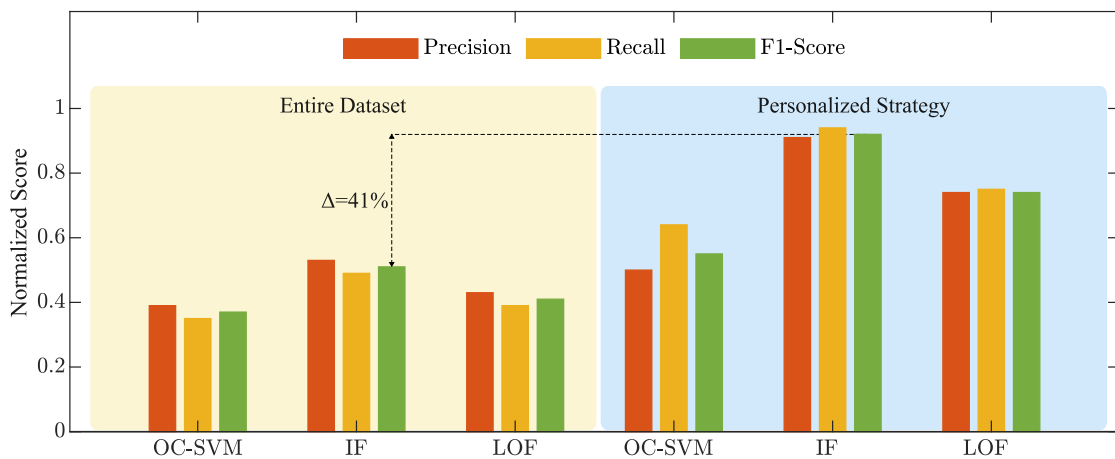


Figure 6.31: Target class aggregated evaluation metrics computed per each anomaly detection model.

Examining the relative position of artifacts in close proximity to the blue cluster offers valuable insights. This observation could clarify the challenges faced by OC-SVM and LOF, both reliant on the spatial distribution of normal points for AD. A personalized solution by tuning each model specifically for individuals exhibiting one or more MAs was adopted to address this issue. The results demonstrated that ML models tailored on specific characteristics of the recording such as baseline level, timing and pattern repeatability, deliver more accurate identification of MAs when compared to a traditional generalized approach. This approach aligns with the broader trend in healthcare studies, where various studies aim to monitor physiological parameters such as blood pressure [126], diabetes management

[223], and stress [224]. An unsupervised approach was adopted to overcome the drawbacks associated with supervised methods, such as the need for data labeling and handling missing data in long-term monitoring using wearable technology [119]. By personalizing each model to subject data and extracting the most informative features, the challenges associated with local AD were successfully mitigated, improving the identification of MAs by up to 41% for the F1-score on the IF, Figure 6.31. However, developing and maintaining these models is resource-intensive and raises privacy concerns due to the need for sensitive data. Generalized models, on the other hand, are built for broad use across diverse populations, making them more scalable and easier to manage. Despite the associated resource costs, our findings suggest that a tailored solution improves the accuracy in detecting MAs, leading to better identification of high-quality records. To conclude, the proposed work effectively demonstrated the feasibility of detecting MAs in biological data using the *catch22* feature subset combined with a personalized strategy. These features are versatile and suitable for various time-series applications, independent of the specific signals being recorded. The personalized approach not only improves the performance of the AD model but also extends its applicability to a wide range of wearable devices beyond PPG sensors. By customizing the model for individual users, this method shows significant potential for future use across diverse wearable health monitoring systems.

Chapter 7

Discussion, Future Works and Conclusions

7.1 Thesis Contributions

Cardiovascular diseases are the foremost cause of mortality globally, resulting in approximately 17.9 million deaths annually [1]. Over 80% of these deaths are attributed to heart attacks and strokes, with one-third occurring prematurely in individuals under 70 years of age. Hypertension, or high blood pressure, markedly elevates the risk of coronary heart diseases, including stroke and heart failure [5]. It is identified as the leading risk factor for mortality and disability in the European Region, responsible for nearly a quarter of deaths and 13% of disabilities. Often presenting without symptoms, uncontrolled high BP can lead to serious outcomes such as heart attacks and strokes [6]. Thus, regular monitoring of critical biomarkers, including blood pressure and pulse wave velocity, is crucial in preventing the onset of CVDs. Integrating these assessments into routine health check-ups enables healthcare providers to better detect and manage the development and progression of CVDs. This proactive strategy improves patient outcomes and reduces healthcare costs by preventing severe complications and optimizing resource use [10].

This thesis aims to explore innovative methodologies and develop advanced hardware and firmware solutions to enhance the accuracy, convenience, and reliability of non-invasive cardiovascular health monitoring systems, with a specific focus on pulse wave velocity and blood pressure monitoring.

7.1.1 Cost and Accessibility

The investigation into the first biomarker centers on addressing the primary challenges related to the cost, accessibility, and reliability of the standard methodology for assessing PWV. Integrating PWV measurements into routine medical practice encounters significant obstacles, mainly due to the complexity and time

required for these assessments. Despite PWV's recognized importance in evaluating arterial stiffness and cardiovascular risk, its clinical adoption remains limited. Although advanced non-invasive devices offer high accuracy, their prohibitive cost and limited availability in various healthcare settings restrict widespread use. Consequently, the first objective is to develop an affordable and user-friendly device that meets the requirements for reliable PWV estimation [82, 85, 88].

As an initial step, extensive research was undertaken to identify a sensing element that meets the specified requirements for the proposed device. The sensor must first have sufficient resolution to accurately capture the pressure waveform. Secondly, it should possess a compact form factor to ensure ease of handling by the operator and seamless integration into the system. Additionally, low power consumption is crucial to achieve the desired autonomy in practical applications, allowing the device to operate efficiently for extended durations. Moreover, the sensing element must be commercially available, as reliance on a prototypal sensor in previous iterations hindered widespread adoption of the former version of the Athos device [139]. Chapter 3 details the analysis conducted on the application of commercial micro force sensors for PWV assessment. The chosen sensing element for this application is the load cell FMAMSDXX005WCSC3, produced by Honeywell. This piezoresistive load cell was selected due to its compact size (5mm x 5mm base, 2.15mm height), low power consumption (approximately 14mW), and affordability. It offers a digital output with a 12-bit data resolution over a 0-5N force range, making it ideal for detecting the arterial pulse necessary for precise PWV measurement.

Once the sensing element was determined, the novel device was developed. Unlike traditional PWV measurement devices [88, 89], this system features real-time data transmission to a receiving station equipped with a graphical user interface (GUI), providing clinicians with immediate PWV values and feedback on signal quality. This real-time feedback loop significantly enhances the process by eliminating the need for post-processing. With respect to its predecessor [139], the new design aimed to eliminate the need for an ECG connection and wired components, resulting in a fully portable and user-friendly device that maintains high accuracy in PWV measurements. The device's accuracy and reliability were validated in a pre-clinical study against the gold-standard SphygmoCor device, demonstrating a strong linear correlation ($R^2 = 0.89$) and acceptable agreement in Bland-Altman analysis [160]. Additionally, the device underwent thorough electromagnetic compatibility and clinical usability testing to ensure adherence to medical safety standards (IEC-60601) and confirm the ease of use in a real-case scenario.

7.1.2 Variability and Inaccuracies in Traditional Methods

In parallel with the development of the wireless acquisition system, the variability and potential sources of inaccuracy in traditional PTT evaluation methods,

specifically fiduciary points, were examined [74, 171, 172]. Nowadays, wearable devices that meet clinical standards can monitor numerous clinical indicators, such as heart rate and blood pressure. Many studies have explored assessing PWV using standalone wearable devices following this trend. Extracting pulse waves from locations other than clinically defined sites can distort signal shapes, thereby reducing the accuracy of these traditional methods [101]. To overcome the limitations of using a single localized feature for PWV evaluation, a new set of algorithms has been developed. These algorithms focus on analyzing specific sections of pulse waveforms, thus avoiding the reliance on a single feature for PWV assessment. Although further validation studies are necessary, region-based approaches like 'diastole patching' [74] and 'region-matching' [68], [75] have demonstrated excellent accuracy in PWV assessment, in line with the accuracy criteria outlined in the 2010 ARTERY Society guidelines [53].

Chapter 5 introduces a region-based cross-correlation (RBCC) method for assessing carotid-femoral pulse wave velocity. Previous research, such as [169, 173, 174], utilized cross-correlation for calculating PTT, but its application was restricted to local PWV assessments due to morphological differences in pulse waves at distant acquisition sites. The proposed RBCC approach addresses this limitation by using a set of signals with a consistent shape for cross-correlation, ensuring the portion of the signal used for PTT calculation remains constant across different sites. This study emphasizes the methodology for identifying a signal window that optimizes the algorithm's performance. As highlighted in [175], pulse waveforms from various body locations exhibit distinct morphologies. Factors such as sensor positioning, operator expertise, and individual anatomy can alter the shape of blood pulses. The need to define a specific signal section arises from the necessity to minimize morphological disparities between pulse waves while maintaining temporal information. Research has shown that the early systolic and end-diastolic portions of the blood pulse are less likely to be affected by reflected waves and MAs compared to the diastolic component [74, 176, 177, 178]. Consequently, the search for the processing window involved analyzing the amplitude and slope of the rising front of all waveforms in the dataset. Three different indicators were employed to identify the optimal feature and best location on the signals for accurate assessment. Two specific points have been considered in the definition of the upper limit. The first one corresponds with the maximum of the slope, (B1), and the one located at 95% of the systolic peak's amplitude (B2).

The *CV* indicator was used to determine whether to select the slope or the amplitude as the parameter to define the processing window's upper boundary. The *intraSV* was used to quantify the consistency of the tested points within each subject. Finally, *interSV* was employed to assess the stability of those across the entire dataset. A set of indicators was defined to quantify the stability of the identified pulse section over the entire dataset. As result of the carried-out analysis, B1 proved to be the most stable point to be used for the application of the algorithm.

The accuracy of PWV estimation was evaluated by comparing cfPWV values obtained using the Intersecting Tangent Point (ITP) method and the RBCC approach on both high-quality data and data corrupted by varying noise levels.

When comparing the IT method and RBCC without noise, the only notable difference in the best-case scenario is the average PWV difference of -0.07 m/s for IT and 0.16 m/s for RBCC. The RMSE difference between the two methods is less than 10%, while the mean difference in standard deviation, Pearson correlation coefficient, and coefficient of determination (R^2) is less than 1%.

The robustness of the algorithms under different noise levels revealed that RBCC is more tolerant compared to the IT method. The Friedman test established the statistical significance of the differences in cfPWV values between IT and RBCC across four noise levels. In all cases, the P value was below 0.05, with three values significantly lower (10^{-5} , 10^{-8} , and 10^{-8} , respectively, for 15, 20, and 25 dB). The exception was at an SNR of 10 dB, where P equaled 0.04. It is important to note that 10 dB is a limiting case and might not be suitable for clinical applications. According to [180], there is an inverse relationship between RMSE and SNR at a constant sampling frequency, indicating the significant impact of SNR on estimation error. Additionally, [181] identifies 15 dB as the SNR threshold below which peak detection algorithm performance declines by more than 20%.

The acquisition process also depends on a skilled operator who would discard a signal with distorted morphology. In all other comparisons, the RBCC method showed a significantly lower mean absolute error in individual PWV evaluation compared to reference values from noise-free signals. This underscores the limitations of relying on a single feature in the signal for PTT assessment, as noise or artifacts can lead to significant estimation errors. By realigning the pulse's upslope and considering more data points, the RBCC method mitigates the potential misdetection of points A or B, resulting in a more robust and accurate PWV assessment. Although the RBCC method performs slightly differently from the intersecting tangent method, it proves to be an excellent and more robust alternative for estimating PWV. The study of PWV is closely connected to blood pressure research, as PWV serves as an essential indicator of arterial stiffness, which is a major determinant of cardiovascular health. Increased arterial stiffness, measured through PWV, is often associated with higher systolic blood pressure and the development of hypertension. This relationship occurs because stiffer arteries lead to faster pulse wave propagation, which in turn reflects elevated blood pressure levels. Furthermore, PWV is used to predict the progression of blood pressure and the potential development of hypertension, offering a valuable tool for early detection and management of cardiovascular risk.

7.1.3 Limitations of Traditional Cuff-Based Devices for BP Monitoring

The field of cuffless blood pressure assessment is set for significant advancements due to clinical needs and technological innovations. While traditional cuff-based methods have been invaluable, they come with limitations that cuffless technologies aim to address. The potential for continuous, non-invasive BP monitoring is becoming more feasible, offering a more comprehensive and dynamic understanding of cardiovascular health.

Cuffless BP measurement technologies present several key advantages over traditional methods. A primary benefit is the ability to provide continuous monitoring. Traditional cuff-based methods only offer intermittent measurements, capturing a snapshot of the patient's BP at a single moment. In contrast, cuffless methods can continuously monitor BP, providing a complete 24-hour profile and capturing its variability. This continuous data stream offers a more accurate and detailed picture of cardiovascular health, reflecting natural BP fluctuations throughout the day. Optical sensors, similar to those in fitness trackers, measure beat-to-beat variability and calculate systolic and diastolic readings through mathematical modeling [90, 91, 92]. These sensors, typically worn on the wrist or finger, enable continuous BP monitoring without the discomfort and sleep disruption caused by traditional cuff inflations.

Another significant advantage of cuffless technologies is their non-invasive nature. Traditional BP cuffs can cause discomfort and may induce stress responses that affect reading accuracy. Cuffless methods eliminate the need for cuff inflation, reducing patient discomfort and providing a more accurate reflection of true BP levels. Additionally, these methods can be used during everyday activities, offering a realistic view of BP fluctuations in real-life conditions.

Several innovative approaches are being explored for cuffless BP measurement. One method is PTT, which estimates BP by measuring the time it takes for the pulse wave to travel between two arterial sites. While promising, this method requires further refinement to improve accuracy and reliability across diverse populations. Another approach involves optical systems based on PPG sensors, which detect blood volume changes in the microvascular bed of tissue. These sensors are integrated into wearable devices and can be used alone or in combination with other metrics to estimate BP. Additionally, machine learning algorithms applied to large datasets are playing a crucial role in developing cuffless BP technologies by analyzing complex data and creating predictive models to enhance BP measurement accuracy.

In collaboration with the Wireless Sensors Network (WSN) Group at the Tyn-dall National Institute, University College Cork, a custom optical-based acquisition system was designed to assess variations in blood volume between the brachial artery and the thumb. This custom device addresses the limitations of traditional

cuff-based devices, which, while effective for on-the-spot BP measurements, are impractical for continuous monitoring. Traditional devices are cumbersome and intrusive, making them unsuitable for long-term use. Continuous monitoring is essential for managing hypertension and assessing cardiovascular risk, yet current devices do not offer the necessary comfort and convenience for extended use. According to [190], PPG-based BP measurement devices, including those that detect PTT, should either maintain a consistent contact pressure (CP) or incorporate CP measurement into the calibration equation for deriving BP.

Therefore, during the creation of the proposed device, careful consideration was given to the design of the enclosures. These enclosures were engineered to ensure that the sensor maintains steady pressure at the sample site without requiring the operator's presence to keep it in place. This design feature allows for consistent acquisition setups for individual subjects, thereby enhancing measurement reproducibility. Additionally, since the device aims to detect blood flow from the brachial artery, the PPG sensors were equipped with multiple LEDs. A comparison was conducted with the Biosignal Flux acquisition system to assess the quality of the retrieved PPG signals. PTT measurements for each subject at rest were performed over three consecutive one-minute data captures. Each acquisition was done with the patient seated, both feet on the floor, and hands on the table at heart level. The results show that the PTT measurements obtained by the proposed device are significantly equivalent to those from the reference system. Furthermore, an assessment of the standard deviation indicates that both systems have comparable repeatability. These results demonstrate that the developed acquisition system is a valuable solution for providing high-quality data over an extended period. Its design effectively overcomes the current limitations of cuff-based monitoring systems, offering a steady and reliable alternative. In conclusion, the proposed device serves as a solid foundation for creating a robust platform that marks a significant advancement in the field of cuffless blood pressure monitoring.

7.1.4 Capturing Individual-Specific Variations in BP Monitoring

The research further explored the promising field of cuffless BP measurement, focusing on developing a machine learning-based approach to capture individual-specific variations in BP monitoring. Traditional BP monitoring methods fall short in addressing these variations, which are crucial for precise blood pressure management and cardiovascular risk assessment. Personalized approaches may offer a solution, but existing methods do not effectively address this need. Improving BP monitoring accuracy and reliability requires models that account for the unique physiological characteristics of each individual.

To address this, a personalized multiclass classification model was developed to detect BP variations associated with physical or cognitive workload. BP is

influenced by various factors, including physical activity, cognitive stress, and environmental conditions. The lack of a standardized protocol for validating cuffless BP devices presents significant challenges in ensuring their accuracy and reliability in clinical settings. To overcome these issues, a structured data collection protocol was created to induce BP variations through physical and cognitive tasks among different subjects. Adhering to strict guidelines during data capture sessions ensured measurement accuracy and minimized errors, attributing BP variations to the specific tasks performed.

This study compares the performance of person-dependent and generalized models in tracking BP macro-variations associated with physical or cognitive workload using a Random Forest (RF) classifier. RF was chosen for its ability to handle nonlinear relationships between extracted features and BP variation. In other studies, RF has outperformed other nonlinear models like SVM with a nonlinear kernel and neural networks, and it is less prone to overfitting.

The choice between personalized and universal models depends on the specific context and objectives. Personalized models, tailored to individual characteristics like age, gender, medical history, and lifestyle, provide more accurate and relevant BP predictions, especially for individuals with complex health conditions or unique risk factors. However, constructing and maintaining personalized models for each user is resource-intensive and raises privacy and data protection concerns. Generalized models, on the other hand, are designed to work across a wide range of users without individual customization, making them more scalable and easier to implement. However, they may lack the accuracy of personalized models.

This study found that the generalized approach struggled with high inter-subject variability, as reflected in the averaged metrics (0.36, 0.36, 0.31, 0.37). A hybrid approach combining personalized and universal models could be beneficial for BP monitoring. A universal model could provide initial predictions, while personalized models could enhance performance for users with complex health conditions or unique risk factors, accommodating the inherent diversity in BP patterns.

In [126], a transfer learning technique that personalizes specific layers of a pre-trained network improved the performance of PPG-based BP estimation, emphasizing the importance of the number of data samples and source subjects used for training. The conducted analysis shows that using 30% of the total available data (approximately 162 seconds) for the personalization phase significantly reduces the required time compared to the approach in [126], which used 250 seconds per subject. Combining a subset of source subjects with an adequate fraction of data for pre-training enhances the robustness and generalizability of personalized models across a broader spectrum of BP assessment cases compared to standard generalized models.

7.1.5 Challenges in Long-Term Monitoring

Finally, the problem of MAs detection over physiological data is examined. A major challenge in long-term monitoring systems, especially in real-world conditions, is the ability to distinguish high-quality signal windows from those affected by MAs. Wearable health monitoring devices, such as those using PPG sensors, often suffer from signal degradation due to MAs. These artifacts can result from changes in blood flow velocity, relative movement between the sensor and the skin, and low tissue perfusion. Traditional filtering techniques are often inadequate for effectively addressing these issues.

For this purpose, a personalized anomaly detection model using a high-performing subset of time-series features called *catch22* was developed to detect the presence of MAs in PPG data. In artifact detection, numerous studies have traditionally employed waveform-derived features, such as heart rate, amplitude, waveform morphology, and spectral features [206, 217]. However, a significant limitation arises from the inter-subject variability in participants with diverse pulse waveform morphologies. In addressing this drawback, *catch22* emerges as a promising solution as it prevents the need for user-specific parameter adjustments and avoids reliance on pre-defined features that may not be universally applicable across subjects. Moreover, they captures a diverse and interpretable signature of time series, encompassing properties like linear and non-linear autocorrelation, successive differences, value distributions, and outliers, as well as fluctuation scaling properties making them suitable for this application. In addition, this study scrutinizes the performance differences when customizing the methods for individual subjects versus employing a more generalized approach. In the context of anomaly detection, three specific algorithms were thoughtfully chosen: OC-SVM, IF, and LOF [117, 118, 222]. In this work, an unsupervised approach was adopted to overcome the drawbacks associated with supervised methods, such as the necessity for data labeling and the challenges of handling missing data in long-term monitoring using wearable technology [119]. In this regard, we explored a personalized solution by tuning each model specifically for individuals exhibiting one or more MAs. The results demonstrated that machine learning models personalized to subjects' physiological characteristics significantly enhanced predictive performance compared to a traditional generalized approach. By personalizing each model to subject data and extracting the most informative features, we successfully mitigated the challenges associated with local anomaly detection, improving the identification of MAs up to 41% for the F1-score on the isolation forest. This approach aligns with the broader trend in healthcare studies, where various studies aim to monitor physiological parameters such as blood pressure [126], diabetes management [223], and stress [224].

The study employs three unsupervised algorithms—One-Class Support Vector Machine (OC-SVM), Isolation Forest (IF), and Local Outlier Factor (LOF)—to

identify anomalies. By focusing on these methods, the paper aims to improve the reliability of PPG-based health monitoring by effectively distinguishing high-quality signal windows from those affected by MAs. This approach is particularly valuable for long-term health monitoring in real-world conditions, where traditional methods fall short.

7.2 Future Works

7.2.1 Pulse Wave Velocity

Despite the improvements reported in this thesis concerning the PWV assessment, several challenges affect the accuracy and reliability of measurements. One significant issue is the accuracy of measuring the pulse travel distance. Traditional methods often use approximations based on body surface measurements or the subject’s height, which can systematically overestimate or underestimate PWV [85, 169, 225]. In this context, vascular curvature poses an additional challenge. External measurements do not consider the complex curvatures within the vasculature, especially in the presence of tortuous vessels. The actual path traveled by the pulse wave is often not linear, and ignoring these curvatures can lead to significant errors in PWV assessment. As a result, the measurements may not accurately reflect the true velocity of the pulse wave, further complicating the evaluation of arterial stiffness and cardiovascular health.

Another critical factor is operator dependence. Many PWV measurement devices, especially those utilizing tonometric or piezoelectric technology, require precise sensor positioning by the operator. The skill and experience of the operator play a crucial role in obtaining accurate measurements. This dependency introduces variability and potential errors, as inconsistent sensor placement can significantly impact the results [85]. In addition to addressing the existing challenges, significant efforts should be made to actively incorporate ML solutions into PWV assessment [226]. ML algorithms have the remarkable capability to process and analyze large volumes of complex data, including time-series and waveform data from pulse signals. By detecting subtle patterns and variations that might be missed by traditional methods, ML significantly improves the precision of PWV measurements [227]. Case studies have demonstrated the successful implementation of ML models to estimate PWV from various inputs, such as age, blood pressure, and pulse wave features. These studies showcase the practical applicability and accuracy of ML-based PWV assessments. Validation studies have shown good agreement between ML models and traditional methods, ensuring the reliability and reproducibility of these models. This body of evidence underscores the potential of ML to transform PWV measurement into a more precise and user-friendly process, facilitating its adoption in clinical settings.

Furthermore, ML would facilitate the integration of PWV assessment into consumer devices like smartphones and fitness trackers. These devices, equipped with sensors such as low-cost and unobtrusive sensors, can capture pulse signals and use ML algorithms to estimate PWV[228]. This integration could make cardiovascular health monitoring more accessible to the general population, promoting proactive health management.

A further aspect requiring a deeper investigation is the relationship between baPWV (or raPWV) and cfPWV [58, 59, 60]. The clinical validity of local PWV assessments remains a subject of debate [169]. Nevertheless, measurement errors related to blood pulse propagation distance, variations in pulse waveform shapes from different arterial sites, and the impact of multiple arterial wave reflections on local PWV estimates are minimal. These factors imply that local PWV measurements could serve as reliable indicators of arterial stiffness with appropriate validation and standardization.

Extensive validation and comparative studies are necessary to determine the feasibility of using peripheral arterial sites as reliable sources of data for arterial stiffness evaluation. This would enhance the accessibility of the measurement, leveraging the large number of wearable devices currently available and introducing PWV assessment into everyday healthcare.

7.2.2 Cuffless Blood Pressure Assessment

The landscape of blood pressure monitoring is undergoing a significant transformation with the advent of cuffless technologies. These innovative approaches promise to make blood pressure measurement more convenient, continuous, and accessible, paving the way for better hypertension management and cardiovascular health monitoring. However, despite of the advancements in the field of cuffless blood pressure measurement need to continue in the future. To fully realize the potential of cuffless BP technologies, several key research areas need to be addressed. Comprehensive data collection and calibration are essential for developing accurate predictive models. Therefore, large training datasets, used to define both new physiological models and machine learning approaches must include a wide range of demographic and physiological variables to ensure that the models can accurately estimate BP across different populations. Calibration methods, whether periodic or one-time, must be standardized and validated to ensure consistency and reliability.

Rigorous clinical trials are also necessary to compare cuffless BP devices against established cuff-based methods and intra-arterial measurements. These trials should assess the reproducibility, accuracy, and clinical relevance of cuffless BP readings in diverse populations and settings. Additionally, developing international standards for the evaluation and validation of cuffless BP devices is crucial. These standards should address the specific challenges of continuous, non-invasive BP monitoring and ensure consistency across different types of devices.

The integration of cuffless BP measurement into everyday healthcare has the potential to transform hypertension management and cardiovascular risk assessment. Continuous BP monitoring allows for more personalized treatment plans, adjusting medication and lifestyle interventions based on real-time data. By capturing BP fluctuations and trends over time, cuffless devices can help in the early detection of hypertension and other cardiovascular conditions, potentially before clinical symptoms appear. On a broader scale, the widespread use of cuffless BP monitors could enhance population-level health monitoring, enabling more effective public health interventions and reducing the burden of cardiovascular diseases.

In conclusion, the future of cuffless blood pressure assessment is bright, with significant advancements expected in technology, research, and clinical applications. As these innovations continue to develop, they promise to offer more accurate, convenient, and comprehensive BP monitoring, ultimately improving patient outcomes and advancing the understanding of cardiovascular health. The shift from traditional cuff-based methods to continuous, non-invasive monitoring represents a major leap forward in the field of hypertension management, promising a new era of personalized and precise healthcare.

7.3 Conclusions

This thesis aimed to enhance the accuracy, convenience, and reliability of non-invasive cardiovascular health monitoring systems, focusing particularly on PWV and BP monitoring. Several innovative solutions were developed to address critical issues in this field.

The problem of cost and accessibility in integrating pulse wave velocity measurements into routine medical practice has been tackled by developing a reliable, affordable, and yet user-friendly device. The proposed system employs commercially available piezoresistive load cell sensors, making it economical and easy to integrate into clinical settings. By lowering the cost and complexity barriers, PWV measurements become more accessible and feasible for regular use in diverse healthcare environments.

Traditional methods for PWV measurement, which rely on point-to-point feature extraction, often suffer from variability and inaccuracies due to the differing morphologies of pulse waveforms at various arterial sites. To address this, a region-based cross-correlation algorithm was developed. This novel method enhances the robustness and accuracy of PWV measurements by analyzing specific sections of pulse waveforms, thus reducing susceptibility to noise and artifacts. This improvement ensures a more reliable assessment of arterial stiffness and cardiovascular risk.

The limitations of traditional cuff-based devices, which are effective for on-the-spot measurements but impractical for continuous monitoring, were also addressed. Thanks to the collaboration with Tyndall National Institute, a custom optical-based

acquisition system that uses PPG sensors to measure blood volume changes was developed. This system utilizes PPG sensors to measure blood volume changes continuously, offering a non-invasive and less intrusive alternative to traditional cuff-based devices. This enables long-term monitoring crucial for managing hypertension and cardiovascular risk.

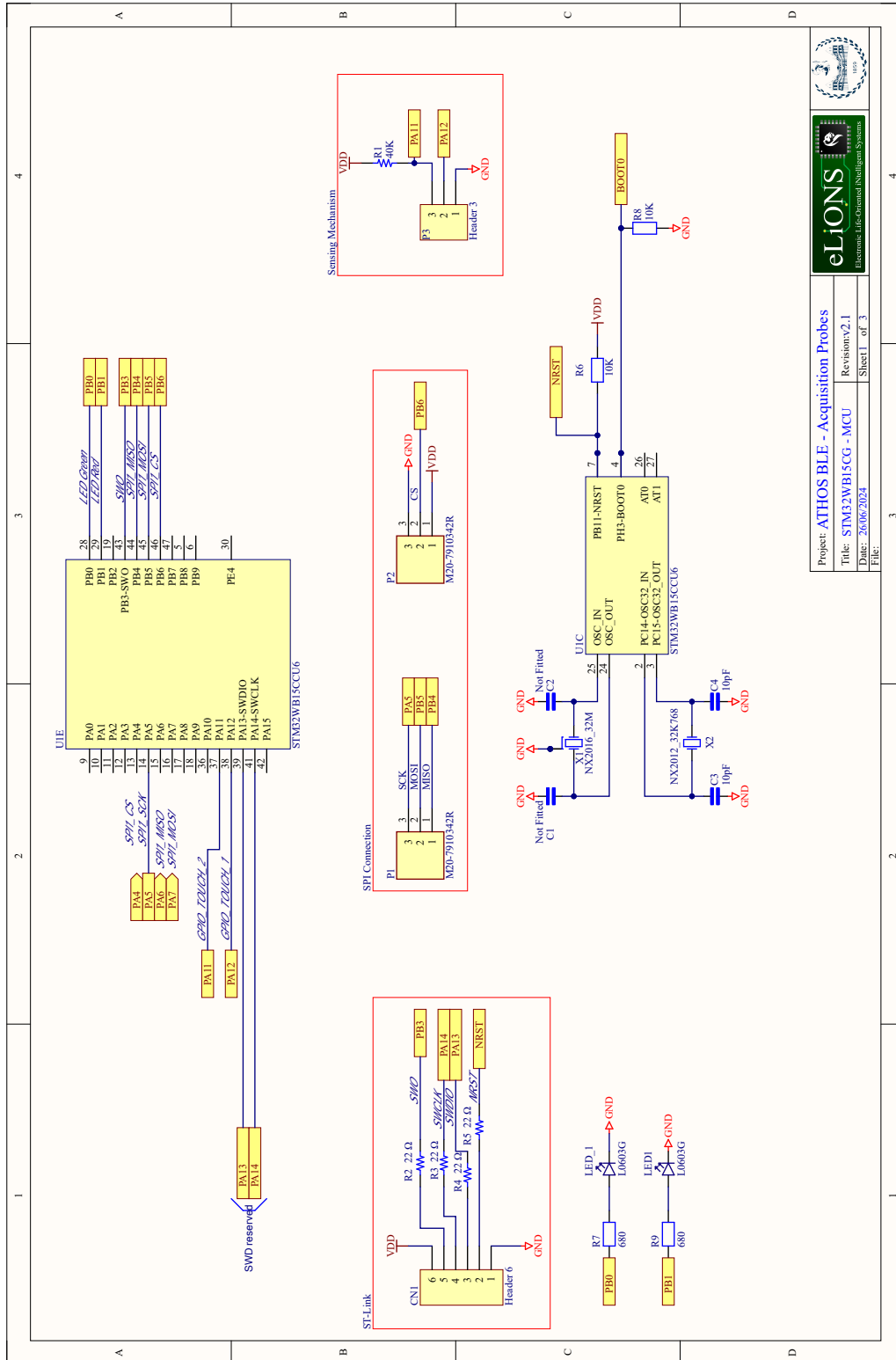
Current BP monitoring methods fall short in capturing individual-specific variations, which are crucial for precise blood pressure management and cardiovascular risk assessment. To address this, the research introduced a personalized multiclass classification model for BP monitoring. This model employs machine learning algorithms tailored to individual physiological characteristics, significantly improving the accuracy and reliability of BP monitoring. By accommodating the unique needs of each individual, this personalized approach ensures precise BP management and cardiovascular risk assessment.

In tackling the challenges of long-term monitoring, particularly the issue of MAs, a personalized anomaly detection model was developed using *catch22* time-series features. This model effectively distinguishes high-quality signal windows from those affected by MAs, thereby improving the reliability of wearable health monitoring devices in real-world conditions. This approach enhances the accuracy of long-term health monitoring by addressing signal degradation issues.

In conclusion, the advancements presented in this thesis offer significant improvements in non-invasive cardiovascular health monitoring. By addressing the limitations of traditional methods and introducing innovative solutions, this work paves the way for more accurate, convenient, and comprehensive monitoring, ultimately improving patient outcomes and advancing the understanding of cardiovascular health.

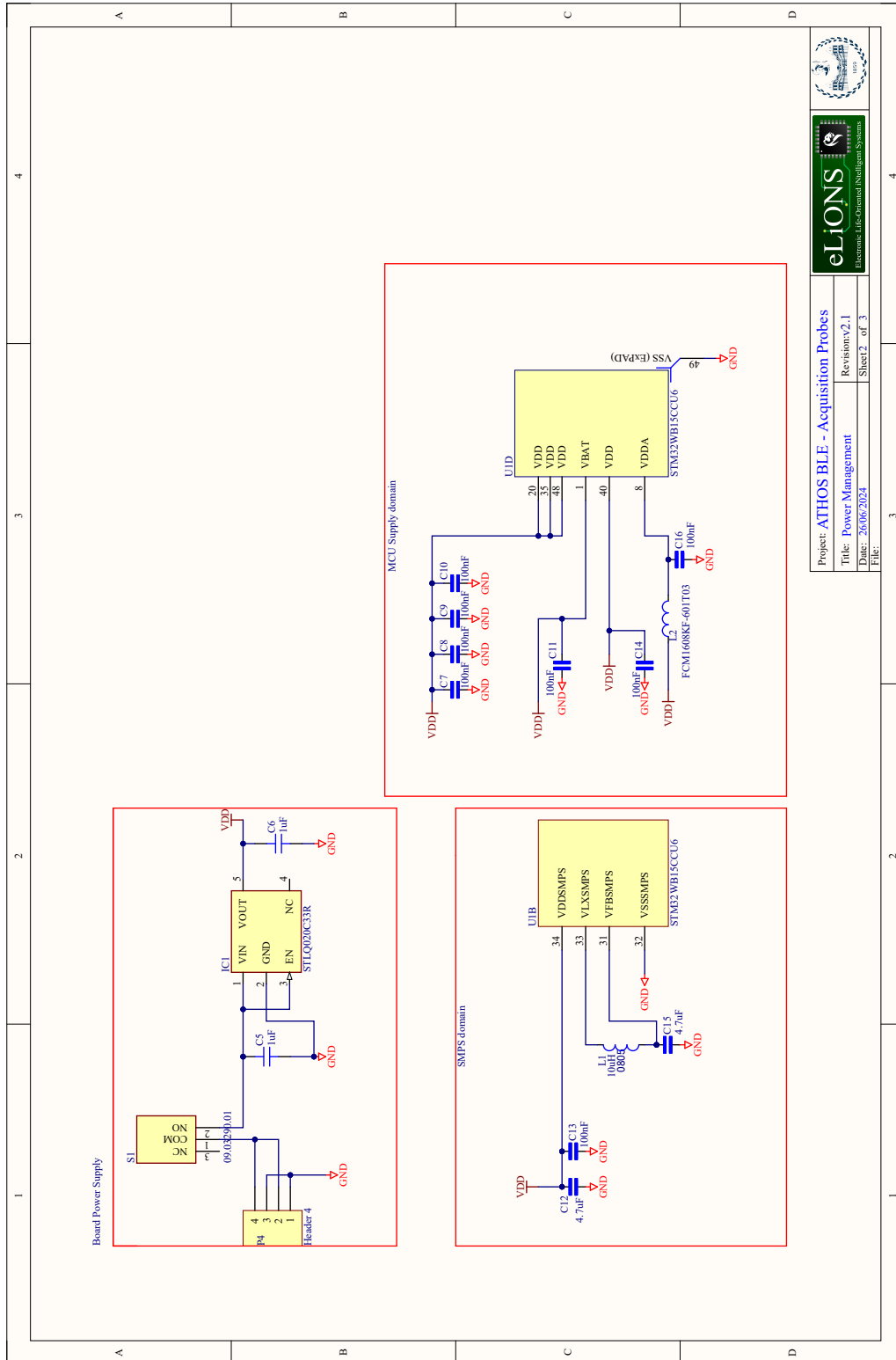
Appendix A

PCB Schematics Wireless System for PWV Assessment



Project: ATHOS BLE - Acquisition Probes
 Title: STM32WB15CC - MCU
 Date: 26/06/2024
 Revision: v2.1
 Sheet 1 of 3

Figure A.1




 Project: ATHOS BLE - Acquisition Probes	
Title: Power Management	Revision: v2.1
Date: 26/06/2024	Sheet 2 of 3
File:	

Figure A.2

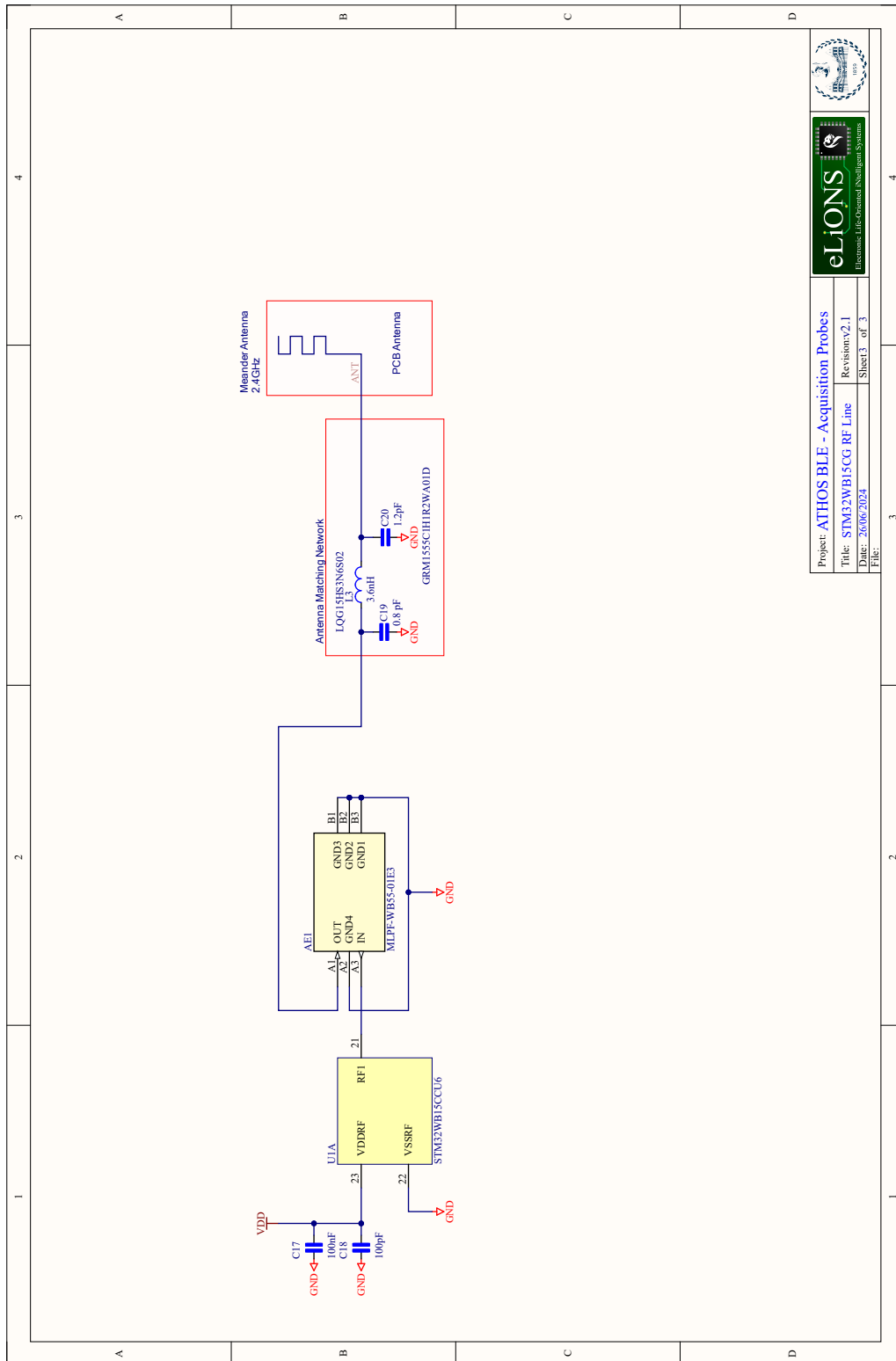


Figure A.3

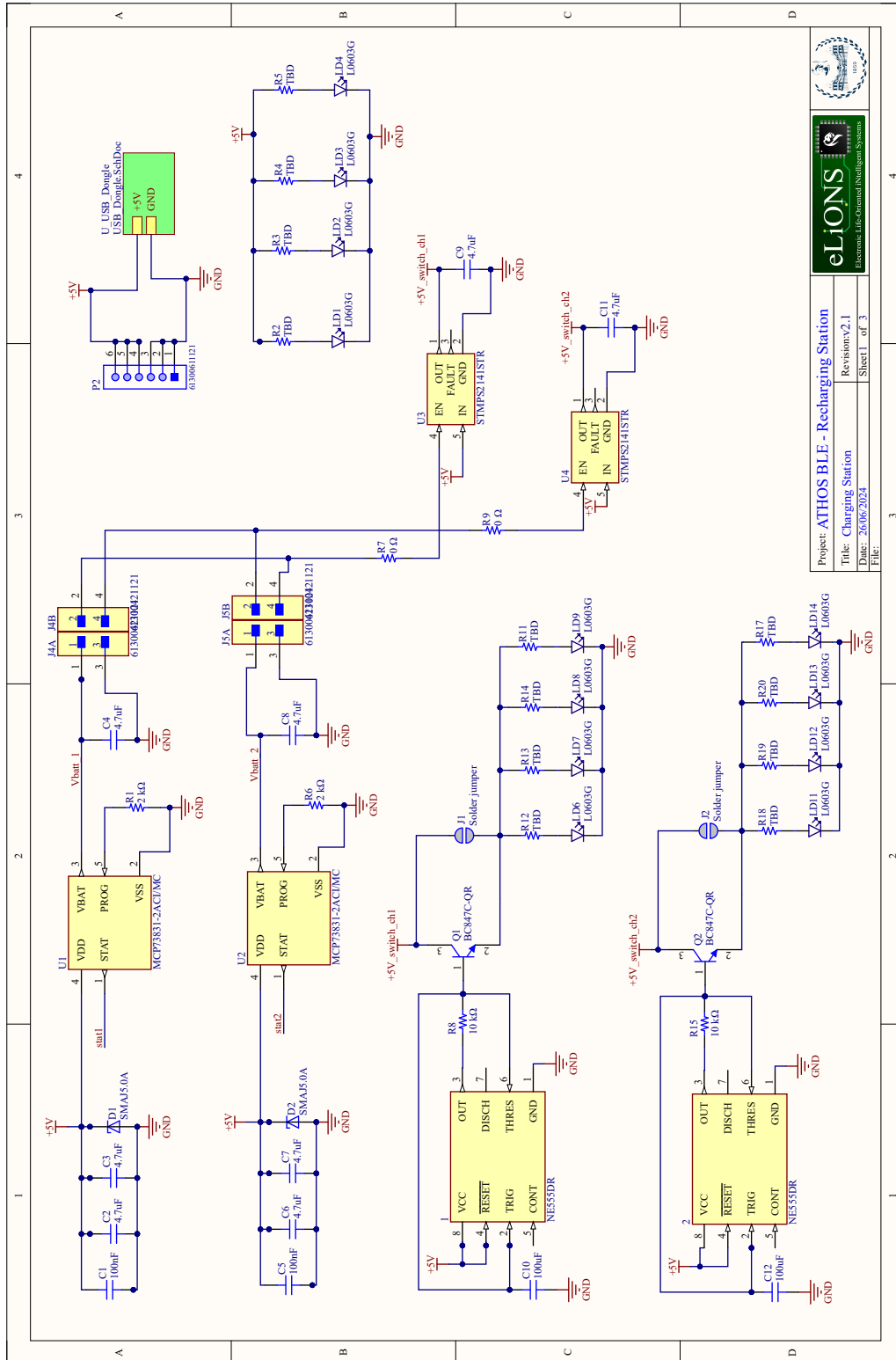


Figure A.4

Appendix B

Results of Generalized and Personalized Strategies for Cuffless BP Assessment

Table B.1: Test set Results using the person independent model (PIM).

Sub-ID	Test Set				RF Hyperparameters	
	Precision	Recall	F1	Accuracy	Max Depth	Estimators
1	0.35	0.36	0.28	0.35	20	80
2	0.19	0.22	0.20	0.23	20	80
3	0.38	0.29	0.19	0.28	20	80
4	0.19	0.27	0.19	0.27	20	80
5	0.54	0.36	0.32	0.34	20	80
6	0.43	0.54	0.44	0.51	20	80
7	0.74	0.74	0.74	0.75	20	80
8	0.36	0.40	0.35	0.39	20	80
9	0.35	0.40	0.36	0.42	20	80
10	0.09	0.27	0.14	0.26	20	80
11	0.41	0.45	0.40	0.53	20	80
12	0.64	0.60	0.60	0.64	20	80
13	0.16	0.16	0.16	0.19	20	80
14	0.77	0.59	0.53	0.60	20	80
15	0.15	0.33	0.21	0.44	20	80
16	0.40	0.19	0.16	0.18	20	80
17	-	-	-	-	-	-
18	0.30	0.30	0.29	0.30	20	80
19	0.09	0.20	0.12	0.20	20	80
20	0.38	0.45	0.38	0.43	20	80
21	0.36	0.27	0.20	0.29	20	80
22	0.18	0.10	0.11	0.10	20	80
23	0.09	0.20	0.13	0.21	20	80
24	0.46	0.54	0.49	0.56	20	80
25	0.56	0.63	0.52	0.63	20	80
26	-	-	-	-	-	-
27	0.15	0.34	0.20	0.35	20	80
28	0.72	0.60	0.53	0.59	20	80
29	-	-	-	-	-	-
30	0.25	0.30	0.20	0.35	20	80
31	0.13	0.24	0.14	0.23	20	80

Table B.2: Test set results using person specific model PSM_{SD} .

Sub-ID	Test Set				RF Hyperparameters	
	Precision	Recall	F1	Accuracy	Max Depth	Estimators
1	1	1	1	1	50	60
2	0.43	0.67	0.52	0.63	10	60
3	1	1	1	1	10	60
4	1	1	1	1	10	60
5	0.95	0.94	0.94	0.95	10	90
6	0.85	0.85	0.86	0.86	50	100
7	0.99	0.99	0.99	0.99	10	60
8	0.98	0.98	0.98	0.98	10	60
9	1	1	1	1	10	60
10	0.98	0.98	0.98	0.98	10	60
11	0.95	0.97	0.96	0.96	10	60
12	0.99	0.98	0.98	0.99	10	90
13	1	1	1	1	20	70
14	0.5	0.67	0.56	0.68	10	60
15	1	1	1	1	10	60
16	1	1	1	1	10	60
17	-	-	-	-	-	-
18	1	1	1	1	10	60
19	1	1	1	1	10	80
20	0.99	0.85	0.84	0.84	10	70
21	0.8	0.78	0.77	0.75	20	60
22	1	1	1	1	10	100
23	1	1	1	1	50	60
24	1	1	1	1	10	60
25	0.8	0.78	0.78	0.78	10	60
26	-	-	-	-	-	-
27	1	1	1	1	10	60
28	0.50	0.67	0.55	0.67	10	90
29	-	-	-	-	-	-
30	0.98	0.98	0.98	0.98	30	60
31	0.86	0.86	0.86	0.86	10	70

Table B.3: Test set results using person specific model $PSM_{5,30\%}$.

Sub-ID	Test Set				RF Hyperparameters		
	Precision	Recall	F1	Accuracy	Max Depth	Estimators	Subjects for Training
1	0.97	0.97	0.97	0.97	40	80	2 10 12 13 31
2	0.97	0.97	0.97	0.97	20	70	3 4 7 20 23
3	0.96	0.96	0.96	0.96	20	70	12 21 23 24 30
4	0.97	0.96	0.97	0.97	50	100	5 9 12 15 25
5	0.89	0.89	0.89	0.89	30	70	15 18 20 25 31
6	0.90	0.90	0.90	0.90	20	70	7 8 20 24 28
7	0.94	0.94	0.94	0.94	50	80	3 7 12 13 31
8	0.97	0.97	0.97	0.97	20	70	3 7 12 13 31
9	0.97	0.97	0.97	0.98	50	70	2 12 13 18 19
10	0.95	0.95	0.95	0.94	40	90	4 13 20 21 24
11	0.97	0.96	0.97	0.97	20	90	7 8 14 15 18
12	0.96	0.94	0.95	0.95	10	70	3 4 14 16 22
13	0.92	0.91	0.91	0.93	50	80	3 5 8 12 30
14	0.99	0.99	0.99	0.99	30	90	4 11 12 24 30
15	0.98	0.97	0.97	0.97	20	70	5 11 21 24 31
16	0.97	0.97	0.97	0.97	30	80	1 12 20 25 31
17	-	-	-	-	-	-	-
18	0.96	0.95	0.96	0.96	50	100	11 20 23 27 30
19	1.00	1.00	1.00	1.00	20	100	2 3 14 24 30
20	0.94	0.94	0.94	0.94	30	100	1 5 8 30 31
21	0.82	0.81	0.82	0.81	20	100	3 4 5 19 25
22	0.97	0.97	0.97	0.97	30	80	12 15 27 28 30
23	0.95	0.95	0.95	0.95	30	70	2 10 14 19 21
24	0.99	0.99	0.99	0.99	20	90	13 19 27 30 31
25	0.93	0.93	0.93	0.93	30	90	18 27 28 30 31
26	-	-	-	-	-	-	-
27	1.00	1.00	1.00	1.00	50	70	8 9 16 25 28
28	0.95	0.94	0.94	0.94	30	70	2 6 20 24 31
29	-	-	-	-	-	-	-
30	0.92	0.93	0.93	0.93	50	70	1 8 11 28 31
31	0.94	0.94	0.94	0.94	30	70	3 19 20 22 30

Table B.4: Test set results using person-specific model $PSM_{10,30\%}$.

Sub-ID	Test Set				RF Hyperparameters		
	Precision	Recall	F1	Accuracy	Max Depth	Estimators	Subjects for Training
1	0.93	0.93	0.93	0.93	20	100	2 7 8 12 13 14 15 20 22 31
2	0.88	0.88	0.88	0.88	40	90	1 3 7 15 18 21 22 23 28 31
3	0.97	0.97	0.97	0.97	40	90	2 8 9 11 12 13 16 20 25 27
4	0.97	0.96	0.97	0.97	30	80	1 2 10 15 16 21 22 23 27 31
5	0.90	0.90	0.90	0.91	40	100	2 4 6 9 21 22 23 27 28 30
6	0.86	0.85	0.85	0.85	50	80	4 5 7 9 13 19 21 22 27 31
7	0.96	0.96	0.96	0.96	30	100	3 4 5 8 10 14 15 20 22 31
8	0.97	0.97	0.97	0.97	40	90	4 5 6 9 12 13 14 16 23 27
9	0.97	0.97	0.97	0.97	50	100	1 3 4 14 15 18 21 23 24 25
10	0.93	0.93	0.93	0.93	20	100	6 9 12 14 15 16 22 25 28 30
11	0.87	0.85	0.86	0.88	30	100	3 10 12 18 21 23 24 27 28 30
12	0.89	0.86	0.86	0.89	50	100	1 4 6 7 11 18 19 21 23 31
13	0.95	0.92	0.93	0.93	20	90	2 3 6 10 11 14 15 18 20 28
14	0.97	0.97	0.97	0.97	30	80	4 7 9 11 12 16 19 20 23 25
15	0.99	0.99	0.99	0.99	30	100	1 2 4 11 13 20 24 25 27 31
16	0.92	0.92	0.92	0.92	50	100	6 10 12 13 15 19 25 27 28 30
17	-	-	-	-	-	-	-
18	0.93	0.93	0.93	0.94	50	70	1 5 6 10 14 20 21 27 28 30
19	0.98	0.98	0.98	0.98	50	70	6 9 10 14 20 22 23 25 27 28
20	0.94	0.94	0.94	0.94	50	90	1 2 6 7 8 11 19 21 27 31
21	0.82	0.77	0.78	0.76	30	90	2 5 6 10 14 16 22 24 25 31
22	0.88	0.85	0.85	0.86	40	80	4 5 6 7 10 12 18 24 25 30
23	0.95	0.95	0.95	0.95	40	70	8 9 16 19 20 21 24 25 28 31
24	0.99	0.99	0.99	0.99	30	100	1 4 6 8 10 11 14 22 27 30
25	0.92	0.92	0.91	0.92	50	100	1 3 4 12 15 19 21 22 28 31
26	-	-	-	-	-	-	-
27	0.94	0.94	0.94	0.94	40	90	6 7 9 14 16 18 24 28 30 31
28	0.97	0.97	0.97	0.97	40	100	1 4 8 13 14 18 19 23 24 25
29	-	-	-	-	-	-	-
30	0.91	0.88	0.89	0.91	30	90	1 4 6 10 13 18 22 25 27 28
31	0.90	0.90	0.90	0.90	50	80	2 5 10 15 16 19 20 23 24 30

Table B.5: Test set results using person-specific model $PSM_{15,30\%}$.

Sub-ID	Test Set				RF Hyperparameters		
	Precision	Recall	F1	Accuracy	Max Depth	Estimators	Subjects for Training
1	0.98	0.98	0.98	0.98	40	90	3 6 9 12 14 18 19 20 22 23 24 27 28 30 31
2	0.91	0.89	0.90	0.89	50	100	1 4 5 7 8 12 13 16 18 19 21 22 27 28 30
3	0.99	0.99	0.99	0.99	40	100	1 2 4 5 6 8 11 13 15 19 22 23 24 27 30
4	0.94	0.92	0.92	0.93	20	100	1 3 5 8 9 11 12 14 15 16 18 20 21 22 27
5	0.89	0.89	0.88	0.89	40	100	3 4 7 11 12 13 15 18 19 20 21 22 24 30 31
6	0.87	0.87	0.87	0.86	40	90	3 5 9 10 15 16 18 19 20 22 23 25 27 28 30
7	0.97	0.96	0.97	0.97	20	70	3 4 5 6 8 11 12 13 16 19 22 23 25 27 31
8	0.95	0.95	0.95	0.95	50	80	1 2 5 6 10 14 15 16 18 19 23 25 27 28 30
9	0.90	0.90	0.90	0.90	30	100	2 6 7 10 11 12 15 16 18 21 22 23 24 28 30
10	0.95	0.95	0.95	0.95	20	100	2 4 6 8 9 15 18 19 22 23 24 27 28 30 31
11	0.92	0.90	0.91	0.92	20	90	2 4 5 6 7 8 12 13 15 16 21 22 27 30 31
12	0.91	0.90	0.90	0.92	40	70	2 3 7 9 10 13 15 18 19 20 21 25 27 30 31
13	0.84	0.86	0.85	0.86	20	70	4 5 6 9 12 14 15 16 20 22 23 24 25 28 31
14	0.96	0.96	0.96	0.96	50	100	1 2 6 8 9 13 16 19 20 21 22 23 24 25 30
15	0.94	0.92	0.93	0.92	20	90	1 2 4 5 8 11 12 13 14 16 19 22 23 28 30
16	0.96	0.95	0.95	0.95	40	90	1 2 3 4 7 8 10 11 12 18 19 20 23 24 25
17	-	-	-	-	-	-	-
18	0.96	0.96	0.96	0.96	40	100	3 6 10 12 13 14 15 16 19 20 21 24 25 27 30
19	0.95	0.94	0.94	0.94	30	90	1 3 5 6 7 11 12 14 18 21 23 24 25 30 31
20	0.92	0.92	0.92	0.92	30	70	1 2 3 5 6 7 9 11 13 14 22 25 27 28 31
21	0.83	0.79	0.80	0.79	50	90	1 2 4 5 6 7 8 9 14 15 20 23 27 28 31
22	0.89	0.89	0.89	0.89	20	80	1 2 5 6 8 10 13 15 16 18 20 24 25 27 31
23	0.90	0.90	0.90	0.90	50	80	4 5 8 10 11 12 14 15 19 21 22 24 25 28 30
24	0.89	0.89	0.88	0.88	30	80	4 5 6 7 9 10 13 18 20 21 23 25 27 28 31
25	0.91	0.91	0.91	0.91	30	90	2 3 4 5 8 9 12 13 16 20 22 24 27 28 31
26	-	-	-	-	-	-	-
27	0.96	0.95	0.95	0.95	20	100	2 3 4 5 7 9 18 19 20 21 22 23 28 30 31
28	0.95	0.95	0.95	0.95	30	80	2 4 5 8 10 11 12 13 14 16 18 19 22 23 25
29	-	-	-	-	-	-	-
30	0.85	0.86	0.85	0.86	50	90	1 2 4 5 7 9 11 13 16 18 19 22 23 27 31
31	0.87	0.85	0.85	0.86	20	90	1 2 4 6 7 8 12 13 16 18 20 23 27 28 30

Table B.6: Test set results using person specific model $PSM_{5,50\%}$.

Sub-ID	Test Set				RF Hyperparameters		
	Precision	Recall	F1	Accuracy	Max Depth	Estimators	Subjects for Training
1	0.98	0.98	0.98	0.98	30	80	10 14 16 27 31
2	0.98	0.98	0.98	0.98	20	60	8 9 22 24 25
3	0.98	0.98	0.98	0.98	20	100	9 10 16 21 25
4	0.98	0.98	0.98	0.98	40	100	13 20 22 30 31
5	0.94	0.94	0.94	0.95	40	80	7 15 22 28 31
6	0.92	0.92	0.92	0.92	50	80	7 8 15 21 22
7	0.96	0.96	0.96	0.96	20	100	1 15 19 28 30
8	0.98	0.98	0.98	0.98	50	70	4 12 20 23 27
9	1	1	1	1	20	90	5 6 8 24 25
10	0.97	0.97	0.97	0.97	20	80	8 9 11 19 23
11	0.98	0.97	0.97	0.98	20	100	2 10 15 19 23
12	0.97	0.95	0.96	0.96	20	60	2 4 15 16 25
13	0.97	0.96	0.96	0.96	30	80	6 10 11 21 27
14	1	1	1	1	40	90	3 7 20 21 27
15	0.98	0.98	0.98	0.98	20	100	6 10 12 16 27
16	0.99	0.99	0.99	0.99	30	70	4 5 9 10 13
17	-	-	-	-	-	-	-
18	0.97	0.98	0.97	0.97	30	90	10 11 14 20 31
19	0.98	0.98	0.98	0.98	20	100	5 6 8 10 13
20	0.97	0.97	0.97	0.97	30	80	6 8 22 23 28
21	0.88	0.88	0.87	0.86	50	80	4 12 14 24 31
22	0.95	0.96	0.95	0.96	50	80	7 15 16 22 28
23	1	1	1	1	40	90	9 11 19 22 27
24	0.99	0.99	0.99	0.99	40	90	7 11 16 18 19
25	0.82	0.81	0.80	0.81	20	80	1 14 15 19 22
26	-	-	-	-	-	-	-
27	1	1	1	1	30	90	1 7 9 12 28
28	0.98	0.98	0.98	0.98	30	70	5 12 21 22 27
29	-	-	-	-	-	-	-
30	0.94	0.95	0.95	0.95	30	60	1 2 5 21 23
31	0.94	0.94	0.94	0.94	40	80	7 22 23 25 30

Table B.7: Test set results using person-specific model $PSM_{10,50\%}$.

Sub-ID	Test Set				RF Hyperparameters		
	Precision	Recall	F1	Accuracy	Max Depth	Estimators	Subjects for Training
1	0.97	0.97	0.97	0.97	20	70	2 4 5 11 14 18 19 22 25 27
2	0.94	0.93	0.94	0.94	30	90	1 4 12 16 18 21 22 23 24 28
3	0.99	0.99	0.99	0.99	30	90	1 2 8 12 16 19 21 25 28 30
4	0.99	0.99	0.99	0.99	30	80	8 9 11 12 13 15 18 20 23 30
5	0.91	0.91	0.91	0.91	20	80	7 9 11 20 21 23 24 28 30 31
6	0.91	0.91	0.91	0.91	20	90	2 9 15 19 22 23 27 28 30 31
7	0.99	0.99	0.99	0.99	40	60	3 5 12 13 21 22 23 25 27 30
8	0.98	0.98	0.98	0.98	20	100	1 5 10 11 12 14 18 19 28 31
9	0.96	0.96	0.96	0.96	40	100	2 3 5 14 15 19 21 23 24 28
10	0.95	0.95	0.95	0.95	30	70	2 9 12 15 19 23 24 25 28 30
11	0.97	0.95	0.96	0.96	40	90	3 5 8 10 13 21 25 27 28 30
12	0.98	0.97	0.98	0.98	40	60	1 2 5 6 8 20 21 23 27 31
13	0.95	0.9	0.92	0.93	30	100	3 6 11 15 16 19 21 23 24 28
14	0.98	0.98	0.98	0.98	50	100	6 10 15 18 20 23 25 27 28 30
15	1	0.99	0.99	0.99	30	100	4 6 8 9 10 13 14 16 19 24
16	0.95	0.95	0.95	0.95	20	70	1 4 9 12 15 20 22 23 25 27
17	-	-	-	-	-	-	-
18	0.97	0.96	0.96	0.96	30	90	1 2 6 7 10 13 15 16 21 24
19	0.97	0.97	0.97	0.97	20	100	3 5 6 12 16 18 21 24 25 28
20	0.96	0.96	0.96	0.96	30	80	2 3 5 9 12 15 18 22 24 25
21	0.88	0.87	0.88	0.86	50	100	1 2 3 5 6 8 10 11 15 16
22	0.96	0.97	0.96	0.96	30	90	2 6 8 13 20 21 23 24 27 30
23	0.96	0.96	0.96	0.96	30	90	7 9 11 12 15 19 22 27 28 30
24	0.96	0.95	0.96	0.96	20	100	4 6 7 13 14 18 19 20 27 30
25	0.93	0.94	0.93	0.93	40	60	1 2 3 10 12 14 18 23 28 31
26	-	-	-	-	-	-	-
27	1	1	1	1	40	70	4 5 16 18 20 21 23 25 30 31
28	0.97	0.97	0.97	0.97	30	90	2 3 6 7 10 15 16 18 21 30
29	-	-	-	-	-	-	-
30	0.94	0.95	0.94	0.95	30	90	5 7 9 10 11 21 22 25 27 28
31	0.93	0.93	0.93	0.93	20	90	1 3 9 10 11 12 18 21 22 30

Table B.8: Test set results using person-specific model $PSM_{15,50\%}$.

Sub-ID	Test Set				RF Hyperparameters		
	Precision	Recall	F1	Accuracy	Max Depth	Estimators	Subjects for Training
1	0.94	0.94	0.94	0.94	50	90	2 3 5 6 9 10 13 15 16 19 22 23 25 27 31
2	0.95	0.94	0.94	0.94	20	100	3 4 5 9 12 13 14 15 16 18 19 20 21 25 30
3	0.97	0.97	0.97	0.97	20	100	1 2 5 9 10 11 12 15 19 21 22 23 24 25 30
4	0.97	0.96	0.96	0.96	50	80	2 3 7 8 10 12 14 16 18 21 22 23 27 28 30
5	0.92	0.92	0.92	0.92	20	90	1 3 10 12 13 14 15 16 18 19 20 24 25 27 28
6	0.9	0.91	0.9	0.9	30	100	1 3 5 7 8 9 11 12 13 16 20 22 25 27 28
7	0.97	0.97	0.97	0.97	20	80	1 2 4 9 10 13 14 16 21 22 23 24 28 30 31
8	0.97	0.97	0.97	0.97	50	80	2 5 7 10 13 14 18 19 21 22 23 25 27 28 31
9	0.97	0.97	0.97	0.97	50	90	2 5 6 7 8 13 14 15 16 19 20 21 23 30 31
10	0.95	0.96	0.95	0.95	20	100	2 3 8 13 14 15 18 21 22 23 24 25 27 28 30
11	0.97	0.96	0.96	0.97	20	80	2 3 7 9 10 12 13 14 15 16 20 22 24 27 28
12	0.96	0.95	0.96	0.96	30	90	3 5 6 8 10 11 18 19 20 22 23 25 27 30 31
13	0.88	0.91	0.89	0.9	30	90	1 2 8 9 10 11 14 15 19 20 21 22 23 25 30
14	0.96	0.96	0.96	0.96	50	90	1 4 6 9 10 11 12 15 16 18 20 23 24 28 31
15	0.98	0.98	0.98	0.98	20	60	1 2 7 9 12 13 14 20 21 22 23 24 25 27 28
16	0.93	0.92	0.92	0.92	40	80	4 5 8 9 10 12 18 20 21 22 25 28 27 30 31
17	-	-	-	-	-	-	-
18	0.98	0.97	0.97	0.98	30	90	1 3 6 12 13 14 15 16 19 21 22 23 27 28 31
19	0.96	0.96	0.96	0.96	40	100	1 3 4 5 8 10 11 12 13 18 20 21 22 25 27
20	0.94	0.94	0.93	0.93	50	100	2 5 7 8 9 11 12 14 16 18 22 23 25 27 28
21	0.91	0.9	0.9	0.88	20	100	2 4 5 9 10 13 14 16 18 19 20 23 24 27 28
22	0.96	0.96	0.96	0.96	40	100	4 6 7 8 11 13 14 15 19 20 21 23 27 28 30
23	0.97	0.97	0.97	0.97	20	100	1 2 8 9 11 12 14 19 20 21 22 24 27 28 30
24	0.95	0.95	0.95	0.95	40	90	2 3 4 6 8 11 14 16 18 20 21 23 28 30 31
25	0.9	0.9	0.9	0.9	30	80	1 2 3 5 6 7 9 14 16 18 19 21 24 27 28
26	-	-	-	-	-	-	-
27	1	1	1	1	20	90	2 4 8 13 14 15 16 18 19 20 21 23 24 28 30
28	0.96	0.96	0.96	0.96	20	80	2 5 7 8 9 11 12 14 16 18 19 23 24 28 30
29	-	-	-	-	-	-	-
30	0.93	0.94	0.93	0.93	30	90	2 5 8 9 10 11 12 14 16 20 21 22 25 28 31
31	0.91	0.91	0.91	0.91	30	90	1 2 3 6 10 11 12 13 14 15 21 22 25 28 30

Appendix C

Clinical Usability Questionnaire

Clinical Usability Questionnaire

This document aims at defining a plan for the Focus Group intended for the formative evaluation of the device. The usability file provides the confirmation of the safety of the user interface of the medical device ATHOS, that enables effective use and protects against potentially harmful use errors.

Participants are selected in accordance with IEC-62366 the participants shall include at least 4 representatives end users. The formative activities shall be performed by at least a product designer, a usability expert, 3 clinical experts.

Closed response based on scores:

0, No issues detected; 1, Cosmetic/aesthetic issue (e.g., difficult to understand figures in the instructions, causes delays in use but does not affect functionality in any way); 2, Minor usability issue (e.g., complex to use, frustrates the user, or is uncomfortable to handle); 3, Major usability issue (e.g., data is lost or it is unclear whether it has been entered correctly); 4, Catastrophic usability issue (e.g., critical error in test execution and clinical data entry, potential diagnosis error).

Q-1.1: Is the method for entering the patient and operator identification data clear and intuitive?

- 0 1 2 3 4

Q-2.1: Is the software installation and initial access procedure simple and efficient?

- 0 1 2 3 4

Q-3.1: Is the system easy to position and manage on a standard table?

- 0 1 2 3 4

Q-4.1: Is the information conveyed by the colored LEDs on the charging station clear?

- 0 1 2 3 4

Q-5.1: Is the information conveyed by the colored LEDs on the probes clear?

- 0 1 2 3 4

Q-5.2: Can the terminal part of the carotid probe be easily handled like a pen?

- 0 1 2 3 4

Q-5.3: Is the femoral probe flatter to be positioned between the fingers of the operator's hand? In this way, can it be handled easily?

- 0 1 2 3 4

Q-5.4: Is the intended use of each probe (femoral and carotid) easily recognizable?

- 0 1 2 3 4

Q-5.5: Is the simultaneous and stable positioning of the probes possible and efficient?

- 0 1 2 3 4

Q-6.1: Does the "acquisition window" allow a clear view of the signal?

- 0 1 2 3 4

Q-6.2: Is the 5-second update of the image adequate to meet physicians' expectations regarding the quality of the information?

- 0 1 2 3 4

Q-6.3: Currently, the signal reading interface features two white lines to guide the user in obtaining a reasonable signal amplitude in each graph. It is recommended to adjust the signal to be as large as the amplitude defined by the two horizontal lines. The operator must adjust the position and pressure of the probe to obtain the correct signal. Are these instructions clear to the physician? Is it intuitive, or is it necessary to consult the manual or a specialist's explanation to understand the meaning of the white lines?

- 0 1 2 3 4

Q-6.4: Based on what was mentioned in the previous question, is this information perceived as useful to have during the analysis?

- 0 1 2 3 4

Q-6.5: Are the relevant parameters displayed on the side of the acquisition screen (mean PTT, mean PWV, and standard deviation of PTT) easily identifiable and clearly visible?

- 0 1 2 3 4

Q-7.1: Can the display time of each screen be modified efficiently by entering a different duration period in the designated box within the window?

- 0 1 2 3 4

Q-8.1: To end the acquisition, the spacebar must be pressed. This requires the operator to remove the probes and press the spacebar within 2 seconds. Is it clear how to end the acquisition? Is it intuitive, or is it necessary to consult the manual or a specialist's explanation to understand how to finish the examination?

- 0 1 2 3 4

Q-8.2: Are the details provided in the report generated at the end of the examination complete and understandable?

- 0 1 2 3 4
-

Q-A: Are the contents of the provided user manual clear and complete?

- 0 1 2 3 4

Q-B.A: Regarding the "Patient Preparation Phase" section of the provided user manual, are the contents clear and complete?

- 0 1 2 3 4

Q-B.B: Regarding the "Safety Aspects" section of the provided user manual, are the contents clear and complete?

- 0 1 2 3 4

Q-B.C: Regarding the "Cleaning and Reuse" section of the provided user manual, are the contents clear and complete?

- 0 1 2 3 4

Q-B.D: Regarding the "System Configuration" section of the provided user manual, are the contents clear and complete?

- 0 1 2 3 4

Q-C: Does the interface display all the relevant information for the correct execution of the test?

- 0 1 2 3 4

Q-D: Is the data presentation clear?

- 0 1 2 3 4

Q-E: Does the interface assist the user in evaluating the adequacy of the probe positioning and pressure?

- 0 1 2 3 4

Q-F: Does the interface support the user during the execution of the test?

- 0 1 2 3 4

Q-G: Are the alerts and notifications clear and self-explanatory?

- 0 1 2 3 4

Q-H: Do the probes allow for easy handling?

- 0 1 2 3 4

Q-I: Are the probes easily distinguishable (femoral vs carotid)?

- 0 1 2 3 4

Date of the test

.....

Signature

.....

Bibliography

- [1] W. H. Organization. *World Health Statistics 2023 Monitoring health for the SDGs Sustainable Development Goals*. 2023. ISBN: 9789240074323. URL: <https://www.who.int/publications/book-orders..>
- [2] W. H. Organization, ed. *World health statistics 2022: monitoring health for the SDGs, sustainable development goals*. World Health Organization, 2022. ISBN: 9789240051140. URL: <http://apps.who.int/bookorders..>
- [3] A. Briasoulis, V. Agarwal, and F. H. Messerli. “Alcohol Consumption and the Risk of Hypertension in Men and Women: A Systematic Review and Meta-Analysis”. In: *The Journal of Clinical Hypertension* 14 (11 Nov. 2012), pp. 792–798. ISSN: 1524-6175. DOI: [10.1111/jch.12008](https://doi.org/10.1111/jch.12008).
- [4] C. Chi, Y. Liu, Y. Xu, and D. Xu. “Association Between Arterial Stiffness and Heart Failure With Preserved Ejection Fraction”. In: *Frontiers in Cardiovascular Medicine* 8 (Aug. 2021). ISSN: 2297-055X. DOI: [10.3389/fcvm.2021.707162](https://doi.org/10.3389/fcvm.2021.707162).
- [5] *World health statistics 2022: monitoring health for the SDGs, sustainable development goals*. 2022. ISBN: 9789240051140. URL: <http://apps.who.int/bookorders..>
- [6] R. L. Sacco et al. “The Heart of 25 by 25: Achieving the Goal of Reducing Global and Regional Premature Deaths From Cardiovascular Diseases and Stroke”. In: *Circulation* 133 (23 June 2016). ISSN: 0009-7322. DOI: [10.1161/CIR.0000000000000395](https://doi.org/10.1161/CIR.0000000000000395).
- [7] I. M. Graham. “The importance of total cardiovascular risk assessment in clinical practice”. In: *European Journal of General Practice* 12 (4 Jan. 2006), pp. 148–155. ISSN: 1381-4788. DOI: [10.1080/13814780600976282](https://doi.org/10.1080/13814780600976282).
- [8] S. Mendis, I. Graham, and J. Narula. “Addressing the Global Burden of Cardiovascular Diseases; Need for Scalable and Sustainable Frameworks”. In: *Global Heart* 17 (1 July 2022). ISSN: 2211-8179. DOI: [10.5334/gh.1139](https://doi.org/10.5334/gh.1139).

- [9] S. Mendis. “The role of cardiovascular risk assessment in addressing prevention of cardiovascular disease and cardiovascular complications of diabetes in South Asia”. In: *Asian Journal of Internal Medicine* 1 (1 Jan. 2022), pp. 38–49. ISSN: 2827-7260. DOI: [10.4038/ajim.v1i1.30](https://doi.org/10.4038/ajim.v1i1.30).
- [10] A. Y. Chang et al. “Past, present, and future of global health financing: a review of development assistance, government, out-of-pocket, and other private spending on health for 195 countries, 1995–2050”. In: *The Lancet* 393 (10187 June 2019), pp. 2233–2260. ISSN: 01406736. DOI: [10.1016/S0140-6736\(19\)30841-4](https://doi.org/10.1016/S0140-6736(19)30841-4).
- [11] C. L. Stanfield, ed. *Principles of Human Physiology*. 6th ed. Pearson, May 2018.
- [12] S. W. acob and M. F. Oliver. *Human Cardiovascular System*. 2024. ISBN: 9789240074323. URL: <https://www.britannica.com/science/human-cardiovascular-system..>
- [13] P. A. Iaizzo, ed. *Handbook of Cardiac Anatomy, Physiology, and Devices*. Springer International Publishing, 2015. ISBN: 978-3-319-19463-9. DOI: [10.1007/978-3-319-19464-6](https://doi.org/10.1007/978-3-319-19464-6).
- [14] Accessed online: 30/06/2024. URL: <https://sciencephotogallery.com/featured/arteriole-sem-steve-gschmeissner.html>.
- [15] J. A. Chirinos, ed. *Textbook of Arterial Stiffness and Pulsatile Hemodynamics in Health and Disease*. 1st ed. Elsevier, Mar. 2022.
- [16] G. Mancia(Chairperson) et al. “2023 ESH Guidelines for the management of arterial hypertension The Task Force for the management of arterial hypertension of the European Society of Hypertension Endorsed by the European Renal Association (ERA) and the International Society of Hypertension (ISH)”. In: *Journal of Hypertension* (June 2023). ISSN: 0263-6352. DOI: [10.1097/HJH.0000000000003480](https://doi.org/10.1097/HJH.0000000000003480).
- [17] B. Williams et al. “2018 ESC/ESH Guidelines for themanagement of arterial hypertension”. In: *European Heart Journal* 39 (33 Sept. 2018), pp. 3021–3104. ISSN: 15229645. DOI: [10.1093/EURHEARTJ/EHY339](https://doi.org/10.1093/EURHEARTJ/EHY339). URL: <https://pubmed.ncbi.nlm.nih.gov/30165516/>.
- [18] K. Yeates, L. Lohfeld, J. Sleeth, F. Morales, Y. Rajkotia, and O. Ogedegbe. “A global perspective on cardiovascular disease in vulnerable populations”. In: *The Canadian journal of cardiology* 31 (9 Sept. 2015), p. 1081. ISSN: 0828282X. DOI: [10.1016/J.CJCA.2015.06.035](https://doi.org/10.1016/J.CJCA.2015.06.035). URL: [/pmc/articles/PMC4787293/%20/pmc/articles/PMC4787293/?report=abstract%20https://www.ncbi.nlm.nih.gov/pmc/articles/PMC4787293/](https://pmc/articles/PMC4787293/%20/pmc/articles/PMC4787293/?report=abstract%20https://www.ncbi.nlm.nih.gov/pmc/articles/PMC4787293/).

- [19] B. Zhou et al. “Worldwide trends in hypertension prevalence and progress in treatment and control from 1990 to 2019: a pooled analysis of 1201 population-representative studies with 104 million participants”. In: *The Lancet* 398 (10304 Sept. 2021), pp. 957–980. ISSN: 01406736. DOI: [10.1016/S0140-6736\(21\)01330-1](https://doi.org/10.1016/S0140-6736(21)01330-1). URL: <https://linkinghub.elsevier.com/retrieve/pii/S0140673621013301>.
- [20] D. T. Lackland and M. A. Weber. *Global burden of cardiovascular disease and stroke: Hypertension at the core*. May 2015. DOI: [10.1016/j.cjca.2015.01.009](https://doi.org/10.1016/j.cjca.2015.01.009).
- [21] T. Panula, J. P. Sirkia, and M. Kaisti. “Continuous Blood Pressure Monitoring Using Nonpulsatile Photoplethysmographic Components for Low-Frequency Vascular Unloading”. In: *IEEE Transactions on Instrumentation and Measurement* 72 (2023). ISSN: 15579662. DOI: [10.1109/TIM.2023.3267378](https://doi.org/10.1109/TIM.2023.3267378).
- [22] J. Choi, Y. Kang, J. Park, Y. Joung, and C. Koo. “Development of Real-Time Cuffless Blood Pressure Measurement Systems with ECG Electrodes and a Microphone Using Pulse Transit Time (PTT)”. In: *Sensors* 23 (3 Feb. 2023). ISSN: 14248220. DOI: [10.3390/s23031684](https://doi.org/10.3390/s23031684).
- [23] M. H. Olsen et al. *A call to action and a lifecourse strategy to address the global burden of raised blood pressure on current and future generations: the Lancet Commission on hypertension*. Nov. 2016. DOI: [10.1016/S0140-6736\(16\)31134-5](https://doi.org/10.1016/S0140-6736(16)31134-5).
- [24] B. Zhou, P. Perel, G. A. Mensah, and M. Ezzati. *Global epidemiology, health burden and effective interventions for elevated blood pressure and hypertension*. Nov. 2021. DOI: [10.1038/s41569-021-00559-8](https://doi.org/10.1038/s41569-021-00559-8).
- [25] “Carotid Pulse Wave Analysis: Future Direction of Hemodynamic and Cardiovascular Risk Assessment”. In: *JMA Journal* 4 (2 2021), pp. 119–128. ISSN: 2433-3298. DOI: [10.31662/jmaj.2020-0108](https://doi.org/10.31662/jmaj.2020-0108).
- [26] S. Chatterjee, K. Budidha, and P. A. Kyriacou. “Investigating the origin of photoplethysmography using a multiwavelength Monte Carlo model”. In: *Physiological Measurement* 41 (8 Sept. 2020), p. 084001. DOI: [10.1088/1361-6579/aba008](https://doi.org/10.1088/1361-6579/aba008).
- [27] *Photoplethysmography Technology, Signal Analysis and Applications*. Elsevier, 2022. ISBN: 9780128233740. DOI: [10.1016/C2020-0-00098-8](https://doi.org/10.1016/C2020-0-00098-8). URL: <https://www.sciencedirect.com/book/9780128233740/photoplethysmography#book-info>.
- [28] J. Park, H. S. Seok, S. S. Kim, and H. Shin. *Photoplethysmogram Analysis and Applications: An Integrative Review*. Mar. 2022. DOI: [10.3389/fphys.2021.808451](https://doi.org/10.3389/fphys.2021.808451).

- [29] S. Chatterjee, J. P. Phillips, and P. A. Kyriacou. “Monte Carlo investigation of the effect of blood volume and oxygen saturation on optical path in reflectance pulse oximetry”. In: *Biomedical Physics and Engineering Express* 2 (6 Dec. 2016), p. 065018. DOI: [10.1088/2057-1976/2/6/065018](https://doi.org/10.1088/2057-1976/2/6/065018).
- [30] S. L. Jacques. “Optical properties of biological tissues: a review”. In: *Physics in Medicine and Biology* 58 (11 June 2013). ISSN: 0031-9155. DOI: [10.1088/0031-9155/58/11/R37](https://doi.org/10.1088/0031-9155/58/11/R37).
- [31] S. Hu, V. Azorin-Peris, and J. Zheng. “Opto-Physiological Modeling Applied to Photoplethysmographic Cardiovascular Assessment”. In: *Journal of Healthcare Engineering* 4 (4 Jan. 2013), pp. 505–528. ISSN: 2040-2295. DOI: [10.1260/2040-2295.4.4.505](https://doi.org/10.1260/2040-2295.4.4.505).
- [32] “The 2023 wearable photoplethysmography roadmap”. In: *Physiological Measurement* 44 (11 Nov. 2023), p. 111001. ISSN: 0967-3334. DOI: [10.1088/1361-6579/acead2](https://doi.org/10.1088/1361-6579/acead2).
- [33] J. Weinman, A. Hayat, and G. Raviv. “Reflection photoplethysmography of arterial-blood-volume pulses”. In: *Medical and Biological Engineering and Computing* 15 (1 Jan. 1977), pp. 22–31. DOI: [10.1007/BF02441571](https://doi.org/10.1007/BF02441571).
- [34] C. R. Simpson, M. Kohl, M. Essenpreis, and M. Cope. “Near-infrared optical properties of *ex vivo* human skin and subcutaneous tissues measured using the Monte Carlo inversion technique”. In: *Physics in Medicine and Biology* 43 (9 Sept. 1998), pp. 2465–2478. DOI: [10.1088/0031-9155/43/9/003](https://doi.org/10.1088/0031-9155/43/9/003).
- [35] C. El-Hajj and P. Kyriacou. “Deep learning models for cuffless blood pressure monitoring from PPG signals using attention mechanism”. In: *Biomedical Signal Processing and Control* 65 (Mar. 2021), p. 102301. DOI: [10.1016/j.bspc.2020.102301](https://doi.org/10.1016/j.bspc.2020.102301).
- [36] J. Park, H. S. Seok, S.-S. Kim, and H. Shin. “Photoplethysmogram Analysis and Applications: An Integrative Review”. In: *Frontiers in Physiology* 12 (Mar. 2022). ISSN: 1664-042X. DOI: [10.3389/fphys.2021.808451](https://doi.org/10.3389/fphys.2021.808451).
- [37] T. Sondej, I. Jannasz, K. Sieczkowski, A. Dobrowolski, K. Obiała, T. Targowski, and R. Olszewski. “Validation of a new device for photoplethysmographic measurement of multi-site arterial pulse wave velocity”. In: *Biocybernetics and Biomedical Engineering* 41 (4 Oct. 2021), pp. 1664–1684. ISSN: 02085216. DOI: [10.1016/j.bbe.2021.11.001](https://doi.org/10.1016/j.bbe.2021.11.001).
- [38] R. A. Xuereb, C. J. Magri, and R. G. Xuereb. *Arterial Stiffness and its Impact on Cardiovascular Health*. 2023. DOI: [10.1007/s11886-023-01951-1](https://doi.org/10.1007/s11886-023-01951-1).

- [39] D. Li, F. Cao, W. Cheng, Y. Xu, and C. Yang. “Predictive value of estimated pulse wave velocity for cardiovascular and all-cause mortality in individuals with obesity”. In: *Diabetology and Metabolic Syndrome* 15 (1 Dec. 2023). ISSN: 17585996. DOI: [10.1186/s13098-023-01011-2](https://doi.org/10.1186/s13098-023-01011-2).
- [40] X. Li, H. Du, X. Li, Q. Gao, J. Chen, and X. Chen. “Brachial-ankle pulse wave velocity is associated with intracranial artery calcification in acute stroke patients”. In: *Clinical Neurology and Neurosurgery* 233 (Oct. 2023), p. 107918. ISSN: 03038467. DOI: [10.1016/j.clineuro.2023.107918](https://doi.org/10.1016/j.clineuro.2023.107918). URL: <https://linkinghub.elsevier.com/retrieve/pii/S0303846723003347>.
- [41] G. Y. Li, Y. Jiang, Y. Zheng, W. Xu, Z. Zhang, and Y. Cao. “Arterial Stiffness Probed by Dynamic Ultrasound Elastography Characterizes Waveform of Blood Pressure”. In: *IEEE Transactions on Medical Imaging* 41 (6 June 2022), pp. 1510–1519. ISSN: 1558254X. DOI: [10.1109/TMI.2022.3141613](https://doi.org/10.1109/TMI.2022.3141613).
- [42] I. Sequí-Domínguez, I. Cavero-Redondo, C. Álvarez-Bueno, D. P. Pozuelo-Carrascosa, S. N. de Arenas-Arroyo, and V. Martínez-Vizcaíno. *Accuracy of pulse wave velocity predicting cardiovascular and all-cause mortality. A systematic review and meta-analysis*. July 2020. DOI: [10.3390/jcm9072080](https://doi.org/10.3390/jcm9072080).
- [43] A. V. S. kumar, K. MaheshKumar, K. N. Maruthy, and R. Padmavathi. “Comparision of photo pulse plethysmography module with Mobil-O-graph for measurement of pulse wave velocity”. In: *Clinical Epidemiology and Global Health* 9 (Jan. 2021), pp. 216–220. ISSN: 22133984. DOI: [10.1016/j.cegh.2020.09.001](https://doi.org/10.1016/j.cegh.2020.09.001).
- [44] K. S. Heffernan, D. Charry, J. Xu, H. Tanaka, and J. R. Churilla. “Estimated pulse wave velocity and incident heart failure and its subtypes: Findings from the multi-ethnic study of atherosclerosis”. In: *American Heart Journal Plus: Cardiology Research and Practice* 25 (Jan. 2023). ISSN: 26666022. DOI: [10.1016/j.ahjo.2022.100238](https://doi.org/10.1016/j.ahjo.2022.100238).
- [45] W. W. Nichols, M. F. O’Rourke, E. R. Edelman, and C. Vlachopoulos. “McDonald’s Blood Flow in Arteries: Theoretical, Experimental and Clinical Principles: Seventh Edition”. In: *McDonald’s Blood Flow in Arteries: Theoretical, Experimental and Clinical Principles: Seventh Edition* (Jan. 2022), pp. 1–821. DOI: [10.1201/9781351253765](https://doi.org/10.1201/9781351253765).
- [46] N. Westerhof, N. Stergiopulos, M. I. Noble, and B. E. Westerhof. “Snapshots of hemodynamics: An aid for clinical research and graduate education”. In: *Snapshots of Hemodynamics: An Aid for Clinical Research and Graduate Education* (Sept. 2018), pp. 1–314. DOI: [10.1007/978-3-319-91932-4/COVER](https://doi.org/10.1007/978-3-319-91932-4/COVER).

- [47] C. K. Sun. “Cardio-ankle vascular index (CAVI) as an indicator of arterial stiffness”. In: *Integrated blood pressure control* 6 (2013), pp. 27–38. ISSN: 1178-7104. DOI: [10.2147/IBPC.S34423](https://doi.org/10.2147/IBPC.S34423). URL: <https://pubmed.ncbi.nlm.nih.gov/23667317/>.
- [48] “Toward Ubiquitous Blood Pressure Monitoring via Pulse Transit Time: Theory and Practice”. In: *IEEE transactions on bio-medical engineering* 62 (8 Aug. 2015), pp. 1879–1901. ISSN: 1558-2531. DOI: [10.1109/TBME.2015.2441951](https://doi.org/10.1109/TBME.2015.2441951). URL: <https://pubmed.ncbi.nlm.nih.gov/26057530/>.
- [49] P. Boutouyrie et al. “Assessment of arterial stiffness for clinical and epidemiological studies: methodological considerations for validation and entry into the European Renal and Cardiovascular Medicine registry”. In: *Nephrology, dialysis, transplantation : official publication of the European Dialysis and Transplant Association - European Renal Association* 29 (2 Feb. 2014), pp. 232–239. ISSN: 1460-2385. DOI: [10.1093/NDT/GFT309](https://doi.org/10.1093/NDT/GFT309). URL: <https://pubmed.ncbi.nlm.nih.gov/24084326/>.
- [50] P. Meani et al. “Determinants of carotid-femoral pulse wave velocity progression in hypertensive patients over a 3.7 years follow-up”. In: *Blood pressure* 27 (1 Jan. 2018), pp. 32–40. ISSN: 1651-1999. DOI: [10.1080/08037051.2017.1378069](https://doi.org/10.1080/08037051.2017.1378069). URL: <https://pubmed.ncbi.nlm.nih.gov/28922954/>.
- [51] B. M. Pannier, A. P. Avolio, A. Hoeks, G. Mancia, and K. Takazawa. “Methods and devices for measuring arterial compliance in humans”. In: *American journal of hypertension* 15 (8 2002), pp. 743–753. ISSN: 0895-7061. DOI: [10.1016/S0895-7061\(02\)02962-X](https://doi.org/10.1016/S0895-7061(02)02962-X). URL: <https://pubmed.ncbi.nlm.nih.gov/12160200/>.
- [52] M. A. Supiano et al. “Pulse wave velocity and central aortic pressure in systolic blood pressure intervention trial participants”. In: *PloS one* 13 (9 Sept. 2018). ISSN: 1932-6203. DOI: [10.1371/JOURNAL.PONE.0203305](https://doi.org/10.1371/JOURNAL.PONE.0203305). URL: <https://pubmed.ncbi.nlm.nih.gov/30256784/>.
- [53] I. B. Wilkinson, C. M. McEniery, G. Schillaci, P. Boutouyrie, P. Segers, A. Donald, and P. J. Chowienzyk. “ARTERY Society guidelines for validation of non-invasive haemodynamic measurement devices: Part 1, arterial pulse wave velocity”. In: *Artery Research* 4 (2 June 2010), pp. 34–40. ISSN: 1872-9312. DOI: [10.1016/J.ARTRES.2010.03.001](https://doi.org/10.1016/J.ARTRES.2010.03.001).
- [54] A. Álvarez-Bustos et al. “Association Between Pulse Wave Velocity and Frailty, Disability, and Mortality in Community-Dwelling Older Adults”. In: *JACC: Advances* 2 (5 July 2023), p. 100423. ISSN: 2772963X. DOI: [10.1016/j.jacadv.2023.100423](https://doi.org/10.1016/j.jacadv.2023.100423). URL: <https://linkinghub.elsevier.com/retrieve/pii/S2772963X2300282X>.

- [55] M. J. van Hout et al. “Estimated pulse wave velocity (ePWV) as a potential gatekeeper for MRI-assessed PWV: a linear and deep neural network based approach in 2254 participants of the Netherlands Epidemiology of Obesity study”. In: *International Journal of Cardiovascular Imaging* 38 (1 Jan. 2022), pp. 183–193. ISSN: 15730743. DOI: [10.1007/s10554-021-02359-0](https://doi.org/10.1007/s10554-021-02359-0).
- [56] P. M. Nabeel, S. Karthik, J. Joseph, and M. Sivaprakasam. “Arterial blood pressure estimation from local pulse wave velocity using dual-element photoplethysmograph probe”. In: *IEEE Transactions on Instrumentation and Measurement* 67 (6 June 2018), pp. 1399–1408. ISSN: 00189456. DOI: [10.1109/TIM.2018.2800539](https://doi.org/10.1109/TIM.2018.2800539).
- [57] V. P. Rachim, S. Kang, J. H. Baek, and S. M. Park. “Unobtrusive, Cuffless Blood Pressure Monitoring Using a Soft Polymer Sensor Array with Flexible Hybrid Electronics”. In: *IEEE Sensors Journal* 21 (8 Apr. 2021), pp. 10132–10142. ISSN: 15581748. DOI: [10.1109/JSEN.2021.3059864](https://doi.org/10.1109/JSEN.2021.3059864).
- [58] Y. Lu et al. “Global distributions of age- and sex-related arterial stiffness: systematic review and meta-analysis of 167 studies with 509,743 participants”. In: *eBioMedicine* 92 (June 2023). ISSN: 23523964. DOI: [10.1016/j.ebiom.2023.104619](https://doi.org/10.1016/j.ebiom.2023.104619).
- [59] Y. Arita, T. Fukui, N. Ogasawara, and S. Hasegawa. “Clinical implication of the brachial-ankle pulse wave velocity for endovascular treatment”. In: *Indian Heart Journal* 73 (5 Sept. 2021), pp. 650–652. ISSN: 22133763. DOI: [10.1016/j.ihj.2021.07.001](https://doi.org/10.1016/j.ihj.2021.07.001).
- [60] S. Kwak, H.-L. Kim, M. In, W.-H. Lim, J.-B. Seo, S.-H. Kim, J.-H. Zo, and M.-A. Kim. “Associations of Brachial-Ankle Pulse Wave Velocity With Left Ventricular Geometry and Diastolic Function in Untreated Hypertensive Patients”. In: *Frontiers in Cardiovascular Medicine* 8 (May 2021). ISSN: 2297-055X. DOI: [10.3389/fcvm.2021.647491](https://doi.org/10.3389/fcvm.2021.647491).
- [61] K. Stone et al. “Reimagining the Value of Brachial-Ankle Pulse Wave Velocity as a Biomarker of Cardiovascular Disease Risk-A Call to Action on Behalf of VascAgeNet.” In: *Hypertension (Dallas, Tex. : 1979)* (July 2023). ISSN: 1524-4563. DOI: [10.1161/HYPERTENSIONAHA.123.21314](https://doi.org/10.1161/HYPERTENSIONAHA.123.21314). URL: <http://www.ncbi.nlm.nih.gov/pubmed/37470189>.
- [62] A. Saz-Lara, I. Cavero-Redondo, V. Martínez-Vizcaíno, M. Lucerón-Lucas-Torres, C. Pascual-Morena, and I. Sequí-Domínguez. *Association between arterial stiffness and orthostatic hypotension: A systematic review and meta-analysis*. 2023. DOI: [10.3389/fphys.2023.1164519](https://doi.org/10.3389/fphys.2023.1164519).

- [63] H. R. LIU, C. Y. LI, X. XIA, S. F. CHEN, X. F. LU, D. F. GU, F. C. LIU, and J. F. HUANG. “Association of Estimated Pulse Wave Velocity and the Dynamic Changes in Estimated Pulse Wave Velocity with All-Cause Mortality among Middle-Aged and Elderly Chinese”. In: *Biomedical and Environmental Sciences* 35 (11 Nov. 2022), pp. 1001–1011. ISSN: 08953988. DOI: [10.3967/bes2022.129](https://doi.org/10.3967/bes2022.129).
- [64] A. Milan, G. Zocaro, D. Leone, F. Tosello, I. Buraioli, D. Schiavone, and F. Veglio. “Current assessment of pulse wave velocity”. In: *Journal of Hypertension* 37 (8 Aug. 2019), pp. 1547–1557. ISSN: 0263-6352. DOI: [10.1097/HJH.0000000000002081](https://doi.org/10.1097/HJH.0000000000002081).
- [65] A. Valerio, D. Demarchi, B. O’Flynn, P. M. Ros, and S. Tedesco. “Development of a Personalized Multiclass Classification Model to Detect Blood Pressure Variations Associated with Physical or Cognitive Workload”. In: *Sensors* 24 (11 June 2024), p. 3697. DOI: [10.3390/s24113697](https://doi.org/10.3390/s24113697).
- [66] L. M. V. Bortel et al. “Expert consensus document on the measurement of aortic stiffness in daily practice using carotid-femoral pulse wave velocity”. In: *Journal of hypertension* 30 (3 2012), pp. 445–448. ISSN: 1473-5598. DOI: [10.1097/HJH.0B013E32834FA8B0](https://doi.org/10.1097/HJH.0B013E32834FA8B0). URL: <https://pubmed.ncbi.nlm.nih.gov/22278144/>.
- [67] F. Beutel, C. V. Hoof, X. Rottenberg, K. Reesink, and E. Hermeling. “Pulse Arrival Time Segmentation Into Cardiac and Vascular Intervals - Implications for Pulse Wave Velocity and Blood Pressure Estimation”. In: *IEEE transactions on bio-medical engineering* 68 (9 Sept. 2021), pp. 2810–2820. ISSN: 1558-2531. DOI: [10.1109/TBME.2021.3055154](https://doi.org/10.1109/TBME.2021.3055154). URL: <https://pubmed.ncbi.nlm.nih.gov/33513094/>.
- [68] F. S. Hu, Y. L. Zhang, Z. C. Ma, Q. Q. Cao, Y. B. Xu, Z. J. He, and Y. N. Sun. “A region-matching method for pulse transit time estimation: potential for improving the accuracy in determining carotid femoral pulse wave velocity”. In: *Journal of human hypertension* 29 (11 Nov. 2015), pp. 675–682. ISSN: 1476-5527. DOI: [10.1038/JHH.2015.9](https://doi.org/10.1038/JHH.2015.9). URL: <https://pubmed.ncbi.nlm.nih.gov/25694218/>.
- [69] X. R. Ding, N. Zhao, G. Z. Yang, R. I. Pettigrew, B. Lo, F. Miao, Y. Li, J. Liu, and Y. T. Zhang. “Continuous Blood Pressure Measurement From Invasive to Unobtrusive: Celebration of 200th Birth Anniversary of Carl Ludwig”. In: *IEEE Journal of Biomedical and Health Informatics* 20 (6 Nov. 2016), pp. 1455–1465. ISSN: 21682208. DOI: [10.1109/JBHI.2016.2620995](https://doi.org/10.1109/JBHI.2016.2620995).
- [70] A. L. Wentland, T. M. Grist, and O. Wieben. “Review of MRI-based measurements of pulse wave velocity: A biomarker of arterial stiffness.” In: *Cardiovascular Diagnosis and Therapy* 4.2 (2014), pp. 193–206.

- [71] A. Valerio, A. Hajzeraaj, O. V. Talebi, M. Belcastro, S. Tedesco, D. Demarchi, and B. O’Flynn. “Development of a PPG-based hardware and software system deployable on elbow and thumb for real-time estimation of pulse transit time”. In: *2023 45th Annual International Conference of the IEEE Engineering in Medicine and Biology Society (EMBC)*. IEEE, July 2023, pp. 1–5. DOI: [10.1109/EMBC40787.2023.10340784](https://doi.org/10.1109/EMBC40787.2023.10340784).
- [72] V. Fabian, L. Matera, K. Bayerova, J. Havlik, V. Kremen, J. Pudil, P. Sajgalik, and D. Zemanek. “Noninvasive Assessment of Aortic Pulse Wave Velocity by the Brachial Occlusion-Cuff Technique: Comparative Study”. In: *Sensors* 19 (16 Aug. 2019), p. 3467. ISSN: 1424-8220. DOI: [10.3390/s19163467](https://doi.org/10.3390/s19163467).
- [73] H. Obeid, G. Soulat, E. Mousseaux, S. Laurent, N. Stergiopulos, P. Boutouyrie, and P. Segers. “Numerical assessment and comparison of pulse wave velocity methods aiming at measuring aortic stiffness”. In: *Physiological measurement* 38 (11 Oct. 2017), pp. 1953–1967. ISSN: 1361-6579. DOI: [10.1088/1361-6579/AA905A](https://doi.org/10.1088/1361-6579/AA905A). URL: <https://pubmed.ncbi.nlm.nih.gov/28968226/>.
- [74] O. Vardoulis, T. G. Papaioannou, and N. Stergiopulos. “Validation of a novel and existing algorithms for the estimation of pulse transit time: advancing the accuracy in pulse wave velocity measurement”. In: *American journal of physiology. Heart and circulatory physiology* 304 (11 2013). ISSN: 1522-1539. DOI: [10.1152/AJPHEART.00963.2012](https://doi.org/10.1152/AJPHEART.00963.2012). URL: <https://pubmed.ncbi.nlm.nih.gov/23604712/>.
- [75] S. Seoni et al. “Template Matching and Matrix Profile for Signal Quality Assessment of Carotid and Femoral Laser Doppler Vibrometer Signals”. In: *Frontiers in Physiology* 12 (Jan. 2022). ISSN: 1664042X. DOI: [10.3389/fphys.2021.775052](https://doi.org/10.3389/fphys.2021.775052).
- [76] G. Mancia et al. “2007 Guidelines for the Management of Arterial Hypertension”. In: *Journal of Hypertension* 25 (6 June 2007), pp. 1105–1187. ISSN: 0263-6352. DOI: [10.1097/HJH.0b013e3281fc975a](https://doi.org/10.1097/HJH.0b013e3281fc975a).
- [77] L. M. V. Bortel et al. “Expert consensus document on the measurement of aortic stiffness in daily practice using carotid-femoral pulse wave velocity”. In: *Journal of Hypertension* 30 (3 Mar. 2012), pp. 445–448. ISSN: 0263-6352. DOI: [10.1097/HJH.0b013e32834fa8b0](https://doi.org/10.1097/HJH.0b013e32834fa8b0).
- [78] “2013 ESH/ESC Guidelines for the management of arterial hypertension”. In: *European Heart Journal* 34 (28 July 2013), pp. 2159–2219. ISSN: 0195-668X. DOI: [10.1093/eurheartj/ehq151](https://doi.org/10.1093/eurheartj/ehq151).
- [79] H.-P. B.-L. Rocca. “Towards applicability of measures of arterial stiffness in clinical routine”. In: *European Heart Journal* 31 (19 Oct. 2010), pp. 2320–2322. ISSN: 0195-668X. DOI: [10.1093/eurheartj/ehq211](https://doi.org/10.1093/eurheartj/ehq211).

- [80] D. Baier, A. Teren, K. Wirkner, M. Loeffler, and M. Scholz. “Parameters of pulse wave velocity: determinants and reference values assessed in the population-based study LIFE-Adult”. In: *Clinical Research in Cardiology* 107 (11 Nov. 2018), pp. 1050–1061. ISSN: 1861-0684. DOI: [10.1007/s00392-018-1278-3](https://doi.org/10.1007/s00392-018-1278-3).
- [81] A. M. G. Paiva, M. A. Mota-Gomes, A. A. Brandão, F. S. Silveira, M. S. Silveira, R. T. P. Okawa, A. D. M. Feitosa, A. C. Sposito, and W. Nadruz. “Reference values of office central blood pressure, pulse wave velocity, and augmentation index recorded by means of the Mobil-O-Graph PWA monitor”. In: *Hypertension Research* 43 (11 Nov. 2020), pp. 1239–1248. ISSN: 0916-9636. DOI: [10.1038/s41440-020-0490-5](https://doi.org/10.1038/s41440-020-0490-5).
- [82] M.-H. Hwang, J.-K. Yoo, H.-K. Kim, C.-L. Hwang, K. Mackay, O. Hemstreet, W. W. Nichols, and D. D. Christou. “Validity and reliability of aortic pulse wave velocity and augmentation index determined by the new cuff-based SphygmoCor Xcel”. In: *Journal of Human Hypertension* 28 (8 Aug. 2014), pp. 475–481. ISSN: 0950-9240. DOI: [10.1038/jhh.2013.144](https://doi.org/10.1038/jhh.2013.144).
- [83] R. Asmar, A. Benetos, J. Topouchian, P. Laurent, B. Pannier, A.-M. Brisac, R. Target, and B. I. Levy. “Assessment of Arterial Distensibility by Automatic Pulse Wave Velocity Measurement”. In: *Hypertension* 26 (3 Sept. 1995), pp. 485–490. ISSN: 0194-911X. DOI: [10.1161/01.HYP.26.3.485](https://doi.org/10.1161/01.HYP.26.3.485).
- [84] F. Stea, E. Bozec, S. Millasseau, H. Khettab, P. Boutouyrie, and S. Laurent. “Comparison of the Complior Analyse device with Sphygmocor and Complior SP for pulse wave velocity and central pressure assessment”. In: *Journal of Hypertension* 32 (4 Apr. 2014), pp. 873–880. ISSN: 0263-6352. DOI: [10.1097/HJH.000000000000091](https://doi.org/10.1097/HJH.000000000000091).
- [85] G. Fiori, F. Fuiano, A. Scorza, S. Conforto, and S. A. Sciuto. “Non-Invasive Methods for PWV Measurement in Blood Vessel Stiffness Assessment”. In: *IEEE Reviews in Biomedical Engineering* 15 (2022), pp. 169–183. ISSN: 1937-3333. DOI: [10.1109/RBME.2021.3092208](https://doi.org/10.1109/RBME.2021.3092208).
- [86] P. Salvi, G. Lio, C. Labat, E. Ricci, B. Pannier, and A. Benetos. “Validation of a new non-invasive portable tonometer for determining arterial pressure wave and pulse wave velocity: the PulsePen device.” In: *Journal of hypertension* 22 (12 Dec. 2004), pp. 2285–93. ISSN: 0263-6352. DOI: [10.1097/00004872-200412000-00010](https://doi.org/10.1097/00004872-200412000-00010).
- [87] I. G. Horváth, Á. Németh, Z. Lenkey, N. Alessandri, F. Tufano, P. Kis, B. Gaszner, and A. Cziráki. “Invasive validation of a new oscillometric device (Arteriograph) for measuring augmentation index, central blood pressure and aortic pulse wave velocity”. In: *Journal of Hypertension* 28 (10 Oct. 2010), pp. 2068–2075. ISSN: 0263-6352. DOI: [10.1097/HJH.0b013e32833c8a1a](https://doi.org/10.1097/HJH.0b013e32833c8a1a).

- [88] J. Calabria, P. Torguet, M. Garcia, I. Garcia, N. Martin, B. Guasch, D. Faur, and M. Vallés. “Doppler ultrasound in the measurement of pulse wave velocity: agreement with the Complior method”. In: *Cardiovascular Ultrasound* 9 (1 Dec. 2011), p. 13. ISSN: 1476-7120. DOI: [10.1186/1476-7120-9-13](https://doi.org/10.1186/1476-7120-9-13).
- [89] J. J. Westenberg, E. P. van Poelgeest, P. Steendijk, H. B. Grotenhuis, J. Jukema, and A. de Roos. “Bramwell-Hill modeling for local aortic pulse wave velocity estimation: a validation study with velocity-encoded cardiovascular magnetic resonance and invasive pressure assessment”. In: *Journal of Cardiovascular Magnetic Resonance* 14 (1 Jan. 2012), p. 15. ISSN: 10976647. DOI: [10.1186/1532-429X-14-2](https://doi.org/10.1186/1532-429X-14-2).
- [90] P. Zhang, Q. Qiu, and Y. Zhou. “Reconstruction of continuous brachial artery pressure wave from continuous finger arterial pressure in humans”. In: *Australasian Physical and Engineering Sciences in Medicine* 41 (4 Dec. 2018), pp. 1115–1125. ISSN: 0158-9938. DOI: [10.1007/s13246-018-0652-9](https://doi.org/10.1007/s13246-018-0652-9).
- [91] J. Mariscal-Harana et al. “Estimating central blood pressure from aortic flow: development and assessment of algorithms”. In: *American Journal of Physiology-Heart and Circulatory Physiology* 320 (2 Feb. 2021), H494–H510. ISSN: 0363-6135. DOI: [10.1152/ajpheart.00241.2020](https://doi.org/10.1152/ajpheart.00241.2020).
- [92] G. Zhang, J.-O. Hahn, and R. Mukkamala. “Tube-Load Model Parameter Estimation for Monitoring Arterial Hemodynamics”. In: *Frontiers in Physiology* 2 (2011). ISSN: 1664-042X. DOI: [10.3389/fphys.2011.00072](https://doi.org/10.3389/fphys.2011.00072).
- [93] R. Mukkamala, M. Yavarimanesh, K. Natarajan, J.-O. Hahn, K. G. Kyriakoulis, A. P. Avolio, and G. S. Stergiou. “Evaluation of the Accuracy of Cuffless Blood Pressure Measurement Devices: Challenges and Proposals”. In: *Hypertension* 78 (5 Nov. 2021), pp. 1161–1167. ISSN: 0194-911X. DOI: [10.1161/HYPERTENSIONAHA.121.17747](https://doi.org/10.1161/HYPERTENSIONAHA.121.17747).
- [94] H. A. Owida. *Biomechanical Sensing Systems for Cardiac Activity Monitoring*. 2022. DOI: [10.1155/2022/8312564](https://doi.org/10.1155/2022/8312564).
- [95] R. Mukkamala, G. S. Stergiou, and A. P. Avolio. “Annual Review of Biomedical Engineering Cuffless Blood Pressure Measurement”. In: *Annual Review of Biomedical Engineering* (2022). DOI: [10.1146/annurev-bioeng-110220](https://doi.org/10.1146/annurev-bioeng-110220). URL: <https://doi.org/10.1146/annurev-bioeng-110220->.
- [96] V. Dhamotharan et al. “Mathematical Modeling of Oscillometric Blood Pressure Measurement: A Complete, Reduced Oscillogram Model”. In: *IEEE Transactions on Biomedical Engineering* 70 (2 Feb. 2023), pp. 715–722. ISSN: 15582531. DOI: [10.1109/TBME.2022.3201433](https://doi.org/10.1109/TBME.2022.3201433).

- [97] M. Saito, M. Matsukawa, T. Asada, and Y. Watanabe. “Noninvasive assessment of arterial stiffness by pulse wave analysis”. In: *IEEE Transactions on Ultrasonics, Ferroelectrics, and Frequency Control* 59 (11 2012), pp. 2411–2419. ISSN: 08853010. DOI: [10.1109/TUFFC.2012.2473](https://doi.org/10.1109/TUFFC.2012.2473).
- [98] D. Barvik, M. Cerny, M. Penhaker, and N. Noury. *Noninvasive Continuous Blood Pressure Estimation from Pulse Transit Time: A Review of the Calibration Models*. 2022. DOI: [10.1109/RBME.2021.3109643](https://doi.org/10.1109/RBME.2021.3109643).
- [99] M. Freithaler, A. Chandrasekhar, V. Dhamotharan, C. Landry, S. G. Shroff, and R. Mukkamala. “Smartphone-Based Blood Pressure Monitoring via the Oscillometric Finger Pressing Method: Analysis of Oscillation Width Variations Can Improve Diastolic Pressure Computation”. In: *IEEE Transactions on Biomedical Engineering* (Nov. 2023). ISSN: 15582531. DOI: [10.1109/TBME.2023.3275031](https://doi.org/10.1109/TBME.2023.3275031).
- [100] A. M. Zakrzewski, A. Y. Huang, R. Zubajlo, and B. W. Anthony. “Real-time blood pressure estimation from force-measured ultrasound”. In: *IEEE Transactions on Biomedical Engineering* 65 (11 Nov. 2018), pp. 2405–2416. ISSN: 15582531. DOI: [10.1109/TBME.2018.2873297](https://doi.org/10.1109/TBME.2018.2873297).
- [101] P. H. Charlton et al. “Assessing hemodynamics from the photoplethysmogram to gain insights into vascular age: a review from VascAgeNet”. In: *American Journal of Physiology - Heart and Circulatory Physiology* 322 (4 Apr. 2022), H493–H522. ISSN: 15221539. DOI: [10.1152/ajpheart.00392.2021](https://doi.org/10.1152/ajpheart.00392.2021).
- [102] R. C. Block et al. “Conventional pulse transit times as markers of blood pressure changes in humans”. In: *Scientific Reports* 10 (1 Dec. 2020). ISSN: 20452322. DOI: [10.1038/s41598-020-73143-8](https://doi.org/10.1038/s41598-020-73143-8).
- [103] J. Solà and R. Delgado-Gonzalo. *The Handbook of Cuffless Blood Pressure Monitoring A Practical Guide for Clinicians, Researchers, and Engineers*.
- [104] S. G. Khalid, J. Zhang, F. Chen, and D. Zheng. “Blood Pressure Estimation Using Photoplethysmography Only: Comparison between Different Machine Learning Approaches”. In: *Journal of Healthcare Engineering* 2018 (2018). ISSN: 20402309. DOI: [10.1155/2018/1548647](https://doi.org/10.1155/2018/1548647).
- [105] J. Joung et al. “Continuous cuffless blood pressure monitoring using photoplethysmography-based PPG2BP-net for high intrasubject blood pressure variations”. In: *Scientific Reports* 13 (1 Dec. 2023). ISSN: 20452322. DOI: [10.1038/s41598-023-35492-y](https://doi.org/10.1038/s41598-023-35492-y).
- [106] S. Ismail, I. Siddiqi, and U. Akram. “Heart rate estimation in PPG signals using Convolutional-Recurrent Regressor”. In: *Computers in Biology and Medicine* 145 (June 2022). ISSN: 18790534. DOI: [10.1016/j.combiomed.2022.105470](https://doi.org/10.1016/j.combiomed.2022.105470).

- [107] N. F. Ali and M. Atef. “An efficient hybrid LSTM-ANN joint classification-regression model for PPG based blood pressure monitoring”. In: *Biomedical Signal Processing and Control* 84 (July 2023). ISSN: 17468108. DOI: [10.1016/j.bspc.2023.104782](https://doi.org/10.1016/j.bspc.2023.104782).
- [108] C. El-Hajj and P. A. Kyriacou. *A review of machine learning techniques in photoplethysmography for the non-invasive cuff-less measurement of blood pressure*. Apr. 2020. DOI: [10.1016/j.bspc.2020.101870](https://doi.org/10.1016/j.bspc.2020.101870).
- [109] J. Barnes, C. Crowe, B. O’Flynn, and S. Tedesco. “Evaluation of Cuff-less Blood Pressure Monitoring Models over Multiple Data Sets”. In: *2023 34th Irish Signals and Systems Conference (ISSC)*. Institute of Electrical and Electronics Engineers Inc., 2023. DOI: [10.1109/ISSC59246.2023.10162037](https://doi.org/10.1109/ISSC59246.2023.10162037).
- [110] J. Jin, X. Geng, Y. Zhang, H. Zhang, and T. Ye. “Pulse Wave Analysis Method of Cardiovascular Parameters Extraction for Health Monitoring”. In: *International Journal of Environmental Research and Public Health* 20 (3 Jan. 2023), p. 2597. ISSN: 1660-4601. DOI: [10.3390/ijerph20032597](https://doi.org/10.3390/ijerph20032597).
- [111] A. Shrivastava, M. Chakkaravarthy, and M. A. Shah. “A new machine learning method for predicting systolic and diastolic blood pressure using clinical characteristics”. In: *Healthcare Analytics* 4 (Dec. 2023). ISSN: 27724425. DOI: [10.1016/j.health.2023.100219](https://doi.org/10.1016/j.health.2023.100219).
- [112] F. Tabei, R. Kumar, T. N. Phan, D. D. McManus, and J. W. Chong. “A Novel Personalized Motion and Noise Artifact (MNA) Detection Method for Smartphone Photoplethysmograph (PPG) Signals”. In: *IEEE Access* 6 (2018), pp. 60498–60512. ISSN: 2169-3536. DOI: [10.1109/ACCESS.2018.2875873](https://doi.org/10.1109/ACCESS.2018.2875873).
- [113] H. Herrmann and H. Ewald. “False Positives Avoidance in Pulse Detection from ECG and PPG Sensor Signals”. In: *Proceedings of IEEE Sensors* (2021). ISSN: 21689229. DOI: [10.1109/SENSORS47087.2021.9639525](https://doi.org/10.1109/SENSORS47087.2021.9639525).
- [114] T. Athaya and S. Choi. “Evaluation of Different Machine Learning Models for Photoplethysmogram Signal Artifact Detection”. In: *IEEE*, Oct. 2020, pp. 1206–1208. ISBN: 978-1-7281-6758-9. DOI: [10.1109/ICTC49870.2020.9289366](https://doi.org/10.1109/ICTC49870.2020.9289366).
- [115] X. Zhang, C. Gu, and J. Lin. “Support Vector Machines for Anomaly Detection”. In: *IEEE*, 2006, pp. 2594–2598. ISBN: 1-4244-0332-4. DOI: [10.1109/WCICA.2006.1712831](https://doi.org/10.1109/WCICA.2006.1712831).
- [116] A. Diro, N. Chilamkurti, V. D. Nguyen, and W. Heyne. *A comprehensive study of anomaly detection schemes in iot networks using machine learning algorithms*. Dec. 2021. DOI: [10.3390/s21248320](https://doi.org/10.3390/s21248320).

- [117] L. Fan, J. Ma, J. Tian, T. Li, and H. Wang. “Comparative Study of Isolation Forest and LOF algorithm in anomaly detection of data mining”. In: *Proceedings - 2021 International Conference on Big Data, Artificial Intelligence and Risk Management, ICBAR 2021* (2021), pp. 1–5. DOI: [10.1109/ICBAR55169.2021.00008](https://doi.org/10.1109/ICBAR55169.2021.00008).
- [118] L. Zhang and L. Liu. “Data Anomaly Detection Based on Isolation Forest Algorithm”. In: *Proceedings of the International Conference on Computation, Big-Data and Engineering 2022, ICCBE 2022* 26 (12 Dec. 2022), pp. 87–89. ISSN: 21682208. DOI: [10.1109/ICBE56101.2022.9888169](https://doi.org/10.1109/ICBE56101.2022.9888169).
- [119] J. S. Sunny, C. P. K. Patro, K. Karnani, S. C. Pingle, F. Lin, M. Anekoji, L. D. Jones, S. Kesari, and S. Ashili. *Anomaly Detection Framework for Wearables Data: A Perspective Review on Data Concepts, Data Analysis Algorithms and Prospects*. Feb. 2022. DOI: [10.3390/s22030756](https://doi.org/10.3390/s22030756).
- [120] A. Mahmoudzadeh, I. Azimi, A. M. Rahmani, and P. Liljeberg. “Lightweight photoplethysmography quality assessment for real-time IoT-based health monitoring using unsupervised anomaly detection”. In: *Procedia Computer Science* 184 (2021), pp. 140–147. ISSN: 18770509. DOI: [10.1016/j.procs.2021.03.025](https://doi.org/10.1016/j.procs.2021.03.025).
- [121] S. Scheurer, S. Tedesco, K. N. Brown, and B. O’Flynn. “Subject-dependent and -independent human activity recognition with person-specific and -independent models”. In: Association for Computing Machinery, Sept. 2019. ISBN: 9781450377140. DOI: [10.1145/3361684.3361689](https://doi.org/10.1145/3361684.3361689).
- [122] S. Scheurer, S. Tedesco, B. O’flynn, and K. N. Brown. “Comparing person-specific and independent models on subject-dependent and independent human activity recognition performance”. In: *Sensors (Switzerland)* 20 (13 July 2020), pp. 1–22. ISSN: 14248220. DOI: [10.3390/s20133647](https://doi.org/10.3390/s20133647).
- [123] W. Shi, C. Zhou, Y. Zhang, K. Li, X. Ren, H. Liu, and X. Ye. “Hybrid modeling on reconstitution of continuous arterial blood pressure using finger photoplethysmography”. In: *Biomedical Signal Processing and Control* 85 (Aug. 2023), p. 104972. ISSN: 17468094. DOI: [10.1016/j.bspc.2023.104972](https://doi.org/10.1016/j.bspc.2023.104972).
- [124] A. Olyanasab and M. Annabestani. “Leveraging Machine Learning for Personalized Wearable Biomedical Devices: A Review”. In: *Journal of Personalized Medicine* 14 (2 Feb. 2024). ISSN: 20754426. DOI: [10.3390/jpm14020203](https://doi.org/10.3390/jpm14020203).
- [125] D. Wang, X. Yang, J. Wu, and W. Wang. “Personalized Modeling of Blood Pressure With Photoplethysmography: An Error-Feedback Incremental Support Vector Regression Model”. In: *IEEE Internet of Things Journal* 11 (1 Jan. 2024), pp. 1732–1745. ISSN: 23274662. DOI: [10.1109/JIOT.2023.3290557](https://doi.org/10.1109/JIOT.2023.3290557).

- [126] J. Leitner, P.-H. Chiang, and S. Dey. “Personalized Blood Pressure Estimation Using Photoplethysmography: A Transfer Learning Approach”. In: *IEEE Journal of Biomedical and Health Informatics* 26 (1 Jan. 2022), pp. 218–228. ISSN: 2168-2194. DOI: [10.1109/JBHI.2021.3085526](https://doi.org/10.1109/JBHI.2021.3085526).
- [127] S. Abrar, C. K. Loo, N. Kubota, and G. A. Tahir. “A Personalised Blood Pressure Prediction System using Gaussian Mixture Regression and Online Recurrent Extreme Learning Machine”. In: IEEE, Sept. 2020, pp. 1–7. ISBN: 978-1-7281-8741-9. DOI: [10.1109/CcS49175.2020.9231328](https://doi.org/10.1109/CcS49175.2020.9231328).
- [128] C. Crowe, M. Sica, L. Kenny, B. O’Flynn, D. S. Mueller, S. Timmons, J. Barton, and S. Tedesco. “Cuff-Less Blood Pressure Monitoring in a Cohort of People with Parkinson’s Disease”. In: *2023 IEEE Sensors Applications Symposium (SAS)*. Institute of Electrical and Electronics Engineers Inc., 2023. DOI: [10.1109/SAS58821.2023.10253995](https://doi.org/10.1109/SAS58821.2023.10253995).
- [129] Honeywell. *MICROFORCE SENSOR COUPLING Technical Note*. URL: <https://www.honeywell.com/us/en/search?search=FMA&tab=All+Sites>.
- [130] Honeywell. *Digital Output Force Sensors SPI Communications*.
- [131] Honeywell. *FSA Series and FMA Series Force Sensors Diagnostics*. 2020. URL: <https://www.honeywell.com/us/en/search?search=FMA&tab=All+Sites>.
- [132] Honeywell. *FMA SERIES Datasheet*. URL: <https://www.honeywell.com/us/en/search?search=FMA&tab=All+Sites>.
- [133] *P-NUCLEO-WB55 STM32WB*. URL: www.st.com.
- [134] A. Valerio, I. Buraioli, A. Sanginario, D. Leone, G. Mingrone, A. Milan, and D. Demarchi. “A New True Wireless System for Real-Time Pulse Wave Velocity Assessment”. In: *IEEE SENSORS JOURNAL XX* (June 2024), p. 1. DOI: [10.1109/JSEN.2024.3415714](https://doi.org/10.1109/JSEN.2024.3415714).
- [135] I. M. Zota et al. “Arterial Stiffness Assessment Using the Arteriograph in Patients with Moderate–Severe OSA and Metabolic Syndrome—A Pilot Study”. In: *Journal of Clinical Medicine* 10 (18 Sept. 2021), p. 4238. ISSN: 2077-0383. DOI: [10.3390/jcm10184238](https://doi.org/10.3390/jcm10184238).
- [136] S. Bichali, A. Bruel, M. Boivin, G. Roussey, B. Romefort, J.-C. Rozé, and E. Allain-Launay. “Simplified pulse wave velocity measurement in children: Is the pOpmètre valid?” In: *PLOS ONE* 15 (3 Mar. 2020), e0230817. ISSN: 1932-6203. DOI: [10.1371/journal.pone.0230817](https://doi.org/10.1371/journal.pone.0230817).
- [137] H. Gyöngyösi et al. “Comparison of Different Cardiovascular Risk Score and Pulse Wave Velocity-Based Methods for Vascular Age Calculation”. In: *Heart Lung and Circulation* 30 (11 Nov. 2021), pp. 1744–1751. ISSN: 14442892. DOI: [10.1016/j.hlc.2021.06.518](https://doi.org/10.1016/j.hlc.2021.06.518).

- [138] K. S. Heffernan, L. Stoner, A. S. London, J. A. Augustine, and W. K. Lefferts. “Estimated pulse wave velocity as a measure of vascular aging”. In: *PLoS ONE* 18 (1 January Jan. 2023). ISSN: 19326203. DOI: [10.1371/journal.pone.0280896](https://doi.org/10.1371/journal.pone.0280896).
- [139] I. Buraioli, D. Lena, A. Sanginario, D. Leone, G. Mingrone, A. Milan, and D. Demarchi. “A New Noninvasive System for Clinical Pulse Wave Velocity Assessment: The Athos Device”. In: *IEEE transactions on biomedical circuits and systems* 15 (1 Feb. 2021), pp. 133–142. ISSN: 1940-9990. DOI: [10.1109/TBCAS.2021.3058010](https://doi.org/10.1109/TBCAS.2021.3058010). URL: <https://pubmed.ncbi.nlm.nih.gov/33560991/>.
- [140] D. Leone et al. “Accuracy of a new instrument for noninvasive evaluation of pulse wave velocity: the Arterial sTiffness faitHful tOol aSessment project”. In: *Journal of Hypertension* 39 (11 Nov. 2021), pp. 2164–2172. ISSN: 0263-6352. DOI: [10.1097/HJH.0000000000002925](https://doi.org/10.1097/HJH.0000000000002925).
- [141] D. S. Ouamer, M. K. Guerchani, A. Azaza, and S. Benkhedda. “Arterial stiffness assessed by pulse wave velocity in young athletes practicing endurance or intense resistance training”. In: *Science and Sports* 38 (3 May 2023), pp. 266–273. ISSN: 17784131. DOI: [10.1016/j.scispo.2022.02.003](https://doi.org/10.1016/j.scispo.2022.02.003).
- [142] M. Butlin and A. Qasem. “Large Artery Stiffness Assessment Using SphygmoCor Technology”. In: *Pulse* 4 (4 2016), pp. 180–192. ISSN: 2235-8676. DOI: [10.1159/000452448](https://doi.org/10.1159/000452448).
- [143] A. Sanginario, I. Buraioli, M. Pogliano, P. Natale, D. Leone, G. Mingrone, A. Milan, and D. Demarchi. “Live Demonstration: Wireless Device for Pulse Wave Velocity Evaluation”. In: *2023 IEEE International Symposium on Circuits and Systems (ISCAS)*. 2023, pp. 1–1. DOI: [10.1109/ISCAS46773.2023.10181368](https://doi.org/10.1109/ISCAS46773.2023.10181368).
- [144] *Bluetooth Core Specification Bluetooth® Specification*. 1999. URL: <https://www.bluetooth.com/specifications/adopted-specifications>.
- [145] *CELLEVIA BATTERIES LP401235*. URL: www.tme.eu.
- [146] *Datasheet Honeywell FMA Series FMAMSDXX005WCSC3*. URL: www.honeywell.com.
- [147] *Datasheet STLQ020*. URL: www.st.com.
- [148] *STM32WB15CC Multiprotocol wireless 32-bit MCU Arm®-based Cortex®-M4 with FPU, Bluetooth® 5.2 radio solution Datasheet-production data*. URL: www.st.com.
- [149] *AN5165-How to develop RF hardware using STM32WB microcontrollers*. URL: www.st.com.

- [150] *Datasheet NX2012SA NDK -32.768 kHz crystal oscillator*. URL: <https://www.ndk.com/en/>.
- [151] *Datasheet NDK high speed crystal oscillator NX2016SA-32M-EXS00A-CS06465*. URL: <https://www.ndk.com/en/>.
- [152] *MLPFWB55 01E3*. URL: www.st.com.
- [153] *Datasheet MCP738312*. URL: www.microchip.com.
- [154] *STM32WB55xx STM32WB35xx Multiprotocol wireless 32-bit MCU Arm®-based Cortex®-M4 with FPU, Bluetooth® 5.3 and 802.15.4 radio solution Datasheet-production data*. URL: www.st.com.
- [155] Stmicroelectronics. *STM32WB BLE stack programming guidelines - Programming manual*. URL: www.st.com.
- [156] *How to build a Bluetooth® Low Energy mesh application for STM32WB Series microcontrollers*. URL: www.st.com.
- [157] P. Bulić, G. Kojek, and A. Biasizzo. “Data transmission efficiency in blue-tooth low energy versions”. In: *Sensors (Switzerland)* 19 (17 Sept. 2019). ISSN: 14248220. DOI: [10.3390/s19173746](https://doi.org/10.3390/s19173746).
- [158] D. Demarchi, I. Buraioli, A. Milan, F. Veglio, and F. Vallelonga. *Method and system for real-time measurement of a sphygmoc wave velocity*. international patent - Priority number: 102020000027846. 2020.
- [159] *Datasheet NI-USB-6259 Specifications*. URL: <https://www.ni.com>.
- [160] B. Spronck et al. “2024 Recommendations for Validation of Noninvasive Arterial Pulse Wave Velocity Measurement Devices”. In: *Hypertension* 81 (1 Jan. 2024), pp. 183–192. ISSN: 0194-911X. DOI: [10.1161/HYPERTENSIONAHA.123.21618](https://doi.org/10.1161/HYPERTENSIONAHA.123.21618).
- [161] M. Ring, M. J. Eriksson, P. Farahnak, L.-O. Farnebo, I.-L. Nilsson, and K. Caidahl. “Arterial Stiffness Evaluation by SphygmoCor and Arteriograph”. In: *Heart, Lung and Circulation* 17 (2008), S16–S17. ISSN: 14439506. DOI: [10.1016/j.hlc.2008.05.036](https://doi.org/10.1016/j.hlc.2008.05.036).
- [162] M.-R. Rezai, B. R. Cowan, N. Sherratt, J. D. Finn, F. C. Wu, and J. K. Cruickshank. “A magnetic resonance perspective of the pulse wave transit time by the Arteriograph device and potential for improving aortic length estimation for central pulse wave velocity”. In: *Blood Pressure Monitoring* 18 (2 Apr. 2013), pp. 111–118. ISSN: 1359-5237. DOI: [10.1097/MBP.0b013e32835d3663](https://doi.org/10.1097/MBP.0b013e32835d3663).
- [163] P. Salvi et al. “Noninvasive Estimation of Aortic Stiffness Through Different Approaches”. In: *Hypertension* 74 (1 July 2019), pp. 117–129. ISSN: 0194-911X. DOI: [10.1161/HYPERTENSIONAHA.119.12853](https://doi.org/10.1161/HYPERTENSIONAHA.119.12853).

- [164] A. Valerio, I. Buraioli, A. Sanginario, D. Leone, G. Mingrone, A. Milan, and D. Demarchi. “Live Demonstration: Wireless Device for Clinical Pulse Wave Velocity Evaluations”. In: *2022 IEEE Biomedical Circuits and Systems Conference (BioCAS)*. 2022, pp. 247–247. DOI: [10.1109/BioCAS54905.2022.9948659](https://doi.org/10.1109/BioCAS54905.2022.9948659).
- [165] A. Valerio, I. Buraioli, A. Sanginario, G. Mingrone, D. Leone, A. Milan, and D. Demarchi. “A region-based cross-correlation approach for tonometric carotid–femoral Pulse Wave Velocity Assessment”. In: *Biomedical Signal Processing and Control* 93 (2024), p. 106161. ISSN: 1746-8094. DOI: <https://doi.org/10.1016/j.bspc.2024.106161>. URL: <https://www.sciencedirect.com/science/article/pii/S1746809424002192>.
- [166] A. Laina, K. Stellos, and K. Stamatelopoulos. “Vascular ageing: Underlying mechanisms and clinical implications”. In: *Experimental gerontology* 109 (Aug. 2018), pp. 16–30. ISSN: 1873-6815. DOI: [10.1016/J.EXGER.2017.06.007](https://doi.org/10.1016/J.EXGER.2017.06.007). URL: <https://pubmed.ncbi.nlm.nih.gov/28624356/>.
- [167] B. J. North and D. A. Sinclair. “The intersection between aging and cardiovascular disease”. In: *Circulation research* 110 (8 Apr. 2012), pp. 1097–1108. ISSN: 1524-4571. DOI: [10.1161/CIRCRESAHA.111.246876](https://doi.org/10.1161/CIRCRESAHA.111.246876). URL: <https://pubmed.ncbi.nlm.nih.gov/22499900/>.
- [168] J. Blacher, A. P. Guerin, B. Pannier, S. J. Marchais, M. E. Safar, and G. M. London. “Impact of aortic stiffness on survival in end-stage renal disease”. In: *Circulation* 99 (18 May 1999), pp. 2434–2439. ISSN: 1524-4539. DOI: [10.1161/01.CIR.99.18.2434](https://doi.org/10.1161/01.CIR.99.18.2434). URL: <https://pubmed.ncbi.nlm.nih.gov/10318666/>.
- [169] P. M. Nabeel, V. R. Kiran, J. Joseph, V. V. Abhidev, and M. Sivaprakasam. “Local Pulse Wave Velocity: Theory, Methods, Advancements, and Clinical Applications”. In: *IEEE reviews in biomedical engineering* 13 (2020), pp. 74–112. ISSN: 1941-1189. DOI: [10.1109/RBME.2019.2931587](https://doi.org/10.1109/RBME.2019.2931587). URL: <https://pubmed.ncbi.nlm.nih.gov/31369386/>.
- [170] Y. C. Chiu, P. W. Arand, S. G. Shroff, T. Feldman, and J. D. Carroll. “Determination of pulse wave velocities with computerized algorithms”. In: *American heart journal* 121 (5 1991), pp. 1460–1470. ISSN: 0002-8703. DOI: [10.1016/0002-8703\(91\)90153-9](https://doi.org/10.1016/0002-8703(91)90153-9). URL: <https://pubmed.ncbi.nlm.nih.gov/2017978/>.
- [171] S. C. Millasseau, A. D. Stewart, S. J. Patel, S. R. Redwood, and P. J. Chowienczyk. “Evaluation of carotid-femoral pulse wave velocity: influence of timing algorithm and heart rate”. In: *Hypertension (Dallas, Tex. : 1979)* 45 (2 Feb. 2005), pp. 222–226. ISSN: 1524-4563. DOI: [10.1161/01.HYP.0000154229.97341.D2](https://doi.org/10.1161/01.HYP.0000154229.97341.D2). URL: <https://pubmed.ncbi.nlm.nih.gov/15642772/>.

- [172] P. Salvi, E. Magnani, F. Valbusa, D. Agnoletti, C. Alecu, L. Joly, and A. Benetos. “Comparative study of methodologies for pulse wave velocity estimation”. In: *Journal of human hypertension* 22 (10 2008), pp. 669–677. ISSN: 0950-9240. DOI: [10.1038/JHH.2008.42](https://doi.org/10.1038/JHH.2008.42). URL: <https://pubmed.ncbi.nlm.nih.gov/18528411/>.
- [173] L. Xu et al. “Improving the accuracy and robustness of carotid-femoral pulse wave velocity measurement using a simplified tube-load model”. In: *Scientific reports* 12 (1 Dec. 2022). ISSN: 2045-2322. DOI: [10.1038/S41598-022-09256-Z](https://doi.org/10.1038/S41598-022-09256-Z). URL: <https://pubmed.ncbi.nlm.nih.gov/35338246/>.
- [174] H. Shin and A. Choi. “Calculation and Validation of Continuous Pulse Transit Time Based on Normalized Pulse Wave Velocity”. In: *IEEE Access* 8 (2020), pp. 221632–221639. ISSN: 21693536. DOI: [10.1109/ACCESS.2020.3041498](https://doi.org/10.1109/ACCESS.2020.3041498).
- [175] P. Charlton, J. Mariscal Harana, S. Vennin, Y. Li, P. Chowienczyk, and A. J. “Modeling arterial pulse waves in healthy aging: a database for in silico evaluation of hemodynamics and pulse wave indexes.” In: *Am. J. Physiol. Heart. Circ. Physiol.* 82.1 (2019), pp. 1062–1065.
- [176] J. A. Chirinos and N. Sweitzer. “Ventricular–Arterial Coupling in Chronic Heart Failure”. In: *Cardiac Failure Review* 03 (01 2017), p. 12. ISSN: 2057-7540. DOI: [10.15420/cfr.2017:4:2](https://doi.org/10.15420/cfr.2017:4:2). URL: <https://www.cfrjournal.com/articles/ventricular-arterial-coupling-chronic-heart-failure>.
- [177] Y. Chiu, P. W. Arand, S. G. Shroff, T. Feldman, and J. D. Carroll. “Determination of pulse wave velocities with computerized algorithms”. In: *American Heart Journal* 121.5 (1991), pp. 1460–1470. ISSN: 0002-8703. DOI: [https://doi.org/10.1016/0002-8703\(91\)90153-9](https://doi.org/10.1016/0002-8703(91)90153-9). URL: <https://www.sciencedirect.com/science/article/pii/S0002870391901539>.
- [178] S. Laurent et al. “Expert consensus document on arterial stiffness: Methodological issues and clinical applications”. In: *European Heart Journal* 27.21 (2006). Cited by: 4759; All Open Access, Bronze Open Access, pp. 2588–2605. DOI: [10.1093/eurheartj/ehl254](https://doi.org/10.1093/eurheartj/ehl254).
- [179] C. Argyriou, E. Georgakarakos, G. S. Georgiadis, N. Schoretsanitis, and M. K. Lazarides. “The Effect of Revascularization on the Hemodynamic Profile of Patients with Infrarenal Aortic Occlusion”. In: *Annals of Vascular Surgery* 43 (Aug. 2017), pp. 210–217. ISSN: 08905096. DOI: [10.1016/j.avsg.2016.11.025](https://doi.org/10.1016/j.avsg.2016.11.025).
- [180] S. Zaunseder, A. Vehkaoja, V. Fleischhauer, and C. H. Antink. “Signal-to-noise ratio is more important than sampling rate in beat-to-beat interval estimation from optical sensors”. In: *Biomedical Signal Processing and Control* 74 (Apr. 2022), p. 103538. ISSN: 17468094. DOI: [10.1016/j.bspc.2022.103538](https://doi.org/10.1016/j.bspc.2022.103538).

- [181] K. Kazemi, J. Laitala, I. Azimi, P. Liljeberg, and A. M. Rahmani. “Robust PPG Peak Detection Using Dilated Convolutional Neural Networks”. In: *Sensors* 22 (16 Aug. 2022), p. 6054. ISSN: 1424-8220. DOI: [10.3390/s22166054](https://doi.org/10.3390/s22166054).
- [182] *MAX86140 MAX86141 - Best-in-Class Optical Pulse Oximeter and Heart-Rate Sensor for Wearable Health*. URL: www.maximintegrated.com.
- [183] *SFH 7015 CN*.
- [184] *CT DBLP31.12*.
- [185] *Silicon PIN Photodiode*. URL: www.vishay.com/doc?91000.
- [186] *Silicon PIN Photodiode*. URL: www.vishay.com/doc91000.
- [187] *SFH 2713 CHIPLELED*. URL: www.osram-os.com.
- [188] *STM32WB55xx STM32WB35xx Multiprotocol wireless 32-bit MCU Arm - based Cortex -M4 with FPU, Bluetooth 5.3 and 802.15.4 radio solution Datasheet-production data*. URL: www.st.com.
- [189] O. Semiconductor. *NCP170 - LDO Regulator - Ultra-Low IQ, CMOS 150 mA*. URL: www.onsemi.com.
- [190] A. Chandrasekhar, M. Yavarimanesh, K. Natarajan, J. O. Hahn, and R. Mukkamala. “PPG Sensor Contact Pressure Should Be Taken into Account for Cuff-Less Blood Pressure Measurement”. In: *IEEE Transactions on Biomedical Engineering* 67 (11 Nov. 2020), pp. 3134–3140. ISSN: 15582531. DOI: [10.1109/TBME.2020.2976989](https://doi.org/10.1109/TBME.2020.2976989).
- [191] V. Figini, S. Galici, D. Russo, I. Centonze, M. Visintin, and G. Pagana. “Improving Cuff-Less Continuous Blood Pressure Estimation with Linear Regression Analysis”. In: *Electronics (Switzerland)* 11 (9 May 2022). ISSN: 20799292. DOI: [10.3390/electronics11091442](https://doi.org/10.3390/electronics11091442).
- [192] *Biosignalsplux-8-Channel Hub Datasheet*. URL: <https://www.pluxbiosignals.com/collections/shop/products/8-channel-biosignals-kit>.
- [193] *Blood Volume Pulse (BVP) Sensor Data Sheet*. 2015. URL: <http://biosignalsplux.com/>.
- [194] *fNIRS Sensor Data Sheet*. 2017. URL: <http://biosignalsplux.com/>.
- [195] A. Mousavi, O. T. Inan, R. Mukkamala, and J. O. Hahn. “A Physical Model-Based Approach to One-Point Calibration of Pulse Transit Time to Blood Pressure”. In: *IEEE Transactions on Biomedical Engineering* (2023). ISSN: 15582531. DOI: [10.1109/TBME.2023.3307658](https://doi.org/10.1109/TBME.2023.3307658).
- [196] G. S. Stergiou et al. *Cuffless blood pressure measuring devices: Review and statement by the European Society of Hypertension Working Group on Blood Pressure Monitoring and Cardiovascular Variability*. Aug. 2022. DOI: [10.1097/HJH.0000000000003224](https://doi.org/10.1097/HJH.0000000000003224).

- [197] Z. H. Wang and Y. C. Wu. “A Novel Rapid Assessment of Mental Stress by Using PPG Signals Based on Deep Learning”. In: *IEEE Sensors Journal* 22 (21 Nov. 2022), pp. 21232–21239. ISSN: 15581748. DOI: [10.1109/JSEN.2022.3208427](https://doi.org/10.1109/JSEN.2022.3208427).
- [198] *Datasheet Withings BPM Connect*. URL: <https://www.withings.com/it/en/bpm-connect>.
- [199] S. Gedam and S. Paul. *A Review on Mental Stress Detection Using Wearable Sensors and Machine Learning Techniques*. 2021. DOI: [10.1109/ACCESS.2021.3085502](https://doi.org/10.1109/ACCESS.2021.3085502).
- [200] W. Li, Q. Zhang, H. Qiao, D. Jin, R. K. Ngetich, J. Zhang, Z. Jin, and L. Li. “Dual n-back working memory training evinces superior transfer effects compared to the method of loci”. In: *Scientific Reports* 11 (1 Dec. 2021). ISSN: 20452322. DOI: [10.1038/s41598-021-82663-w](https://doi.org/10.1038/s41598-021-82663-w).
- [201] J. D. Parreira et al. “A proof-of-concept investigation of multi-modal physiological signal responses to acute mental stress”. In: *Biomedical Signal Processing and Control* 85 (Aug. 2023). ISSN: 17468108. DOI: [10.1016/j.bspc.2023.105001](https://doi.org/10.1016/j.bspc.2023.105001).
- [202] J. Rodrigues, H. Liu, D. Folgado, D. Belo, T. Schultz, and H. Gamboa. “Feature-Based Information Retrieval of Multimodal Biosignals with a Self-Similarity Matrix: Focus on Automatic Segmentation”. In: *Biosensors* 12 (12 Dec. 2022), p. 1182. ISSN: 2079-6374. DOI: [10.3390/bios12121182](https://doi.org/10.3390/bios12121182).
- [203] D. Folgado, M. Barandas, M. Antunes, M. L. Nunes, H. Liu, Y. Hartmann, T. Schultz, and H. Gamboa. “TSSEARCH: Time Series Subsequence Search Library”. In: *SoftwareX* 18 (June 2022), p. 101049. ISSN: 23527110. DOI: [10.1016/j.softx.2022.101049](https://doi.org/10.1016/j.softx.2022.101049).
- [204] H. Barki and W. Y. Chung. “Mental Stress Detection Using a Wearable In-Ear Plethysmography”. In: *Biosensors* 13 (3 Mar. 2023). ISSN: 20796374. DOI: [10.3390/bios13030397](https://doi.org/10.3390/bios13030397).
- [205] C. Orphanidou. *SPRINGER BRIEFS IN BIOENGINEERING Signal Quality Assessment in Physiological Monitoring State of the Art and Practical Considerations*. URL: <http://www.springer.com/series/10280>.
- [206] P. H. Charlton, P. Celka, B. Farukh, P. Chowienczyk, and J. Alastruey. “Assessing mental stress from the photoplethysmogram: A numerical study”. In: *Physiological Measurement* 39 (5 May 2018). ISSN: 13616579. DOI: [10.1088/1361-6579/aabe6a](https://doi.org/10.1088/1361-6579/aabe6a).
- [207] E. Finnegan, S. Davidson, M. Harford, P. Watkinson, L. Tarassenko, and M. Villarreal. “Features from the photoplethysmogram and the electrocardiogram for estimating changes in blood pressure”. In: *Scientific Reports* 13 (1 Dec. 2023). ISSN: 20452322. DOI: [10.1038/s41598-022-27170-2](https://doi.org/10.1038/s41598-022-27170-2).

- [208] E. Mejía-Mejía et al. *Photoplethysmography Signal Processing and Synthesis*.
- [209] F. Miao, Z. D. Liu, J. K. Liu, B. Wen, Q. Y. He, and Y. Li. “Multi-Sensor Fusion Approach for Cuff-Less Blood Pressure Measurement”. In: *IEEE Journal of Biomedical and Health Informatics* 24 (1 Jan. 2020), pp. 79–91. ISSN: 21682208. DOI: [10.1109/JBHI.2019.2901724](https://doi.org/10.1109/JBHI.2019.2901724).
- [210] L. Zhao, C. Liang, Y. Huang, G. Zhou, Y. Xiao, N. Ji, Y. T. Zhang, and N. Zhao. *Emerging sensing and modeling technologies for wearable and cuffless blood pressure monitoring*. Dec. 2023. DOI: [10.1038/s41746-023-00835-6](https://doi.org/10.1038/s41746-023-00835-6).
- [211] *Developing Personalized Models of Blood Pressure Estimation from Wearable Sensors Data Using Minimally-trained Domain Adversarial Neural Networks*.
- [212] M. Salah, O. A. Omer, L. Hassan, M. Ragab, A. M. Hassan, and A. Abdelreheem. “Beat-Based PPG-ABP Cleaning Technique for Blood Pressure Estimation”. In: *IEEE Access* 10 (2022), pp. 55616–55626. ISSN: 21693536. DOI: [10.1109/ACCESS.2022.3175436](https://doi.org/10.1109/ACCESS.2022.3175436).
- [213] J. M. Raja, C. Elsakr, S. Roman, B. Cave, I. Pour-Ghaz, A. Nanda, M. Maturana, and R. N. Khouzam. “Apple Watch, Wearables, and Heart Rhythm: where do we stand?” In: *Annals of Translational Medicine* 7 (17 Sept. 2019), pp. 417–417. ISSN: 23055839. DOI: [10.21037/atm.2019.06.79](https://doi.org/10.21037/atm.2019.06.79).
- [214] D. Pollreisz and N. TaheriNejad. “Detection and Removal of Motion Artifacts in PPG Signals”. In: *Mobile Networks and Applications* 27 (2 Apr. 2022), pp. 728–738. ISSN: 15728153. DOI: [10.1007/s11036-019-01323-6](https://doi.org/10.1007/s11036-019-01323-6).
- [215] M. Wang, Z. Li, Q. Zhang, and G. Wang. “Removal of motion artifacts in photoplethysmograph sensors during intensive exercise for accurate heart rate calculation based on frequency estimation and notch filtering”. In: *Sensors (Switzerland)* 19 (15 Aug. 2019). ISSN: 14248220. DOI: [10.3390/s19153312](https://doi.org/10.3390/s19153312).
- [216] F. Peng, Z. Zhang, X. Gou, H. Liu, and W. Wang. “Motion artifact removal from photoplethysmographic signals by combining temporally constrained independent component analysis and adaptive filter”. In: *BioMedical Engineering Online* 13 (1 Apr. 2014). ISSN: 1475925X. DOI: [10.1186/1475-925X-13-50](https://doi.org/10.1186/1475-925X-13-50).
- [217] Z. Guo, C. Ding, X. Hu, and C. Rudin. “A supervised machine learning semantic segmentation approach for detecting artifacts in plethysmography signals from wearables”. In: *Physiological Measurement* 42 (12 Dec. 2021). ISSN: 13616579. DOI: [10.1088/1361-6579/ac3b3d](https://doi.org/10.1088/1361-6579/ac3b3d).

- [218] C. H. Lubba, S. S. Sethi, P. Knaute, S. R. Schultz, B. D. Fulcher, and N. S. Jones. “catch22: CAnonical Time-series CHaracteristics: Selected through highly comparative time-series analysis”. In: *Data Mining and Knowledge Discovery* 33 (6 Nov. 2019), pp. 1821–1852. ISSN: 1573756X. DOI: [10.1007/s10618-019-00647-x](https://doi.org/10.1007/s10618-019-00647-x).
- [219] O. Y. Rodionova, P. Oliveri, and A. L. Pomerantsev. “Rigorous and compliant approaches to one-class classification”. In: *Chemometrics and Intelligent Laboratory Systems* 159 (Dec. 2016), pp. 89–96. ISSN: 01697439. DOI: [10.1016/j.chemolab.2016.10.002](https://doi.org/10.1016/j.chemolab.2016.10.002).
- [220] G. O. Campos, A. Zimek, J. Sander, R. J. G. B. Campello, B. Micenková, E. Schubert, I. Assent, and M. E. Houle. “On the evaluation of unsupervised outlier detection: measures, datasets, and an empirical study”. In: *Data Mining and Knowledge Discovery* 30 (4 July 2016), pp. 891–927. ISSN: 1384-5810. DOI: [10.1007/s10618-015-0444-8](https://doi.org/10.1007/s10618-015-0444-8).
- [221] F. T. Liu, K. M. Ting, and Z.-H. Zhou. “Isolation Forest”. In: *2008 Eighth IEEE International Conference on Data Mining* (Dec. 2008), pp. 413–422. DOI: [10.1109/ICDM.2008.17](https://doi.org/10.1109/ICDM.2008.17).
- [222] E. H. Budiarto, A. E. Permanasari, and S. Fauziati. “Unsupervised Anomaly Detection Using K-Means, Local Outlier Factor and One Class SVM”. In: *2019 5th International Conference on Science and Technology (ICST)* (July 2019), pp. 1–5. DOI: [10.1109/ICST47872.2019.9166366](https://doi.org/10.1109/ICST47872.2019.9166366).
- [223] A. Rezgui. “Scaling Personalized Machine Learning through DTW Clustering: Predicting Glycemia Levels as an Example”. In: *IEEE*, Dec. 2023, pp. 5356–5364. DOI: [10.1109/BigData59044.2023.10386408](https://doi.org/10.1109/BigData59044.2023.10386408). URL: <https://ieeexplore.ieee.org/document/10386408/>.
- [224] R. G. Bangani, V. Menon, and E. Jovanov. “Personalized Stress Monitoring AI System for Healthcare Workers”. In: *Institute of Electrical and Electronics Engineers Inc.*, 2021, pp. 2992–2997. ISBN: 9781665401265. DOI: [10.1109/BIBM52615.2021.9669321](https://doi.org/10.1109/BIBM52615.2021.9669321).
- [225] A. Avolio, J. Zuo, I. Tan, and M. Butlin. “Pathway for Elimination of Distance Measurement in Studies of Pulse Wave Velocity”. In: *Hypertension* 71 (5 May 2018), pp. 819–821. ISSN: 0194-911X. DOI: [10.1161/HYPERTENSIONAHA.118.10839](https://doi.org/10.1161/HYPERTENSIONAHA.118.10839).
- [226] W. Jin, P. Chowienczyk, and J. Alastruey. “Estimating pulse wave velocity from the radial pressure wave using machine learning algorithms”. In: *PLoS ONE* 16 (6 June 2021). ISSN: 19326203. DOI: [10.1371/journal.pone.0245026](https://doi.org/10.1371/journal.pone.0245026).

- [227] V. Bikia, T. Fong, R. E. Climie, R. M. Bruno, B. Hametner, C. Mayer, D. Terentes-Printzios, and P. H. Charlton. “Leveraging the potential of machine learning for assessing vascular ageing: State-of-The-Art and future research”. In: *European Heart Journal - Digital Health* 2 (4 Dec. 2021), pp. 676–690. ISSN: 26343916. DOI: [10.1093/ehjdh/ztab089](https://doi.org/10.1093/ehjdh/ztab089).
- [228] J. M. Vargas, M. A. Bahloul, and T. M. Laleg-Kirati. “A learning-based image processing approach for pulse wave velocity estimation using spectrogram from peripheral pulse wave signals: An in silico study”. In: *Frontiers in Physiology* 14 (2023). ISSN: 1664042X. DOI: [10.3389/fphys.2023.1100570](https://doi.org/10.3389/fphys.2023.1100570).

This Ph.D. thesis has been typeset by means of the \TeX -system facilities. The typesetting engine was \pdfL\TeX . The document class was `toptesi`, by Claudio Beccari, with option `tipotesi=scudo`. This class is available in every up-to-date and complete \TeX -system installation.